ISSN: 1847-9286
Open Access Journal
www.jese-online.org

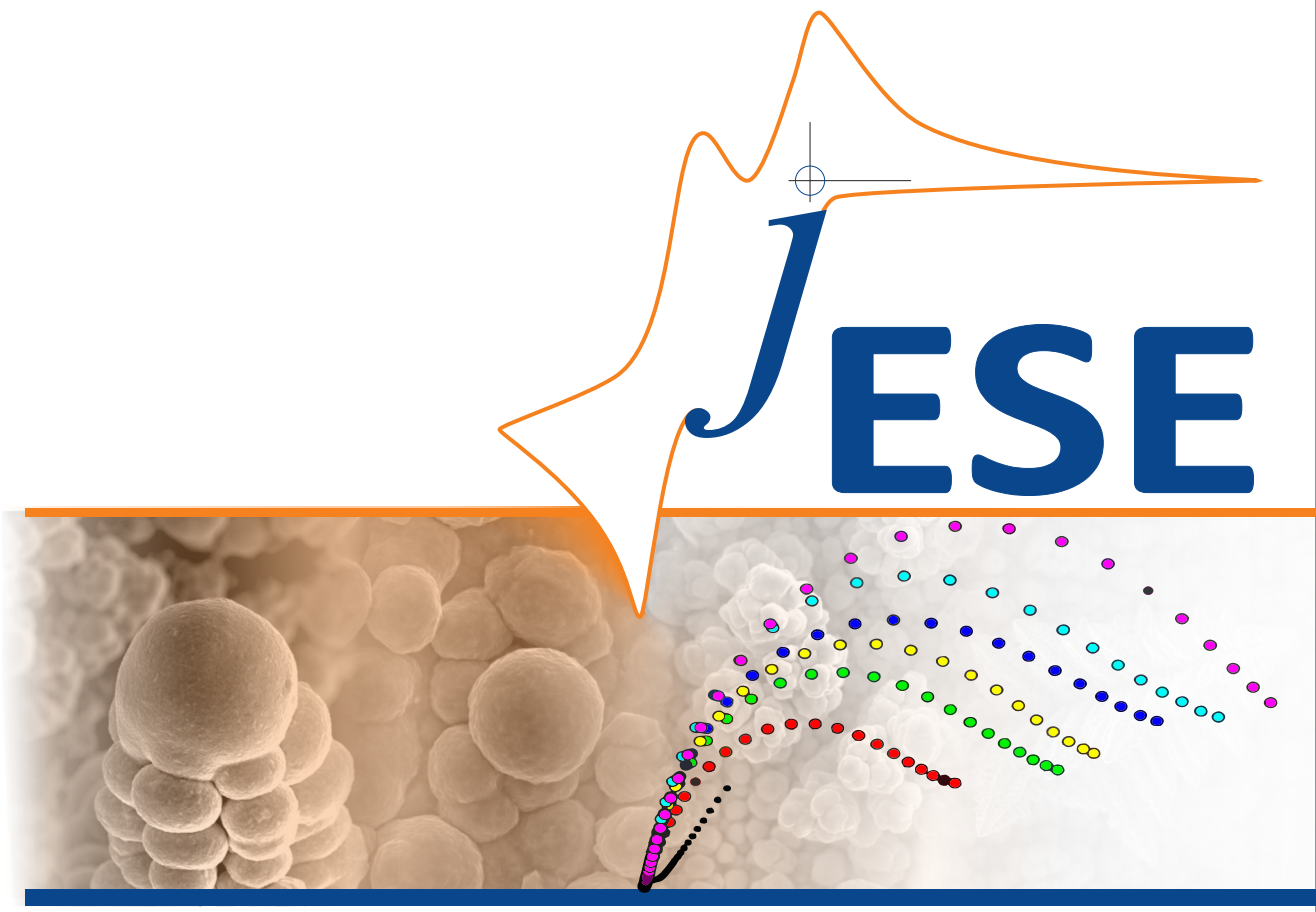

Journal of Electrochemical Science and Engineering

J. Electrochem. Sci. Eng. **14**(**2**) 2024, 119-273

IAPC Publishing

J. Electrochem. Sci. Eng. **14(2)** (2024) 119-133; http://dx.doi.org/10.5599/jese.2145

Open Access : : ISSN 1847-9286
www.jESE-online.org

Original scientific paper

Fe_3O_4 nanoparticles decorated reduced graphene oxide and carbon nanotubes-based composite for sensitive detection of imatinib in plasma and urine

Nasim Naderi[1], Bahare Sabeti[1] and Fereshteh Chekin[2,✉]

[1]*Department of Pharmacy, Ayatollah Amoli Branch, Islamic Azad University, Amol, Iran*
[2]*Department of Chemistry, Ayatollah Amoli Branch, Islamic Azad University, Amol, Iran*

Corresponding author: ✉fchekin@yahoo.com; Tel.: +981 143 217 076

Received: October 25, 2023; Accepted: November 30, 2023; Published: December 20, 2023

Abstract

In this study, a new reduced graphene oxide (rGO) has been synthesized via a facile and environmentally friendly process using Callicarpa maingayi leaf extract. A novel magnetic catalyst based on Fe_3O_4 nanoparticles-reduced graphene oxide&carbon nanotubes ((Fe_3O_4--(rGO&CNT)) was prepared and characterized by hydrothermal method. The Fe_3O_4 nanoparticles with an average size of 25 to 40 nm were placed on carbon nanotubes and reduced graphene oxide sheets, while carbon nanotubes inserted between the reduced graphene oxide sheets effectively prevented their aggregation. The (Fe_3O_4-(rGO&CNT) composite has a large surface area and good electrocatalytic properties, suiting for the detection and determination of imatinib (IM) anticancer drug by voltammetry method. Under optimized conditions, good linearity was achieved in the concentration range of 0.1 to 40 µmol L^{-1} and the limit of detection and sensitivity were 57 nmol L^{-1} and 3.365 µA $µM^{-1}$, respectively. Furthermore, the fabricated sensor demonstrated acceptable reproducible behaviour and accuracy and a high level of stability during all electrochemical tests. In addition, the proposed method was applied for the detection of IM in biological samples and the recoveries were 94.0 to 98.5 %, with relative standard deviations of 2.1 to 4.4 %.

Keywords

Magnetite/carbon nanocomposite, electrochemical sensor; imatinib drug; real samples

Introduction

Cancer is one of the most important diseases facing humanity today. Cancer is lethal because its cells are uncontrolled and proliferate indefinitely and spread throughout the body [1,2]. Cytostatic agents are the most commonly used class of anticancer drugs. Their purpose is to inhibit the growth of cancer cells. However, the widespread use of cytostatic agents has caused some other effects, such as on environmental toxicology [3]. Among them, imatinib (IM), with the chemical structure shown in Figure 1, is a specific inhibitor. Imatinib (4-[(4-methylpiperazin-1-yl) methyl]-N-[4-methyl-

3-[(4-pyridin-3-ylpyrimidin-2-yl)amino]phenyl]benzamide) is used to treat chronic myeloid leukemia (CML) and diseases such as gastrointestinal stromal tumours [4]. Imatinib, known as Gleevec, is a chemotherapy drug used to treat some cancers. This drug was approved by the Food and Drug Administration (FDA) to treat different cancers [5]. By inhibiting the activity of synthetic tyrosine kinase, specifically designed to inhibit Bcr-Abl fusion protein, it reduces cell growth or apoptosis in some cancer cells [6]. IM is a drug for anticancer treatment, used selectively to annihilate cancer cells instead of damaging them by rapidly dividing cells [7].

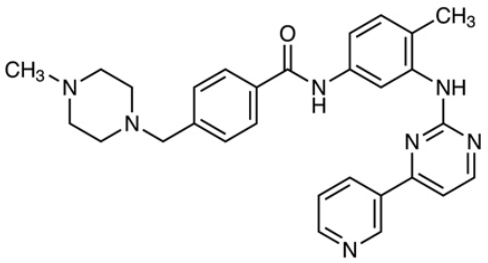

Figure 1. *Chemical structure of imatinib*

A number of analytical techniques have been applied to IM analysis, such as fluorescence, liquid chromatography, capillary electrophoresis and UV-Vis spectroscopy methods [8-12]. Owing to the sites with an electroactive nature on the IM surface, the electrochemical procedure has been offered for this drug detection. Therefore, selecting an appropriate method with sensitivity and efficiency in detection and reducing operating costs to evaluate lower IM values is a challenging endeavour. Several electrochemical investigations based on electrochemical sensors have been performed to date [13-16].

Carbon electrodes have a stable electrochemical window and do not react easily with other substances [17,18]. However, the electrochemical signal of ordinary carbon electrodes is weak, so it is difficult to meet the demand for highly sensitive detection [19]. Modification of the surface of ordinary carbon electrodes is a common method to improve the electrochemical activity of sensors. Recent studies have shown that modification of carbon nanomaterials on the surface of electrodes can increase electrical conductivity. Among carbon nanomaterials, carbon nanotubes (CNTs) are wholly employed as conductors due to their attractive and useful characteristics. The high chemical stability, excellent mechanical properties, high surface area, and prominent electrical conductivity make them appropriate for employment in electrochemical procedures [20]. It is known that CNTs promote electron transfer reactions when used as electrode-modifying material [21]. They display a highly hydrophobic surface by π-conjugative structure. This distinctive feature of CNTs could increase their ability to interact with some compounds *via* hydrophobic and/or π-π bonding.

Reduced graphene oxide (rGO) is a nanostructured material with high surface area, excellent thermal and mechanical stability, and remarkable electrical conductivity [22]. The rGO- has a more specific surface area and can easily be hybridized with Fe_3O_4 nanoparticles to form heterostructures [23]. The Fe_3O_4&rGO nanocomposites, with the advantages of magnetism and conductivity, could be easily adhered to the electrode surface to achieve the direct redox reactions and electrocatalytic behavior of analytes adsorbed on the modified surface [24]. Moreover, the functional groups (COOH and OH) of rGO allow it to conjugate with various molecules and act as an excellent performance carrier, while nanoparticles can be highly dispersed on its surface. The charge transfer at the interface of these hybrid materials can provide a synergistic effect to bring properties different from those of each component [25].

To the best of our knowledge, there are no prior reports in the literature on the electrocatalytic behavior of Fe_3O_4-(rGO&CNT) nanocomposites. In this work, the *Callicarpa maingayi* leaf extract is chosen as a reducing agent to reduce graphene oxide to the reduced graphene oxide (rGO) by a one-step method. By combining CNT tubes, rGO sheets and Fe_3O_4 nanoparticles, an excellent nanocomposite was created with high surface area and good conductivity to improve the surface of electrodes. The prepared modified electrode demonstrated remarkable electrocatalytic activity for the detection of IM in biological samples with reasonable analytical results.

Experimental

Materials

Multi-walled carbon nanotubes (MWCNTs, outer diameter: 20-40 nm, length: 5-15 µm, >97 %) were purchased from Shenzhen Nano-Technologies Port Co., Ltd. (China). Graphene oxide was purchased from Nano Materials Pioneers (Iran). The *Callicarpa maingayi* leaves were obtained from Kuala Lumpur, Malaysia. Imatinib ($C_{29}H_{31}N_7O$, 98 %), potassium hexacyanoferrate (II) ($[K_4Fe(CN)_6$, 98.5 %]), phosphoric acid (H_3PO_4, >99 %), sodium dihydrogen phosphate (NaH_2PO_4, >98 %), disodium hydrogen phosphate (Na_2HPO_4, >99 %), sodium phosphate (Na_3PO_4, >99 %) and graphite powder (99.99 %) were purchased from Sigma-Aldrich (Germany) and used as received. Human plasma samples were kindly provided by the clinical laboratory tests (Amol, Iran). The samples were stored at 4 °C.

Apparatus

Surface morphology and chemical composition of the nanocomposites were examined by a scanning electron microscope of MIRATESCAN-XMU (Czech Republic) combined with EDX (energy-dispersive X-ray spectroscopy) machine. Electrochemical measurements were performed with a potentiostat/galvanostat (Sama 500-c Electrochemical Analysis system, Sama, Iran). A conventional three-electrode configuration consisting of Ag|AgCl|KCl3M as the reference electrode, a platinum wire as the auxiliary electrode and Fe_3O_4-(rGO&CNT) modified CPE as the working electrode was employed. UV-Vis spectra of samples were recorded by UV-Vis spectrophotometer (UV-1900, Shimadzu Co., Japan). X-ray diffraction measurement was recorded on a Bruker D8-Advance X-ray diffractometer (Germany).

Synthesis of Fe_3O_4-(rGO&CNT) composite

The reduced graphene oxide was prepared according to previous works [26,27]. The amount of 10 g of fresh *Callicarpa maingayi* leaves were crushed, transferred into a round bottom flask containing 100 mL ionized water, and then placed in an ultrasound bath (60 kHz frequency) at 50 °C for 60 min. After completion of sonication, the mixture was allowed to cool down to room temperature and filtered to obtain a yellowish-green colour extract. 10 mg GO was added to the 50 mL extract and sonicated for 30 min at 25 °C in order to disperse the GO uniformly throughout the extract. The mixture was refluxed for 6 h at 50 °C until the suspension solution colour changed to brown-black. The product (rGO) was filtrated, washed with water and dried in the oven at 100 °C overnight. To 10 mL of rGO (1 mg mL^{-1}), 10 mg of CNT was added and the mixture was sonicated for 45 min at 25 °C. The product (rGO&CNT) was filtered, washed with water and dried in the oven at 100 °C overnight. For functionalization of rGO&CNT composite by Fe_3O_4 nanoparticles, 5 mg of rGO&CNT was sonicated in 20 mL water at 25 °C for 1 h. Then, 10 mL of iron(II) sulphate heptahydrate ($FeSO_4{\times}7H_2O$) solution (0.1 mol L^{-1}) was added to rGO&CNT suspension solution under

vigorous stirring. The pH of the solution was adjusted to 10 with NaOH, transferred to Teflon-lined stainless steel autoclave, and heated at 180 °C for 8 h. Water was used to wash the sample and then the product (Fe_3O_4-(rGO&CNT)) was dried at 60 °C overnight.

Total phenolic content (TPC)

The total phenolic content absorbed on rGO, rGO&CNT and Fe_3O_4-(rGO&CNT) samples was determined according to the Folin-Ciocalteu spectrophotometric method [28]. The 1 mL of samples (1 mg mL^{-1}) solution was mixed with 2.5 mL of Folin-Ciocalteu reagent 10 vol.% and neutralized with 2 mL of sodium carbonate 7.5 % (W/V). The reaction mixture was incubated at 45 °C for 40 min and the absorbance of solution was measured at 765 nm using a UV-Vis spectrophotometer. The total phenolic content is calculated based on gallic acid. To prepare a calibration curve from gallic acid, the results were expressed in terms of ppm of solutions. The test was done in triplicate.

Fabrication of Fe_3O_4-(rGO&CNT) nanocomposite modified electrode

The carbon paste electrode (CPE) was prepared as described in our previous reports [29,30]. The graphite powder plus paraffin was hand-mixed until a uniformly wetted paste was obtained. Then, the carbon paste was packed into a glass tube (with an internal radius 3 mm). Electrical contact was made by a copper wire. The new electrode surface was obtained by polishing it on a weighing paper. 1 mg of Fe_3O_4-(rGO&CNT) nanocomposite was added to 1 mL of water and sonicated for 30 min. 5 µL of this solution was drop-casted onto the CPE and allowed to dry in an oven at 50 °C for 30 min.

Analysis of plasma and urine

500 µL of human serum plasma or urine was transferred to the electrochemical cell containing 10 mL phosphate buffer solution (PB, 0.1 mol L^{-1}; pH 7.0) and the oxidation current was determined by cyclic voltammetry. Also, the samples were determined by UV-Vis spectroscopy at the wavelength of 243 nm with diluting 500 µL of plasma or urine in 5 mL PB (0.1 mol L^{-1}; pH 7.0).

Results and discussion

Characterization

Figure 2 (A) shows the electrochemical behaviour of *Callicarpa maingayi* leaf extract (100 mg L^{-1}) in 0.1 mol L^{-1} PB, pH 7.0 at CPE. A pair of well-defined redox peaks was obtained in the cyclic voltammogram, where anodic peak potential at ~260 mV and cathodic peak potential at ~220 mV could be ascribed to many phytocompounds redox couples in 0.1 mol L^{-1} PB that oxidize in the potential field. In order to realize the surface functional group information on samples, TPC on rGO, rGO&CNT and Fe_3O_4-(rGO&CNT) was calculated based on gallic acid (GA) with calibration linear function A = 0.022 c_{GA} - 0.008 and R^2 = 0.9915. TPC of rGO, rGO&CNT and Fe_3O_4-(rGO&CNT) was calculated as 0.93, 0.82 and 0.73 ppm, respectively compared with GO (0 ppm). *Callicarpa maingayi* leaf extract is a rich source of phytochemicals such as polyphenols, flavonoids and catechins, and shows remarkable performance as a reducing agent. The phytochemicals present in the *Callicarpa maingayi* leaf extract are of great medicinal value and also environmentally benign.

The formed rGO, rGO&CNT and Fe_3O_4-(rGO&CNT) are characterized by UV-Vis spectroscopy in the range of 200 to 600 nm (Figure 2B). The CNT shows an absorption broad peak at ~270 nm. The absorption peak of the rGO suspension is around 279 nm, which, on interaction with CNT, shifted towards 311 nm for rGO&CNT. The absorption peaks of Fe_3O_4-(rGO&CNT) at 271 nm and 320 nm belong to CNT and rGO, respectively, while the peaks of 361 and 376 nm are in good agreement with

Fe_3O_4 nanoparticles. Thus, the UV-Vis spectrum confirms the presence of the Fe_3O_4-(rGO&CNT) hybrid.

The electrochemical behaviour of CPE electrodes modified with rGO, CNT, rGO&CNT and Fe_3O_4-(rGO&CNT) through drop casting were tested using $[Fe(CN)_6]^{3-/4-}$ redox couple, and presented in Figure 2C. The redox current increased in the presence of Fe_3O_4-(rGO&CNT) and is larger than those recorded for bare CPE and rGO, CNT and rGO&CNT modified CPE. The good electronic properties of rGO and CNT support rapid electron transfer and are most likely responsible for the current enhancement. The real electrochemical active surface area of rGO/CPE, CNT/CPE, rGO&CNT/CPE and Fe_3O_4-(rGO&CNT)/CPE was determined by plotting the oxidation peak current as a function of the square root of the scan rate for $[Fe(CN)_6]^{4-}$ (2 mM). From the slopes of these graphs, the values of active surface area were obtained using equation (1) [27]:

$$A = \text{slope} / (268.6 n^{3/2} D^{1/2} c) \quad (1)$$

where A is the electrochemical active surface area (cm^2), n is the number of electrons transferred (n = 1), D is diffusion coefficient of $[Fe(CN)_6]^{4-}$ (3.09×10^{-6} cm^2 s^{-1}) and c is concentration of $[Fe(CN)_6]^{4-}$. For rGO/CPE, CNT/CPE and rGO&CNT/CPE, active surface area values were 0.19, 0.22 and 0.25 cm^2, respectively, while for Fe_3O_4-(rGO&CNT)/CPE an increased surface area (0.27 cm^2) was obtained. The significantly high electroactive area of Fe_3O_4-(rGO&CNT)/CPE recommends Fe_3O_4-(rGO&CNT) as an efficient substrate to fabricate sensors and biosensors.

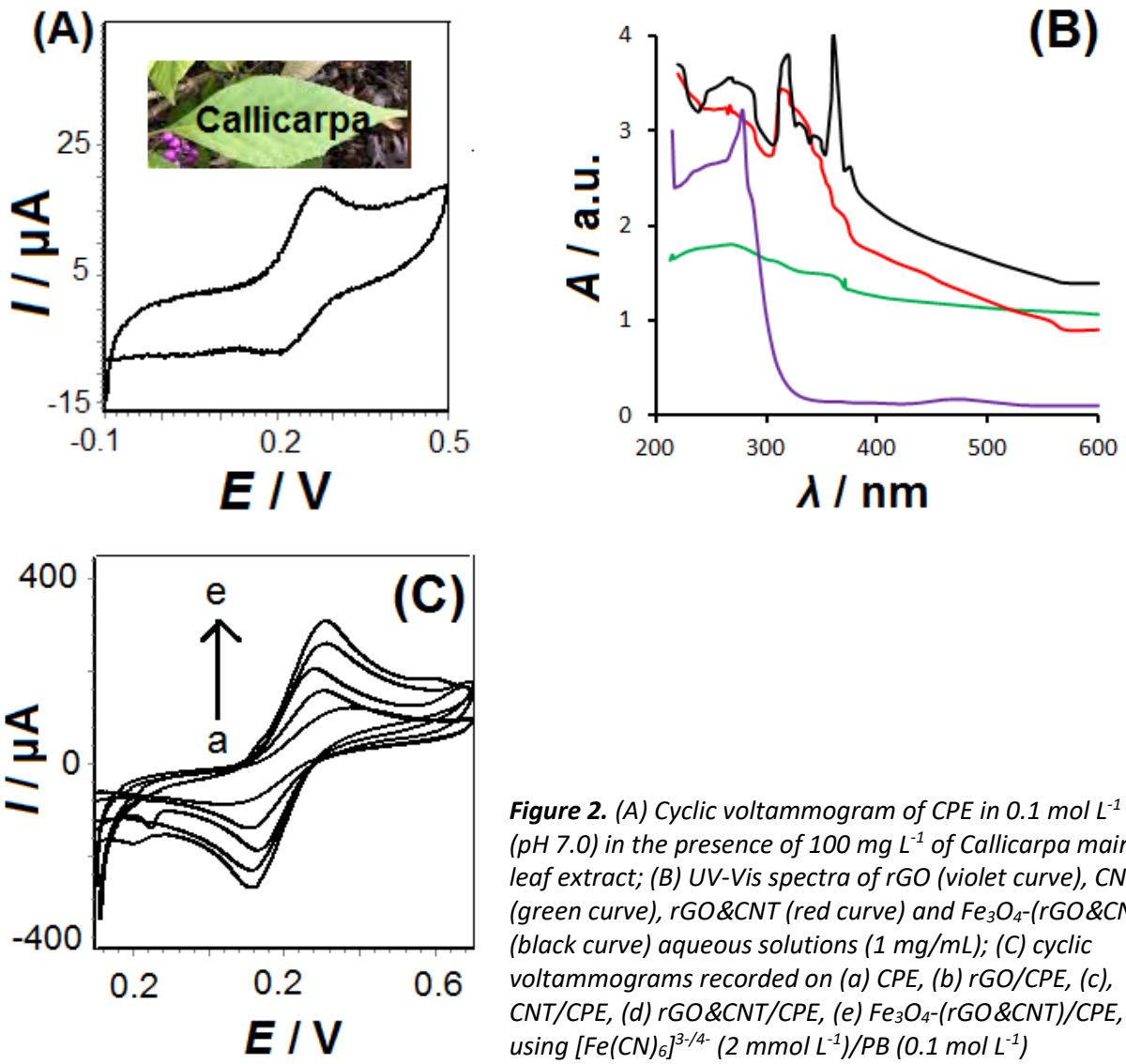

Figure 2. *(A) Cyclic voltammogram of CPE in 0.1 mol L^{-1} PB (pH 7.0) in the presence of 100 mg L^{-1} of Callicarpa maingayi leaf extract; (B) UV-Vis spectra of rGO (violet curve), CNT (green curve), rGO&CNT (red curve) and Fe_3O_4-(rGO&CNT) (black curve) aqueous solutions (1 mg/mL); (C) cyclic voltammograms recorded on (a) CPE, (b) rGO/CPE, (c), CNT/CPE, (d) rGO&CNT/CPE, (e) Fe_3O_4-(rGO&CNT)/CPE, using $[Fe(CN)_6]^{3-/4-}$ (2 mmol L^{-1})/PB (0.1 mol L^{-1})*

The powder X-ray diffraction (XRD) could provide effective evidence of synthesized Fe_3O_4--(rGO&CNT) hybrid. Figure 3 shows the XRD patterns of rGO, CNT, rGO&CNT and Fe_3O_4-(rGO&CNT) samples. As seen, rGO shows a diffraction peak at ~26° corresponding to the (002) reflection. CNT exhibited an intense diffraction pattern at 25.6° and a weak pattern at 44.4° originating from the (002) and (100), respectively, which, on interaction with rGO, shifted towards 2θ values of 26.14 and 43.3° for rGO&CNT. The diffraction peaks at 30.5, 36.1, 43.4, 53.8, 57.5 and 63.1 of Fe_3O_4-(rGO&CNT) could be indexed as that of face-centered cubic (fcc) spinel phase of Fe_3O_4 nanoparticles (JCPDS:19-0629) [31].

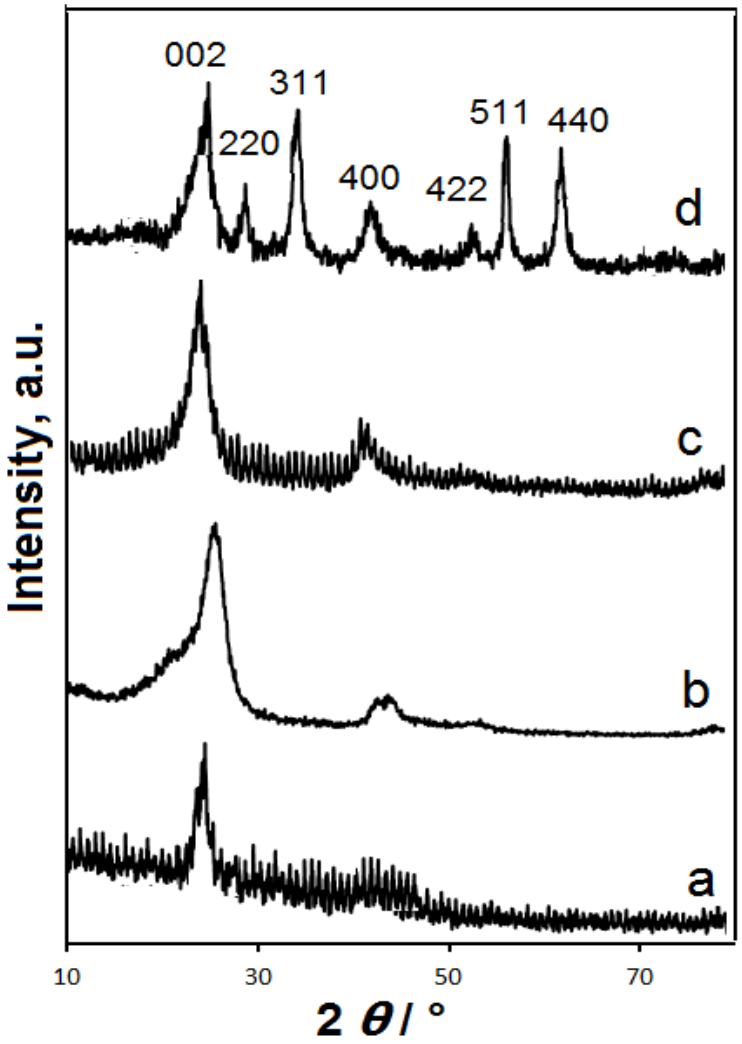

Figure 3. *XRD patterns of (a) rGO, (b) CNT, (c) rGO&CNT and (d) Fe_3O_4-(rGO&CNT)*

The morphology of rGO, CNT, rGO&CNT and Fe_3O_4-(rGO&CNT) is characterized with FE-SEM. As seen in Figure 4, the rGO shows the multilayered sheets onto each other, a rougher surface and wave-shaped corrugated structures. The CNTs are tubular and have open macropore structures. In contrast, the surface of rGO&CNT appears coarse, indicating most of the CNTs were relatively well dispersed in the rGO matrix. The image of Fe_3O_4-(rGO&CNT) shows that the rGO&CNT composite is decorated by sphere shape Fe_3O_4 nanoparticles with a diameter in the range of 25 to 40 nm.

Figure 5 illustrates the elemental analysis (EDX) of synthesized Fe_3O_4-(rGO&CNT) nanocomposite. The specific peak of Fe element in Figure 5 (a) indicates the presence of Fe_3O_4 nanoparticles on the rGO&CNT nanostructure. Also, the homogenous distribution of Fe can be seen in the elemental mapping of Fe_3O_4-(rGO&CNT) presented in Figure 5 (b).

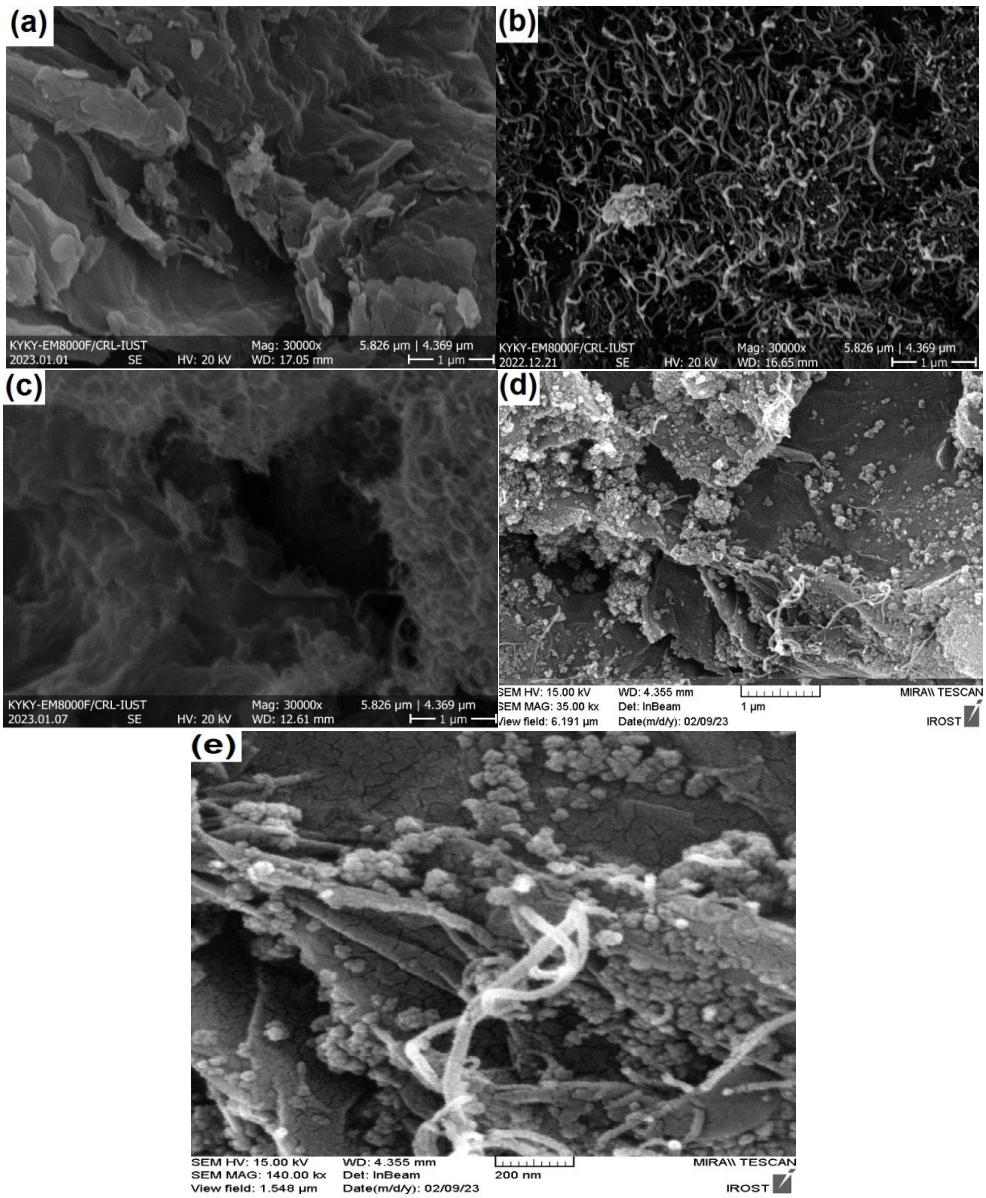

Figure 4. *FE-SEM images of: (a) rGO; (b) CNT; (c) rGO&CNT; (d) Fe_3O_4-(rGO&CNT); (e) Fe_3O_4-(rGO&CNT) with larger magnification*

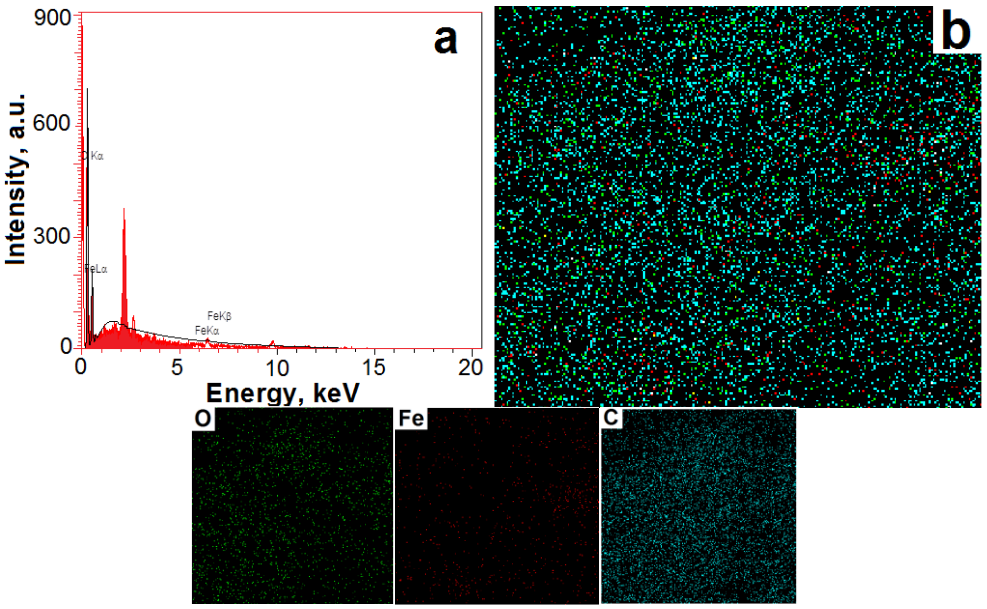

Figure 5. *(a) EDX spectra of Fe_3O_4-(rGO&CNT) and (b) elemental mapping of Fe_3O_4-(rGO&CNT)*

Voltammetric behavior of imatinib

The cyclic voltammetry (CV) method was used to investigate the electrochemical behaviour of IM on CPE, rGO/CPE, CNT/CPE, rGO&CNT/CPE and Fe_3O_4-(rGO&CNT)/CPE in 0.1 mol L^{-1} PB, pH 7.0. The voltammograms obtained for 50 µmol L^{-1} IM at 100 mV/s are shown in Figure 6(A). According to the results, the oxidation peak current of IM at the surface of the unmodified CPE is ~40 µA, while for rGO/CPE, CNT/CPE, rGO&CNT/CPE and Fe_3O_4-(rGO&CNT)/CPE electrodes, the oxidation peak current values are ~70, ~90, ~110 and ~170 µA, respectively. Moreover, the oxidation potential of IM on the surfaces of CPE and rGO/CPE is ~0.9 V, while the oxidation potential of IM on the surfaces of CNT/CPE, rGO&CNT/CPE and Fe_3O_4-(rGO&CNT)/CPE is ~0.86. Due to the high surface area of the electrode and the effects of rGO, CNT and Fe_3O_4 nanoparticle materials, the oxidation current of Fe_3O_4-(rGO&CNT)/CPE increases. In addition, these points improve the conductivity of Fe_3O_4--(rGO&CNT) composite, which results in a higher oxidation current on the surface of this electrode than on other electrodes.

The 0.1 mol L^{-1} PB with pH 5.0-9.0 was used to detect IM response on the surface of Fe_3O_4--(rGO&CNT)/CPE. As shown in Figure 6 (B), the maximum oxidation current of IM at Fe_3O_4--(rGO&CNT)/CPE was obtained at pH 7.0, then used as the optimal pH for other tests. The dependence of the oxidation peak potential of IM on pH is also shown in Figure 6 (C). The slope of the line obtained for this relation was 54 mV per pH unit, which is close to the slope of the Nernst equation. Accordingly, the number of electrons and protons participating in the oxidation of IM is the same according to Scheme 1.

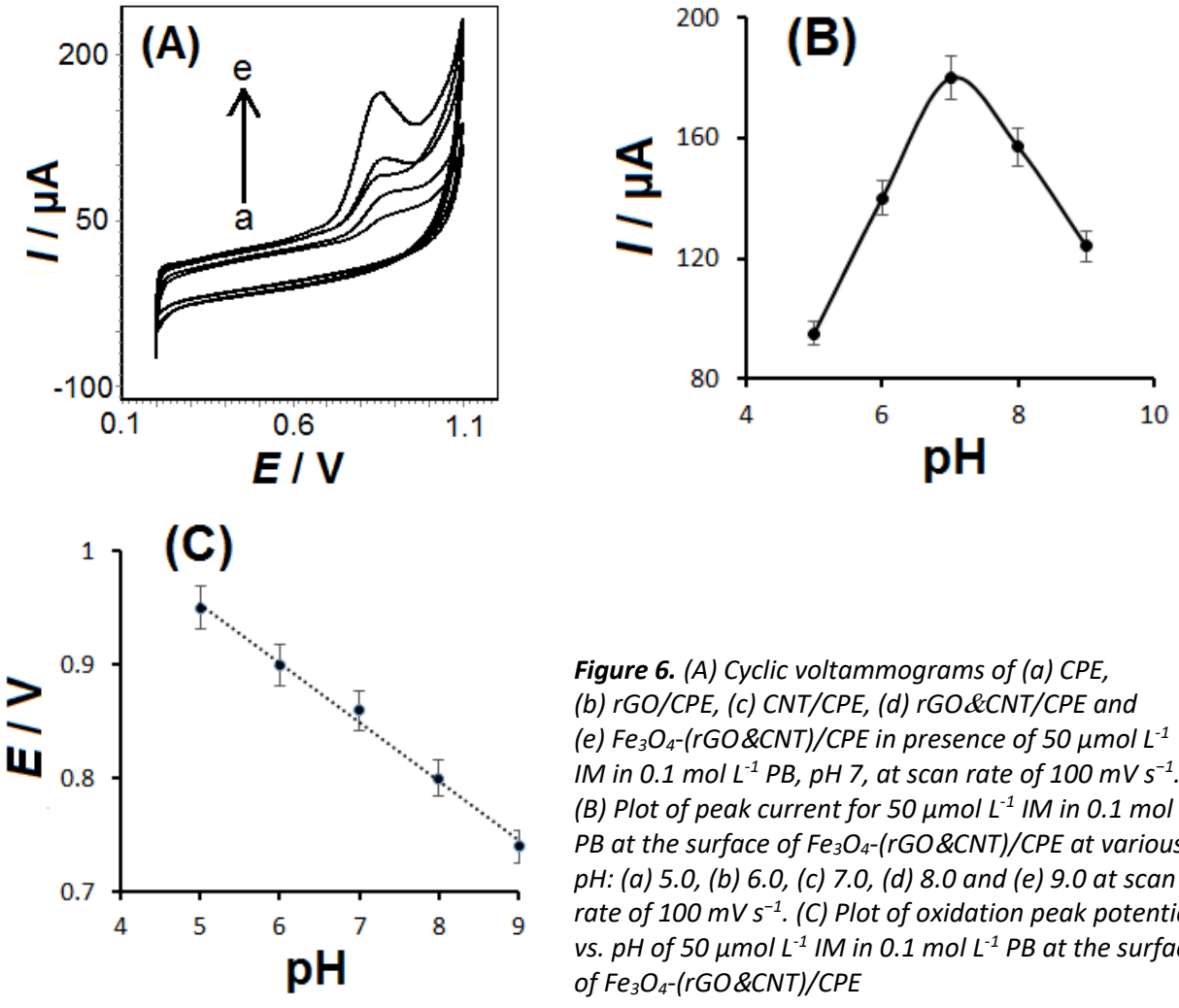

Figure 6. *(A) Cyclic voltammograms of (a) CPE, (b) rGO/CPE, (c) CNT/CPE, (d) rGO&CNT/CPE and (e) Fe_3O_4-(rGO&CNT)/CPE in presence of 50 µmol L^{-1} IM in 0.1 mol L^{-1} PB, pH 7, at scan rate of 100 mV s^{-1}. (B) Plot of peak current for 50 µmol L^{-1} IM in 0.1 mol L^{-1} PB at the surface of Fe_3O_4-(rGO&CNT)/CPE at various pH: (a) 5.0, (b) 6.0, (c) 7.0, (d) 8.0 and (e) 9.0 at scan rate of 100 mV s^{-1}. (C) Plot of oxidation peak potential vs. pH of 50 µmol L^{-1} IM in 0.1 mol L^{-1} PB at the surface of Fe_3O_4-(rGO&CNT)/CPE*

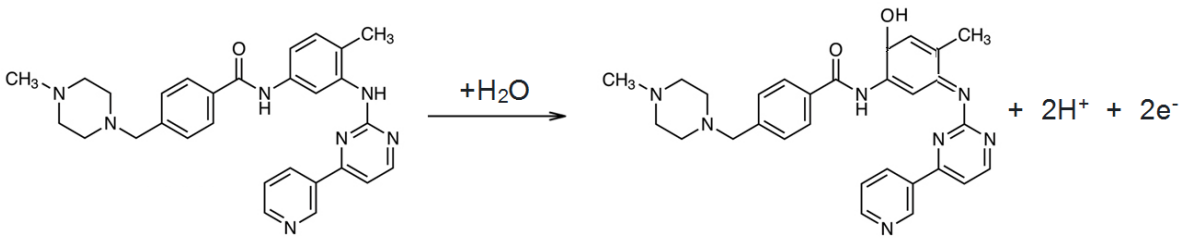

Scheme 1. *Electrochemical oxidation mechanism of IM*

Figure 7 (A) shows the CV curves of Fe_3O_4-(rGO&CNT)/CPE toward IM at different scan rates from 25 to 300 mV s^{-1}. It can be seen that the electrochemical oxidation current (*I*) of IM has a linear relationship with the $v^{1/2}$ (inset) while the oxidation potential is shifted positively with the increase of the scan rate, indicating that the electrochemical reaction of the IM obeyed the diffusion-controlled process. Also, the slope obtained from the graph of log *I* as a function of log *v* is 0.537 (Figure 7B), which is very near to the generally expected slope value of 0.5, showing a purely diffusion-controlled system.

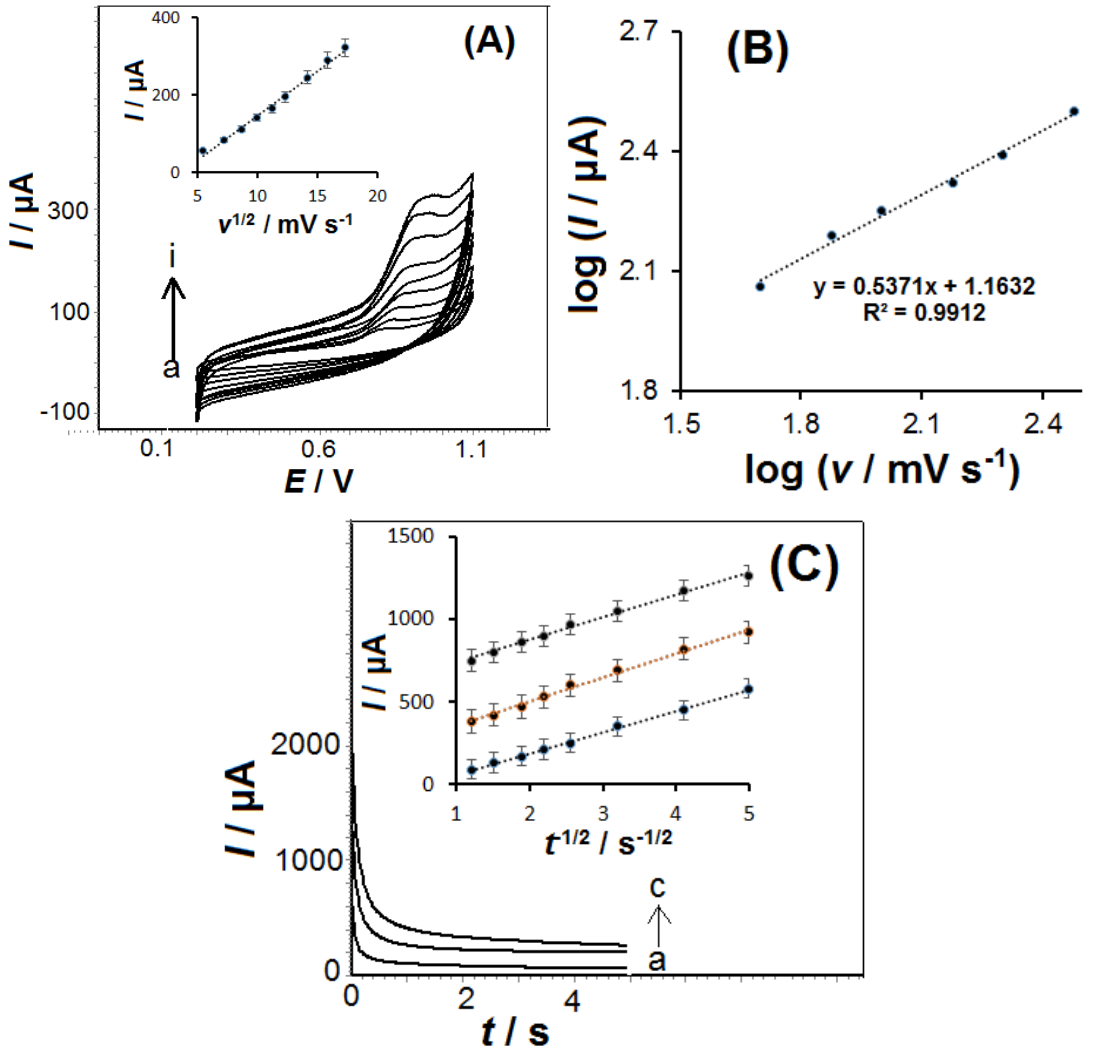

Figure 7. *(A) Cyclic voltammograms of 30 µmol L^{-1} IM in 0.1 mol L^{-1} PB (pH 7.0) and 0.1 mol L^{-1} KCl as supporting electrolyte at the surface of Fe_3O_4-(rGO&CNT)/CPE and various scan rates: (a) 25, (b) 50, (c) 75, (d) 100, (e) 125, (f) 150, (g) 200, (h) 250 and (i) 300 mV s^{-1}; inset: plot of peak currents vs. square root of scan rates. (B) Plot log I as a function of log υ. (C) Chronoamperograms for Fe_3O_4-(rGO&CNT)/CPE in the presence of (a) 50, (b) 100 and (c) 200 µmol L^{-1} IM; (inset) Cottrell's plot for the data from chronoamperograms*

Chromatoamperometry and other electrochemical methods were usually employed to investigate electrode reactions at chemically modified electrodes. Chronoamperometric measurement of IM was done by setting the Fe_3O_4-(rGO&CNT)/CPE working electrode potential at 0.9 V *vs*. Ag/AgCl/$KCl_{(3M)}$ for various concentrations of IM (Figure 7(C)). For IM with a diffusion coefficient of *D*, the current for the electrochemical reaction at a mass transport limited rate is described by the Cottrell equation (2) [32]:

$$I = nFAD^{1/2}c_b\pi^{-1/2}t^{-1/2} \quad (2)$$

where *n*, F, *A*, c_b, *D* and *t* are the number of electrons transferred (2), Faraday constant (96485 C), electrode area (0.27 cm^2), bulk concentration (50, 100 and 200 μmol L^{-1}), diffusion coefficient (cm^2 s^{-1}), and time (s), respectively.

Experimental plots of *I vs*. $t^{-1/2}$ were employed, with the best fits for different concentrations of IM (inset). From the resulting slope and Cottrell equation, the mean value of *D* for IM was calculated as 5.7×10^{-5} cm^2 s^{-1}.

Analytical performance of Fe_3O_4-(rGO&CNT)/CPE sensor

The quantitative analysis of the IM was based on the dependence of the peak current value on the concentration of IM. Cyclic voltammograms depicting the systematic increase in the peak current values with an increase of the concentration in the linear working range 0.1 to 40 μM at Fe_3O_4-(rGO&CNT)/CPE are presented in Figure 8A. The linear calibration plot according to I / μA = 27.22 + + 3.36 c_{IM} / μmol L^{-1} with a correlation coefficient of 0.991 and error bars are presented in the inset. The detection limit (LOD) of 57 nmol L^{-1} was calculated using the formula 3σ/**b**, where σ is the standard deviation of the blank and b is the slope of the calibration curve. The calculated value for the limit of quantification (LOQ) is 187.5 nM, while the sensitivity was estimated to be 3.365 μA μM^{-1}.

Table 1 compares the analytical performance of Fe_3O_4-(rGO&CNT)/CPE for IM determination with these obtained by voltammetry techniques at some other electrodes [13,16,33-36]. Based on the results of this study, the Fe_3O_4-(rGO&CNT) modified CPE electrode appears to be comparable to other electrodes in terms of achieving low detection limit, wide range of concentrations (LDR) and high sensitivity. The LOD is, however, higher as compared to other sensors presented in Table 1, but the proposed modified electrode was prepared by a simple, easy, cost-effective and one-step procedure of making Fe_3O_4-(rGO&CNT)/CPE electrode that is more readily available than materials used in preparation of other electrodes. Moreover, there is no proof that a single electrode can work for a long period of time with almost the same performance, which gives the Fe_3O_4--(rGO&CNT)/CPE the privilege of being used for routine work.

The reproducibility of E_p and I_p values was tested by repeating five experiments with 20 μmol L^{-1} of IM. The RSDs were calculated to be 3.43 % for I_p and 1.61 % for E_p, respectively, using CV, which indicates excellent reproducibility. The four consecutive measurements at one electrode in 0.1 mol L^{-1} PB (pH 7.0) containing 20 μmol L^{-1} IM have shown <5 % RSD at optimum pH to investigate Fe_3O_4--(rGO&CNT)/CPE repeatability. Based on this data, it appears that Fe_3O_4-(rGO&CNT)/CPE has appropriate repeatability. Moreover, six measurements were taken during a month to determine the stability of Fe_3O_4-(rGO&CNT)/CPE for IM measurement. In various measurements conducted over one month, the oxidation current changes of IM were 7.83 %, indicating that the electrode is stable.

In order to examine the selectivity of IM, it must be measured concurrently with compounds present in the body or compounds being administered simultaneously with IM. Many minerals in a body contain cations (Na^+, Ca^{2+}, Mg^{+2}, etc.) and anions. For this reason, we investigated possible

interferents for IM detection, such as glucose, cysteine, lysine, Ca^{+2}, K^{+}, Na^{+}, Mg^{+2}, doxorubicin, acetaminophen, and ascorbic acid.

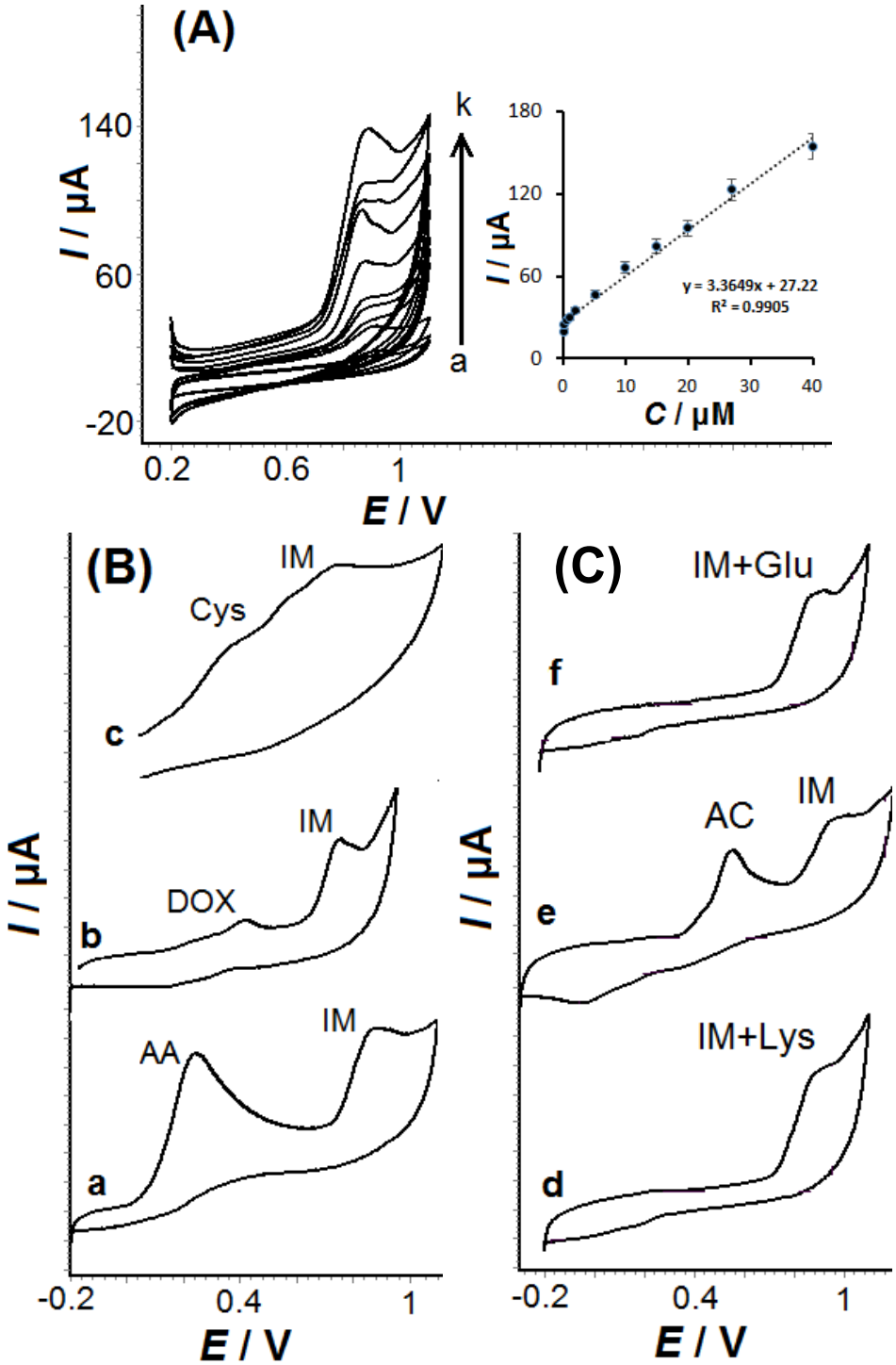

Figure 8. *Cyclic voltammograms of Fe_3O_4-(rGO&CNT)/CPE in 0.1 mol L^{-1} PB (pH 7.0): (A) in the presence of (a) 0.1, (b) 0.2, (c) 0.5, (d) 1, (e) 2, (f) 5, (g) 10, (h) 15, (i) 20, (j) 27 and (k) 40 µmol L^{-1} of IM; Inset: plot of oxidation peak current vs. IM concentration, (B) upon addition of (a) ascorbic acid (AA, 30 µmol L^{-1}) + IM (30 µmol L^{-1}), (b) doxorubicin (DOX, 30 µmol L^{-1}) + IM (30 µmol L^{-1}), (C) cysteine (Cys, 30 µmol L^{-1})+ IM (30 µmol L^{-1}), (d) lysine (Lys, 30 µmol L^{-1}) + IM (30 µmol L^{-1}), (e) acetaminophen (AC, 30 µmol L^{-1}) + IM (30 µmol L^{-1}) and (f) glucose (Glu, 30 µmol L^{-1})+IM (30 µmol L^{-1})*

Some results of IM detection at the Fe_3O_4-(rGO&CNT)/CPE in 0.1M PB (pH 7.0) containing some interferents at equal concentrations as IM, are presented in Figure 8B. As seen in Figure 8B, glucose, cysteine, lysine, doxorubicin, acetaminophen, and ascorbic acid did not cause *any* interference.

Moreover, some results (not shown here) indicated that the 500-fold higher concentrations of glucose and cations (Ca^{+2}, K^+, Na^+ and Mg^{+2}) and 100-fold higher concentrations of lysine, ascorbic acid, acetaminophen and doxorubicin did not affect the determination of IM. However, 5-fold higher concentrations of cysteine showed interference in the determination of IM at Fe_3O_4-(rGO&CNT)/CPE.

Table 1 *Analytical parameters for voltammetric determination of IM at different modified electrodes*

Electrode	Method	Linear range, µmol L^{-1}	LOD, nmol L^{-1}	Sensitivity, µA (µmol L^{-1})$^{-1}$	Ref.
MWCNT/SPCE	SWV[a]	0.005-0.912	7.0	-	[13]
$TbFeO_3$/g-C_3N_4/GCE	DPV[b]	0.002-100	0.6	5.92 cm^{-2}	[16]
MWCNT/NiO-ZnO/GCE	DPV	0.015-2	2.4	2.64	[33]
Cu-BTC/RGO/GCE	DPV	0.04-80	6.0	-	[34]
RGO/AgNPs/GCE	DPV	0.001-280	1.1	0.17	[35]
Cu-BTC/MWCNT/GCE	DPV	0.01-220	4.1	1.65	[36]
Fe_3O_4-(rGO&CNT)/CPE	CV	0.1-40	57	3.36	this work

[a] Square wave voltammetry
[b] Differential pulse voltammetry

The accuracy of the proposed method was assessed by performing recovery experiments. Human plasma and urine samples were measured using the standard addition method at pH 7.0 on Fe_3O_4-(rGO&CNT)/CPE. Table 2 presents the concentrations of IM added to plasma and urine samples, along with their standard deviations and recovery percentages. According to the results, the mean recovery percentage in real samples is approximately 94-98.5, suggesting that the modified electrode can accurately measure IM. The results obtained from the proposed method were compared with the UV-Vis spectroscopy results (Table 2). It was observed that the results of electrochemical analysis show consistency with those obtained by the UV-Vis method (Figure 9) with acceptable recoveries.

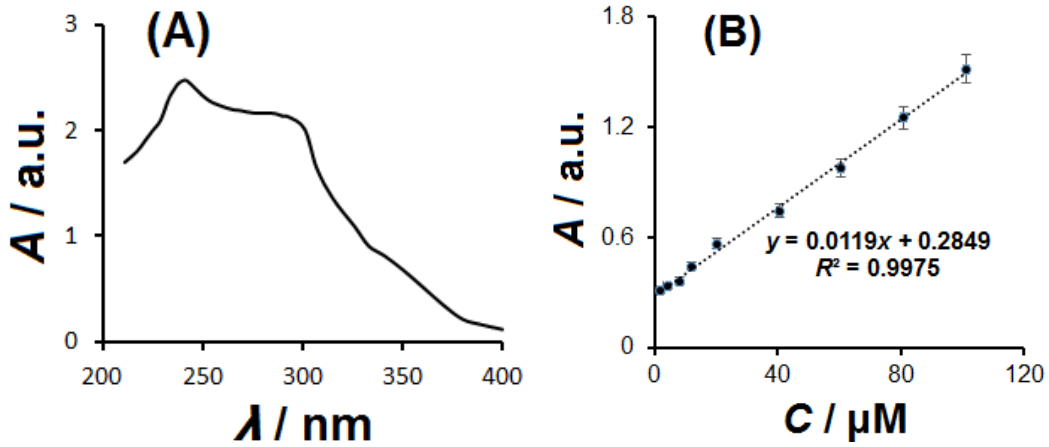

Figure 9. *(A) The UV-Vis spectrum of IM (202.5 µM) in PB solution (pH 7.0); (B) calibration curve of IM determined by UV-Vis spectroscopy*

Table 2. *Determination of IM in urine and blood plasma samples at Fe_3O_4-(rGO&CNT)/CPE in 0.1 mol L^{-1} PB solution (pH 7.0)*

Sample	Amount, µmol L^{-1}		Mean recovery of proposed method, %	Mean recovery of UV-Vis method, %
	Added	Found	(*n*=3)	(*n*=3)
Plasma	10.0	9.5	95.0±4.4	98.0±3.7
Plasma	20.0	19.7	98.5±4.3	102.0±2.9
Urine	10.0	9.4	94.0±2.1	94.0±1.6
Urine	20.0	19.1	95.5±4.1	99.8±3.2

Conclusion

In this study, new rGO sheets have been synthesized *via* a facile and environmentally friendly process using *Callicarpa maingayi* leaf extract. By combining CNT tubes, rGO sheets and Fe_3O_4 nanoparticles, an excellent nanocomposite on the CPE electrode was created with a high surface area and good conductivity, which led to satisfactory results in the IM determination. Due to the increased electron transfer rate at the surface of Fe_3O_4-(rGO&CNT)/CPE electrode at pH 7.0, the oxidation current of IM was higher than at CPE, rGO/CPE, CNT/CPE and rGO&CNT/CPE. The excellent results are attributed to the large electrode surface area provided by CNT, rGO and Fe_3O_4 nanoparticles, as well as their excellent catalytic properties. The proposed Fe_3O_4-(rGO&CNT)/CPE showed fast response, stable measurements, and excellent anti-interference properties. Due to the advantages of magnetism and conductivity, the prepared nanocomposite material could easily adhere to the electrode surface, offering good electrical contact. In addition, Fe_3O_4-(rGO&CNT) nanocomposite-modified CPE can be applied to detect of IM in real samples.

Acknowledgements*: The authors are sincerely thankful for the research facilities provided by the Ayatollah Amoli Branch of the Islamic Azad University.*

References

[1] Y. Liu, M. Wei, Y. Hu, L. Zhu, J. Du, An electrochemical sensor based on a molecularly imprinted polymer for determination of anticancer drug Mitoxantrone, *Sensors and Actuators B* **255** (2018) 544-551. https://doi.org/10.1016/j.snb.2017.08.023

[2] M. Muti, M. Muti, Electrochemical monitoring of the interaction between anticancer drug and DNA in the presence of antioxidant, *Talanta* **178** (2018) 1033-1039. https://doi.org/10.1016/j.talanta.2017.08.089

[3] K. N. Cahill, H. R. Katz, J. Cui, J. Lai, Sh. Kazani, A. Crosby-Thompson, D. Garofalo, M. Castro, N. Jarjour, E. DiMango, S. Erzurum, J. Trevor, K. Shenoy, V. M. Chinchilli, M. E. Wechsler, T. M. Laidlaw, J. A. Boyce, E. Israel, KIT inhibition by imatinib in patients with severe refractory asthma, *The New England Journal of Medicine* **376** (2017) 1911-1920. https://doi.org/10.1056/NEJMoa1613125

[4] P. Sobierajska, A. Serwotka-Suszczak, D. Szymanski, K. Marycz, R. J. Wiglusz, Nanohydroxyapatite-mediated imatinib delivery for specific anticancer applications, *Molecules* **25** (2020) 4602. https://doi.org/10.3390/molecules25204602

[5] A. Hochhaus, R. A. Larson, F. Guilhot, J. P. Radich, S. Branford, T. P. Hughes, M. Baccarani, M. W. Deininger, F. Cervantes, S. Fujihara, Ch. E. Ortmann, H. D. Menssen, H. Kantarjian, S. G. O'Brien, B. J. Druker, Long-term outcomes of imatinib treatment for chronic myeloid leukemia, *The New England Journal of Medicine* **376** (2017) 917-927. https://doi.org/10.1056/NEJMoa1609324

[6] M. A. Babaei, B. Kamalidehghan, M. Saleem, H. Z. Huri, F. Ahmadipour, Receptor tyrosine kinase (c-Kit) inhibitors: a potential therapeutic target in cancer cells, *Drug Design Development Therapy* **10** (2016) 2443-2459. https://doi.org/10.2147/DDDT.S89114

[7] Q. Jiao, L. Bi, Y. Ren, S. Song, Q. Wang, Y. S. Wang, Advances in studies of tyrosine kinase inhibitors and their acquired resistance, *Molecular Cancer* **17** (2018) 36. https://doi.org/10.1186/s12943-018-0801-5

[8] I. Grante, A. Actins, L. Orola, Protonation effects on the UV/Vis absorption spectra of imatinib: A theoretical and experimental study, *Spectrochimica Acta: Molecular and Biomolecular Spectroscopy* **129** (2014) 326-332. https://doi.org/10.1016/j.saa.2014.03.059

[9] O. Roth, O. Spreux-Varoquaux, S. Bouchet, P. Rousselot, S. Castaigne, S. Rigaudeau, V. Raggueneau, P. Therond, P. Devillier, M. Molimard, B. Meneglier, Imatinib assay by HPLC

with photodiode-array UV detection in plasma from patients with chronic myeloid leukemia: Comparison with LC-MS/MS, *Clinica Chimica Acta* **411** (2010) 140-146. https://doi.org/10.1016/j.cca.2009.10.007

[10] G. Bende, S. Kollipara, V. Sekar, R. Saha, UV-spectrophotometric determination of imatinib mesylate and its application in solubility studies, *Pharmazie* **63** (2008) 641-645. https://doi.org/10.1691/ph.2008.8094

[11] J. Rodríguez-Flores, J. B. Nevado, A. C. Salcedo, M. P. Cabello Díaz, Nonaqueous capillary electrophoresis method for the analysis of gleevec and its main metabolite in human urine, *Journal of Chromatography A* **1068** (2005) 175-182. https://doi.org/10.1016/j.chroma.2004.09.089

[12] O. S. Ahmed, M. Malý, Y. Ladner, L. Philibert, P. Dubský, C. Perrin, Influence of salt and acetonitrile on the capillary zone electrophoresis analysis of imatinib in plasma samples, *Electrophoresis* **40** (2019) 2810-2819. https://doi.org/10.1002/elps.201900188

[13] J. Rodríguez, G. Castañeda, I. Lizcano, Electrochemical sensor for leukemia drug imatinib determination in urine by adsorptive striping square wave voltammetry using modified screen-printed electrodes, *Electrochimica Acta* **269** (2018) 668-675. https://doi.org/10.1016/j.electacta.2018.03.051

[14] J. G. Manjunatha, Electroanalysis of estriol hormone using electrochemical sensor, *Sensing and Bio-Sensing Research* **16** (2017) 79-84. https://doi.org/10.1016/j.sbsr.2017.11.006

[15] J. G. Manjunatha, Poly (Nigrosine) Modified Electrochemical Sensor for the Determination of Dopamine and Uric acid: A Cyclic Voltammetric Study, *International Journal of ChemTech Research* **9** (2016) 136-146. https://sphinxsai.com/2016/ch_vol9_no2/1/(136-146)V9N2CT.pdf

[16] M. Baladi, H. Teymourini, E. A. Dawi, M. Amiri, A. Ramazani, M. Salavati-Niasari, Electrochemical determination of imatinib mesylate using TbFeO3/g-C3N4 nanocomposite modified glassy carbon electrode, *Arabian Journal of Chemistry* **16** (2023) 104963. https://doi.org/10.1016/j.arabjc.2023.104963

[17] J. G. Manjunatha, Electrochemical polymerised graphene paste electrode and application to catechol sensing, *The Open Chemical Engineering Journal* **13** (2019) 81-87. https://doi.org/10.2174/1874123101913010081

[18] G. Tigari, J. G. Manjunatha, Optimized voltammetric experiment for the determination of phloroglucinol at surfactant modified carbon nanotube paste electrode, *Instruments and Experimental Techniques* **63** (2020) 750-757. https://doi.org/10.1134/S0020441220050139

[19] A. U. Alam, D. Clyne, H. Jin, N. X. Hu, M. J. Deen, *ACS Sensors* **5** (2020) 412-422. https://doi.org/10.1021/acssensors.9b02095

[20] S. Morais, Advances and applications of carbon nanotubes, *Nanomaterials* **13** (2023) 2674. https://doi.org/10.3390/nano13192674

[21] A. Hosseini Fakhrabad, R. Sanavi Khoshnood, M. R. Abedib, M. Ebrahimi, Fabrication a composite carbon paste electrodes (CPEs) modified with multi-wall carbon nanotubes (MWCNTs/N, N-Bis (salicyliden)-1,3- propandiamine) for determination of lanthanum (III), *Eurasian Chemical Communications* **3** (2021) 627-634. https://www.echemcom.com/article_134775_efa87e18e1e4daddba676005d78a6feb.pdf

[22] A. B. Monnappa, J. G. Manjunatha, A. Sripathi Bhatt, H. Nagarajappa, Sensitive and selective electrochemical detection of vanillin at graphene based poly (methyl orange) modified electrode, *Journal of Science: Advanced Materials and Devices* **6** (2021) 415-424. https://doi.org/10.1016/j.jsamd.2021.05.002

[23] Ch. Zou, J. Hu, Y. Su, F. Shao, Z. Tao, T. Huo, Zh. Zhou, N. Hu, Zh. Yang, E. Siu-Wai Kong, Y. Zhang, Three-dimensional Fe_3O_4@reduced graphene oxide heterojunctions for high-performance room-temperature NO_2 sensors, *Frontiers in Materials* **6** (2019) 195. https://doi.org/10.3389/fmats.2019.00195

[24] G. J. Rani, K. J. Babu, M. J. Rajan, Watsonia meriana flower like Fe_3O_4/reduced graphene oxide nanocomposite for the highly sensitive and selective electrochemical sensing of dopamine, *Journal of Alloys and Compounds* **688** (2016) 500-512. https://doi.org/10.1016/j.jallcom.2016.07.101
[25] E. Aliyev, V. Filiz, M. M. Khan, Y. J. Lee, C. Abetz, V. Abetz, Structural characterization of graphene oxide: surface functional groups and fractionated oxidative debris, *Nanomaterials* **9** (2019) 1180. https://doi.org/10.3390/nano9081180
[26] E. Vatandost, A, Ghorbani-HasanSaraei, F. Chekin, Sh. Naghizadeh Raeisi, S. A. Shahidi, Green tea extract assisted green synthesis of reduced graphene oxide: Application for highly sensitive electrochemical detection of sunset yellow in food products, *Food Chemistry X* **6** (2020) 100085-100090. https://doi.org/10.1016/j.fochx.2020.100085
[27] N. Hazhir, F. Chekin, J. B. Raoof, Sh. Fathi, A porous reduced graphene oxide/chitosan-based nanocarrier as a delivery system of doxorubicin, *RSC Advances* **9** (2019) 30729-30735. https://doi.org/10.1039/C9RA04977K
[28] A. Negi, K. Dobhal, P. Ghildiyal, Antioxidant potential and effect of extraction solvent on total Phenol content, flavonoids, *International Journal of Pharmaceutical Sciences Review and Research* **49** (2018) 19-24. https://doi.org/10.13140/RG.2.2.14158.15687
[29] Sh. Nikkhah, H. Tahermansouri, F. Chekin, Synthesis, characterization, and electrochemical properties of the modified graphene oxide with 4,4'-methylenedianiline, *Materials Letters* **211** (2018) 323-327. https://doi.org/10.1016/j.matlet.2017.10.037
[30] B. Zareyy, F. Chekin, Sh. Fathi, NiO/porous reduced graphene oxide as active hybrid electrocatalyst for oxygen evolution reaction, *Russian Journal of Electrochemistry* **55** (2019) 333-338. https://doi.org/10.1134/S102319351903011X
[31] L. Shen, J. Dong, B. Wen, X. Wen, J. Li, Facile synthesis of hollow Fe_3O_4-rGO nanocomposites for the electrochemical detection of acetaminophen, *Nanomaterials* **13** (2023) 707. https://doi.org/10.3390/nano13040707
[32] B. Davarnia, S. A. Shahidi, H. Karimi-Maleh, A. Ghorbani HasanSaraei, F. Karimi, Biosynthesis of Ag nanoparticle by peganum harmala extract; antimicrobial activity and ability for fabrication of quercetin food electrochemical sensor, *International Journal of Electrochemical Science* **15** (2020) 2549-2560. https://doi.org/10.20964/2020.03.70
[33] H. Chen, K. Luo, K. Li, A facile electrochemical sensor based on NiO-ZnO/MWCNT-COOH modified GCE for simultaneous quantification of imatinib and itraconazole, *Journal of The Electrochemical Society* **166** (2019) B697-B707. https://doi.org/10.1149/2.1071908jes
[34] N. Rezvani Jalal, T. Madrakian, A. Afkhami, A. Ghoorchian, In situ growth of metal–organic framework HKUST-1 on graphene oxide nanoribbons with high electrochemical sensing Performance in imatinib determination, *ACS Applied Materials & Interfaces* **12** (2020) 4859-4869. https://doi.org/10.1021/acsami.9b18097
[35] Z. Wu, J. Liu, M. Liang, H. Zheng, Ch. Zhu, Y. Wang, Detection of imatinib based on electrochemical sensor constructed using biosynthesized graphene-silver nanocomposite, *Frontiers in Chemistry* **9** (2021) 670074. https://doi.org/10.3389/fchem.2021.670074
[36] B. H. Pour, N. Haghnazari, F. Keshavarzi, E. Ahmadi, B. R. Zarif, High sensitive electrochemical sensor for imatinib based on metal-organic frameworks and multiwall carbon nanotubes nanocomposite, *Microchemical Journal* **165** (2021) 106147. https://doi.org/10.1016/j.microc.2021.106147

J. Electrochem. Sci. Eng. **14(2)** (2024) 135-145; http://dx.doi.org/10.5599/jese.2061

Open Access : : ISSN 1847-9286
www.jESE-online.org

Original scientific paper

Voltametric and molecular docking investigations of ferrocenylmethylaniline and its N-acetylated derivative interacting with DNA

Asma Yahiaoui[1,2], Benyza-Nabil[2], Amel Messai[3], Touhami Lanez[1,✉] and Elhafnaoui Lanez[1]

[1]*University of El Oued, Chemistry Department, VTRS Laboratory, B.P.789, 39000, El Oued, Algeria*
[2]*University of Khenchela, laboratory of sensors, instrumentations and process, B.P. 1252, 40000 Khenchela, Algeria*
[3]*University of Khenchela, ISMA Laboratory, Faculty of Sciences and Technology, B.P. 1252, 40000 Khenchela, Algeria*

Corresponding author: ✉*touhami-lanez@univ-eloued.dz; Tel.: +213-661-655-550*

Received: September 4, 2023; Accepted: December 1, 2023; Published: December 14, 2023

Abstract

N-ferrocenylmethylaniline (FA) and its N-acetylated derivative (NFA) have been synthesized and fully characterized by various physicochemical techniques such as ^{1}H and ^{13}C NMR spectroscopy. Interactions of FA and NFA with chicken blood DNA were studied by cyclic voltammetry (CV) and molecular docking (MD). The obtained results suggest that both FA and NFA bind strongly via electrostatic interactions to the minor groove of double helix DNA. These electrostatic interactions were evidenced by the findings like a negative formal potential shift in CV and ionic strength effect. The results further show that the binding constants and free binding energies obtained by MD analysis are roughly matched to those obtained from CV. Furthermore, the binding site size was evaluated from voltammetric data.

Keywords

Ferrocene derivatives; DNA minor groove binding; binding site size; binding free energy; docking simulations

Introduction

The foremost cause of all types of cancer is mostly due to abnormal cell proliferation which can alter as a result of changes in nucleotide sequences of DNA, and this can cause the expression of defective proteins that affect regular cellular physiology [1]. DNA also serves as a protein-coding material and its interactions with drugs can change how those proteins are replicated and lead to potential cures for such diseases [2]. Small compounds with potential anticancer activity, such as organometallic compounds, often target DNA within cells and can interact with DNA to cause DNA

damage in cancer cells either directly or through inhibition of enzymes that control DNA integrity or provide building blocks for DNA, preventing cancer cells from proliferating and leading to cell death [3]. Non-specific DNA-targeting organometallic compounds such as cisplatin are among today's most widely, effective, and successful anticancer medications [4].

Research on the anticancer potential of ferrocene derivatives was started in the late 1970s when Brynes and co-workers discovered that ferrocene derivatives bearing amine or amide functions have antitumor action against lymphocytic leukemia [5]. Since then, many other types of ferrocene derivatives have been synthesized and their anticancer activities have been evaluated [6,7]. Ferrocene derivatives such as ferrocenylanilines, in which the aniline group is either directly linked to the ferrocene moiety or separated by a methylene group, are also well known for their valuable pharmacological properties and they have attracted significant interest as potential anticancer and antioxidant drug candidates [8]. Recently, ferrocenylmethylanilines have been considered a potent anticancer agent [9]. Many reports showed that ferrocenylmethylanilines have positive effects on different types of cancer cell lines, such as breast cancer [10].

DNA is a well-known pharmacological target of most drugs currently in clinical use or in advanced clinical trials, when small molecules bind to DNA, they alter or inhibit its function. These small molecules act as drugs when this alteration or inhibition of DNA function is required to cure or control a disease [11].

Since DNA is now known as the primary intracellular target for cancer treatment, the anticancer potential of small molecules has been studied through their interaction with DNA [12].

Therefore, considering the importance of drug-DNA interaction in designing new drug candidates with useful and effective anticancer properties as well as various biological and therapeutic activities, in this work, a study is presented on the interaction of the amine N-ferrocenylmethyl-aniline and its N-acetylated derivative with chicken blood DNA (CB-DNA). Investigations were performed using voltammetry and molecular docking.

Experimental

Material and method

N-ferrocenylmethylaniline (FA) and its N-acetylated derivative (NFA) investigated in this work are shown in Figure 1 and were synthesized by reacting N,N,N-trimethylammoniomethylferrocene iodide[13] with aniline followed by acetylation of the obtained amine, as described below.

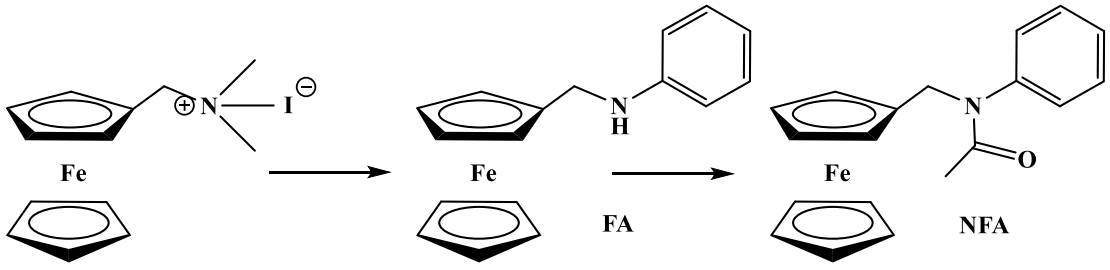

Figure 1. *Reaction scheme and molecular structure of N-ferrocenylmethylaniline (FA) and N-ferrocenylmethyl-N-acetylaniline (NFA)*

Synthesis of N-ferrocenylmethylaniline

The above amine has been synthesized from N,N,N-trimethylammoniomethylferrocene iodide [13] and aniline in water as a solvent. A solution of N,N,N-trimethylammoniomethylferrocene iodide (1 g, 2.6 mmol) in water (20 cm^3) was added dropwise to a solution of aniline (1.4 g,

15.03 mmol) in water (30 cm^3). The mixture was refluxed under nitrogen for 2 hours. Then allowed to cool to room temperature and extracted three times with toluene, the combined toluene layer was dried over magnesium sulphate and evaporated. The obtained residue was recrystallized from a mixture of aqueous ethanol to offer the amine as a yellow leaflet (0.53 g, 69.7 %), melting point (mp) = 85-86 °C.

NMR ^1H (300 MHz, $CDCl_3$): δ = 4.01 ppm (s, 2H, H2), 4.20 ppm (s, 2H, H3), 4.24 ppm (s, 5H, H4), 4.33 ppm (d, 2H, H1), 6.72 ppm (d, 2H, H5), 6.78 ppm (t, 1H, H6), 7.25 ppm (t, 2H, H7), 7.31 ppm (s, 1H, N-H).

NMR ^{13}C (75 MHz, $CDCl_3$) : δ = 44.15 (1C, C1), 68.67 (2C, C2), 68.89 (2C, C3), 69.27 (5C, C4), 87.84 (1C, C5), 113.60 (2C, C7), 118.31 (1C, C9), 130.08 (2C, C8), 149.06 (1C, C6).

Synthesis of N-ferrocenylmethyl-N-acetylaniline

The N-acetyl derivative (0.46 g, 81 %) was obtained by heating the amine N-ferrocenyl-methylaniline (0.5 g, 1.72 mmol) and acetic anhydride (5.1 cm^3) in dry toluene (30 cm^3) at 80 °C for 20 minutes under nitrogen, then poured into water. The toluene layer was separated, dried over magnesium sulphate, and evaporated, and the residue recrystallized from a mixture of aqueous ethanol. The N-acetyl derivative formed yellow plates, mp = 116-117 °C.

NMR ^1H (300 MHz, $CDCl_3$): δ = 1.75 ppm (s, 3H, H8), 4.03 ppm (s, 4H, H2 and H3), 4.08 ppm (s, 5H, H4), 4.61 ppm (s, 2H, H1), 6.99 ppm (d, 2H, H5), 7.28 ppm (t, 1H, H6), 7.32 ppm (t, 2H, H7)

NMR ^{13}C (75 MHz, $CDCl_3$) : δ = 23.55 ppm (1C, C11), 49.12 ppm (1C, C1), 68.86 ppm (2C, C2), 69.27 ppm (5C, C4), 70.62 ppm (2C, C3), 83.86 ppm (1C, C5), 128.60 ppm (2C, C7), 129.28 ppm (1C, C9), 130.16 ppm (2C, C8), 143.56 ppm (1C, C6), 170.47 ppm (1C, C10).

^1H and ^{13}C NMR spectra were obtained on a BRUKER AVANCE DPX 500 MHz spectrometer. Cyclic voltammetry was performed at room temperature (~28 ± 2 °C) using a monocompartment cell with 15 mL capacity. The instrumentation consists of a VoltaLab 40, potentiostat/galvanostat controlled by a microcomputer. The conventional three-electrode system was adopted to perform all the experiments in phosphate buffer solutions. Tetrabutylammonium tetrafluoroborate (Bu_4NBF_4) was used as a supporting electrolyte and its concentration was kept at 0.1 M. The air was removed from the solution by bubbling nitrogen gas through it.

DNA extraction

As described in our previous work [14,15], DNA was isolated from chicken blood, and its stock solution was made by dissolving the DNA in phosphate buffer at pH 7.0, followed by dilution with ethanol to 10 % aqueous ethanol, then it was stored at 4 °C. The concentration of the stock solution was calculated by measuring UV absorbance at λ = 260 nm and using the molar absorption coef-ficient of 6600 M^{-1} cm^{-1} [16].

The evidence that the obtained DNA is protein-free was brought on by measuring the absorbance ratio at λ = 260 and 280 nm, which was 1.97 [17].

The 10 mM stock solutions of FA and NFA were prepared by dissolving the adequate mass of each compound in 5 mL 95 % aqueous ethanol. The solutions were buffered at pH 7 by phosphate buffer (0.1 M KH_2PO_4 + 0.1 M NaOH), this neutral condition prevents the protonation of the ferrocenyl group in strongly acidic conditions [18] and decomposition of the ferrocenium state in basic solutions [19].

Chemicals and reagents

Ferrocene, aniline, acetic anhydride, and tetrabutylammonium tetrafluoroborate were acquired from Sigma-Aldrich and used without purification. All other reagents and solvents were of analytical grade, obtained from different commercial sources and used without further purification. Doubly distilled water was used for all solutions. All the experiments were conducted in 0.1 M phosphate buffer (pH 7) at 28 ± 2 °C. All the results were the average of three experimental measurements.

Cyclic voltammetry measurements

Cyclic voltammetry was measured using a VoltaLab 40 (Radiometer Analytical SAS, France). All assays were carried out in three-electrode electrochemical cells consisting of a saturated calomel electrode as a reference electrode, a platinum wire of thickness 0.5 mm as the counter electrode, and a glassy carbon electrode with an area of 0.077 cm^2 as the working electrode. The voltammogram of a known volume of the solution of each compound was recorded in the absence and presence of a varying concentration of DNA, after flushing out oxygen by bubbling nitrogen gas for 15 minutes. The working electrode was cleaned and polished after every electrochemical assay.

Structural optimization

The structure of the amine and its acetylated derivative used in the molecular docking simulation was fully optimized using density functional theory implemented in the Gaussian 09 package [20] at the theoretical level of B3LYP with two combined basic sets LanL2DZ [21] for optimizing iron atom and 6-311G+(d) for optimizing carbon, hydrogen, oxygen, and nitrogen atoms [22], the fully optimized three-dimensional structures are presented in Figure 2.

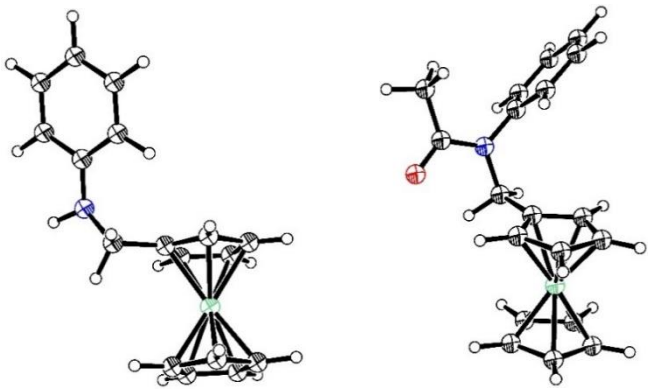

Figure 2. *Fully optimized three-dimensional structures of ligand FA (left) and NFA (right) (ORTEP View 03, V1.08); thermal ellipsoids are plotted at 50 % probability level*

Docking simulations

Molecular docking simulation was performed using AutoDockVina 1.1.2 docking software [23], executed on a personal computer with the following characteristics: Processor: Intel CORE i3-7100U CPU @ 2.40 GHz processor, system memory: 4 GB RAM, system type: 64-bit operating system, Windows 11 as operating system.

Results and discussion

Nuclear magnetic resonance spectral analysis

The ^{1}H NMR spectrums of FA and NFA (Figure 3) reveal two downfield singlets in the range of δ = 4.01-4.20 ppm, which are ascribed respectively to 2- and 3-protons of the substituted cyclopentadienyl ring C_5H_4. The unsubstituted cyclopentadienyl ring C_5H_5 protons appear as a singlet

at 4.24 ppm for FA and 4.08 ppm for NFA. A doublet appeared at δ = 4.33 and 4.61 ppm for FA and NFA, respectively, due to methylene protons. This downfield shift of methylene protons was observed due to the electronegativity of the nitrogen atom. For the proton linked to the nitrogen atom of FA, a singlet was observed at δ = 7.31 ppm, the protons of the methyl group of NFA appeared as a singlet at δ = 1.75 ppm, the aromatic protons appeared in the range of δ = 6.72-7.25 ppm for FA and in the range of 6.99-7.32 ppm for NFA.

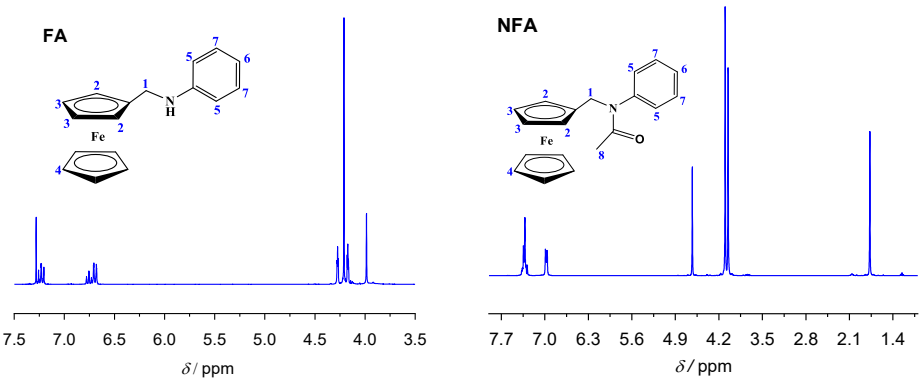

Figure 3. *^{1}H NMR spectra of N-ferrocenylmethylaniline (FA) and N-ferrocenylmethyl-N-acetylaniline (NFA)*

In the ^{13}C NMR spectrum (Figure 4), each carbon atom resonances appears at its characteristic zone according to its carbon atom hybridization. The carbon atom which resonates at δ = 44.15 and 49.12 ppm is associated with the carbon atom of the methylene group. The carbon atoms of the ferrocenyl group resonate between 68.89-87.94 ppm for FA and in the range of 68.86-83.86 for NFA, whereas the carbon atoms of the aromatic rings are observed between 113.60-149.06 ppm for FA and in the range of 128.60 to143.56 ppm for NFA. The carbon of the methylene group is observed at 44.15 and 49.12 ppm for the amine and its acylated form, respectively.

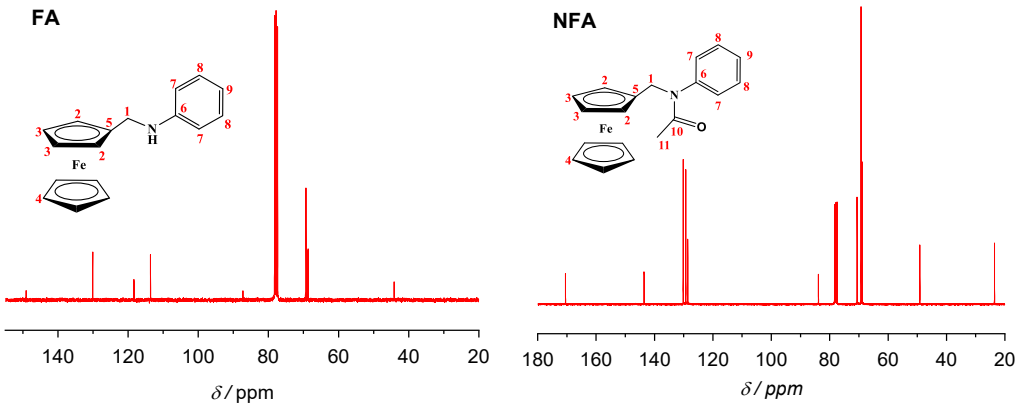

Figure 4. *^{13}C NMR spectra of N-ferrocenylmethylaniline (FA) and N-ferrocenylmethyl-N-acetylaniline (NFA)*

Cyclic voltammetry studies

The cyclic voltammetry behavior of 3 mM FA and NFA in the presence of gradually increasing concentration of CB-DNA at a bare glassy carbon electrode is shown in Figure 5. Upon addition of CB-DNA into FA or NFA solution, the anodic peak potential was shifted in the negative going direction and anodic peak current density was remarkably decreased. The significant decrease in peak current density can be attributed to the formation of the slowly diffusing adducts FA-DNA and NFA-DNA, which lower the concentration of the free ligands FA and NFA responsible for charge transfer reactions. The shift in the anodic peak potential in the negative going direction is attributed to the physical interaction between ligands and CB-DNA [24].

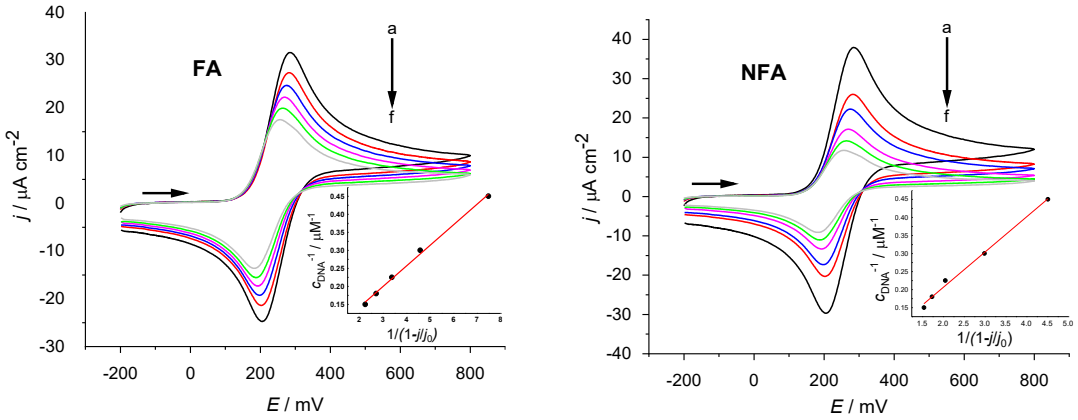

Figure 5. *Cyclic voltammograms of 3 mM phosphate buffer solution of FA and NFA in the absence (a) and presence of 2 (b), 3 (c), 4 (d), 5 (e) and 6 µM (f) of CB-DNA recorded at 0.1 V s^{-1} potential scan rate. Inset: plots of c_{DNA}^{-1} vs. 1/1-(j/j_0)*

The binding constants of the investigated compounds were calculated from the decrease in the anodic peak current density of FA-DNA and NFA-DNA adducts relative to free FA and NFA, respectively, using equation (1) [25]:

$$\frac{1}{c_{DNA}} = \frac{K_b(1-A)}{1-(j/j_0)} - K \quad (1)$$

where A is the proportionality constant, K_b is the binding constant, j and j_0 are the anodic peak current densities in the presence and absence of DNA, and c_{DNA} is DNA concentration. Linear equations were obtained from the plot of c_{DNA}^{-1} *vs.* 1/1-(j/j_0) (inset of Figure 5) with a linear correlation coefficient of 0.995. This suggested that the binding number was 1, thus, the inclusion complexes interacted with CB-DNA to form a 1:1 association complex. The values of the binding free energy of the ligands FA and NFA with CB-DNA were obtained using binding constants obtained from the y-intercept of the linear equation, and their values were found to be -27.15 and -29.76 kJ mol^{-1}, respectively, as shown in Table 1.

Table 1. *The linear equations of c_{DNA}^{-1} vs. 1/1-(j/j_0), binding constant, and binding free energy values of FA-DNA and NFA-DNA obtained from CV data at pH 7.2 and T= 301 K*

Adduct	Equation	R^2	K_b / M^{-1}	-Δ*G* / kJ mol^{-1}
FA-DNA	*y* = 0.06*x* - 0.0028	0.995	5.7×10^4	27.15
NFA-DNA	*y* = 0.163*x* - 0.0465	0.995	16.3×10^4	29.76

Binding site size

The binding site size (*s*) was calculated based on equation (2) [26]:

$$\frac{c_b}{c_f} = K_b\left(\frac{\text{free base pairs}}{s}\right) \quad (2)$$

where *s* represents the binding site size in terms of base pair, K_b is the binding constant, c_f is the concentration of the free compound, and c_b represents the concentration of the DNA-bound compound. As the concentration of a DNA base pair is given in terms of nucleotide phosphate, the concentration of the DNA base pair will be expressed as $c_{DNA}/2$ and hence, equation (2) can be written as equation (3):

$$\frac{c_b}{c_f} = K_b\frac{c_{DNA}}{2s} \quad (3)$$

The c_b/c_f ratio is equal to (j_0-j) / j [27], which are the values of experimental peak current densities. The plots of c_b/c_f versus c_{DNA} are displayed in Figure 6.

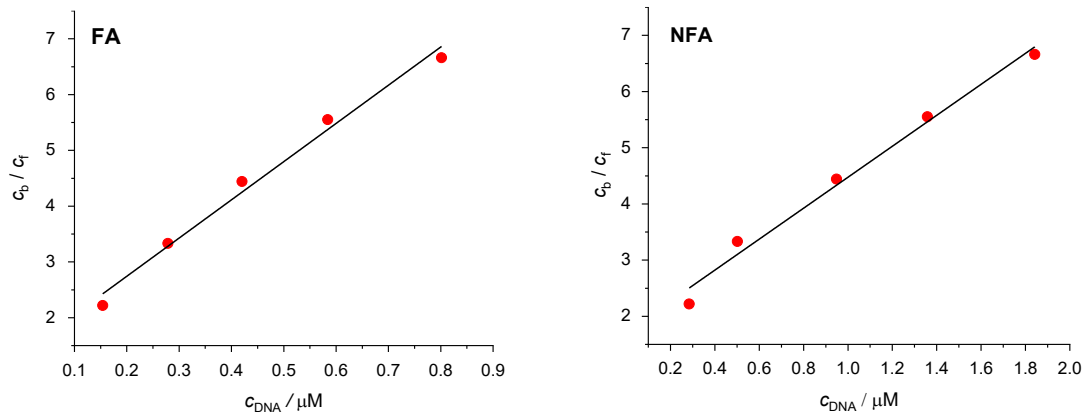

Figure 6. *Plots of c_b/c_f versus c_{DNA} for FA and NFA, used for the calculation of binding site size*

The equations obtained by least squares fitting in the studied concentration range for FA and NFA are shown in Table 2 (where *y* represents the value of the c_b/c_f ratio and *x* the compound concentration, expressed in µM).

Table 2. *Values of binding site size obtained using the plot of c_b/c_f versus C_{DNA}*

Adduct	Equation	R^2	*s* (base pair)
FA-DNA	$y = 6.85x + 1.372$	0.983	0.004
NFA-DNA	$y = 2.75x + 1.719$	0.982	0.029

The small values of binding site size further suggest that FA and NFA interact electrostatically with CB-DNA.

Effect of ionic strength on the interaction of FA and NFA with CB-DNA

Generally, the ionic strength of the reaction medium has a substantial impact on the strength of the electrostatic interaction. In this section, the ionic strength on the binding propriety of FA and NFA was evaluated by adding various concentrations of NaCl solution to a 3 mM solution of DNA with and without 4 µM of FA and NFA. Upon NaCl addition, the anodic current peak densities of the complexes DNA-FA and DNA-NFA gradually decreased as the concentration of NaCl was increased from 0 to 80 mM, indicating the existence of electrostatic interaction as presented in Figure 7.

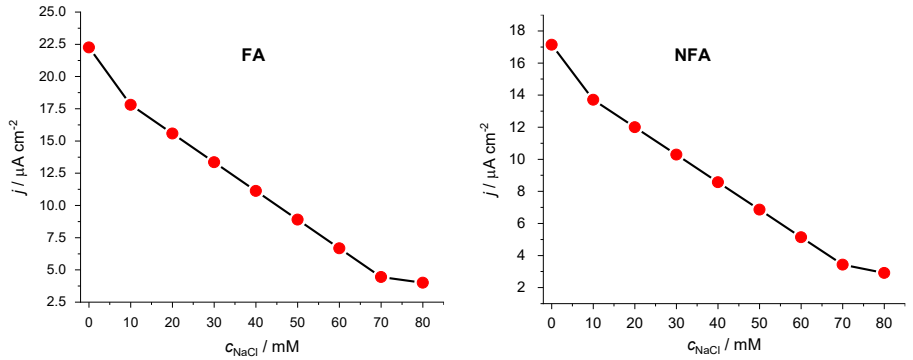

Figure 7. *Influence of the ionic strength of NaCl on the anodic current peak densities of DNA-FA and DNA-NFA complexes*

Molecular docking studies

To simulate the interaction between the target DNA and the test compounds, molecular docking simulation was performed using AutoDockVina 1.1.2 docking software [27]. The 3D-crystal structure

of DNA sequence d(CGCGATATCGCG) dodecamer (ID: 1DNE), shown in Figure 8, was obtained from the online protein data bank (https://www.rcsb.org/pdb) was used as a target [28].

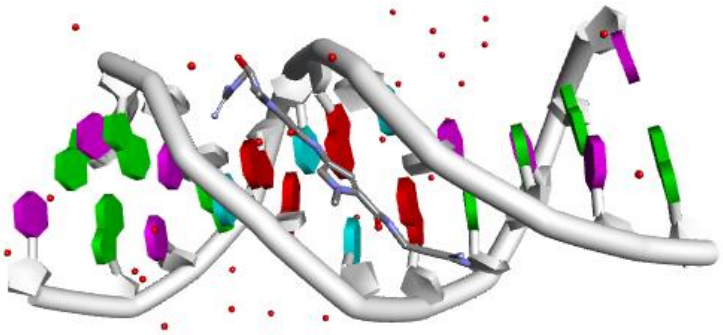

Figure 8. *3D-crystal structure of DNA sequence d(CGCGATATCGCG) 2 dodecamer (ID: 1DNE)*

Furthermore, polar hydrogen atoms and Gasteiger charges were added to the target by AutoDock 4.2 docking software [29]. Then, the Lamarckian genetic algorithm method was used to search for the binding position in the DNA target, and the grid points were determined based on covering the whole of the DNA target. All other parameters were set as default. The lowest energy conformation obtained from the ligand-target complex was considered the predicted binding mode and compared with the experimental results. The output from docking studies was rendered with Discovery Studio [30] to visualize the DNA-ligand interactions. Figure 9 presents the lowest energy docking poses of the compounds FA and NFA inserted into the minor groove at the G/C - rich region of the oligonucleotide.

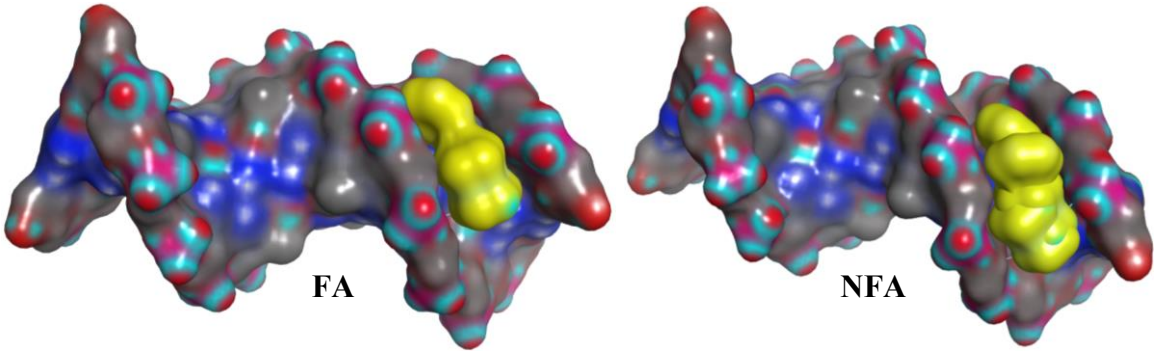

Figure 9. *Surface view of the docked pose of FA and NFA (yellow color) with DNA (PDB ID: 1DNE) illustrating the insertion of FA and NFA in the minor groove of DNA*

The stable conformation corresponding to the lowest binding energy was used for docking analysis. The visualization of the interaction was generated with Discovery Studio [30]. Results from molecular docking suggest that hydrogen bonding interactions are involved in the binding process. NFA had the highest negative binding energy. It interacted with the target DNA (1DNE) *via* three conventional hydrogen bonds with the nucleotides DG16, DG10, and DC11. However, the compound FA interacted only *via* two conventional hydrogen bonds with the nucleotides DC11 and DG10. Table 3 summarizes the interacting nucleotides and their corresponding bond types and length with the binding energy.

Figure 10 illustrates the 3D binding mode of FA and NFA with the nearby nucleotides in the active site of DNA.

The results obtained from molecular docking were entirely in agreement with the experimental data obtained from cyclic voltammetry.

Table 3. *Hydrogen bonding, binding constant, and binding free energy values of FA-DNA and NFA-DNA adducts obtained from molecular docking analysis data*

Adduct	Nucleotide	Distance, nm	K_b / M^{-1}	-Δ*G* / kJ mol^{-1}
FA-DNA	DC11	25.6	6.21×10^4	27.30
	DG10	24.8		
NFA-DNA	DG16	24.7	17.22×10^4	29.82
	DG10	27.0		
	DC11	19.3		

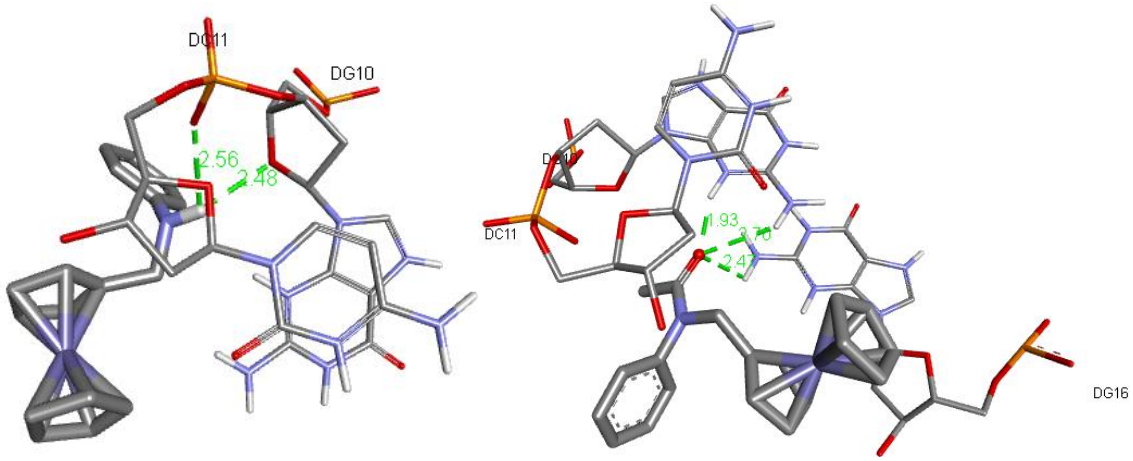

Figure 10. *3D binding mode of the FA and NFA with DNA (PDB ID: 1DNE), hydrogen bonds are denoted by green dashed line*

Conclusions

In this paper, the binding affinity of N-ferrocenylmethylaniline (FA) and its N-acetylated derivative (NFA) with chicken blood DNA (CB-DNA) have been studied. The results suggest that both compounds bind to CB-DNA *via* groove binding mode. The interaction evidence is supported by the following findings:

1) the results showed that the obtained binding free energy by cyclic voltammetry 27.15 and 29.76 kJ mol^{-1} for FA and NFA, respectively, is matched roughly to the binding free energy that was calculated by the molecular docking study 27.3 and 29.82 kJ mol^{-1};
2) decrease of the peak current density of the FA and NFA upon adding the CB-DNA;
3) the results of CV and ionic strength effect indicated the electrostatic interaction of both compound FA and NFA with CB-DNA as the dominant mode. The same mode of interaction was also supported by the results obtained from molecular docking.

Acknowledgements*: This work was supported by the Directorate-General of Scientific Research and technological Development (DGRSDT) and the Laboratory of Valorization and Technology of Saharan Resources (VTRS) (project code: B00L01UN390120150001).*

References

[1] J. F. Alhmoud, J. F. Woolley, A.-E. Al Moustafa, M.I. Malki, DNA Damage/Repair Management in Cancers, *Cancers* (Basel) **12** (2020) 1050. https://doi.org/10.3390/cancers12041050
[2] N. Chowdhury, A. Bagchi, An Overview of DNA-Protein Interactions, *Current Chemical Biology* **9** (2016) 73-83. https://doi.org/10.2174/2212796809666151022202255
[3] M. R. Shorkaei, Z. Asadi, M. Asadi, Synthesis, characterization, molecular docking and DNA binding studies of Al(III), Ga(III) and In(III) water-soluble complexes, *Journal of Molecular Structure* **1109** (2016) 22-30. https://doi.org/https://doi.org/10.1016/j.molstruc.2015.12.070

[4] S. Ghosh, Cisplatin, The first metal based anticancer drug, *Bioorganic Chemistry* **88** (2019) 102925. https://doi.org/10.1016/j.bioorg.2019.102925
[5] V. J. Fiorina, R. J. Dubois, S. Brynes. Ferrocenyl polyamines as agents for the chemoimmunotherapy of cancer, *Journal of Medicinal Chemistry* **21** (1978) 393-395. https://doi.org/10.1021/jm00202a016
[6] N. Zegheb, C. Boubekri, T. Lanez, E. Lanez, In Silico Study on N-Ferrocenylmethyl-N-Phenylpropionohydrazide and N-Ferrocenylmethyl-N-Pheylbenzohydrazide as Anticancer Drugs for Breast and Prostate Cancer, *International Journal of Pharmacology, Phytochemistry and Ethnomedicine* **11** (2018) 17-25. https://doi.org/10.18052/WWW.SCIPRESS.COM/IJPPE.11.17
[7] A. Khennoufa, L. Bechki, T. Lanez, E. Lanez, N. Zegheb, Spectrophotometric, voltametric and molecular docking studies of binding interaction of N-ferrocenylmethylnitroanilines with bovine serum albumin, *Journal of Molecular Structure* **1224** (2021) 129052. https://doi.org/10.1016/j.molstruc.2020.129052
[8] A. Kedadra, T. Lanez, E. Lanez, H. Hemmami, M. Henni, Synthesis and antioxidant activity of six novel N-ferrocenylmethyl-N-(nitrophenyl)- and -N-(cyanophenyl)-acetamides: Cyclic voltammetry and molecular docking studies, *Journal of Electrochemical Science and Engineering* **12** (2022) 293-304. https://doi.org/10.5599/jese.1162
[9] T. Lanez, E. Lanez, A Molecular Docking Study of N-Ferrocenylmethylnitroanilines as Potential Anticancer Drugs, *International Journal of Pharmacology, Phytochemistry and Ethnomedicine* **2** (2016) 5-12. https://doi.org/10.18052/www.scipress.com/IJPPE.2.5
[10] N. Zegheb, C. Boubekri, T. Lanez, E. Lanez, T. T. Küçükkılınç, E. Öz, A. Khennoufa, S. Khamouli, S. Belaidi, In Vitro and In Silico Determination of Some N-ferrocenylmethylaniline Derivatives as Anti-Proliferative Agents Against MCF-7 Human Breast Cancer Cell Lines, *Anti-Cancer Agents in Medicinal Chemistry* **22** (2022) 1426-1437. https://doi.org/10.2174/1871520621666210624141712
[11] O. Kennard, DNA-drug interactions, *Pure and Applied Chemistry* **65** (1993) 1213-1222. https://doi.org/10.1351/pac199365061213
[12] N. Shahabadi, A. Fatahi, Multispectroscopic DNA-binding studies of a tris-chelate nickel(II) complex containing 4,7-diphenyl 1,10-phenanthroline ligands, *Journal of Molecular Structure* **970** (2010) 90-95. https://doi.org/10.1016/j.molstruc.2010.02.048
[13] J. M. Osgerby, P. L. Pauson, 128. Ferrocene derivatives. Part VI. DL-ferrocenylalanine, *Journal of the Chemical Society (Resumed)* (1958) 656-660. https://doi.org/10.1039/JR9580000656
[14] T. Lanez, H. Benaicha, E. Lanez, M. Saidi, Electrochemical, spectroscopic and molecular docking studies of 4-methyl-5-((phenylimino)methyl)-3H- and 5-(4-fluorophenyl)-3H-1,2-dithiole-3-thione interacting with DNA, *Journal of Sulfur Chemistry* **39** (2018) 76-88. https://doi.org/10.1080/17415993.2017.1391811
[15] E. Lanez, L. Bechki, T. Lanez, Computational molecular docking, voltammetric and spectroscopic DNA interaction studies of 9N-(Ferrocenylmethyl)adenine, *Chemistry and Chemical Technology* **13** (2019) 11-17. https://doi.org/10.23939/chcht13.01.011
[16] R. Vijayalakshmi, M. Kanthimathi, V. Subramanian, B.U. Nair, DNA cleavage by a chromium(III) complex, *Biochemical and Biophysical Research Communications* **271** (2000) 731-734. https://doi.org/10.1006/bbrc.2000.2707
[17] J. A. Glasel, Validity of nucleic acid purities monitored by 260nm/280nm absorbance ratios, *Biotechniques* **18** (1995) 62-63.
[18] Anthony J. Pearson, *Metallo-organic chemistry*, Chichester [West Sussex] ; New York, John Wiley & Sons, 1985. ISBN: 978-0471904403

[19] C.-S. Lu, X.-M. Ren, C.-J. Hu, H.-Z. Zhu, Q.-J. Meng, The Inclusion Compound of a New Ionizable Derivative of b b-Cyclodextrin with Ferrocenium Drug, *Chemical and Pharmaceutical Bulletin* **49** (2001) 818-821. https://doi.org/10.1248/cpb.49.818
[20] M. Frisch, G. Trucks, H. Schlegel, G. S. Wallingford, U. CT, U. 2009, Gaussian 09; Gaussian, Inc, Gaussian, (2016). https://gaussian.com/g09citation
[21] C. Chizallet, S. Lazare, D. Bazer-Bachi, F. Bonnier, V. Lecocq, E. Soyer, A.-A. Quoineaud, N. Bats, Catalysis of Transesterification by a Nonfunctionalized Metal−Organic Framework: Acido-Basicity at the External Surface of ZIF-8 Probed by FTIR and ab Initio Calculations, *Journal of the American Chemical Society* **132** (2010) 12365-12377. https://doi.org/10.1021/ja103365s
[22] M. Shahsavari, S. Tajik, I. Sheikhshoaie, H. Beitollahi, Fabrication of Nanostructure Electrochemical Sensor Based on the Carbon Paste Electrode (CPE) Modified with Ionic Liquid and Fe_3O_4/ZIF-67 for Electrocatalytic Sulfamethoxazole Detection, *Topics in Catalysis* **65** (2022) 577-586. https://doi.org/10.1007/s11244-021-01471-8
[23] O. Trott, A. J. Olson, AutoDock Vina: Improving the speed and accuracy of docking with a new scoring function, efficient optimization, and multithreading, *Journal of Computational Chemistry* **30** (2009) 455-461. https://doi.org/10.1002/jcc.21334
[24] N. Li, Y. Ma, C. Yang, L. Guo, X. Yang, Interaction of anticancer drug mitoxantrone with DNA analyzed by electrochemical and spectroscopic methods, *Biophysical Chemistry* **116** (2005) 199-205. https://doi.org/10.1016/j.bpc.2005.04.009
[25] G.-C. Zhao, J.-J. Zhu, J.-J. Zhang, H.-Y. Chen, Voltametric studies of the interaction of methylene blue with DNA by means of β-cyclodextrin, *Analytica Chimica Acta* **394** (1999) 337-344. https://doi.org/10.1016/S0003-2670(99)00292-5
[26] M. Aslanoğlu, N. Öge, Voltametric, UV Absorption and Viscometric Studies of the Interaction of Norepinephrine with DNA, *Turkish Journal of Chemistry* **29** (2005) 477-485. https://journals.tubitak.gov.tr/chem/vol29/iss5/3
[27] M. Aslanoglu, G. Ayne, Voltammetric studies of the interaction of quinacrine with DNA, *Analytical and Bioanalytical Chemistry* **380** (2004) 658-663. https://doi.org/10.1007/s00216-004-2797-5
[28] M. Coll, J. Aymami, G. A. van der Marel, J. H. van Boom, A. Rich, A. H. J. Wang, Molecular structure of the netropsin-d(CGCGATATCGCG) complex: DNA conformation in an alternating AT segment, *Biochemistry* **28** (1989) 310-320. https://doi.org/10.1021/bi00427a042
[29] G. M. Morris, H. Ruth, W. Lindstrom, M. F. Sanner, R. K. Belew, D. S. Goodsell, A. J. Olson, Software news and updates AutoDock4 and AutoDockTools4: Automated docking with selective receptor flexibility, *Journal of Computational Chemistry* **30** (2009) 2785-2791. https://doi.org/10.1002/jcc.21256
[30] BIOVIA, Dassault Systems, Discovery Studio Visualizer, v21.1.1.020289, San Diego: Dassault Systems, 2020. https://www.3ds.com/products/biovia/all-products

J. Electrochem. Sci. Eng. **14(2)** (2024) 147-161; http://dx.doi.org/10.5599/jese.2008

Open Access : : ISSN 1847-9286
www.jESE-online.org

Original scientific paper

Photo-bioelectrochemical cell anodes enhanced with titanium oxide, carbon nanotubes and chlorophyll-based catalyst on different supporting materials

Marcelinus Christwardana[1,2,✉], Athanasia Amanda Septevani[3,4] and Dilla Dayanti[2,3]

[1]*Department of Chemistry, Faculty of Science and Mathematics, Diponegoro University, Jl. Prof. Sudarto, S.H., Tembalang, Semarang 50275 , Indonesia*

[2]*Master Program of Energy, School of Postgraduate Studies, Diponegoro University, Jl. Imam Bardjo, S.H., Pleburan, Semarang50241, Indonesia*

[3]*Research Center for Environmental and Clean Technology, National Research and Innovation Agency, KST BRIN Cisitu, Bandung 40135, Indonesia*

[4]*Collaborative Researh Center for Zero Waste and Sustainability, Universitas Katolik Widya Mandala, Surabaya 60114, Indonesia*

Corresponding author: ✉marcelinus@lecturer.undip.ac.id

Received: July 31, 2023; Accepted: November 16, 2023; Published: December 11, 2023

Abstract

An important part of a photo-bioelectrochemical cell (PBEC) is the photo-biocatalyst substrate taken as anode. This study aims to explain the effect of CNT/TiO_2/chlorophyll photocatalyst coated on the cellulose nanopaper (CNP) substrate on the PBEC performance and to compare the results with those obtained for the commercial indium tin oxide (ITO) glass and flexible ITO as substrates. The results showed high sheet resistance of CNP, which is 61182 Ω sq^{-1}, which is reduced by 80 % in the presence of CNT/TiO_2/Chl biocatalyst. The highest output voltage of 0.95 to 1 V was produced by coating CNT/TiO_2/Chl on the flexible ITO. The maximum current density (J_{max}) of 3726 mA m^{-2} and the highest maximum power density value of around 574 mW m^{-2} were obtained for illuminated CNT/TiO_2/Chl on the rigid ITO anode. In dark conditions, the highest power density was observed for CNP as the supporting substrate. The photo-bioelectrochemical cell adopting CNT/TiO_2/Chl and CNP as the supporting substrate material has great potential for a variety of applications, such as wearable electronics, environmental monitoring, remote or off-grid energy supply, and renewable energy systems, thereby contributing to the advancement of sustainable energy technologies.

Keywords

Photo-bioanode; photo-biocatalyst substrates; flexible materials; natural dye catalyst; artificial photosynthesis; photo-current; maximum power density

Introduction

As a low-cost and eco-friendly alternative to conventional materials with excellent light harvesting efficiency, natural dyes have been the subject of intensive research in recent years [1,2]. This includes their use in photo-bioelectrochemical cells (PBECs) for the generation of electricity. Significant research efforts have been made to build semiconductor/photoelectrode hybrids for high-efficiency PBECs, which will help to bring sustainable solar energy to a commercially ready state [3,4]. For this reason, several natural pigments have been investigated as biocatalysts in PBECs systems [5]. Plant or microalgae pigments are able to do this because their electrical structure may alter the wavelength of incoming sunlight, creating an electric current [6,7]. This is due to the fact that photosynthesis may be performed by both land plants and microalgae.

Converting light energy into chemical energy in PBECs *via* photosynthesis is an efficient, sustainable, and complicated process [8,9]. Chlorophyll-rich thylakoid membranes and photo-systems from plants and microalgae are isolated and often employed as a source to convert light into electrical energy. Another crucial step in the creation of photo-current is the transit of electrons from the reaction center to the electrodes after their conversion from light [10,11]. Researchers have ramped up their efforts to create higher photo-currents by using natural and manmade components in the design of systems [12].

Previous research has shown that the photoanode of PBEC made up of a network of TiO_2 nanoparticles provides substantial specific surface area support sites for the adsorption of dye molecules [13]. To date, the highest reported relative photoconversion efficiency in PBECs has been achieved using TiO_2 [14]. However, the comparatively wide band gap of TiO_2 is a common deficiency of this material, which may be lowered by addition or alteration with a dye. The injected electrons tend to diffuse *via* trap-restricted diffusion processes across the matrix of random colloidal particles and grain boundaries of TiO_2 [15].

A substrate of photoanode is critical to PBECs as it serves as a support for the biocatalyst. Many solar cells rely on rigid substrates like ITO, but a flexible ITO was also employed in their development. Since the substrate is flexible, PBECs may be housed in a large variety of reactor geometries than possible with a rigid one. Rigid ITO is brittle and cracks easily during application, whereas flexible substrates can wear out over a long time. Rigid ITO costs more to produce since indium will be scarce in the future because it is a non-renewable material [16]. Flexible substrates can be bent or shaped according to the desired surface or shape, allowing solar cells to be fabricated on surfaces and shapes that rigid substrates cannot reach. Flexible substrates are typically lighter and slimmer than rigid substrates, reducing the weight and thickness of the whole PBEC. The use of flexible substrates can decrease the quantity of raw materials required to manufacture PBECs. Flexible substrates are typically more resistant to stress and vibration than rigid substrates that are brittle.

In this research, we describe the fabrication of a photo-biocatalyst composed of CNT, TiO_2, and chlorophyll coated on several substrates, including ITO glass, ITO flexible, and cellulose nano paper (CNP). The properties of CNP being produced on a lab scale will be compared to commercial ITO glass and flexible ITO. The hypothesis in this study is that the photo-biocatalyst coated on CNP has performance that is close to, or even better than, the photo-biocatalyst coated on either ITO glass or flexible ITO. Research on the influence of anode substrate on PBEC performance has never been conducted before. Hence, we consider this study to be an academic novelty. To assess the performance of PBECs, output voltage, current density, and power density will be evaluated. Some of the advantages and benefits resulting from this research include the development of innovative photo-biocatalysts, use of various supporting electrode materials, development of sustainable

materials, wide application such as water photocatalysis, pollutant detection, chlorophyll sensitive solar cells, as well as contribution to the environmental research and renewable energy.

Experimental

Catalyst fabrication

The extraction of chlorophyll from Spirulina is described in detail in the referenced articles [9,13]. In the first step, a commercial ITO glass (Hangzhou DCT Technology, Hangzhou, China), flexible ITO (Hangzhou DCT Technology, Hangzhou, China), and CNP [17] with dimensions of 1×1 cm were sonicated with ethanol medium for 15 minutes. The supporting materials were then placed on tissue paper and air-dried at room temperature. During the coating process, each edge of the supporting material was sealed to ensure that the catalyst paste was formed correctly in the center. Amounts of 0.25 g CNT (>95 % purity; 50 to 90 nm diameter) and 0.25 g TiO_2 (<100 nm; 99.5 % purity), purchased from Merck (Darmstadt, Germany), were mixed with 2 mL ethanol (95 %, commercial grade) during the catalyst coating preparation procedure. The liquid was combined until it formed a paste and poured over the isolated, four-sided support materials. On the surface of these supporting materials, catalyst paste was distributed consistently using a ruler. The prepared CNT/TiO_2 on supporting materials were then annealed for 15 minutes at 240 °C and washed using DI water to remove unbound CNTs. Then, these catalysts on support materials were left at room temperature (27 to 30 °C) for 2 hours. A 3 mL of chlorophyll (Chl) was dripped and left to stand for one day at room temperature. Before being used as a photo-bioanode, the CNT/TiO_2/Chl coating on the surface of the supporting material was washed with ethanol to remove unbound chlorophyll. Figure 1a illustrates the chemical pathway of forming the substrate coating using CNT, TiO_2, and chlorophyll. Figure 1b shows the image of a photo-bioanode with different supporting materials, while Figure 1c demonstrates the flexibility of CNT/TiO_2/Chl@CNP.

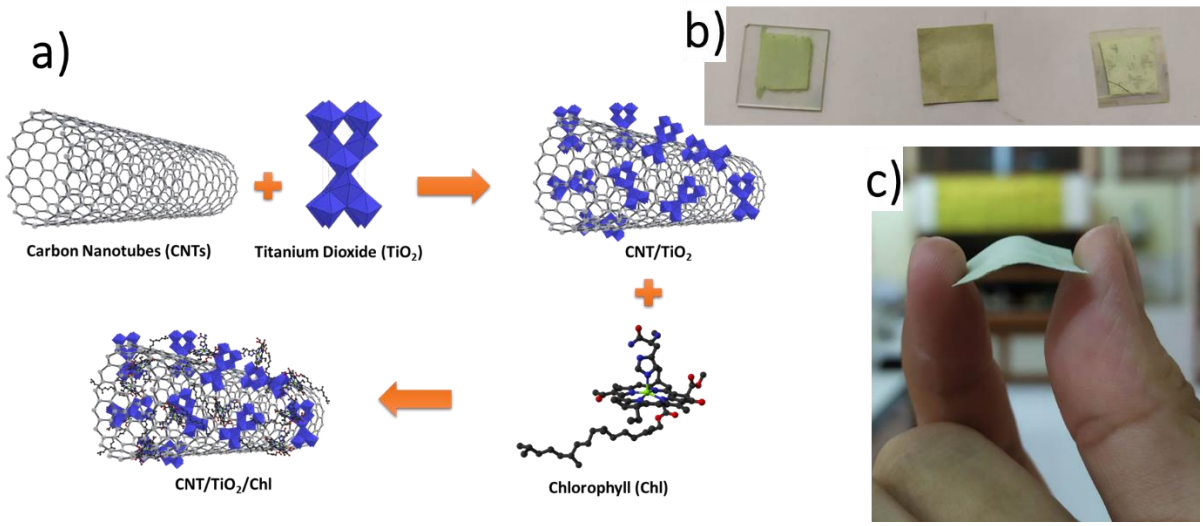

Figure 1. *a) Schematic of the synthesis of CNT/TiO_2/Chl deposited on b) ITO glass (left), cellulose nanopaper (middle), flexible ITO (right), and c) flexible cellulose nanopaper*

Reactor configuration

The scheme of PBEC is presented in Figure 2. The anode was composed of CNT/TiO_2/Chl bonded to supporting materials, while the cathode was composed of ITO/C placed at a distance of 5 cm from the anode. In the reaction chamber, the cathode transforms the oxygen released from the anode surface into water. A glass beaker served as the reaction cell, and the anode and cathode electrodes

were connected in series. For the purpose of this research, a photo-bioelectrochemical cell will use water as its electrolyte solution.

The photo-current tests were conducted using a customized solar simulator system, including a customized three-electrode electrochemical chamber, a customized light chamber equipped with a desk LED lamp (no brand) of changing light intensity and color temperature (2700 to 6000 K), and a digital light meter LX1010B to measure the actual light intensity within the chamber in real-time. The photo-bioelectrochemical system was then enclosed in a customized light chamber and sealed to prevent outside light from reaching it. This analysis is conducted twice, and the results shown are the mean.

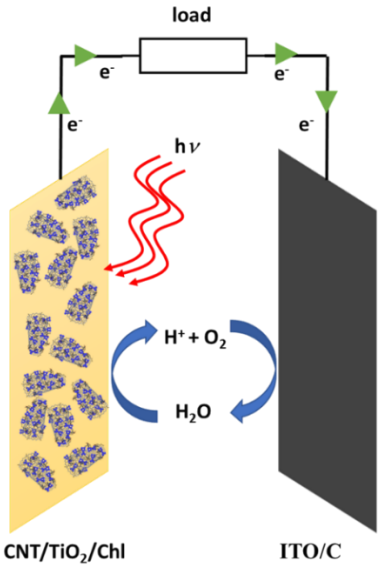

Figure 2. *Schematic diagram of photo-bioelectrochemical cell*

Electrochemical analysis

An Arduino-based potentiostat was connected to a computer to conduct electrochemical measurements, including half-cell and full-cell experiments. In half-cell measurements, the reference electrode was Ag/AgCl, and a Pt wire was employed as the counter electrode. The working electrode was a glassy carbon electrode (GCE) (Wuhan Corrtest Instruments Corp. Ltd., Hubei, China) with a diameter of 3.5 mm, on which the photo-biocatalyst was loaded. A small amount (10 µL) of photocatalyst ink with a concentration of 1 mg mL^{-1} was applied to the GCE surface and allowed to dry for 1 hour. The electrolyte solution used was 1 M PBS (pH 7.4) (Sigma Aldrich, St. Louis, USA), and the entire process was conducted under aerobic conditions without the addition of air gas.

To determine the open circuit voltage (OCV), the electrode of a photo-bioelectrochemical cell was methodically connected to a multimeter device (UNI-T UT-61E) without the addition of any external resistance. Then, the chronoamperometry (CA) measurement was established, and all CA readings were recorded using a multimeter in a light chamber with cyclic on/off illumination set at 1600 cd·sr m^{-2} (lux). Cell photo-current was measured at varying light illumination (900 to 1600 cd·sr m^{-2}) to determine light sensitivity. Polarization and power curves were determined at a closed-circuit voltage (CCV) using a range of resistor values from 10 MΩ to 100 Ω. Electric current was determined by dividing the measured voltage by the resistance of the load, power density was determined with the help of Ohm's law, and polarization curves were made using equations (1-3) [18]:

$$V = IR \quad (1)$$

$$J = I / A \quad (2)$$

$$P = VJ \quad (3)$$

where V / V is voltage, R / Ω is resistance, A / m^2 is electrode area, P / mW m^{-2} is power density, I / mA is current, and J / mA m^{-2} is current density.

FTIR and SEM analysis

FTIR (Perkin Elmer) instrument was used to examine the bond structures of the synthesized materials. The spectra were recorded from 4000 to 500 cm^{-1} at a spectra resolution of 4.0 cm^{-1}. A V-630 UV- VIS spectrometer (JASCO International Co., Japan) was used to record UV-Vis absorption spectra of synthesized samples from 300 to 800 nm. SEM-EDX JEOL JSM-6510LA (Tokyo, Japan) was used to inspect the morphology of the photo-biocatalyst.

Sheet resistance analysis

For measuring sheet resistance (R_s) of thin films, the four-point probe method is the most popular and straightforward approach [19]. In order to establish electrical contact with the material being characterized, a standard four-point probe instrument will typically include four equally spaced and co-linear probes. Applying a direct current (DC) through the outside probes causes a voltage to be induced between the two inner probes, which can then be used to determine the R_s. The sheet resistance may be determined by detecting this voltage drop using equation (4):

$$R_s = 4.53236\ \Delta V/I \quad (4)$$

where R_s / Ω sq^{-1} is the sheet resistance, ΔV is the voltage drop measured across the inner probes, and I is the current delivered at the outer probes.

Results and discussion

Physicochemical analysis

SEM analysis

Figure 3 depicts the SEM images of TiO_2, CNT/TiO_2, and CNT/TiO_2/Chl photo-biocatalysts. In the image of TiO_2 (Figure 3a), only agglomerated TiO2 is present. Van der Waals forces exist between individual TiO_2 particles, which helps form agglomerations by drawing together tiny particles [20].

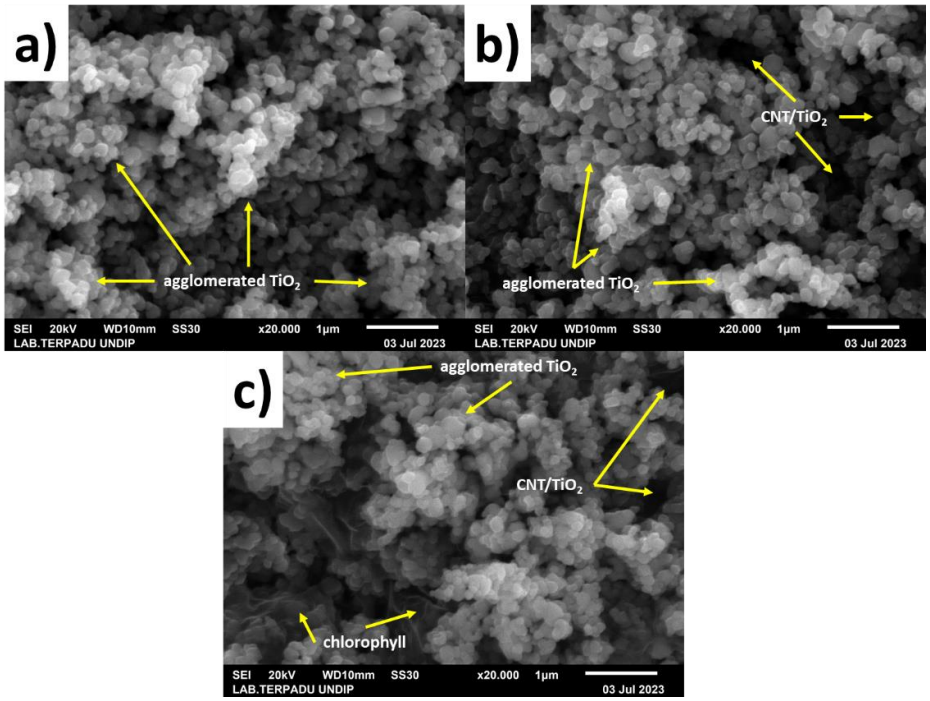

Figure 3. *SEM images of a) TiO_2, b) CNT/TiO_2, and c) CNT/TiO_2/Chl*

In CNT/TiO_2 image (Figure 3b), in addition to TiO_2 aggregates, there are also CNTs coated to TiO_2. Van der Waals forces can produce tangible connections between CNT and TiO_2. CNT and TiO_2 can also form hydrogen bonds, particularly through the oxygen atoms on TiO_2 and the hydrogen atoms affixed to the surface or extremities of CNT [21]. Due to the non-covalent nature of the interaction between CNTs and TiO_2, the binding strength is quite low. Consequently, it is hypothesized that a significant number of CNTs did not adhere to the TiO_2 surface and were subsequently removed during the washing procedure. Consequently, the observation of carbon nanotubes (CNTs) adhered to TiO_2 presents significant difficulties. In CNT/TiO_2/Chl image (Figure 3c), in addition to agglomerated TiO_2 and CNT/TiO_2/Chl, chlorophyll is also present, which was not the case with the previous photocatalyst. Chlorophyll contains numerous hydroxyl and carbonyl groups that can form hydrogen bonds with oxygen-rich CNT or TiO_2 molecules [13]. CNTs and the porphyrin ring in chlorophyll possess a plethora of π electrons. Interactions between the chlorophyll porphyrin ring and the carbon ring on the CNT or between two chlorophyll molecules can involve π-π stacking.

FTIR analysis

Figure 4 depicts the FTIR spectra of TiO_2, CNT/TiO_2, and CNT/TiO_2/Chl. These spectra disclose distinct characteristics of TiO_2, CNT/TiO_2, and CNT/TiO_2/Chl. A prominent peak at 1638 cm^{-1} in the CNT/TiO_2/Chl spectrum indicates the presence of representative C=C bonds between CNT and chlorophyll, an interaction not observed in the CNT/TiO_2 and TiO_2 spectra. The peak observed at 3354 cm^{-1} corresponds to the -OH bond, indicating an increase in intensity in CNT/TiO_2 and CNT/TiO_2/Chl, which suggests increased water absorption due to adsorption [22].

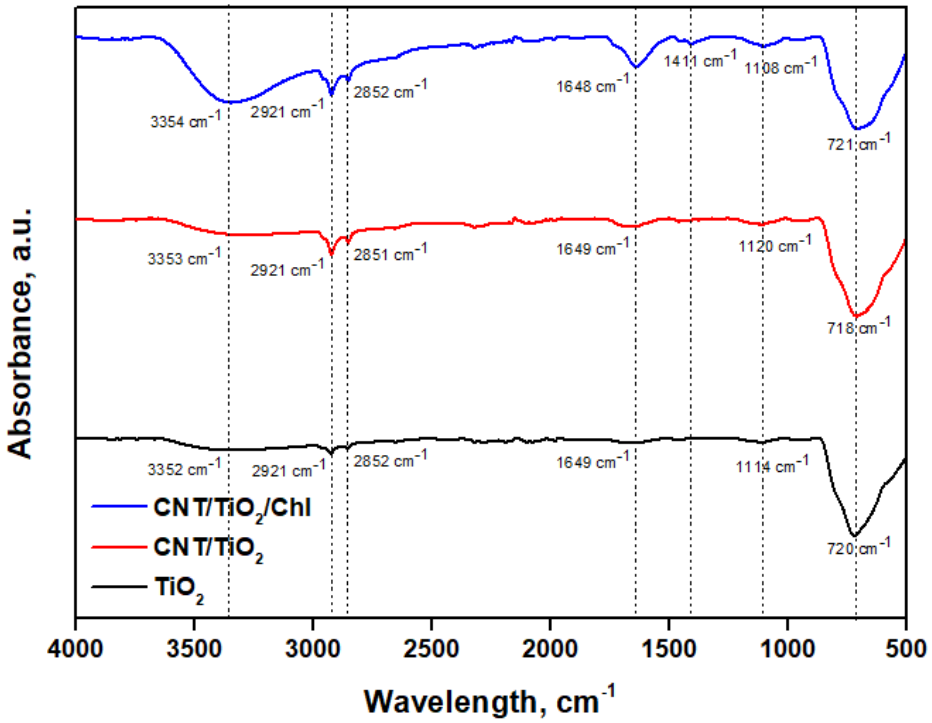

Figure 4. *FTIR spectra of TiO_2, CNT/TiO_2 and CNT/TiO_2/Chl*

The presence of peaks at 2851 and 2921 cm^{-1} provides additional support for this theory. A minor peak at 1649 cm^{-1} in CNT/TiO_2 is attributed to -N-O- bonds [23], whereas the peak at 1411 cm^{-1} in CNT/TiO_2/Chl represents CN stretching in chlorophyll [24,25]. In addition, a minor peak at 1108 to 1120 cm^{-1} indicates the presence of C-N-bonded or nitrogen oxide species [22]. According to Jiang *et al.* [26], the broad peak between 718 and 721 cm^{-1} corresponds to the O-Ti-O or Ti-O-Ti stretching

adsorption band in the TiO_2 lattice. These observations strongly suggest that chlorophyll binds strongly to the surface of CNT/TiO_2.

Half-cell characteristics

Cyclic voltammetry analysis

This study investigates the behavior and catalytic activity of PBEC anode structure made up of TiO_2, CNT/TiO_2 and CNT/TiO_2/Chl coated GC electrodes. Figure 5 shows CV profiles, which provide significant insight into the catalytic properties of the systems. Figure 5a highlights a number of observed phenomena. No redox peaks were observed in the GC, TiO_2, CNT/TiO_2, and CNT/TiO_2/Chl biocatalysts, suggesting the absence of any redox processes during the CV analysis. Furthermore, the introduction of TiO_2, CNT, and Chl to the GC results in a shifting of curves towards more negative current densities. This observation suggests that the presence of these materials promotes the oxygen reduction reaction (ORR), with the carbon-based electrode (GC and CNT) playing a more significant role in facilitating this reaction. Moreover, the specific capacitance value can be determined by assessing the area encompassed by the cyclic voltammetry curve. The specific capacitance values of GC, TiO_2, CNT/TiO_2, and CNT/TiO_2/Chl are 22.10, 23.30, 28.43, and 18.59 F g^{-1}, respectively.

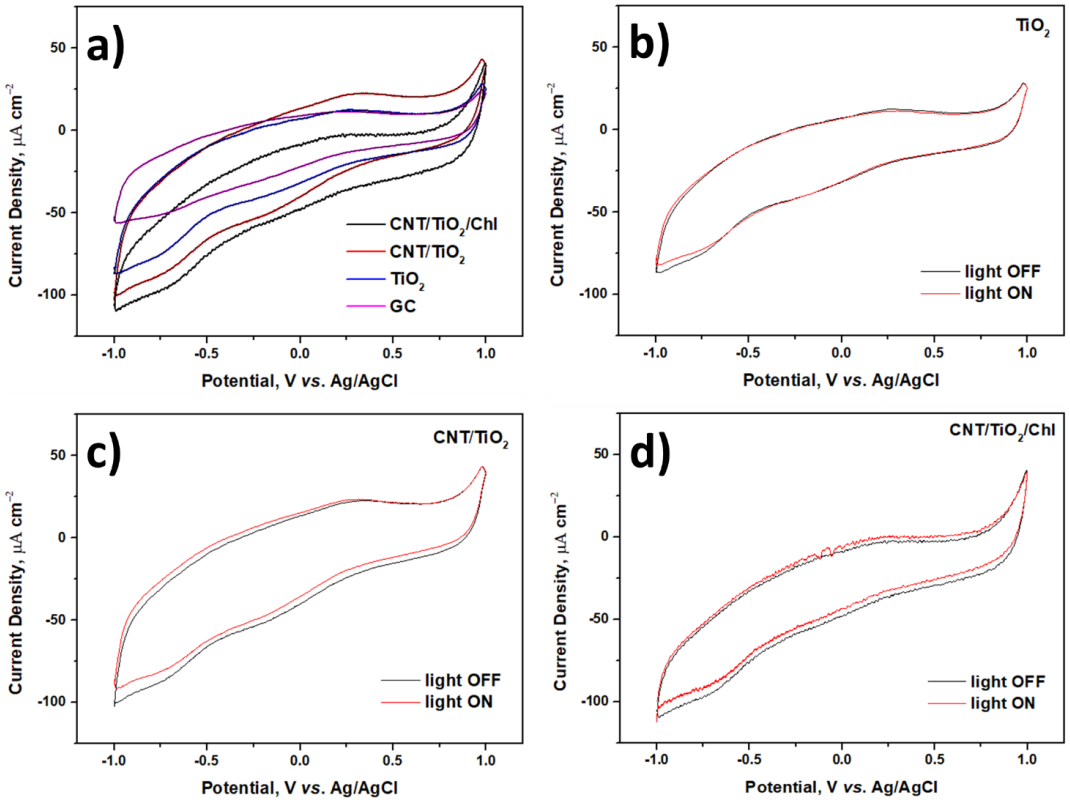

Figure 5. *a) CVs of GC, TiO_2, CNT/TiO_2 and CNT/TiO_2/Chl, and CVs with and without the presence of light for: b) TiO_2, c) CNT/TiO_2, and d) CNT/TiO_2/Chl*

Based on the specific capacitance findings, it can be concluded that CNT/TiO_2/Chl and TiO_2 exhibit favorable characteristics for utilization in energy conversion systems, such as PBEC, due to their comparatively lower specific capacitance values. In contrast, it is worth noting that the CNT/TiO_2 composite exhibits a comparatively higher specific capacitance, hence rendering it a more viable option for utilization in energy storage devices.

Due to their capacity to convert solar energy into electricity, PBEC systems are promising candidates for sustainable energy conversion, according to research findings. In these systems, the

anode catalyzes the oxidation of water molecules into oxygen and protons. TiO_2, an extensively used photocatalyst, has been shown to improve the charge transfer properties of the anode, thereby enhancing its catalytic activity. Due to their high surface area, electrical conductivity, and electrocatalytic properties, carbon nanotubes have also been used as catalysts in PBEC systems. The photosynthetic pigment chlorophyll increases the catalytic activity of the PBEC anode structure by facilitateing the transfer of electrons from the anode to the cathode. Overall, these findings suggest that PBEC systems have the potential to be efficient and environmentally friendly energy conversion solutions.

Figure 5b-d displays the CV curves of TiO_2, CNT/TiO_2, and CNT/TiO_2/Chl-coated GC electrodes in the presence or absence of light. In the presence of light, the CV curve of TiO_2 (Figure 4b) is at potentials less than -0.75 V *vs.* Ag/AgCl shifted marginally to less negative currents. Figures 5c and 5d demonstrate that this effect of less negative currents was also observed for CNT/TiO_2 and CNT/TiO_2/Chl. The presence of CNT on CNT/TiO_2 assists in the excitation of electrons when light is present and the transfer of electrons from the semiconductor material to the current collector, which also functions as a supporting material.

Sheet resistance of CNT/TiO_2/Chl at various supporting materials

Different substrates coated by CNT/TiO_2/Chl catalysts create different sheet resistances, where the type of supporting material has the strongest impact on the conductivity of the obtained materials (Figure 6). There are several points to consider. First, before being coated with CNT/TiO_2/Chl, the sheet resistance of CNP was 61182 Ω sq^{-1}, which is considerably higher in comparison to ITO glass and flexible ITO having sheet resistance values of 140 and 88 Ω sq^{-1}, respectively.

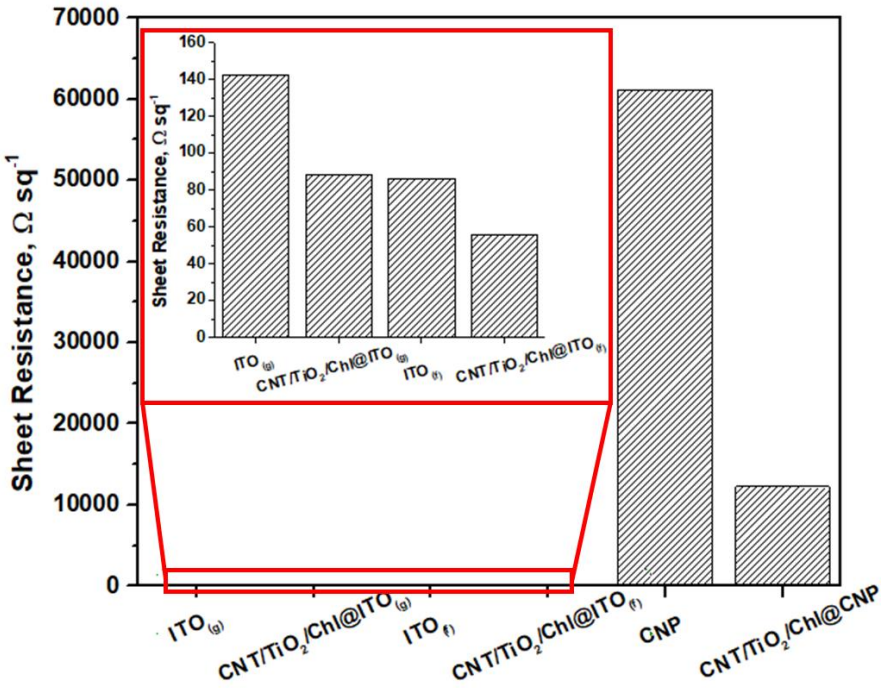

Figure 6. *Sheet resistance of $ITO_{(g)}$, $ITO_{(f)}$, CNP, CNT/TiO_2/Chl@$ITO_{(g)}$, CNT/TiO_2/Chl@$ITO_{(f)}$, and CNT/TiO_2/Chl@CNP*

This demonstrates that ITO is much more conductive than CNP. It is well known that ITO is a conductive substance and therefore, it may be employed as a supporting material for electrochemical cell electrodes [27]. Second, when CNT/TiO_2/Chl was coated on the surface of the supporting material, the sheet resistance was lowered, where CNT/TiO_2/Chl@CNP exhibited the greatest reduction (80 %). At the same time, the sheet resistances of ITO glass and flexible ITO

decreased by 38 and 35 %, respectively. This demonstrates that the CNT/TiO_2/Chl catalyst has excellent conductivity, allowing it to decrease the resistivity of the supporting material. This is the initial investment for use as the anode of a photo-bioelectrochemical cell in which the electrode must be conducting. According to the sheet resistance results, CNP as a supporting material for PBEC anodes is indeed much less conductive than ITO glass or flexible ITO, but CNP is more sustainable in terms of raw material production, and the coating of CNT/TiO_2/Chl catalysts is very good and very helpful for increasing the conductivity.

Full cell characteristics

The potential and photo-current density of photo-bioelectrochemical cell with different supporting materials

The effect of CNT/TiO_2/Chl coated on the surface of different supporting materials on bioelectrical power generation of built-up PBECs was investigated by varying the light intensity. As seen in Figure 7a, light/dark voltage and photo-current were created continuously and maintained for 50 minutes during a daily light/dark cycle for all tested light intensities. It was shown that the presence of chlorophyll in the biocatalyst structure generates energy with light intensities up to 1400 cd·sr m^{-2} (lux). Notably, there was a considerable rise in voltage when the light intensity was raised in the PBEC and a drop in voltage production when the light was turned off. All PBECs exhibited a fast rise in OCV upon exposure to light. However, the output voltage of the PBFC with CNT/TiO_2/Chl@$ITO_{(f)}$ anode was about 0.95 to 1 V, which is greater than for the same biocatalyst coated on $ITO_{(g)}$ and CNP, whose values were 0.84 to 0.85 and 0.8 to 0.83 V, respectively. As demonstrated in Figure 7b, upon illumination, the CNT/TiO_2/ /Chl at $ITO_{(g)}$, $ITO_{(f)}$, and CNP could create photo-current densities up to 3800, 2000 and 1500 mA m^{-2}, suggesting the higher photocurrent generated at $ITO_{(f)}$, than at $ITO_{(g)}$ and CNP. The sudden spike in photo-current is explained by the light intensity, and it was stabilized after 1-2 minutes. In particular, the photo-current density of CNT/TiO_2/Chl at $ITO_{(g)}$, $ITO_{(f)}$, and CNP in steady-state (stable) conditions are approaching 500, 730, and 620 mA m^{-2}, respectively. After turning off the light, the photo-current decreased.

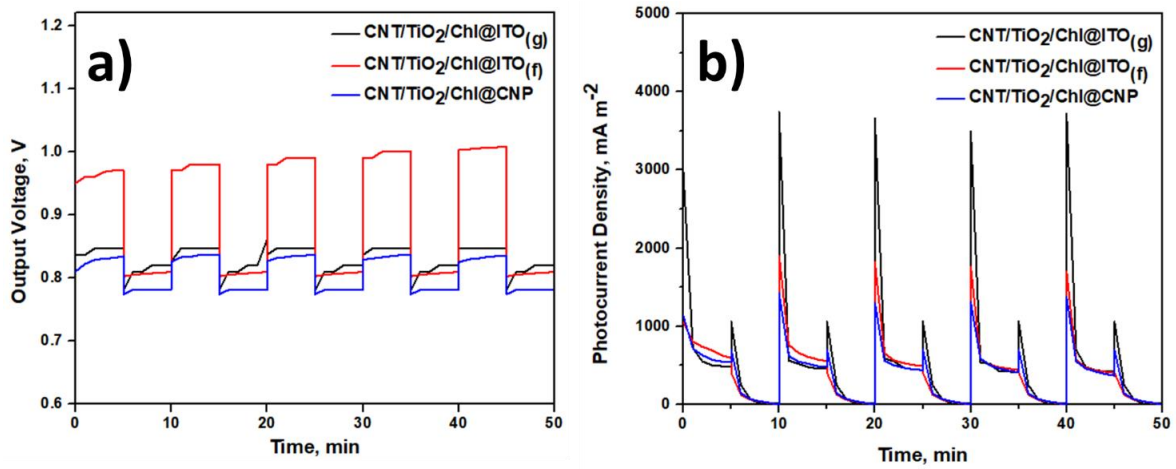

Figure 7. *a) Output voltage and b) photo-current density of CNT/TiO_2/Chl at different supporting materials with and without presence of light*

The conductivity of the biocatalyst and supporting materials of the anode, which influenced the electron transfer process, was responsible for the aforementioned findings. It is well established that reactive oxygen species (ROS) are generated during the photosynthetic process in the thylakoid membrane [28,29]. Damage to the reaction center proteins and their surroundings by reactive oxygen

species (ROSs) such as singlet oxygen ($^1O_2$), superoxide (O^{2-}), hydroxyl radicals (OH•), and hydrogen peroxide (H_2O_2) may slow down photosynthesis. These substances may also restrict the overall amount of electron transport by interfering with the path of electrons used to go from one place to another [30]. On the one hand, the conductivity of the supporting material and the biocatalyst, both of which enhance the transfer of electrons, may explain the superiority of the biocatalyst coated at ITO(f). However, poor conductivity would hinder the diffusional mass movement of electrons, a slow kinetic process that is likely rate-limiting for electron transfer inside a biocatalyst-modified electrode.

Sensitivity of photo-bioelectrochemical cell

PBEC performance might indicate the sensitivity between biocatalyst and light as fuel, making it crucial to investigate how light intensity affects the electrical current generated by these cells. Michaelis-Menten is a mathematical model used in biochemistry and pharmacology to describe the kinetics of enzymes (biocatalysts) with organic materials (fuel). For PBEC, Michaelis-Menten can be adapted since chlorophyll acts as a biocatalyst and light acts as a fuel, even though it is "apparent" fuel. Meanwhile, maximum current density (J_{max}) in PBEC is the maximum photo-current density that can be produced when the light illumination is unlimited. The Michaelis-Menten formula adopted in the photo-biocatalyst application can be written as in equation (5):

$$J_0 = \frac{J_{max} E_v}{K_m E_v} \quad (5)$$

where J_0 and J_{max} are initial and maximum current density, K_m is the Michaelis-Menten constant, and E_v is light illumination. The apparent Michaelis–Menten constant (K_m), J_{max}, and light sensitivity were also measured, as shown in Figure 8 [31].

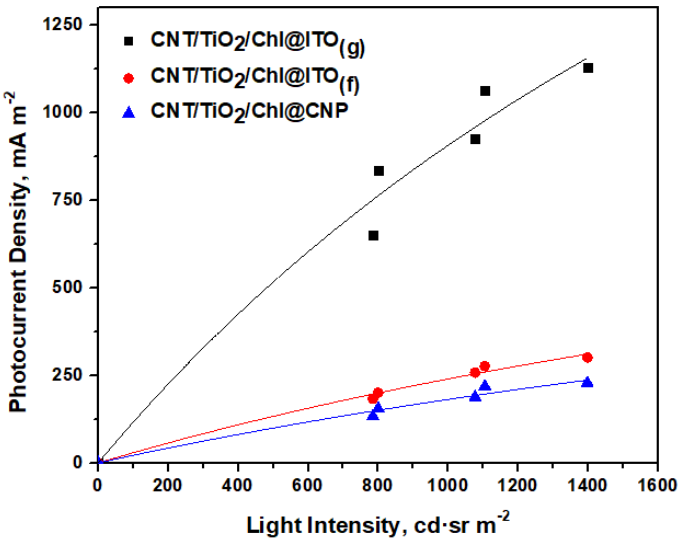

Figure 8. *Michaelis-Menten plot of CNT/TiO_2/Chl at different supporting materials with various light intensities*

The K_m and J_{max} values of CNT/TiO_2/Chl at $ITO_{(g)}$, $ITO_{(f)}$, and CNP were 3106, 4040 and 4564 cd·sr m^{-2} and 3726, 1209, and 1009 mA m^{-2}, respectively. When the K_m value is less, the catalyst of the photo-bioanode is more responsive to light [13]. Each curve slope was measured to confirm the sensitivity. CNT/TiO_2/Chl@$ITO_{(g)}$ continues to have the highest sensitivity among the three samples with 1.199 mA cd·sr m^{-4} (mA m^{-2} lx^{-1}), followed by CNT/TiO_2/Chl@$ITO_{(f)}$ with 0.299 mA cd·sr m^{-4} and CNT/TiO_2/Chl@CNP with 0.221 mA cd·sr m^{-4}. According to the data shown above, the CNT/TiO_2/ /Chl@$ITO_{(g)}$ sample is the most light-responsive among the three investigated samples.

Analysis of polarization and power curves of photo-bioelectrochemical cell

The performance of the PBEC was further tested by subjecting it to discharge tests using various external resistances. As can be seen in Figure 9a, CNT/TiO_2/Chl@$ITO_{(g)}$ applied as the anode produced the highest power density under illumination, at roughly 574 mW m^{-2}, followed by CNT/TiO_2/Chl@CNP at 247 mW m^{-2}, or 60 % lower. The lowest maximum power density of 140 mW m^{-2} was achieved with CNT/TiO_2/Chl@$ITO_{(f)}$. The CNT/TiO_2/Chl coated on the surface of $ITO_{(f)}$, $ITO_{(g)}$, and CNP were all examined for their ability to generate power in the dark (Figure 9b), with obtained maximum power density values of 81, 107, and 122 mW m^{-2}. This is due to the following reasons: (i) conductive anode supporting materials, (ii) the presence of CNT/TiO_2/Chl biocatalyst that, due to its conductivity and active surface area, can increase the rate at which electrons are transferred, increasing thus the maximum power density, and (iii) CNP is better able to store energy. Hence it has more capacitance-related properties than conductance-related ones. Concerning the biological process, chlorophyll performed admirably in converting H_2O into H^+, electrons (e^-), and oxygen (O_2). Because of the interaction between the dye molecules and TiO_2 molecules, electrons may be transferred from the excited dye molecules to the TiO_2 layer, resulting in increased energy production [32]. In a PBEC, adding oxygen gas may maximize the oxygen reduction reaction (ORR) on the cathode side. The efficiency of the cells is dependent on the electrode material, the usage of membrane separators, and the cell system or design, much as in enzymatic or microbial fuel cells. The production costs of electrodes made using precious metals (gold or platinum) are higher than those made from non-metals. This also includes the creation of sophisticated electrode byproducts. Complex synthesis procedures lead to greater manufacturing costs; thus, marketing should be prioritized accordingly.

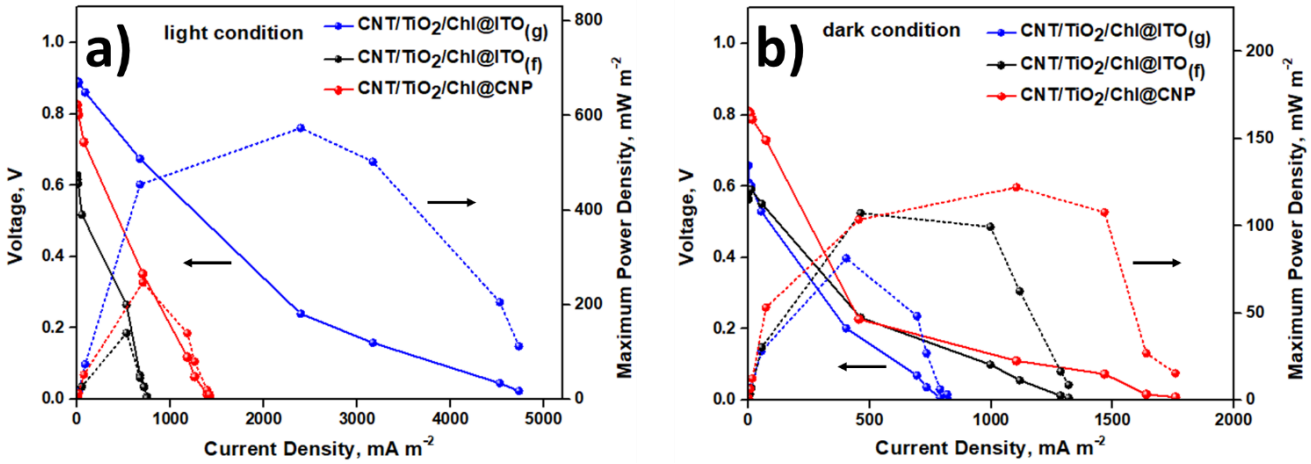

Figure 9. *Polarization (solid lines) and power curves (dotted lines) of photo-bioelectrochemical cell adopting CNT/TiO_2/Chl on different supporting materials in a) light and b) dark conditions*

Future prospects of TiO_2/CNT/Chl as the anode catalyst of flexible photo-bioelectrochemical cell

Flexible PBEC with CNT/TiO_2/Chl as the anode photocatalyst at the cellulose nanopaper (CNP) as the supporting substrate material is very promising for various applications. In the field of wearable electronics, these cells could be incorporated into garments or accessories to power devices like fitness monitors, medical sensors, and wearables. This provides a renewable and self-sufficient energy source for such devices. Another potential use is in environmental monitoring. This flexible and environmentally friendly cell can serve as a sensor for monitoring parameters like water quality, air pollution, and soil health. They could be deployed in remote or inaccessible areas to provide real-

time environmental data for assessment and management. These cells are also suitable for powering small-scale electronic devices in remote or off-grid locations with limited access to conventional energy sources, such as communication systems, illumination, or sensors, offering a source of sustainable energy. The scalability and cost-effectiveness of manufacturing processes for these cells make them suitable for widespread application in renewable energy systems. They can be integrated into building facades, ceilings, or windows to harness solar energy and generate on-site electricity, contributing to green buildings and sustainable urban environments.

Conclusions

This comprehensive study investigates the performance of PBECs utilizing a novel anode catalyst, CNT/TiO_2/Chl, coated on different supporting materials. The research encompasses a rigorous analysis of physicochemical properties, cyclic voltammetry, sensitivity assessments, and power generation capabilities, providing valuable quantitative results. Physicochemical analyses, such as SEM and FTIR, elucidate the structural composition of the catalysts. The SEM images reveal the successful incorporation of chlorophyll, while FTIR spectra demonstrate distinctive characteristics, including the presence of C=C bonds and -OH bonds. Quantitatively, the specific capacitance values of GC, TiO_2, CNT/TiO_2, and CNT/TiO_2/Chl are determined as 22.10, 23.30, 28.43, and 18.59 F g^{-1}, respectively, indicating the favorable characteristics of CNT/TiO_2/Chl and TiO_2 for energy conversion. Cyclic voltammetry profiles uncover the catalytic activity, with the electrical double layer current densities shifting towards more negative values upon the introduction of TiO_2, CNT, and Chl due to the contribution of ORR reaction. Specific capacitance values further confirm the superior performance of CNT/TiO_2, particularly in energy storage applications. Quantitatively, the photocurrent densities of CNT/TiO_2/Chl at $ITO_{(g)}$, $ITO_{(f)}$, and CNP in steady-state conditions approach 500, 730, and 620 mW m^{-2}, respectively. The study explores the sensitivity of PBECs, employing a mathematical model adapted from Michaelis-Menten kinetics. Quantitative results include K_m and J_{max} values for CNT/TiO_2/Chl at $ITO_{(g)}$, $ITO_{(f)}$, and CNP, revealing the biocatalyst light responsiveness. Full cell characteristics unveil the quantitative power generation capabilities of PBECs. Under illumination, CNT/TiO_2/Chl@$ITO_{(g)}$ produces the highest power density at approximately 574 mW m^{-2}, followed by CNT/TiO_2/Chl@CNP at 247 mW m^{-2}. In the dark, maximum power density values of 81, 107, and 122 mW m^{-2} are observed for CNT/TiO_2/Chl at $ITO_{(g)}$, $ITO_{(f)}$, and CNP, respectively. Quantitative results from polarization and power curves affirm the superior performance of CNT/TiO_2/Chl@$ITO_{(g)}$ in power generation, with a maximum power density of approximately 574 mW m^{-2} under illumination.

In conclusion, the quantitative data substantiates the efficacy of the CNP as supporting material, positioning it as a robust candidate to substitute existing ITO glass or flexible ITO as supporting material of PBECs when CNT/TiO_2/Chl acted as photo-biocatalyst. Its superior capacitance, light responsiveness, and power generation capabilities, coupled with flexibility and environmental compatibility, underscore its potential for diverse applications in sustainable energy solutions. These flexible photo-bioelectrochemical cells hold great promise in the realm of sustainable energy technologies. Their ability to efficiently convert solar energy into electricity, as demonstrated in our research, underscores their potential significance in advancing sustainable energy solutions.

Acknowledgements*: This research was supported in full with Toray Science & Technology Research Grant 2020 provided by Indonesia Toray Science Foundation.*

References

[1] N. Mariotti, M. Bonomo, L. Fagiolari, N. Barbero, C. Gerbaldi, F. Bella, C. Barolo, Recent advances in eco-friendly and cost-effective materials towards sustainable dye-sensitized solar cells, *Green Chemistry* **22** (2020) 7168-7218. https://doi.org/10.1039/D0GC01148G

[2] P. Semalti, S. N. Sharma, Dye sensitized solar cells (DSSCs) electrolytes and natural photo-sensitizers: a review, *Journal of Nanoscience and Nanotechnology* **20** (2020) 3647-3658. https://doi.org/10.1166/jnn.2020.17530

[3] C. M. Hanna, R. T. Pekarek, E. M. Miller, J. Y. Yang, N. R. Neale, Decoupling Kinetics and Thermodynamics of Interfacial Catalysis at a Chemically Modified Black Silicon Semiconductor Photoelectrode, *ACS Energy Letters* **5** (2020) 1848-1855. https://doi.org/10.1021/acsenergylett.0c00714

[4] F. Niu, D. Wang, F. Li, Y. Liu, S. Shen, T. J. Meyer, Hybrid photoelectrochemical water splitting systems: from interface design to system assembly, *Advanced Energy Materials* **10** (2020) 1900399. https://doi.org/10.1002/aenm.201900399

[5] E. Musazade, R. Voloshin, N. Brady, J. Mondal, S. Atashova, S. K. Zharmukhamedov, I. Huseynova, S. Ramakrishna, M. M. Najafpour, J.-R. Shen, B. D. Bruce, S. I. Allakhverdiev, Biohybrid solar cells: Fundamentals, progress, and challenges, *Journal of Photochemistry and Photobiology C: Photochemistry Reviews* **35** (2018) 134-156. https://doi.org/10.1016/j.jphotochemrev.2018.04.001

[6] A. Orona-Navar, I. Aguilar-Hernández, T. López-Luke, A. Pacheco, N. Ornelas-Soto, Dye sensitized solar cell (DSSC) by using a natural pigment from microalgae, *International Journal of Chemical Engineering and Applications* **11** (2020) 14-17. https://doi.org/10.18178/ijcea.2020.11.1.772

[7] N. T. R. N. Kumara, A. Lim, C. M. Lim, M. I. Petra, P. Ekanayake, Recent progress and utilization of natural pigments in dye sensitized solar cells: A review, *Renewable and Sustainable Energy Reviews* **78** (2017) 301-317. https://doi.org/10.1016/j.rser.2017.04.075

[8] A. Efrati, C. H. Lu, D. Michaeli, R. Nechushtai, S. Alsaoub, W. Schuhmann, I. Willner, Assembly of photo-bioelectrochemical cells using photosystem I-functionalized electrodes, *Nature Energy* **1** (2016) 15021. https://doi.org/10.1038/nenergy.2015.21

[9] M. Christwardana, A. A. Septevani, L. A. Yoshi, Sustainable electricity generation from photo-bioelectrochemical cell based on carbon nanotubes and chlorophyll anode, *Solar Energy* **227** (2021) 217-223. https://doi.org/10.1016/j.solener.2021.09.002

[10] V. Mascoli, A. F. Bhatti, L. Bersanini, H. van Amerongen, R. Croce, The antenna of far-red absorbing cyanobacteria increases both absorption and quantum efficiency of Photosystem II, *Nature Communications* **13** (2022) 3562. https://doi.org/10.1038/s41467-022-31099-5

[11] M. Li, V. Svoboda, G. Davis, D. Kramer, H. H. Kunz, H. Kirchhoff, Impact of ion fluxes across thylakoid membranes on photosynthetic electron transport and photoprotection, *Nature Plants* **7** (2021) 979-988. https://doi.org/10.1038/s41477-021-00947-5

[12] Y. S. Chang, H. C. Yang, L. Chao, Formation of Supported Thylakoid Membrane Bioanodes for Effective Electron Transfer and Stable Photo-current, *ACS Applied Materials & Interfaces* **14** (2022) 22216-22224. https://doi.org/10.1021/acsami.2c04764

[13] M. Christwardana, A. A. Septevani, L. A. Yoshi, Outstanding Photo-bioelectrochemical Cell by Integrating TiO_2 and Chlorophyll as Photo-bioanode for Sustainable Energy Generation, *International Journal of Renewable Energy Development* **11** (2022) 385. https://doi.org/10.14710/ijred.2022.41722

[14] D. Kim, A. Ghicov, P. Schmuki, TiO_2 Nanotube arrays: Elimination of disordered top layers ("nanograss") for improved photoconversion efficiency in dye-sensitized solar cells, *Electrochemistry Communications* **10** (2008) 1835-1838. https://doi.org/10.1016/j.elecom.2008.09.029

[15] W. Hou, R. Hu, S. Zhu, Y. Xiao, G. Han, A thiourea resin polymer as a multifunctional modifier of the buried interface for efficient perovskite solar cells with reduced lead leakage, *Materials Chemistry Frontiers* **6** (2022) 3338-3348. https://doi.org/10.1039/D2QM00703G
[16] S. Lu, Y. Sun, K. Ren, K. Liu, Z. Wang, S. Qu, Recent development in ITO-free flexible polymer solar cells, *Polymers* **10** (2017) 5. https://doi.org/10.3390/polym10010005
[17] A. K. Prabowo, A. P. Tiarasukma, M. Christwardana, D. Ariyanti, Microbial Fuel Cells for Simultaneous Electricity Generation and Organic Degradation from Slaughterhouse Wastewater, *International Journal of Renewable Energy Development* **5** (2016) 107-112. http://dx.doi.org/10.14710/ijred.5.2.107-112
[18] A. A., Septevani, D., Burhani, Y., Sampora, Indriyati, Shobih, E. S., Rosa, D. Sondari, N. I. Margyaningsih, M. Septiyani, F. Yurid, & A. S. Handayani, A systematic study on the fabrication of transparent nanopaper based on controlled cellulose nanostructure from oil palm empty fruit bunch, *Journal of Polymers and the Environment* **30** (2022) 3901-3913. https://doi.org/10.1007/s10924-022-02484-4
[19] J. H. Lee, S. H. Kang, H. Ruh, K. M. Yu, Development of a thickness meter for conductive thin films using four-point probe method, *Journal of Electrical Engineering & Technology* **16** (2021) 2265-2273. https://doi.org/10.1007/s42835-021-00725-5
[20] Z. E. Allouni, M. R. Cimpan, P. J. Høl, T. Skodvin, N. R. Gjerdet, Agglomeration and sedimentation of TiO_2 nanoparticles in cell culture medium, *Colloids and Surfaces B: Biointerfaces* **68** (2009) 83-87. https://doi.org/10.1016/j.colsurfb.2008.09.014
[21] S. M. Miranda, G. E. Romanos, V. Likodimos, R. R. Marques, E. P. Favvas, F. K. Katsaros, K. L. Stefanopoulos, V. J. P. Vilar, J. L. Faria, P. Falaras, A. M. T. Silva, Pore structure, interface properties and photocatalytic efficiency of hydration/dehydration derived TiO_2/CNT composites, *Applied Catalysis B: Environmental*, **147** (2014) 65-81. https://doi.org/10.1016/j.apcatb.2013.08.013
[22] L., Lv, K., Li, Y., Xie, Y., Cao, X. Zheng, Enhanced osteogenic activity of anatase TiO_2 film: Surface hydroxyl groups induce conformational changes in fibronectin, *Materials Science and Engineering: C* **78** (2017) 96-104. https://doi.org/10.1016/j.msec.2017.04.056
[23] G. Huang, T. W. Ng, T. An, G. Li, B. Wang, D. Wu, H. Y. Yip, H. Zhao, P. K. Wong, Interaction between bacterial cell membranes and nano-TiO_2 revealed by two-dimensional FTIR correlation spectroscopy using bacterial ghost as a model cell envelope, *Water Research* **118** (2017) 104-113. https://doi.org/10.1016/j.watres.2017.04.023
[24] W. A. Dhafina, M. Z. Daud, H. Salleh, The sensitization effect of anthocyanin and chlorophyll dyes on optical and photovoltaic properties of zinc oxide based dye-sensitized solar cells, *Optik* **207** (2020) 163808. https://doi.org/10.1016/j.ijleo.2019.163808
[25] H. Nan, H. P. Shen, G. Wang, S. D. Xie, G. J. Yang, H. Lin, Studies on the optical and photoelectric properties of anthocyanin and chlorophyll as natural co-sensitizers in dye sensitized solar cell, *Optical Materials* **73** (2017) 172-178. https://doi.org/10.1016/j.optmat.2017.07.036
[26] D. Jiang, Y. Xu, D. Wu, Y. Sun, Visible-light responsive dye-modified TiO_2 photocatalyst, *Journal of Solid State Chemistry* **181** (2008) 593-602. https://doi.org/10.1016/j.jssc.2008.01.004
[27] Z. Karami, A. Soleimani-Gorgan, G. R. Vakili-Nezhaad, F. A. Roghabadi, A layer-by-layer green inkjet printing methodology for developing indium tin oxide (ITO)-based transparent and conductive nanofilms, *Journal of Cleaner Production* **379** (2022) 134455. https://doi.org/10.1016/j.jclepro.2022.134455
[28] D. V. Vetoshkina, M. M. Borisova-Mubarakshina, I. A. Naydov, M. A. Kozuleva, B. N. Ivanov, Impact of high light on reactive oxygen species production within photosynthetic biological

membranes, *Journal of Biology and Life Science* **6** (2015) 50-60. http://dx.doi.org/10.5296/jbls.v6i2.7277

[29] A. Krieger-Liszkay, G. Shimakawa, Regulation of the generation of reactive oxygen species during photosynthetic electron transport, *Biochemical Society Transactions* **50** (2022) 1025-1034. https://doi.org/10.1042/BST20211246

[30] G. Lenaz, Mitochondria and reactive oxygen species. Which role in physiology and pathology?, *Advances in Mitochondrial Medicine* (2012) 93-136. https://doi.org/10.1007/978-94-007-2869-1_5

[31] M. Christwardana, Combination of physico-chemical entrapment and crosslinking of low activity laccase-based biocathode on carboxylated carbon nanotube for increasing biofuel cell performance, *Enzyme and Microbial Technology* **106** (2017) 1-10. https://doi.org/10.1016/j.enzmictec.2017.06.012

[32] A. Boyo, O. Paul, I. Abdulsalami, O. Surukite, H. O. Boyo, H. Boyo, Application of Hibiscus sabdariffa and leaves of Azardirachta indica calyxes as sensitizers in dye-sensitized solar cells, *International Journal of Engineering Research and Development* **8** (2013) 38-42. https://www.ijerd.com/paper/vol8-issue12/F08123842.pdf

J. Electrochem. Sci. Eng. **14(2)** (2024) 163-175; http://dx.doi.org/10.5599/jese.2096

Open Access : : ISSN 1847-9286
www.jESE-online.org

Original scientific paper

Cobalt and copper-based metal-organic frameworks synthesis and their supercapacitor application

Sneha Tomar and Vinod Kumar Singh✉

Department of Chemical Engineering, National Institute of Technology Raipur, Raipur, Chhattisgarh, 492001, India

Corresponding author: ✉vksingh.che@nitrr.ac.in

Received: September 25, 2023; Accepted: January 16, 2024; Published: February 11, 2024

Abstract

*In this study, two different metal-organic frameworks (*MOFs*) were synthesized using copper and cobalt metal ions with benzenedicarboxylic acid (bdc) as a common ligand. The prepared MOFs were characterized using X-ray diffraction, Fourier transform infrared spectroscopy, and scanning electron microscopy-energy dispersive spectroscopy. Also, the electrochemical characteristics were analyzed using cyclic voltammetry, galvanostatic charge/discharge, and electrochemical impedance spectroscopy methods. Structural characterizations indicate that Co-bdc MOF is composed of three-dimensional non-uniform colloids and Cu-bdc MOF has a regular three-dimensional cuboidal structure, possessing good crystalline structure. The Cu-bdc MOF exhibited a maximum specific capacitance of 171 F/g, while Co-bdc MOF showed 368 F/g at the current density of 1 A/g. The solution resistance for the Co-bdc MOF was 0.09 Ω in comparison to 1.25 Ω for the Cu-bdc MOF. Also, the Co-bdc MOF demonstrated better cycling performance by retaining 85 % of its capacity after 2000 charge-discharge cycles. In contrast, the stability of the Cu-bdc MOF was lower, with only 78 % retention in capacity. Conclusively, the Co-bdc MOF demonstrated superior specific capacitance, lower resistance, and enhanced cyclic stability in 3 M KOH electrolyte system.*

Keywords

Solvothermal synthesis; benzene dicarboxylic acid ligand; energy storage; specific capacitance

Introduction

The energy crisis has spurred the exploration and development of new energy stockpiling and storage technologies to address issues related to energy supply and demand fluctuations. Renewable energy sources, such as solar and wind, are intermittent. They do not produce a consistent and predictable amount of energy throughout the day. Energy storage allows excess energy generated during peak production times to be stored for later use, smoothing out fluctuations in energy supply.

Supercapacitors (SCs) are considered promising energy storage devices for future applications due to their numerous characteristics, such as long cycling capability, ability to deliver high power, and exceptional reversibility [1]. SCs have successfully entered commercialization because of their exceptional performance characteristics, which are benefited by the physical and chemical characteristics of the active material. SCs assembly mainly consists of anode and cathode electrodes that are immersed in electrolyte (aqueous and nonaqueous) and separated by separators that allow the free flow of ions and electrons [2]. The electrode material plays a crucial role in determining the electrochemical performance of supercapacitor electrodes. It directly influences the overall performance and characteristics of the electrode. The choice of electrode material affects important factors such as capacitance, charge/discharge rates, cycling stability, and overall energy storage capabilities of the supercapacitor [3]. The materials commonly employed in supercapacitor applications include graphene (graphene quantum dots or rGO) [4,5], carbon nanotubes [6], metal oxides (such as NiO, Mn_3O_4, RuO_2) [7-9], transition metal carbides [10], metal-organic frameworks [11], hybrid, and composite materials. Thus, the careful selection of electrode material is crucial for attaining the best possible electrochemical performance for supercapacitors.

Metal-organic frameworks (MOFs) are widely recognized as highly suitable electrode materials for energy storage applications. This is primarily due to their inherent qualities, such as stability, flexibility, structural versatility, and other essential properties [12-14]. MOFs, or porous coordination polymers, are created using the principles of coordination chemistry. In the process of self-assembling, multitopic organic ligands and metal ions, commonly referred to as secondary building units, result in the development of MOFs. In most studies, the solvothermal technique is used to prepare MOFs as it is a simple and cost-effective technique, like microwave-assisted synthesis, sono-chemical synthesis, or electrochemical synthesis [15-18].

In this study, two distinct MOFs were synthesized using different metal salts while employing a common ligand using the solvothermal method. The prepared MOFs were Co-bdc and Cu-bdc MOF (Co: cobalt, Cu: copper, bdc: benzenedicarboxylic acid). Professor O. M. Yaghi and his research group [19] initially identified Co-bdc MOF in 2005, and they designated it as MOF-71. The framework structure comprises endless chains of CoO_6 octahedra, where each chain shares corners. These chains are interconnected with four parallel chains through the bdc linkers. It has attracted noteworthy attention in the field of water splitting [20], supercapacitors [20], sensors [21], and catalysis [22]. Cu-bdc MOF (CCDC no. 687690) is identified by its two-dimensional structure. It is composed of copper ions serving as a metal ion source and 1,4-benzenedicarboxylic acid acting as the bridging organic ligand [23]. It has drawn considerable interest in the domain of Li-ion battery [24], catalyst [25,26], methane storage [27] and adsorption [28]. Both MOFs have been utilized in supercapacitors, and specific details are outlined in Table 1, including a comparative analysis of this study.

Table 1. *Cu and Co-based MOFs and their respective specific capacitance values*

MOF	Ligand	Synthesis method	Electrolyte	Specific capacity, F/g	Ref.
Cu-MOF/rGO	3,3',5,5'-tetracarboxy-diphenylmethane	Solvothermal	1 M Na_2SO_4	21 at 1 A/g	[29]
Cu-MOF/rGO	5,5'-(piperazine-1,4-diyl) di isophthalic acid	Slow evaporation	3 M KCl	135 at 1 A/g	[30]
Cu-MOF/rGO	Benzene-1,3,5-tri-carboxylic acid	Solvothermal	1 M Na_2SO_4	4.1 at 0.8 A/g	[31]

MOF	Ligand	Synthesis method	Electrolyte	Specific capacity, F/g	Ref.
PANI/Cu-MOF	Benzene-1,3,5-tri-carboxylic acid	Co-precipita-tion at room temperature	6 M KOH	459 at 50 mV/s	[32]
Cobalt MOF	Trimesic acid	Solvothermal	1 M KOH	280	[33]
Copper MOF				228	
Copper MOF	Benzene-1,3,5-tri-carboxylic acid	Solvothermal	3 M KOH	228 at 1.5 A/g	[34]
Graphene/ Cu-MOF	Benzene-1,3,5-tri-carboxylic acid	Solvothermal	6 M KOH	190 at 10 mV/s	[35]
Co-MOF	Polycarboxylic acid ligand based tritopic ligand	Solvothermal	1 M tetraethylam-monium tetrafluoro-borate in acetonitrile	300 at 1 A/g	[36]
Co-MOF/ graphene nanosheets	Benzene-1,3,5-tri-carboxylic acid	Precipitation at room temp	1 M KOH	187.3 at 0.25 A/g	[37]
Co-based MOF/graphene nanocomposite	2-methylimidazole	Precipitation at room temperature	6 M KOH	260 at 10 mV/s	[38]
Cu-bdc MOF	Benzene dicarboxylic acid	Solvothermal	3 M KOH	368 at 1 A/g	This work
Co-bdc MOF				171 at 1 A/g	

Experimental

Chemicals and reagents

The reagents and chemicals that were used in the present study were cupric nitrate trihydrate (Loba Chemie, 99.5 %), cobaltous nitrate hexahydrate (Qualigens Thermo Fischer, 97 %), benzene dicarboxylic acid (Merck, ≥98 %), dimethyl formamide (Merck, 99.8 %), polytetrafluoroethylene (PTFE), N-methyl pyrrolidone, and acetylene carbon black. All experiments were conducted using deionized water.

Characterization techniques

Fourier transform infrared spectroscopy (FTIR), Bruker Alpha Model spectrometer was used to examine the secondary structure and functional groups present in Cu-bdc and Co-bdc MOF. X-ray diffraction (XRD), a PANalytical 3 kW X'pert diffractometer outfitted with Ni-filtered CuK radiation was used to examine the patterns of the samples. The morphology and elemental composition of the material were determined using scanning electron microscopy (SEM, Zeiss Evo, Evo18) and energy dispersive spectroscopy (EDS, INCA 250 EDS with X-MAX 20mm Detector).

Synthesis of cobalt- and copper-bdc metal-organic frameworks

Co-bdc MOF was synthesized using 2 mmol of cobalt nitrate salt and 1 mmol of benzene dicarboxylic acid in 50 ml of dimethyl formamide solution. The solution was agitated for 30 minutes to achieve a homogeneous mixture. Then, the resulting solution was transferred into a Teflon-lined autoclave and maintained at 150 °C for 12 hours. The obtained precipitate was subsequently washed three times with ethanol (30 ml) to eliminate impurities and then dried at 50 ˚C for 6 h in hot air oven. Cu-bdc MOF was synthesized using the same method as Co-bdc MOF, with the only difference being the use of cupric nitrate salt instead of cobalt nitrate salt in the synthesis process, as demonstrated in Scheme 1.

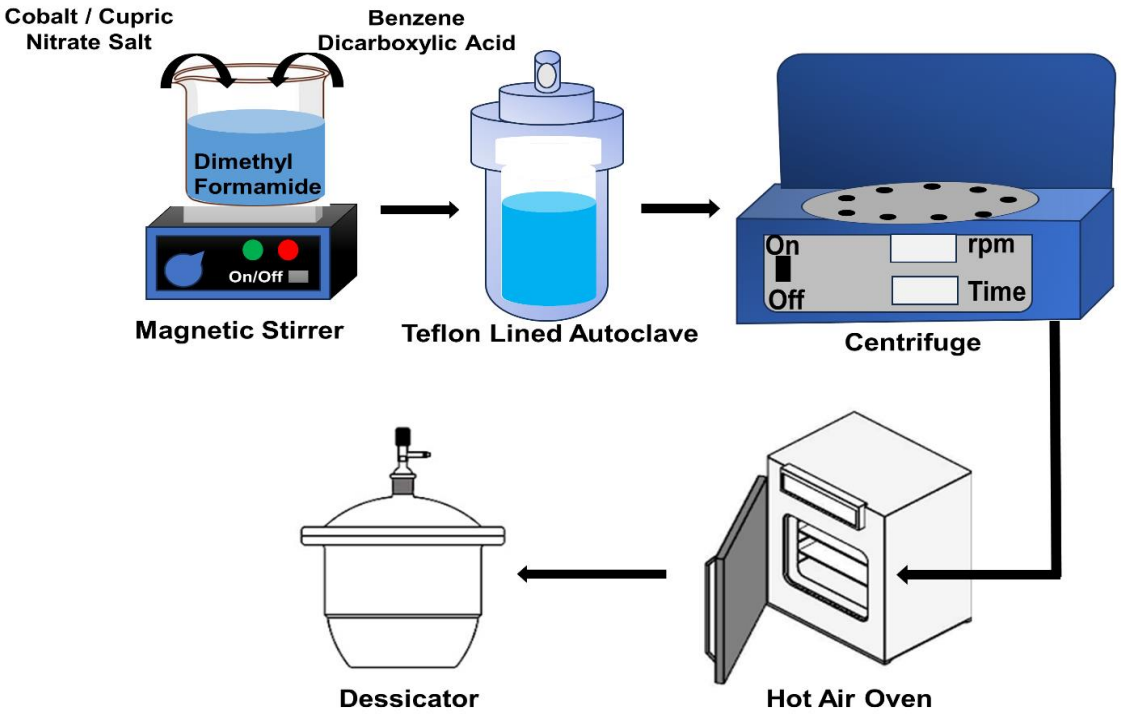

Scheme 1. *Schematic representation of the synthesis procedure for Co-bdc and Cu-bdc MOFs*

Electrochemical measurements

Electrochemical workstation was used to conduct several experiments such as electrochemical impedance spectroscopy (EIS), cyclic voltammetry (CV), galvanostatic charge-discharge (GCD) and cyclic stability in 3 M KOH electrolyte. In the experimental setup, the working electrode consisted of nickel foam coated with the MOF material. The reference electrode used was silver/silver chloride, which provides a stable reference potential for electrochemical measurements. The counter electrode, on the other hand, was a platinum wire, which facilitates the flow of current in the electrochemical cell and completes the circuit. The 3 M KOH solution was used as an electrolyte for the Co-bdc and Cu-bdc electrodes.

The working electrode slurry was a mixture of the active material (Co-MOF or Cu-MOF), conductivity agent (acetylene carbon black), and PTFE binder in the weight ratio of 80:15:5. The pieces of nickel foam (size 1×1 cm) were taken and the slurry was applied layer by layer to achieve the mass loading of 1.2 mg/cm ^{2}. The coated nickel foam pieces were dried under vacuum at 60 ˚C for 24 h to get the working electrode. An EIS study was conducted within a frequency range of 100 kHz to 0.01 Hz, using a 10 mV amplitude. Additionally, CV analysis was performed on Co-bdc MOF within a potential range of -0.5 to 0 V, while for Cu-bdc MOF, the potential range was -0.5 to 0.5 V. The CV measurements were carried out at various scan rates ranging from 10 to 50 mV/s. GCD of MOF electrodes was done for the same potential window as CV at different current densities ranging from 1 to 18 A/g. The cyclic stability test was carried out up to 2000 cycles at 18 A/g.

Results and discussion

Scanning electron microscopy - energy dispersive spectroscopy

Scanning electron microscopy-energy dispersive spectroscopy (SEM-EDS) analysis reveals the morphology and elemental composition of both MOF samples. In the case of the Co-bdc MOF, Figure 1(a) and 1(b) demonstrates non-uniformity among particles, with predominant elements being

cobalt, carbon, and oxygen. Conversely, the Cu-bdc MOF exhibits a well-defined cuboidal morphology, indicating successful structure formation, as depicted in Figure 1(c). By displaying EDS analysis, Figure 1(d) for the Cu-bdc MOF confirms the presence of copper, carbon, and oxygen, thus supporting the successful synthesis of MOFs.

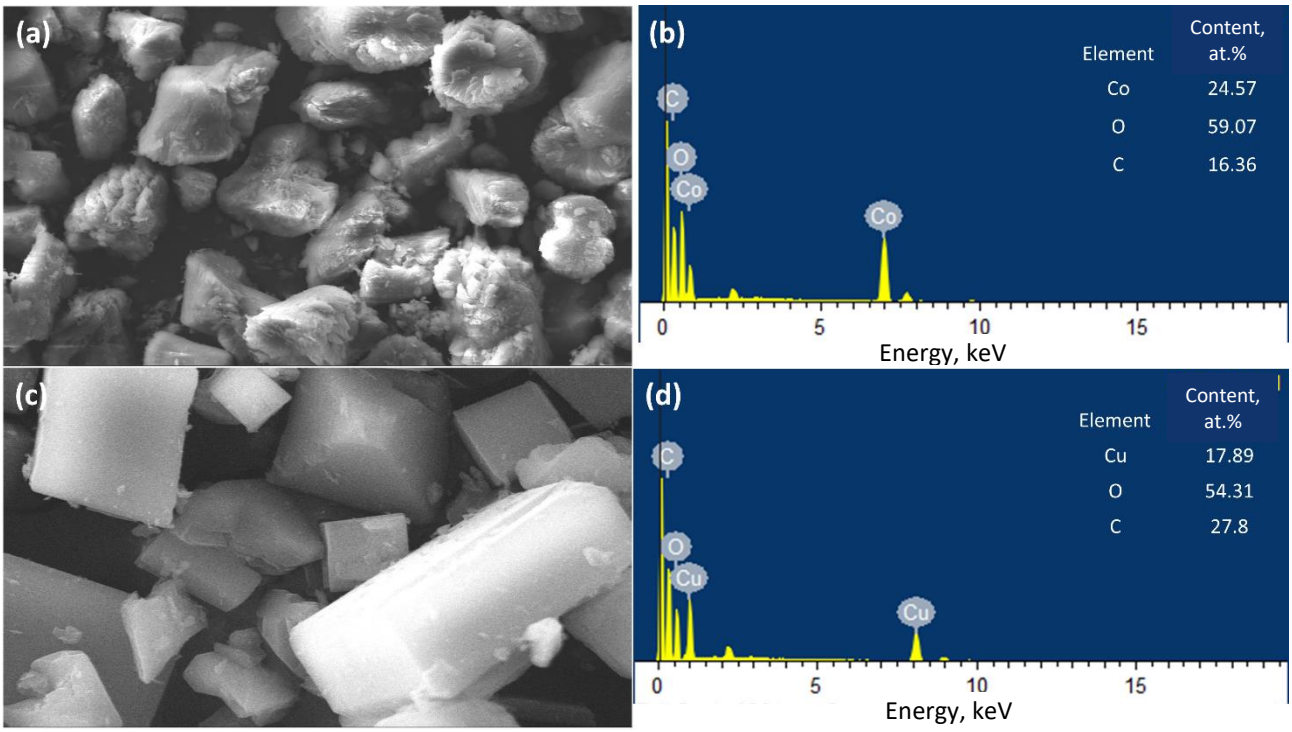

***Figure 1**. SEM-EDS images of Co-bdc MOF (a and b) and Cu-bdc MOF (c and d)*

X-ray diffraction

The geometry used for the powder sample analysis was a Bragg-Brentano. The test conditions were Cu-Kα source, acceleration voltage 40 kV, acceleration current 30 mA, scan speed 0.032 s per step, step interval 0.026° and scan range 5 to 60°. Co-bdc MOF diffraction peaks were located at 2θ values of approximately 8.8, 11.5, 12.0 and 15.9° representing the diffraction planes of (100), (110), (101), and (200), respectively [39] (Figure 2).

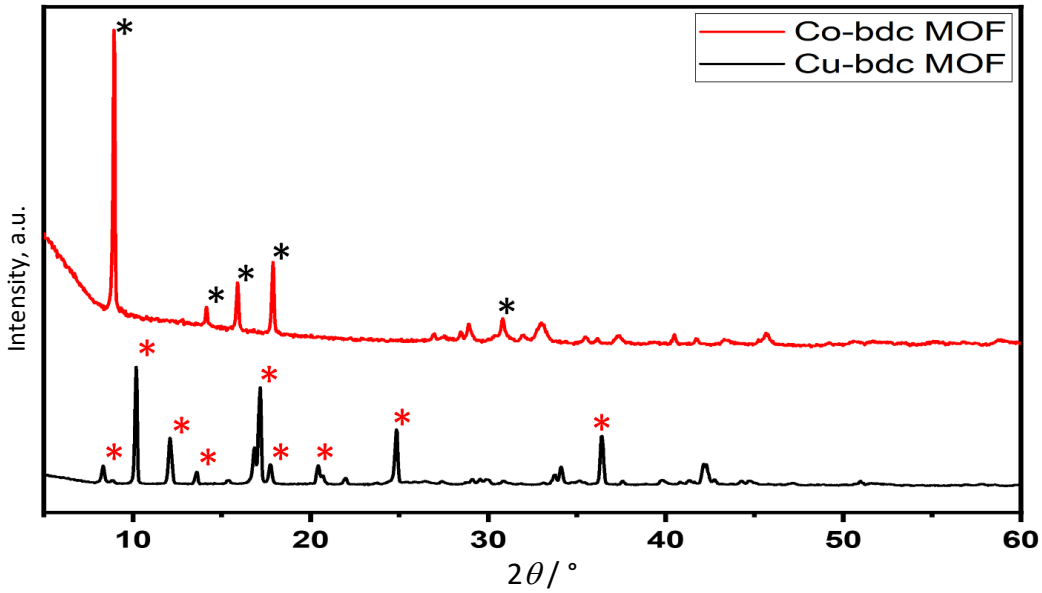

***Figure 2.** XRD patterns of Co-bdc MOF and Cu-bdc MOF*

The peaks at angles of 10.2, 12.05, 13.5, 17.1, 17.6, 20.5 and 24.77° correspond to the lattice planes (110), (220), (020), (333), (211), (202), and (222) of the Cu-bdc MOF. These peaks confirm the successful production of a highly crystalline crystal with strong intensity and strong peaks, which indicate excellent crystalline characteristics of both MOFs (Figure 2). The intensity of the diffraction pattern suggests that the synthesized MOF crystal exhibits a well-organized structure. Additionally, it is observed that the Co-bdc and Cu-bdc XRD patterns are dissimilar due to variations in the metal coordination geometry [40,41].

Fourier-transform infrared spectroscopy

Fourier-transform infrared spectroscopy (FTIR) analysis of Cu-bdc and Co-bdc MOFs is displayed in Figure 3. Cu-bdc underwent FTIR, and the spectrum is shown in Figure 3(a). The interaction between the Cu metal and BDC ligands is validated by the existence of the -COO- group, designated by two bands at 1566 and 1370 cm^{-1}, corresponding to the antisymmetric and symmetric stretch modes, respectively [43]. At 1447 and 2988 cm^{-1}, the C-C and C-H of benzene from benzene dicarboxylic acid were seen, respectively. The spectrum also contained the Cu-O band at 581 cm^{-1} in addition to the BDC [43]. Figure 3(b) shows that the sharp peak at 3700 cm^{-1} originates from OH bound to BDC ligands [44,45]. The broad peak centered at the wavenumber 3100 cm^{-1} originates from the stretching vibration OH group of water vapor adsorbed on the surface. The peaks were obtained at around 1710 cm-1 due to stretching vibrations of C=O, 1300 cm-1 due to -OH stretching in water molecules present, and around 1000 cm^{-1} due to C-O stretching vibration [41].

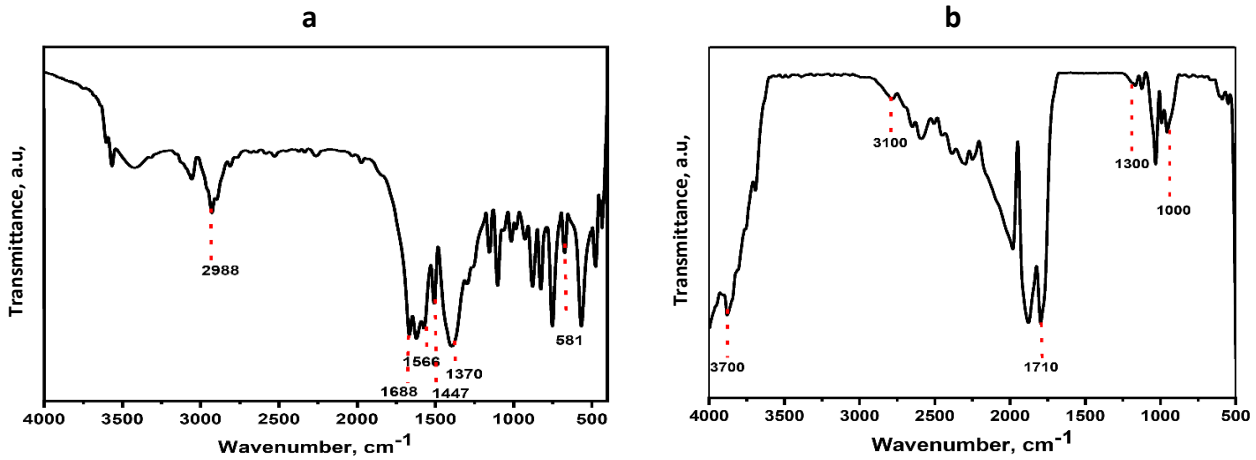

Figure 3. *FTIR plots between 500 to 4000 cm^{-1} for Cu-bdc (a) and Co-bdc (b) MOFs*

Cyclic voltammetry

In order to assess the electrochemical characteristics of the synthesized Co-bdc and Cu-bdc materials, a three-electrode setup was used.

The CV patterns depicted in Figure 4(a) for Co-bdc and Figure 4(b) for Cu-bdc clearly demonstrate that the metal centers had an influence on the electrochemical performance of both MOFs. The voltage range for each electrode material was different. Figure 4(a), it can be observed that Co-bdc displays electrochemical double-layer capacitor (EDLC) behavior within the voltage range of -0.5 to 0 V. It implies that the material intends to undergo more favorable electrochemical reactions at negative potentials. The nearly symmetrical shape and broader CV region indicate a characteristic electrochemical reaction that exhibits high reversibility. The CV profile of Cu-bdc (voltage range of -0.5 to 0.5 V) is shown in Figure 4(b). All of the CV profiles for both the MOFs had quasi-rectangular

shapes, and there were no noticeable shape changes as the scan rate increased, confirming optimal charge-discharge characteristics and outstanding reversibility in the test conditions.

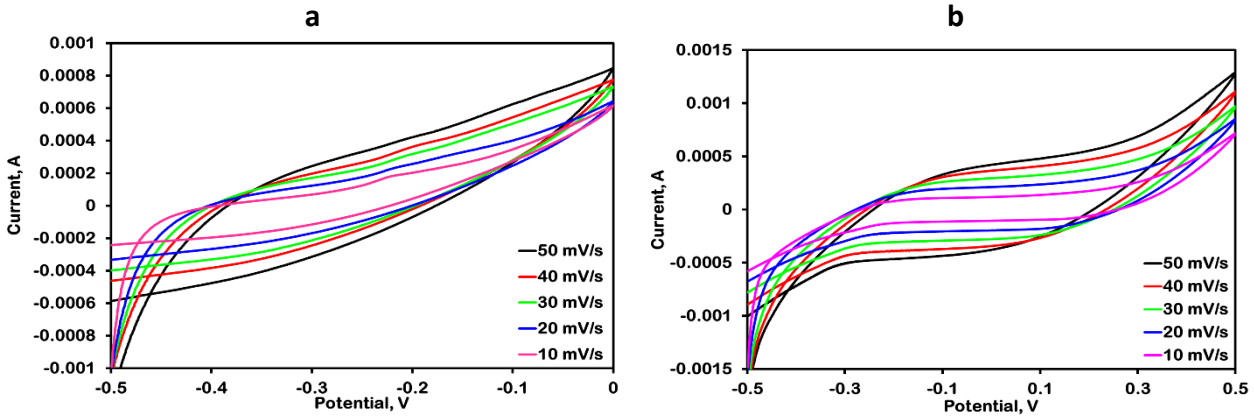

Figure 4. *Cyclic voltammetry profiles of Co-bdc MOF within a potential window of -0.5 to 0 V (a) and Cu-bdc MOF within a potential window of -0.5 to 0.5 V (b), both recorded at a scan rate of 10-50 mV/s*

Electrochemical impedance spectroscopy

The Nyquist plots of Co-bdc and Cu-bdc MOFs are given in Figure 5 (a and b), and the EIS measurements were performed in the 100 kHz to 0.01 Hz frequency range. In Table 1, the values for solution resistance (R_s) and charge transfer resistance (R_{ct}) are displayed. These values suggest a strong potential for high charge transfer capacity and enhanced electronic conductivity in the material or device. The R_s values for the Cu-bdc and Co-bdc electrodes are 1.25 and 0.089 Ω, respectively, as can be deduced from Table 2. The results clearly indicate that the Co-bdc electrode exhibits a reduced R_s value, implying enhanced conductivity and improved wettability. This suggests improved contact between the electrode and the electrolyte solution, facilitating more efficient electrochemical reactions. Lower resistance allows for efficient ion transport, enabling faster kinetics and improved performance in terms of charge/discharge rates. The reduced charge transfer resistance and solution resistance of the Co-bdc electrode would contribute to its higher capacitance value when compared to the Cu-bdc electrode. The accuracy of the results is checked by fitting the impedance data with an appropriate circuit model to assess the accuracy of the measurements. The goodness of fit is examined by statistical measure such as χ^2 values. A low value of χ^2 indicates the chosen circuit model accurately represents the electrochemical process. The circuit used for the fit was $R(CR)W$, where the R_s stands for the solution resistance, R_{ct} for charge transfer resistance, C_{dl} for interfacial double layer capacitance and W for diffusion (Warburg) impedance. In the plot, the blue/red marker indicates the measured values of the Co-bdc and Cu-bdc electrodes, respectively, and the black marker indicates the calculated value.

Figure 5(c) indicates the EIS for both the materials after 2000 consecutive cycles. It is evident that there is an increase in the radius of the depressed semicircle for both the MOFs, which reveals a decrease in the interfacial charge transfer between electrode and electrolyte.

Table 2. *EIS resistance data for Cu-bdc and Co-bdc MOFs*

	Cu-bdc MOF	Co-bdc MOF
R_s / Ω	1.25	0.089
R_{ct} / Ω	2.646	2.239
χ^2	0.04027	0.02906

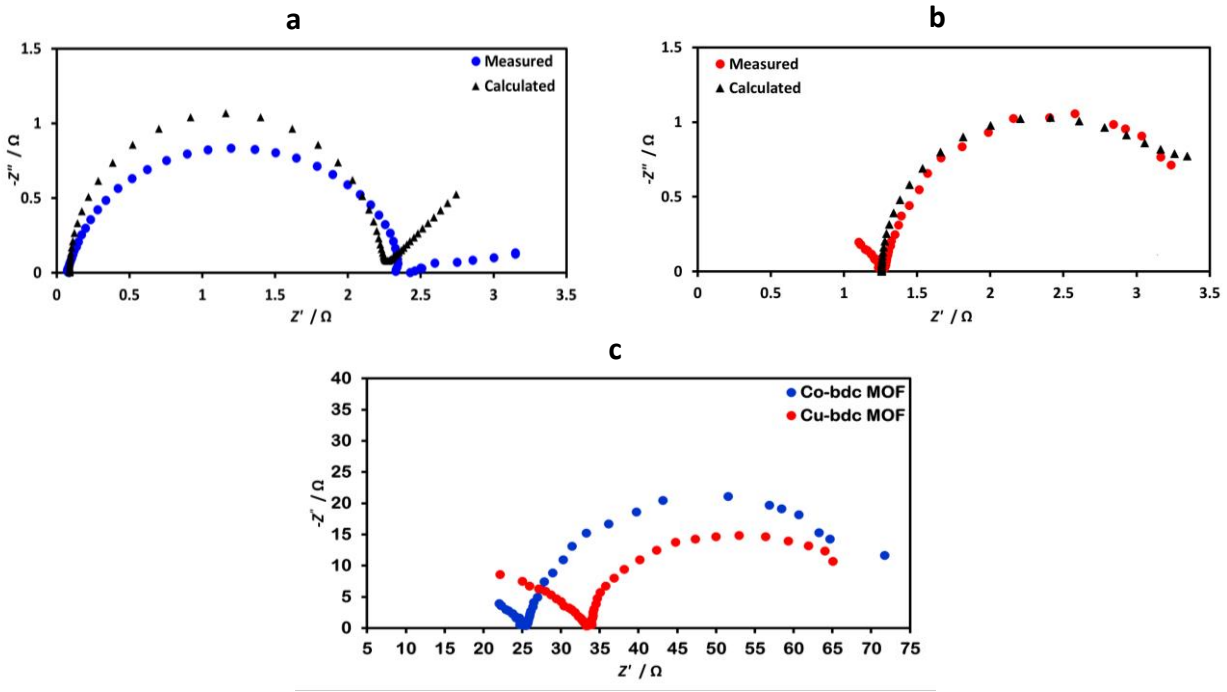

Figure 5. *EIS within a frequency range of 100 kHz to 0.01 Hz of: (a) Cu-bdc MOF; (b) Co-bdc MOF; (c) after 2000 consecutive cycles*

Galvanostatic charge-discharge

The specific capacitance (C_s) of the electrode was calculated using the following equation:

$$C_s = \frac{I\Delta t}{m\Delta V} \tag{1}$$

where I is the charge-discharge current, Δt is the time of discharge, ΔV is the difference between the upper and the lower potential limits, and m is the mass of the material [46].

Figure 6(a) and 6(b) illustrates the GCD curves for Co-bdc and Cu-bdc, respectively. Comparison of the GCD curves of Co-bdc and Cu-bdc electrodes at current densities of 0.5 to 18 A/g reveals a longer discharge time for the Co-bdc electrode, signifying notably larger capacitance for this electrode. Table 3 provides the specific capacitance values and the corresponding voltage drops for Co-bdc and Cu-bdc MOFs at varying current densities. The maximum specific capacitance obtained for Co-bdc MOF and Cu-bdc MOF was 368 and 171 F/g, respectively. It was observed that the voltage drop in the discharge curve rises with increasing applied current density. This escalating voltage drop adversely impacts the accessibility of active sites by ions during electrochemical reactions, leading to a reduction in capacitance. Conversely, at low current density, the voltage drop is minimal, enabling ions to access more active sites, resulting in higher capacitance [47].

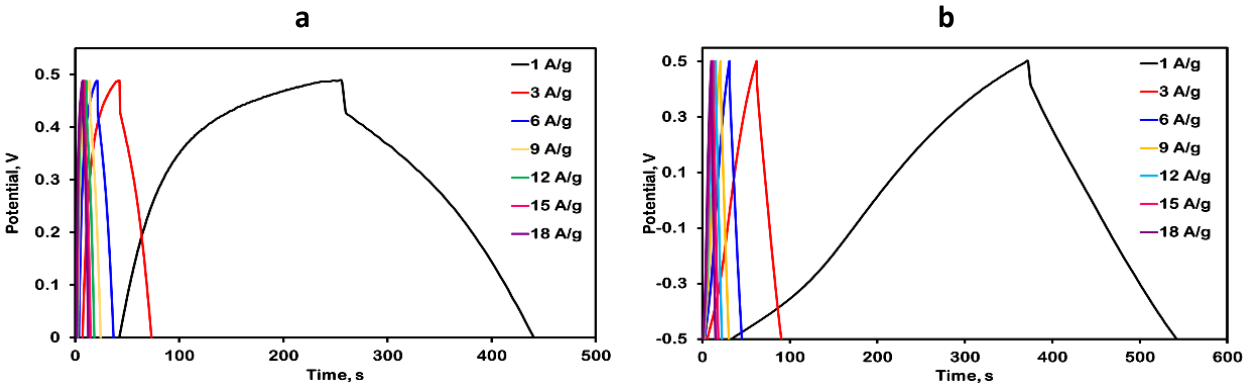

Figure 6. *GCD plots of (a) Co-bdc and (b) Cu-bdc MOF at different current densities ranging from 1 to 18 A/g*

Table 3. *Specific capacitance values of Co-bdc and Cu-bdc MOFs with their corresponding voltage drops at different current densities*

Current density, A/g	Co-bdc MOF		Cu-bdc MOF	
	Voltage drop, mV	Specific capacitance, F/g	Voltage drop, mV	Specific capacitance, F/g
1	32	368	28	171
3	41	199	36	86
6	48	194	44	84
9	62	189	49	81
12	69	187	53	78
15	77	186	55	75
18	81	180	60	72

Cyclic stability and columbic efficiency

The cyclic stability test of the electrodes was carried out using GCD measurement at a current density of 18 A/g for 2000 cycles. Figure 7 shows the capacitance retentions and the columbic efficiency with respect to a number of cycles, while the inset figures show the first 30 charge/discharge cycles for both MOFs. According to the plot presented in Figure 7(a), the Cu-bdc MOF exhibits an impressive retention of approximately 78 % of its initial capacitance after 2000 cycles, even when subjected to a high current density of 18 A/g. This highlights the excellent cyclic stability of the material when utilized as an electrode, even under high-current conditions. Similarly, Figure 7(b) illustrates that the Co-bdc MOF maintains 85 % of its initial capacitance after 2000 cycles at a notable current density of 18 A/g, further emphasizing its stable performance as an electrode material. This suggests that the electrode fabricated using Co-bdc MOF exhibits a longer cycle life and electrochemical reversibility as compared to the Cu-bdc MOF in the 3M KOH electrolyte system. The decrease in capacitance over a period for both MOFs could be attributed to the loss of active material during the cycling process.

Figure 7(a) displays the device coulombic efficiency of Cu-bdc MOF, computed using Eq. (2). The graph indicates consistent stability, hovering around 96 % across the varying number of cycles. This suggests that the charge acquired during the charging phase equals the amount lost during discharging, and notably, this proportion remains constant despite the increasing number of cycles. In Figure 7(b), the coulombic efficiency for Cu-bdc MOF is depicted, revealing a steadfast stability at 98 % over the observed cycles.

The coulombic efficiency (η), which allows us to evaluate the reversibility of the charge/discharge processes, was calculated from Eq. (2):

$$\eta = \frac{t_d}{t_c} 100 \tag{2}$$

where t_d is the time of discharge and t_c is the time of charge [47].

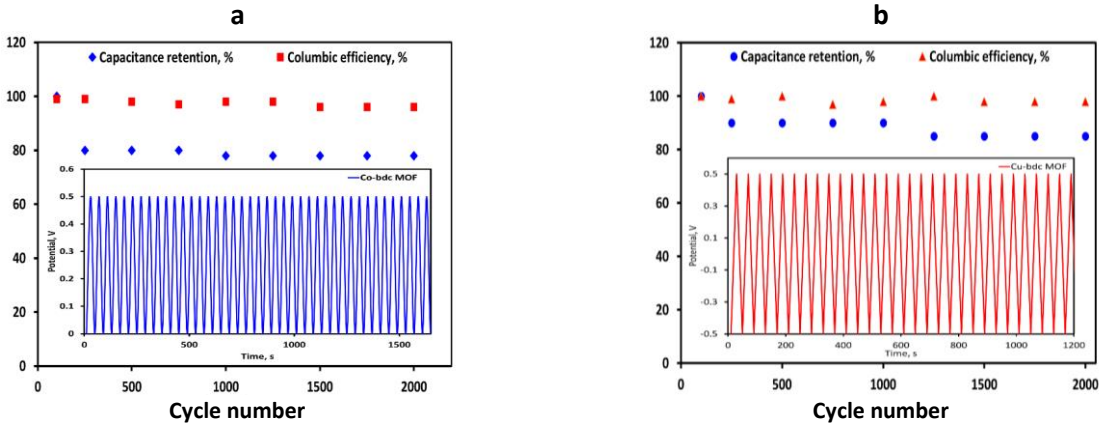

Figure 7. *Cyclic stability test at 18 A/g of (a) Co-bdc and (b) Cu-bdc MOF*

Conclusion

In this study, a facile and environmentally friendly method was employed to synthesize two distinct MOFs, Co-bdc and Cu-bdc MOF, respectively. The MOFs synthesis employed a common ligand material and a nearly identical procedure. The successful synthesis of the MOFs was confirmed through various characterizations, including SEM-EDX, FTIR, and XRD analyses. The goal of this study was to streamline the material synthesis process, emphasizing simplicity and reduced labor, with the aim of minimizing production time and material costs. Then, both materials were compared for their efficiency within the same electrolyte system for supercapacitor applications. Among both MOFs, Cu-bdc MOF demonstrated minimal solution and charge transfer resistance, effectively shortening diffusion paths and facilitating rapid ion transport, leading to exceptional rate performance and long-term stability. The Co-bdc MOF and Cu-bdc MOF exhibited the highest specific capacitance values of 368 and 171 F/g at 1 A/g. Cyclic stability and coulombic efficiency were also evaluated over various cycles, with both MOFs demonstrating outstanding cycling properties and stability. However, the Co-bdc MOF outperformed its counterpart in terms of overall performance for supercapacitor application for a 3M KOH electrolyte system.

***Acknowledgements**: The authors are thankful to the Department of Chemical Engineering, NIT Raipur, Chhattisgarh, India for their support.*

References

[1] J. R. Miller, P. Simon, Electrochemical capacitors for energy management, *Science* **321** (2008) 651-652. https://doi.org/10.1126/science.1158736

[2] P. Simon, Y. Gogotsi, Materials for electrochemical capacitors, *Nature Materials* **7** (2008) 845-854. https://doi.org/10.1038/nmat2297

[3] S. G. Sayyed, M. A. Mahadik, A. V. Shaikh, J. S. Jang, H. M. Pathan, Nano-metal oxide based supercapacitor via electrochemical deposition, *ES Energy & Environment* **3** (2019) 25-44. https://doi.org/10.30919/esee8c211

[4] A. R. Ansari, S. A. Ansari, N. Parveen, M. O. Ansari, Z. Osman, Ag nanoparticles anchored reduced graphene oxide sheets@ nickel oxide nanoflakes nanocomposites for enhanced capacitive performance of supercapacitors, *Inorganic Chemistry Communications* **150** (2023) 110519. https://doi.org/10.1016/j.inoche.2023.110519

[5] S. A. Ansari, Graphene quantum dots: novel properties and their applications for energy storage devices *Nanomaterials* **12(21)** (2022) 3814. https://doi.org/10.3390/nano12213814

[6] F. Zhu, W. Liu, Y. Liu, and W. Shi, Construction of porous interface on CNTs@ NiCo-LDH core-shell nanotube arrays for supercapacitor applications, *Chemical Engineering Journal* **383** (2020) 123150. https://doi.org/10.1016/j.cej.2019.123150

[7] G. Srikesh, A. Samson Nesaraj, Wet Chemical Synthesis of Graphene Containing Co/Mn Co-doped NiONanocrystalline Materials: Efficient Electrode for Electrochemical Supercapacitors, *Iranian Journal of Chemistry and Chemical Engineering* **40(5)** (2021) 1406-1413. https://doi.org/10.30492/ijcce.2020.40537

[8] N. Parveen, G. M. Alsulaim, S. A. Alsharif, H. H. Almutairi, H. A. Alali, S. A. Ansari, M. M. Ahmad Renewable biopolymer-derived carbon–nickel oxide nanocomposite as an emerging electrode material for energy storage applications, *Journal of Science: Advanced Materials and Devices* **8(3)** (2023) 100591. https://doi.org/10.1016/j.jsamd.2023.100591

[9] F. Arshad, N. Parveen, S. A. Ansari, J. A. Khan, M. P. Sk, Renewable biopolymer-derived carbon–nickel oxide nanocomposite as an emerging electrode material for energy storage applications, *Environmental Science and Pollution Research,* **30(28)** (2023) 71464-71471. https://doi.org/10.1007/s11356-022-22626-4

[10] D. D. Babu, M. Mathew, S. Thomas, Supercapacitors based on MXenes (transition metal carbides and nitrides) and their hybrids, *Fundamentals and Supercapacitor Applications of 2D Materials* (2021) 217-233. https://doi.org/10.1016/B978-0-12-821993-5.00006-6
[11] S. Krishnan, A. K. Gupta, M. K. Singh, N. Guha, D. K. Rai, Nitrogen-rich Cu-MOF decorated on reduced graphene oxide nanosheets for hybrid supercapacitor applications with enhanced cycling stability, *Chemical Engineering Journal* **435** (2022) 135042. https://doi.org/10.1016/j.cej.2022.135042
[12] H. García, S. Navalón (Eds.), *Metal-organic frameworks: Applications in separations and catalysis,* John Wiley & Sons, 2018. ISBN: 978-3-527-34313-3
[13] L. He, W. Li, Z. W. Jiang, T. T. Zhao, Y. Li, C. M. Li, Y. F. Li. Novel solvent-triggered transformation of Cu-based metal-organic gels to highly monodisperse metal-organic frameworks with controllable shapes, *Chemical Engineering Journal* **374** (2019) 1231-1240. https://doi.org/10.1016/j.cej.2019.06.026
[14] S. Wang, S. Tang, Rapid and facile synthesis of metal organic framework materials by reaction crystallization in supercritical CO_2, *Materials Letters* **251** (2019) 65-68. https://doi.org/10.1016/j.matlet.2019.05.038
[15] S. A. Tirmizi, A. Badshah, H. M. Ammad, M. Jawad, S. M. Abbas, U. A. Rana S. U. D. Khan, Synthesis of highly stable MOF-5@ MWCNTs nanocomposite with improved hydrophobic properties, *Arabian Journal of Chemistry* **11** (2018) 26-33. https://doi.org/10.1016/j.arabjc.2017.01.012
[16] J. Klinowski, F. A. A. Paz, P. Silva, J. Rocha, Microwave-assisted synthesis of metal–organic frameworks, *Dalton Transactions* **40** (2011) 321-330. https://doi.org/10.1039/C0DT00708K
[17] D. W. Jung, D. A. Yang, J. Kim, J. Kim, and W. S. Ahn, Facile synthesis of MOF-177 by a sonochemical method using 1-methyl-2-pyrrolidinone as a solvent, *Dalton Transactions* **39** (2010) 2883-2887. https://doi.org/10.1039/B925088C
[18] H. M. Yang, L. I. U. Xian, X. L. Song, T. L. Yang, Z. H. Liang, C. M. Fan, In situ electrochemical synthesis of MOF-5 and its application in improving photocatalytic activity of BiOBr, *Transactions of Nonferrous Metals Society of China* **25** (2015) 3987-3994. https://doi.org/10.1016/S1003-6326(15)64047-X
[19] N. L. Rosi, J. Kim, M. Eddaoudi, B. Chen, M. O'Keeffe, O. M. Yaghi. Rod packings and metal–organic frameworks constructed from rod-shaped secondary building units, *Journal of the American Chemical Society* **127(5)** (2005) 1504-1518. https://doi.org/10.1021/ja045123
[20] R. Nivetha, J. Jana, S. Ravichandran, H. N. Diem, T. Van Phuc, J. S. Chung, S. H. Hur, Two-dimensional bimetallic Fe/M-(Ni, Zn, Co and Cu) metal organic framework as efficient and stable electrodes for overall water splitting and supercapacitor applications, *Journal of Energy Storage* **61** (2023) 106702. https://doi.org/10.1016/j.est.2023.106702
[21] T. Sivam, N. S. K.Gowthaman, H. N. Lim, Y. Andou, P. Arul, E. Narayanamoorthi, S. A. John, Tunable electrochemical behavior of dicarboxylic acids anchored Co-MOF: Sensitive determination of rutin in pharmaceutical samples, *Colloids and Surfaces A: Physicochemical and Engineering Aspects* **622** (2021) 126667. https://doi.org/10.1016/j.colsurfa.2021.126667
[22] A. Ehsani, S. Nejatbakhsh, A. M. Soodmand, M. E. Farshchi, H. Aghdasinia, High-performance catalytic reduction of 4-nitrophenol to 4-aminophenol using M-BDC (M= Ag, Co, Cr, Mn, and Zr) metal-organic frameworks, *Environmental Research* **227** (2023) 115736. https://doi.org/10.1016/j.envres.2023.115736
[23] G. Zhan, L. Fan, F. Zhao, Z. Huang, B. Chen, X. Yang, S. F. Zhou, Fabrication of Ultrathin 2D Cu-BDC Nanosheets and the Derived Integrated MOF Nanocomposites, *Advanced Functional Materials* **29(9)** (2019) 1806720. https://doi.org/10.1002/adfm.201806720

[24] G. Zheng, Z. Xing, X. Gao, C. Nie, Z. Xu, Z. Ju, Fabrication of 2D Cu-BDC MOF and its derived porous carbon as anode material for high-performance Li/K-ion batteries, *Applied Surface Science* **559** (2021) 149701. https://doi.org/10.1016/j.apsusc.2021.149701
[25] S. Sadjadi, F. Koohestani, Palladated composite of Cu-BDC MOF and perlite as an efficient catalyst for hydrogenation of nitroarenes, *Journal of Molecular Structure* **1250** (2022) 131793. https://doi.org/10.1016/j.molstruc.2021.131793
[26] S. Rostamnia, H. Alamgholiloo, X. Liu, Pd-grafted open metal site copper-benzene-1, 4-dicarboxylate metal organic frameworks (Cu-BDC MOF's) as promising interfacial catalysts for sustainable Suzuki coupling, *Journal of Colloid and Interface Science* **469** (2016) 310-317. https://doi.org/10.1016/j.jcis.2016.02.021
[27] N. Y. Nikravesh, M. Beygzadeh, M. Adl, Microporous MOF-5@ AC and Cu-BDC@ AC Composite Materials for Methane Storage, *International Journal of Energy Research* **2023** (2023) 2282746. https://doi.org/10.1155/2023/2282746
[28] R. S. Salama, S. A. El-Hakam, S. E. Samra, S. M. El-Dafrawy, A. I. Ahmed, Adsorption, equilibrium and kinetic studies on the removal of methyl orange dye from aqueous solution by using of copper metal organic framework (Cu-BDC), *International Journal of Modern Chemistry* **10(2)** (2018) 195-207.
[29] M. K. Singh, A. K. Gupta, S. Krishnan, N. Guha, S. Marimuthu, D. K. Rai, A new hierarchically porous Cu-MOF composited with rGO as an efficient hybrid supercapacitor electrode material *Journal of Energy Storage* **43** (2021) 103301. https://doi.org/10.1016/j.est.2021.103301
[30] S. Krishnan, A. K. Gupta, M. K. Singh, N.Guha, D. K. Rai, Nitrogen-rich Cu-MOF decorated on reduced graphene oxide nanosheets for hybrid supercapacitor applications with enhanced cycling stability, *Chemical Engineering Journal* **435** (2022) 135042. https://doi.org/10.1016/j.cej.2022.135042
[31] A. K. Gupta, M. Saraf, P. K. Bharadwaj, S. M. Mobin, Dual functionalized CuMOF-based composite for high-performance supercapacitors, *Inorganic Chemistry* **58** (2019) 9844-9854. https://doi.org/10.1021/acs.inorgchem.9b00909
[32] Z. Neisi, Z. Ansari-Asl, A. S. Dezfuli, Polyaniline/Cu (II) metal-organic frameworks composite for high performance supercapacitor electrode, *Journal of Inorganic and Organometallic Polymers and Materials* **29** (2019) 1838-1847. https://doi.org/10.1007/s10904-019-01145-9
[33] Z. Maliha, M. Rani, R. Neffati, A. Mahmood, M. Z. Iqbal, A. Shah, Investigation of copper/cobalt MOFs nanocomposite as an electrode material in supercapacitors, *International Journal of Energy Research* **46** (2022) 17404-17415. https://doi.org/10.1002/er.8406
[34] R. Ramachandran, C. Zhao, D. Luo, K. Wang, F. Wang, Synthesis of copper benzene-1, 3, 5-tricarboxylate metal organic frameworks with mixed phases as the electrode material for supercapacitor applications, *Applied Surface Science* **460** (2018) 33-39. https://doi.org/10.1016/j.apsusc.2017.11.271
[35] M. Azadfalah, A. Sedghi, H. Hosseini, Synthesis of nano-flower metal–organic framework/graphene composites as a high-performance electrode material for supercapacitors, *Journal of Electronic Materials* **48** (2019) 7011-7024. https://doi.org/10.1007/s11664-019-07505-y
[36] S. Ghosh, C. K. Maity, G. C. Nayak, H. P. Nayek, A cobalt (II) metal-organic framework featuring supercapacitor application, *Journal of Solid State Chemistry* **282** (2020) 121093 https://doi.org/10.1016/j.jssc.2019.121093
[37] N. S. Punde, C. R. Rawool, A. S. Rajpurohit, S. P. Karna, A. K. Srivastava, Hybrid composite based on porous cobalt-benzenetricarboxylic acid metal organic framework and graphene nanosheets as high performance supercapacitor electrode, *ChemistrySelect* **3** (2018) 11368-11380. https://doi.org/10.1002/slct.201802721

[38] M. Azadfalah, A. Sedghi, H. Hosseini, H. Kashani, Cobalt based metal organic framework/graphene nanocomposite as high performance battery-type electrode materials for asymmetric supercapacitors, *Journal of Energy Storage* **33** (2021) 101925. https://doi.org/10.1016/j.est.2020.101925

[39] R. Yuniasari, F. Amri, S. A. Abrori, N. L. W. Septiani, M. Rezki, M. Z. Fahmi, B. Yuliarto, A graphene-modified Co-BDC metal-organic frameworks (Co-MOF) for electrochemical non-enzymatic glucose sensing, *IOP Conference Series: Materials Science and Engineering* **1045** (2021) 012010. 10.1088/1757-899X/1045/1/012010

[40] R. Khajavian, K. Ghani, Fabrication of $[Cu_2(bdc)_2(bpy)]_n$ thin films using coordination modulation-assisted layer-by-layer growth, *CrystEngComm* **20** (2018) 1546-1552. https://doi.org/10.1039/C7CE02031G

[41] M. Pamei, S. Kumar, A. G. Achumi, A. Puzari, Supercapacitive amino-functionalized cobalt and copper metal-organic frameworks with varying surface morphologies for energy storage, *Journal of Electroanalytical Chemistry* **924** (2022) 116885. https://doi.org/10.1016/j.jelechem.2022.116885

[42] G. Zhan, L. Fan, F. Zhao, Z. Huang, B. Chen, X. Yang, F. Zhou, Fabrication of Ultrathin 2D Cu-BDC Nanosheets and the Derived Integrated MOF Nanocomposites, *Advanced Functional Materials* **29(9)** (2019) 1806720. https://doi.org/10.1002/adfm.201806720

[43] A. Nayak, S. Viegas, H. Dasari, N. Sundarabal, Cu-BDC and Cu_2O Derived from Cu-BDC for the Removal and Oxidation of Asphaltenes: A Comparative Study, *ACS Omega* **7** (2022) 34966-34973. https://doi.org/10.1021/acsomega.2c03574

[44] L. X. Li, D. Xu, X. Q. Li, W. C. Liu, Y. Jia, Excellent fluoride removal properties of porous hollow MgO microspheres, *New Journal of Chemistry* **38** (2014) 5445-5452. https://doi.org/10.1039/C4NJ01361A

[45] A. Ansari, A. Ali, M. Asif, Shamsuzzaman, Microwave-assisted MgO NP catalyzed one-pot multicomponent synthesis of polysubstituted steroidal pyridines, *New Journal of Chemistry* **42** (2018) 184-197. https://doi.org/10.1039/C7NJ03742B

[46] M. da Silva, D. A. de Lima Almeida, S. S. Oishi, A. B. Couto, N. G. Ferreira, From electrode to device characterizations of polyaniline/micro and nanodiamond/carbon fiber as ternary composites applied as supercapacitor, *Journal of Solid State Electrochemistry* **23** (2019) 1871-1885. https://doi.org/10.1007/s10008-019-04297-3

[47] Q. Li, Q. Zhang, C. Liu, J. Sun, J. Guo, J. Zhan, Y. Yao, Flexible all-solid-state fiber-shaped Ni–Fe batteries with high electrochemical performance, *Journal of Materials Chemistry A* **7(2)** (2019) 520-530.-https://doi.org/10.1039/C8TA09822K

J. Electrochem. Sci. Eng. **14(2)** (2024) 177-192; http://dx.doi.org/10.5599/jese.1991

Open Access : : ISSN 1847-9286
www.jESE-online.org

Original scientific paper

Moth flame-random search optimization of a zero-dimensional model of a proton exchange membrane fuel cell

Ali Maroosi[1,✉] and Amir Mohammadbeigi[2]

[1]*Department of Computer Engineering, University of Torbat Heydarieh, Torbat Heydarieh, Iran*
[2]*Department of Electrical Engineering, University of Torbat Heydarieh, Torbat Heydarieh, Iran*

Corresponding author: ✉ali.maroosi@torbath.ac.ir; Tel.: +98-51-512-40150; Fax: +98-51-512-40150

Received: July 21, 2023; Accepted: January 8, 2024; Published: February 16, 2024

Abstract

Modelling of proton exchange membrane fuel cell (PEMFC) is important for better understanding, simulation, and design of high-efficiency fuel cell systems. PEMFC models are often multivariate with several nonlinear elements. Metaheuristic algorithms that are successful in solving nonlinear optimization problems are good candidates for this purpose. This study proposes a new metaheuristic algorithm called MFORS that uses the advantages of the moth-flame optimization algorithm in global search and the non-deterministic properties of the random search algorithm to identify the optimal parameters of the PEMFC model. The sum of squared errors between the estimated and measured voltage is a quality of fit criterion. To show the effectiveness of the proposed algorithm, two case studies of zero-dimensional models of SR-12 Modular PEM Generator and Ballard Mark V fuel cell are considered. The sum of squared errors for the parameter estimated of electrical PEMFCs by the proposed MFORS algorithm is compared with recent works. The results showed that by the MFORS algorithm, the minimum sum of absolute errors of the actual stack voltage and the simulated stack voltage in the two PEMFC are 0.095037 and 0.018019, compared with the second-best algorithm results giving 0.09681 and 0.8092, respectively.

Keywords

Fuel cell system; parameters estimation; global optimization algorithm; chemical energy; hybrid algorithm

Introduction

The energy demand, environmental pollution, global warming and limited amount of fossil fuel sources are reasons to encourage researchers to study fuel cells (FCs) [1,2]. Fuel cells (FC) are an emerging technology used in portable power generation, electrification to island areas, *etc*. [3,4]. The proton exchange membrane fuel cell (PEMFC) converts most of the chemical energy of the hydrogen and oxygen reactions into electrical energy (along with the production of water and a heat

release) near room temperature without pollutant emissions [5]. Other advantages of PEMFC include low noise, high specific power and good energy efficiency [6,7].

Recently, evolutionary and metaheuristic algorithms have been applied for optimizing the parameters of FCs. A moth-flame optimization algorithm is employed in [8] to estimate the optimal parameters of solid oxide fuel cells to improve the output power of this model. They compared the study with a genetic algorithm (GA), radial movement optimizer (RMO) and social spider optimizer (SSO). Abdullah *et al*. proposed a moth flame optimization algorithm for optimal modeling of the PEMFC [9]. To show the approach efficiency, the results were validated by comparing with the particle swarm optimization(PSO) algorithm and sine cosine algorithm (SCA). The hybrid water cycle moth-flame optimization (WCMFO) was applied to lessen the sum of squared errors (SSE) between the measured and the experimental stack voltage of PEMFC [10]. A comparative study was proposed on the optimal estimation of the PEMFC parameters based on two different metaheuristics. The results indicated that using MFO gives better results than methods in [11].

Diab *et al*. [12] proposed a PEMFC numerical model using metaheuristic tools to estimate model parameters. Houssein *et al.* applied Archimedes optimization algorithm (AOA) using orthogonal learning to identify PEMFC parameters [13]. A robust method based on the gradient-based optimizer (GBO) was proposed to identify unknown parameters of PEMFC [14]. During the optimization process, the unknown parameters of PEMFC were used as decision variables, whereas the objective function needs to be minimum is presented by the SSE between the estimated and measured production voltage of the PEMFC.

Three algorithms, namely the imperialist competitive algorithm (ICA), firefly optimization algorithm (FOA), and shuffled frog-leaping algorithm (SFLA), have been employed for the extraction of unknown BCS 500-W, Horizon 500-W FC and NedStack PS6 parameters [15]. A flower pollination algorithm (FPA) has been used to estimate the optimal parameters of different PEMFCs by selecting SSE as an objective function [16]. A combination of the two algorithms, including the JAYA algorithm and the Nelder-Mead simplex search algorithm (JAYA-NM), was presented to estimate the optimal parameters of PEMFC [17]. A hybrid of vortex search algorithm and differential evolution has been used for extracting the parameters of FC under different conditions [18]. A cuckoo search algorithm with an explosion operator (CS-EO) was proposed for solving unknown parameters of PEMFC. CS-EO has the ability to obtain better performance and avoid precipitate convergence [19]. The transient search optimization (TSO) algorithm was used to estimate the parameters by minimizing the SSEs between the calculated and measured voltages [20]. The chimp optimization algorithm (ChOA) has also been presented to determine the unknown parameters of the PEMFC [21].

Many optimization alghoritms have been used to identify parameters of PEMFC (Table 1).

However, the accuracy of the previous algorithms is not satisfactory. Some algorithms converge to suboptimum solutions. Thus, a new algorithm that could improve the quality of the solution is needed. Recently, a new metaheuristic algorithm called moth-flame optimization (MFO) was presented [22]. This algorithm has a promising performance in solving optimization problems [22]. An MFO was applied for the problem related to the strategic accommodation of fuel cells in an active distribution network that consists of wind turbines and photovoltaic modules [23].

An MFO was applied for the artificial neural network to improve its operational accuracy for providing an accurate predicting control scenario for the integration of fuel cells with photovoltaic and wave energy sources using the field programmable gate array (FPGA) technology [24]. An MFO based on sine mapping and Gaussian mutation was used for the economic optimization dispatch of the microgrid [25].

***Table 1**. Some of algorithms utilized in recent years in PEMFC case studies*

Optimization algorithm	Case studies									Year	Ref.
	Ballard Mark V	BCS 500 W	SR-12 500 W	NedStack PS6	250-W PEMFC	Temasek 1 kW	Horizon 500-W	H-12 stack	250W stack		
Shuffled frog-leaping algorithm (SFLA), firefly optimization algorithm (FOA), and imperialist competitive algorithm (ICA)	+			+			+			2019	[15]
Transient search optimization (TSO)	+			+				+		2022	[20]
Heap-based optimizer (HBO)		+	+	+				+		2021	[27]
Simplified teaching-learning-based optimization algorithm (STLBO)									+	2014	[28]
Aging and challenging P systems-based optimization algorithm (AC-POA)									+	2016	[29]
Harris Hawks optimizer (HHO)	+	+	+	+				+		2021	[30]
Gravitational search algorithm (GSA), grey wolf optimizer (GWO), differential evolution (DE), sine cosine algorithm (SCA), RSA algorithm, and arithmetic optimization algorithm (AOA)		+		+						2022	[31]
Pathfinder algorithm (PA)	+							+		2021	[32]
Salp Swarm algorithm (SSA)		+	+		+	+				2020	[33]
Flower pollination algorithm (FPA)	+	+		+		+				2019	[16]
Sparrow search algorithm (SSA)	+			+				+		2021	[34]
Bald eagle search (BES)		+		+				+	+	2022	[35]
Black widow optimization (BWO)	+		+							2021	[36]
Whale optimization algorithm (WOA)	+		+					+	+	2019	[37]
Artificial bee colony differential evolution shuffled complex (ABCDESC)	+	+		+				+	+	2022	[38]
Artificial bee colony differential evolution optimizer (ABCDE)	+	+	+	+			+	+		2022	[39]
Bonobo optimizer (BO)		+	+						+	2020	[40]
Jellyfish search algorithm (JSA)		+		+					+	2021	[41]
Ecosystem optimization (AEO)		+	+			+			+	2020	[42]
Marine predators algorithm (MPA)		+	+						+	2020	[43]
Shark smell optimizer (SSO)	+	+	+			+				2019	[44]
Grey wolf optimization (GWO)		+	+						+	2022	[45]

The MFO algorithm searches the solution space rapidly. However, sometimes, it cannot find the correct solution for a highly nonlinear problem and contains many local minima. A random search algorithm (RS) can obtain the global optimum solution for highly nonlinear functions [26]. However, it is slow in convergence. Unlike other heuristic algorithms inclined to close the best current solutions, the RS algorithm explores the space randomly without considering the best solutions [26]. In this study, a new optimization algorithm called MFORS is introduced. This algorithm uses the ability of the MFO algorithm in global search and non-deterministic properties of RS to obtain the optimal parameters of the PEMFC model.

The remainder of this paper is organized as follows: the problem formulation of PEMFC is presented in the Problem description section, and the basic MFO and RS algorithm are presented in the next section. After that, simulations and discussions about PEMFC are provided, followed by conclusions.

Problem description

The theory of PEMFC

A PEMFC is electrochemical device that converts the chemical energy of oxygen and hydrogen into electrical and thermal energy. The chemical reactions that occur at PEMFC cathode and anode are defined as follows [46]:

Anode side: $H_{2(g)} \rightarrow 2H^+ + 2e^-$ (1)

Cathode side: $2H^+ + 2e^- + 1/2O_2 \rightarrow H_2O$ (2)

Overall reaction: $H_{2(g)} + 1/2O_2 \rightarrow H_2O$ (3)

The overall reaction (3) between oxygen (O_2) and hydrogen (H_2) has a large negative Gibbs energy change, which dictates a theoretical open circuit voltage of ~1.23 V. During the overall reaction, the products are liquid water, electricity, and heat. To provide the required amount of power, many single cells can be assembled into a fuel cell stack system [47]. The operating temperature of PEMFC typically ranges from 70 to 85 °C. Figure 1 illustrates a basic scheme of a single PEMFC [46].

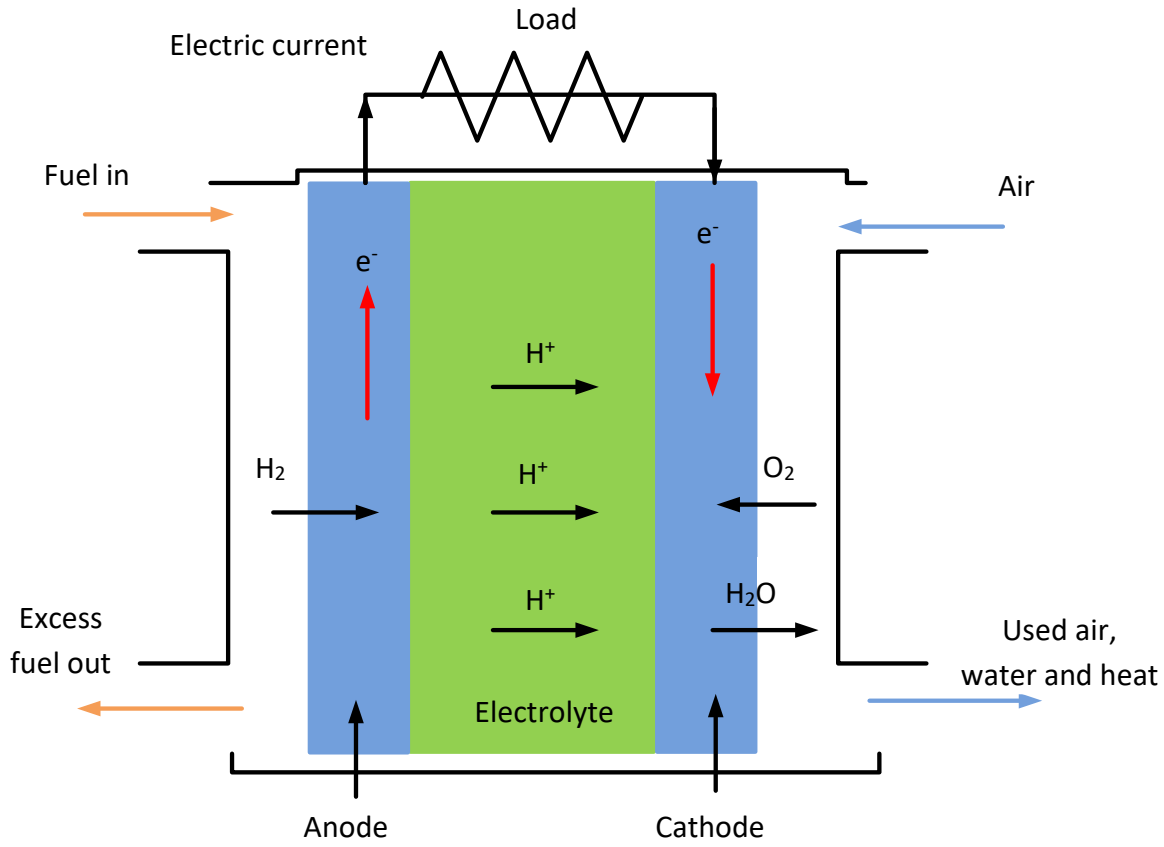

Figure 1. *Basic PEMFC operation*

The mathematical model of PEMFC

In the present study, a zero-dimensional PEMFC model described earlier in [46] was employed. The value of the equilibrium potential voltage E_{Nernst} is obtained by the Nernst equation. Many factors cause voltage losses, including activation voltage drop (V_{act}), ohmic voltage drop (V_{ohmic}), and concentration voltage drop (V_{con}). The production voltage of the FC is given by equations (4-8) [48,49]:

$$V_{STACK} = N_S(E_{Nernst} - V_{act} - V_{ohmic} - V_{con}) \quad (4)$$

$$E_{Nernst} = 1.229 + 4.3085\times10^{-5}T_{FC}\ln\left(P_{H_2}\sqrt{P_{O_2}}\right) - 0.846\times10^{-3}\left(T_{FC} - 298.15\right) \quad (5)$$

$$V_{act} = I_{fc}\left(R_C + \frac{L}{A}\frac{181.6\left[1 + 0.03\frac{I_{fc}}{A} + 0.062\left(\frac{T_{FC}}{303}\right)^2\left(\frac{I_{fc}}{A}\right)^{2.5}\right]}{\left[\lambda - 0.634 - 3\frac{I_{fc}}{A}\right]\exp\left(4.18\left[\frac{T_{FC} - 303}{T_{FC}}\right]\right)}\right) \quad (6)$$

$$V_{\text{ohmic}} = \xi_1 + \xi_2 T + \xi_3 T \ln\left(\frac{P_{O_2}}{5.08\times10^6 \exp\left(-\frac{498}{T_{FC}}\right)}\right) + \xi_4 T \ln I_{fc} \quad (7)$$

$$V_{con} = b \ln\left(1 - \frac{j}{j_{max}}\right) \quad (8)$$

In the above equations, the fuel cell temperature (T_{FC}), the hydrogen partial pressure (P_{H_2}) and the oxygen partial pressure (P_{O_2}) are dependent on the operating conditions of the system and are measurable. I_{fc} and N_s are the cell current and number of cells, j is the current, and j_{max} is the maximum current density.

The other parameters (ξ_1, ξ_2, ξ_3, ξ_4, R_c, b, λ) are unknown parameters that need to be extracted for designing and simulation of the PEMFC model.

The sum square error (SSE) between the measured and experimental production voltage of the PEMFC stack model can serve as an objective function (*OF*) to determine unknown parameters, which is represented by equations (9) and (10):

$$OF = \text{SSE} = \sum_{n=1}^{N} \left(V_{\text{measured}} - V_{\text{stack}}\right)^2 \quad (9)$$

Subject to:

$$\begin{aligned} &\xi_{k_{min}} \le \xi_k \le \xi_{k_{max}} \quad k = 1:4 \\ &\lambda_{min} \le \lambda \le \lambda_{max} \\ &R_{c_{min}} \le R_c \le R_{c_{max}} \\ &b_{min} \le b \le b_{max} \end{aligned} \quad (10)$$

where N is the sampling rate of data points, V_{measured} is the measured output voltage PEMFC stack, V_{stack} is the computed output voltage by equation (2). Table 2 represents the lower and upper bounds of these parameters.

***Table 2**. Lower and upper bounds of PEMFC parameters*

Parameter	ξ_1	$\xi_2\times10^3$	$\xi_3\times10^5$	$\xi_4\times10^4$	R_c / mΩ	λ	b(V)
Max	-0.5832	5	9.8	-0.954	0.8	24	5.0000
Min	-1.1997	1	3.6	-2.600	0.1	10	0.0136

Proposed algorithm for optimizing the parameters of a PEMFC model

This section presents the main conceptions of moth-flame optimization (MFO) and random search.

1. Moth-flame optimization (MFO algorithm)

Moth-flame optimization (MFO) is a promising optimization algorithm that is inspired by moth navigation at night when moths use moonlight for navigation. Moths are flying at an angle to the direction of the Moon. The orientation of moth travel during the night is shown in Figure 2. Since the distance between the Moon and the moth is long, the moth moves in a linear path [22]. However, when the light source is close to the moth flying at a constant angle toward the light, a spiral trajectory

is observed. The model of a flying path surrounding flame or light by moths is depicted in Figure 3 [22]. It can be concluded from Figure 3 that the moth lastly converges near the flame or light source.

This is formulated mathematically to arrive at an optimizer termed the moth-flame optimization algorithm. In this method, candidate solutions are represented by the moths and parameters of the problems are described by moth positions. This approach allows moths to move in one or more dimensions by replacing their position vectors. The moth population is represented as a matrix (11):

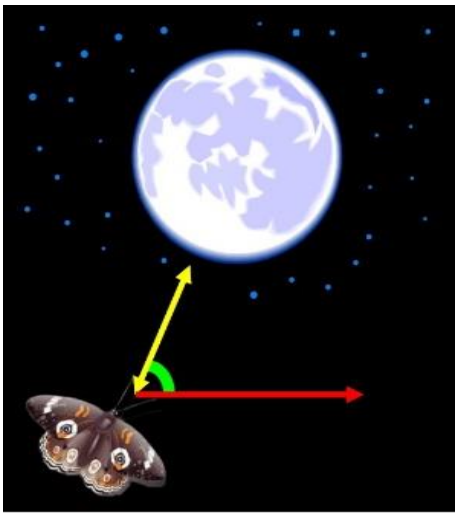

Figure 2. *Moth orientation toward the light*

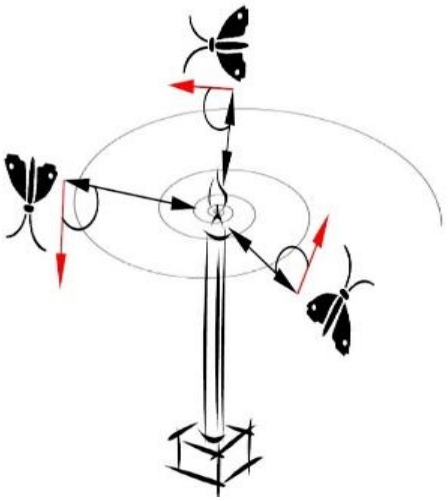

Figure 3. *Spiral flying path of moth around the light*

$$M = \begin{bmatrix} m_{1,1} & m_{1,2} & .... & .... & m_{1,d} \\ m_{2,1} & m_{2,2} & .... & .... & m_{2,d} \\ & & \vdots & & \\ m_{n,1} & m_{n,2} & .... & .... & m_{n,d} \end{bmatrix} \quad (11)$$

where n is the number of moths, and the number of variables is d. The array OM stores the corresponding fitness values for moths, equation (12).

$$OM = [OM_1, OM_2, OM_3] \quad (12)$$

The fitness value is the value of the objective function for each moth. Another main element of the algorithm is the flame matrix:

$$F = \begin{bmatrix} F_{1,1} & F_{1,2} & .... & .... & F_{1,d} \\ F_{2,1} & F_{2,2} & .... & .... & F_{2,d} \\ & & \vdots & & \\ F_{n,1} & F_{n,2} & .... & .... & F_{n,d} \end{bmatrix} \quad (13)$$

Size of matrices M and F are equal. For storing the fitness values of the flames, the array OF is defined by equation (14):

$$OF = [OF_1, OF_2, OF_3] \quad (14)$$

It is notable that moths and flames are both solutions, but how they are updated and generated differs. The moths are considered to be search candidates that explore the search space. The best positions of moths during the search are considered flames. Thus, a flame can be updated by a better solution obtained by a moth that searches around the flame. This mechanism keeps the best solution found by a moth. The MFO can be defined as tree-tuple approximation functions as follows. A random population and their corresponding fitness value are generated by I. Moths are moved

around search space by the *P* function. The matrix *M* is the input of function *P* and the output is its updated one, equation (15).

$$\text{MOF} = (I,P,T);\ I:\phi \rightarrow \{M,OM\};\ P:M \rightarrow M \quad (15)$$

The *T* function output is true when termination criteria are satisfied, otherwise, it is false, equation (16).

$$T:M\{\text{true, false}\};\ M_i = S\ (M_i, F_j) \quad (16)$$

The updated formula for the moth position with respect to the flame position is as presented by equation (17):

$$S\ (M_i, F_j) = D_i\ e^{bt} \cos(2\pi t) \quad (17)$$

where M_i and F_j are i^{th} moth and j^{th} flame, respectively. The *t* is a random variable belonging to [-1,1]. The spiral shape is defined by *b*. The D_i (equation (18)) is the distance between the i^{th} moth and j^{th} flame.

$$D_i = |F_j - M_i| \quad (18)$$

The number of flames is reduced during the iterations as equation (19):

$$\text{Number of flame} = \text{round}\left(\text{N-}L\,\frac{\text{N-1}}{T}\right) \quad (19)$$

where the maximum number of the flame population is *N*, the current iteration is *L* and *T* is the maximum number of iterations.

2. Random search (RS) algorithm

A global optimization problem with continuous variables may be highly nonlinear or contain several local optima. Heuristic algorithms like random search can obtain the global optimum solution [26]. A random search (RS) algorithm uses a stochastic approach for randomness. A random search method has the ability to solve large-scale problems efficiently with respect to the deterministic approaches. It is a derivation-free algorithm and easy to implement on problems without knowing about the gradient information of the problem functions [50]. The main advantages of the RS method are: a) simple algorithm and easy implementation, b) robustness to the noise in the objective function, c) insensitivity to irregularity of the objective function behavior and increasing dimension of the problem.

The procedure for this algorithm can be summarized as follows. In the initial step, a feasible solution is randomly chosen from the search space as the optimal solution. Then, other solutions are randomly generated in the feasible region and any solution with better fitness than the optimal solution updates it. After some iterations, the optimal solution can be shrunk around the optimal solution. The RS algorithm with more details has been described in [51,52].

3. Hybrid MFO and RS algorithm (MFORS)

Usually, some optimization algorithms are good in global exploration, while others are good in local exploitation [53]. The MFO is a promising optimization algorithm with high performance in global optimization problems [54-56]. The hybrid of MFO and RS, which is called MFORS, has been applied to keep a balance between exploitation and exploration search space. In this study, RS has been used for exploiting the best solution around the initial solution obtained by MFO. MFO shows good performance in global optimization, while RS is good in local exploitation. Thus, by a hybrid of these two algorithms, the advantages of both can be utilized. Figure 4 shows the pseudo-code of the RS algorithm, while Figure 5 shows the stages of the proposed MFORS algorithm.

Step0: Initialize:
Select initial optimal solution x_0 from the region $x_0 \in [LB\ UB]$ where LB and UB are upper and lower bound of solutions, initialize the refining region factor (K_{Ref}), period of region refining T, dimension of the solutions Dim, and initial iteration number (Iter) to zero
While stop condition is not true:
Iter=Iter+1
Step1: Random Move: Select a randomly solution in the solution space
for i=1: Dim
$x(i) = LB(i) + rand * (UB(i) - LB(i))$
End
Step2: Optimal Solution Update: update optimal solution (x_0) when new solution (x) better than optimal solution
If($f(x) < f(x_0)$)
$x_0 = x$
End
Step3: Refine solution space: Refine the region in the respect with the optimal solution every T times
If(mod(Iter, T) equal to zero)
For i=1 to Dim
Width(i)= (UB(i)-LB(i))* K_{Ref};
If(x_0(i)-Width(i)/2< LB (i))
LB (i)= LB (i);
UB(i)= UB(i)- Width(i)/2
Else If(x_0(i)+Width(i)/2 > UB (i))
LB(i)= LB(i)+ Width(i)/2
UB(i)= UB (i);
Else
LB (i)= x_0(i)-Width(i)/2
UB(i)= x_0(i)+Width(i)/2
End If
End for
End If
End While

x_0 is the refined optimization solution

***Figure 4**. The pseudo code of RS algorithm*

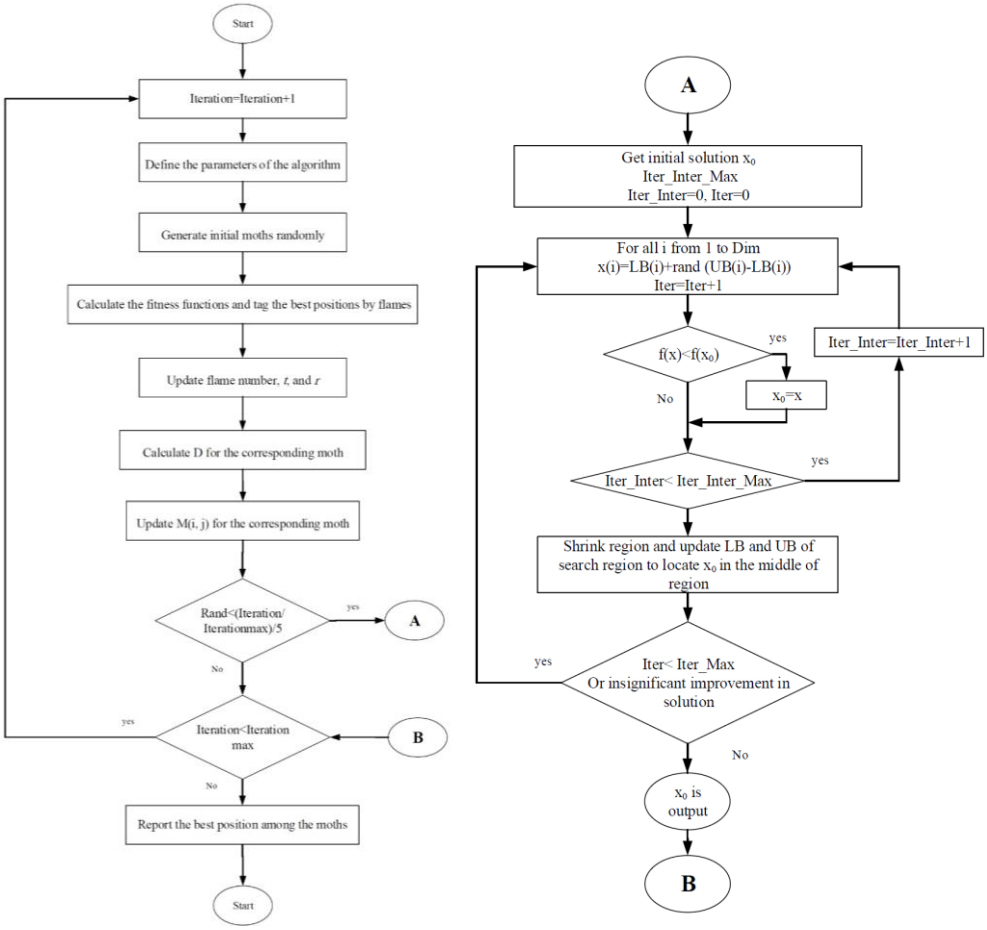

***Figure 5.** The flowchart of proposed MFORS algorithm*

Results and discussion

Simulation of PEMFC

In this subsection, the simulation results are presented in order to validate the proposed MFORS algorithm for estimating the PEMFC parameters. The MFORS and other algorithms were implemented under MATLAB 2014 and simulations have been done on an Intel, core i5 CPU, 6 GB RAM and 2.4 GHz computer. In this study, the population size for MFORS and other algorithms is equal to 30 and the maximum iteration is 5000 [47]. Simulations have been done for two case studies, including the SR-12 modular PEM generator and the Ballard Mark V FC [46,57,58].

Case study 1: SR-12 modular PEM generator

The SR-12 Modular PEM Generator was used as the first case study. Its rated power is 500W. The operating conditions parameters are T = 323 K, P_{H_2}=149.584 Pa (1.47628 atm), P_{O_2}= 21.228 Pa (0.2095 atm), N_s = 48, J_{max} = 672 mA/cm^2 maximum current density [37,46,57].

Table 3 shows the optimal parameters related to the optimum implementation of the algorithms and a comparison of the proposed MFO and MFORS with other metaheuristic algorithms. The algorithms studied in Table 3 are as follows: Shark smell optimizer (SSO) [44], Cuckoo search (CS) [19], Cuckoo search algorithm with explosion operator (CS-EO) [19], Vortex search algorithm and differential evolution (VSDE) [18], Bonobo optimizer (BO) [40], Harris hawks optimization (HHO) [40], Chaotic Harris Hawks optimization (CHHO) [40], Grey Wolf optimization (GWO) [45], Improved Grey Wolf optimization (IGWO) [45], Multi-verse optimization (MVO) [45], Selective opposition-based Grey Wolf optimization (SOGWO) [45], Dragonfly algorithm (DA) [45], Atom search optimization (ASO) [45], Ant lion optimization (ALO) [44, 45], Sparrow search algorithm (SSO) [34], Salp swarm optimization (SSO) [34], Flower pollination algorithm (FPA) [59], Shuffled frog-leaping algorithm (SFLA), Firefly algorithm (FA), Artificial bee colony (ABC), Moth-flame optimization (MFO).

Table 3. *The optimal parameters for different algorithms of Sr-12*

Algorithm	ξ_1	$\xi_2\times10^3$	$\xi_3\times10^5$	$\xi_4\times10^4$	λ	b / V	R_c / mΩ	SSE	Year	Ref.
SSO	-0.9664	2.2833	2.2833	-0.954	15.796	0.1804	0.66853	1.15080	2019	[44]
SC	1.0782	3.7309	8.8207	0.9540	10.0	0.1471	0.71274	7.57590	2019	[19]
SC-EO	-1.0353	-1.0353	3.354	-0.954	10.0	0.1471	0.71233	7.57530	2019	[19]
VSDE	−0.8576	3.0100	7.7800	9.5400	23	0.1339	0.01516	1.26600	2019	[18]
BO	-1.0972	3.80925	9.8000	-0.95 400	23	0.175320	0.67231	1.05663	2020	[40]
CHHO	-0.8532	3.0918	8.2387	-0.9540	22.91	0.17623	0.62468	1.05716	2020	[40]
HHO	-0.8533	2.4173	4.2487	-0.95412	15.34	0.17794	0.37166	1.05931	2020	[40]
IGWO	-1.14361	-0.14361	3.5748	-0.95405	22.87	0.17533	0.66936	1.05660	2022	[45]
MVO	-0.90495	-0.90495	3.4871	-0.9540	22.87	0.1757	0.64633	1.05680	2022	[45]
GWO	-1.17592	-1.1759	3.3486	-0.9540	21.93	0.1755	0.64448	1.057000	2022	[45]
SOGWO	-1.1759	-1.1759	3.34861	-0.9540	21.93	0.1755	0.64448	1.05702	2022	[45]
DA	-1.07150	-1.0715	3.55304	-0.9540	23.0	0.1743	0.72377	1.05724	2022	[45]
ASO	-0.9940	-0.9940	3.40927	-0.9540	21.142	0.1751	0.64766	1.05724	2022	[45]
ALO	-1.10334	-1.1033	4.1130	-0.954	22.722	0.173	0.76773	1.05895	2022	[45]
SSO	-1.03331	3.72	9.57	-9.58	14.301	0.799	0.01421	0.09681	2021	[34]
ALO	-0.9438	3.4734	9.7898	1.1811	24.0	0.0136	0.03000	1.15130	2019	[44]
FPA	−0.85320	31.0	9.15	−0.954	13.00	0.571	0.01455	0.15982	2019	[59]
ABC	-1.082	3.4956	7.5015	-0.954	24	0.1711	0.17882	0.70821	-	This study
SFLA	-0.9569	3.10183	7.45219	-0.954	24	0.171489	0.10000	0.70800	-	This study
FA	-1.0882	3.7288	8.8773	-0.954	24	0.17149	0.10001	0.70800	-	This study
MFO	-1.1733	3.18622	3.66397	-0.954	10	0.171487	0.10001	0.70801	-	This study
MFORS	**-1.1103**	**3.1041**	**3.75906**	**-0.954**	**15.532**	**0.2246**	**0.35008**	**0.09503**	**-**	**This study (proposed)**

As shown in Table 3, the proposed MFORS could achieve the best results compared with the other algorithms. The average time to obtain parameters by the MFORS algorithm is 809 seconds. Current-

Voltage dataset values, together with results of estimated voltage ($V_{measured}$) and SSE values obtained by proposed MFORS, are given in Table 4.

Table 4. *The I/V datasets of SR-12 found by the MFORS and voltage stack*

Sampling number	I_{stack} / A	$V_{measured}$ / V	V_{stack} / V	$(V_{measured} - V_{stack})^2$ / V^2
1	0	41.7791	42.1705	0.1532
2	1.0188	41.1145	41.2848	0.0290
3	1.9303	40.5010	40.6568	0.0243
4	2.9491	40.0409	40.0512	0.0001
5	3.9678	39.6319	39.5069	0.0156
6	4.9330	38.9162	39.0276	0.0124
7	6.0054	38.5583	38.5228	0.0013
8	6.8633	38.1493	38.1335	0.0003
9	7.9893	37.8425	37.6357	0.0427
10	8.9544	37.3824	37.2171	0.0273
11	9.8659	36.8712	36.8256	0.0021
12	10.9383	36.2065	36.3674	0.0259
13	11.9035	35.9509	35.9551	0.0000
14	12.9759	35.4397	35.4950	0.0031
15	13.8874	35.2352	35.1010	0.0180
16	14.9598	34.7239	34.6322	0.0084
17	15.8713	34.1616	34.2281	0.0044
18	16.9437	34.1104	33.7446	0.1338
19	17.9088	33.3947	33.3006	0.0089
20	18.8204	33.0368	32.8725	0.0270
21	19.8928	32.5256	32.3563	0.0287
22	20.9651	31.9632	31.8250	0.0191
23	21.9303	31.5031	31.3320	0.0293
24	22.9491	30.9918	30.7947	0.0388
25	23.9142	30.0716	30.2678	0.0385
26	24.9866	29.4581	29.6596	0.0406
27	26.0054	29.3047	29.0567	0.0615
28	27.0241	27.7710	28.4266	0.4298
29	27.9893	27.3108	27.8011	0.2404
30	28.9544	27.3620	27.1447	0.0472
31	30.0268	26.9530	26.3740	0.3353
32	30.9383	26.0838	25.6799	0.1631
33	31.9035	24.3967	24.9003	0.2536
34	32.9759	23.0164	23.9716	0.9125
35	34.0483	22.9952	22.9657	0.0009
36	34.9598	21.9916	22.0384	0.0022
37	35.9786	21.4871	20.9074	0.3360
SSE				**0.095037**

Case study 2: Ballard Mark V FC

In this section, simulation has been done for Ballad Mark V FC, made by the Canadian company, with a rated power of 5 kW and operating conditions are T = 343 K, P_{H_2}=101 kPa (1 atm), P_{O_2} = 101 kPa (1 atm), N_s = 1, and J_{max} = 1500 mA/cm^2 [46,58]. Table 5 shows the optimal results obtained *via* the proposed and other algorithms [21].

The simulation results and experimental polarization curves *I-V* data for the SR-12 modular PEM generator and Ballard Mark V FC are illustrated in Figures 6 and 7. These results show that the model obtained by the proposed MFORS matches well with the experimental data. Figures 8 and 9 show convergence curves of MFORS and other algorithms for minimizing SSE. The algorithms studied in Table 5 are as follows: Whale optimization algorithm (WOA) [37], Grasshopper optimizer (GHO) [37], Enhanced transient search optimization (ETSO) [20], Lightning search algorithm (LSA) [60], Dandelion optimizer (DO) [61], Artificial rabbits optimization (ARO) [62], Transient search optimization (ETSO)

[20], Harris hawks optimization (HHO) [20], Artificial bee colony (ABC), Shuffled frog-leaping algorithm (SFLA), Firefly algorithm (FA), Moth-flame optimization (MFO).

These results show that the convergence behavior of MFO is improved by using the RS algorithm, showing that MFORS could converge to better results. The average time to obtain parameters by the MFORS algorithm is 455 seconds. Furthermore, we ran the algorithm many times. When the obtained solution did not change much during different runs, the data variance was low and better results could be achieved from other algorithms. This shows the robustness of the algorithm, which is an advantage of RS in the proposed algorithm.

Table 5*. The optimal parameters for different algorithms of Ballard V Fc*

Algorithm	ξ_1	$\xi_2\times10^3$	$\xi_3\times10^5$	$\xi_4\times10^4$	λ	b / V	R_c / mΩ	SSE	Year	Ref.
WOA	-1.1978	4.4183	9.72	-16.27	23.0	1.002	0-1002	0.8537	2019	[37]
GHO	-0.8532	3.4173	9.8	-15.95	22.84	1.000	0.1000	0.871	2019	[37]
ETSO	-0.8534	2.5591	3.61	-16.28	23.0	1.000	0.1000	0.8536	2022	[20]
LSA	-1.0624	3.597	6.65	-16.49	23.00	1.030	0.1030	0.8140	2022	[60]
DO	-0.8532	2.8687	5.93	-14.75	23.00	1.000	0.1000	0.8092	2023	[61]
ARO	-1.1588	3.5208	4.05	-16.72	23.99	1.000	0.1000	0.81391	2023	[62]
TSO	-0.8741	3.0843	7.96	-9.77	2.713	7.636	0.7636	1.721	2022	[20]
HHO	-1.0098	3.492	7.82	-11.00	22.98	5.5000	0.5500	1.418	2022	[20]
ABC	-1.1985	1.5000	0.0001	-1.19	24	1.000	0.1000	1.7426	-	This study
SFLA	-1.1077	1.4505	8.73	-1.03	19.97	1.944	0.1944	2.0138	-	This study
FA	-1.0876	1.4408	8.62	-1.17	19.21	3.053	0.3053	2.9369	-	This study
MFO	-1.0768	1.2329	7.83	-1.02	18.55	2.532	0.2532	1.9731	-	This study
MFORS	**-1.0593**	**2.9279**	**3.737**	**-1.3920**	**23.025**	**1.1815**	**0.1002**	**0.01802**	**-**	**This study (proposed)**

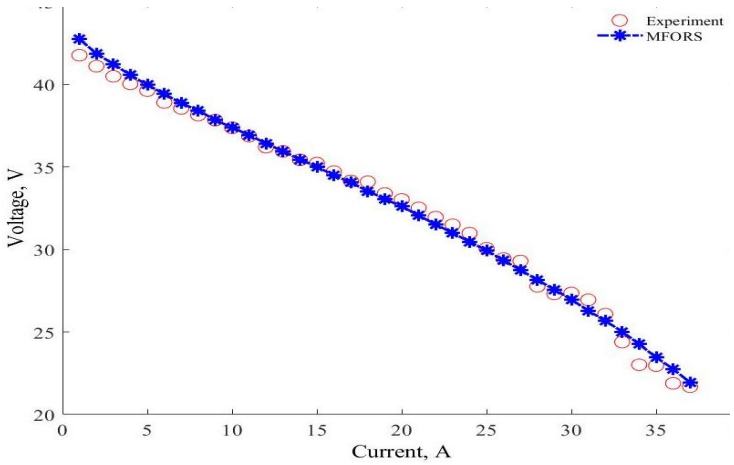

Figure 6. I-V *characteristic for experimental and simulation results of sr-12 problem*

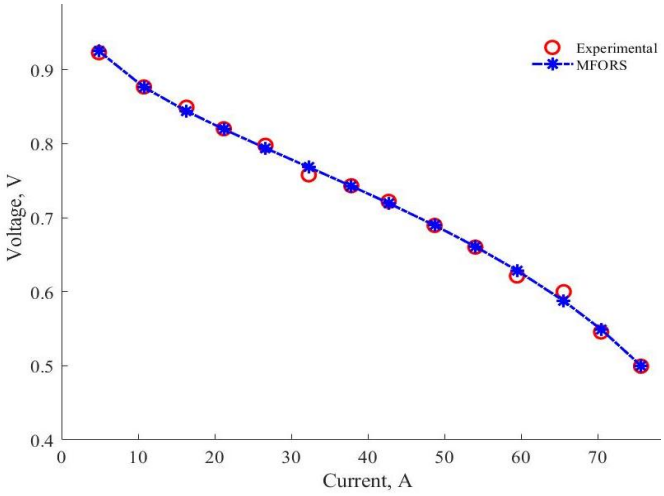

Figure 7*.* I-V *characteristic for experimental and simulation results of Ballard V FC*

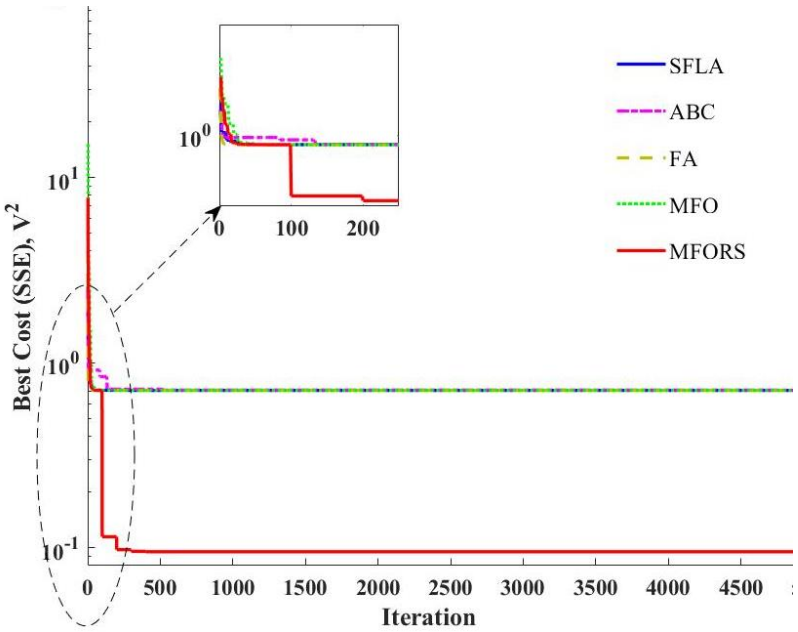

***Figure 8**. The convergence behavior of MFO and proposed MFORS for SR-12*

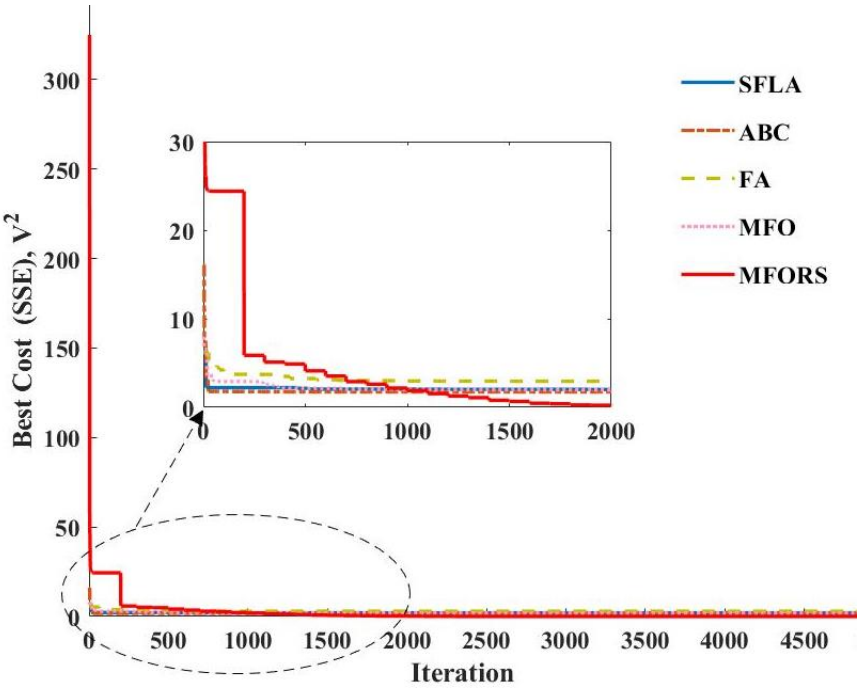

***Figure 9.** The convergence behavior of MFO and proposed MFORS for Ballard V FC*

Conclusion

An accurate mathematical model of the FC system is suitable for control, evaluation, simulation and optimal operation of the FC system. However, the I-V characteristic of FC is nonlinear and an optimization algorithm is needed to find optimal parameters of its model. In this study, a new hybrid optimized algorithm called moth flame optimization-random search (MFORS) was proposed to identify the optimal parameters of PEMFC. This algorithm used the power of MFO in global exploration and the advantage of RS in the exploitation of the search space around the solutions. Simulation results showed that the proposed algorithm could achieve less SSE in comparison with the other algorithms. Based on the performance of this algorithm, using MFORS for complex energy problems, such as optimization in active distribution with microgrids, is proposed for future works.

Another direction for future work is considering uncertainty in modeling energy systems and adopting MFORS to solve these problems.

***Acknowledgements**: This work has been financially supported by the University of Torbat Heydarieh. The grant number is UTH1401/10/05147.*

***Conflicts of interest**: The authors have no potential conflict of interest.*

References

[1] M. K. Singla, P. Nijhawan, A. S. Oberoi, Hydrogen fuel and fuel cell technology for cleaner future: a review, *Environmental Science and Pollution Research* **28** (2021) 15607-15626. https://doi.org/10.1007/s11356-020-12231-8

[2] S. Turkdogan, Design and optimization of a solely renewable based hybrid energy system for residential electrical load and fuel cell electric vehicle, *Engineering Science and Technology, an International Journal* **24** (2021) 397-404. https://doi.org/10.1016/j.jestch.2020.08.017

[3] Z. Zakaria, S. K. Kamarudin, K. A. Abd Wahid, S. H. A. Hassan, The progress of fuel cell for malaysian residential consumption: Energy status and prospects to introduction as a renewable power generation system, *Renewable and Sustainable Energy Reviews* **144** (2021) 110984. https://doi.org/10.1016/j.rser.2021.110984

[4] Z. Zakaria, S. K. Kamarudin, K. A. A. Wahid, Fuel cells as an advanced alternative energy source for the residential sector applications in Malaysia, *International Journal of Energy Research* **45** (2021) 5032-5057. https://doi.org/10.1002/er.6252

[5] E. El-Hay, M. El-Hameed, A. El-Fergany, Optimized parameters of SOFC for steady state and transient simulations using interior search algorithm, *Energy* **166** (2019) 451-461. https://doi.org/10.1016/j.energy.2018.10.038

[6] A. A. El-Fergany, Electrical characterisation of proton exchange membrane fuel cells stack using grasshopper optimiser, *IET Renewable Power Generation* **12** (2018) 9-17. https://doi.org/10.1049/iet-rpg.2017.0232

[7] X. Cai, D. Wu, J. Sun, B. Chen, The effect of cathode channel blockages on the enhanced mass transfer and performance of PEMFC, *Energy* **222** (2021) 119951. https://doi.org/10.1016/j.energy.2021.119951

[8] A. Fathy, H. Rezk, H. S. M. Ramadan, Recent moth-flame optimizer for enhanced solid oxide fuel cell output power via optimal parameters extraction process, *Energy* **207** (2020) 118326. https://doi.org/10.1016/j.energy.2020.118326

[9] A. Abdullah, H. Rezk, A. Hadad, M. Hassan, A. Mohamed, Optimal parameter estimation of proton exchange membrane fuel cells, *Intelligent Automation & Soft Computing* **29** (2021) 619-631. https://doi.org/10.32604/iasc.2021.018289

[10] R. Ben Messaoud, Parameters determination of proton exchange membrane fuel cell stack electrical model by employing the hybrid water cycle moth-flame optimization algorithm, *International Journal of Energy Research* **45** (2021) 4694-4708. https://doi.org/10.1002/er.6065

[11] R. B. Messaoud, A. Midouni, S. Hajji, PEM fuel cell model parameters extraction based on moth-flame optimization, *Chemical Engineering Science* **229** (2021) 116100. https://doi.org/10.1016/j.ces.2020.116100

[12] A. A. Z. Diab, H. Ali, H. Abdul-Ghaffar, H. A. Abdelsalam, M. Abd El Sattar, Accurate parameters extraction of PEMFC model based on metaheuristics algorithms, *Energy Reports* **7** (2021) 6854-6867. https://doi.org/10.1016/j.egyr.2021.09.145

[13] E. H. Houssein, B. E. Helmy, H. Rezk, A. M. Nassef, An enhanced Archimedes optimization algorithm based on Local escaping operator and Orthogonal learning for PEM fuel cell parameter identification, *Engineering Applications of Artificial Intelligence* **103** (2021) 104309. https://doi.org/10.1016/j.engappai.2021.104309

[14] H. Rezk, S. Ferahtia, A. Djeroui, A. Chouder, A. Houari, M. Machmoum, M. A. Abdelkareem, Optimal parameter estimation strategy of PEM fuel cell using gradient-based optimizer, *Energy* **239** (2022) 122096. https://doi.org/10.1016/j.energy.2021.122096

[15] M. Kandidayeni, A. Macias, A. Khalatbarisoltani, L. Boulon, S. Kelouwani, Benchmark of proton exchange membrane fuel cell parameters extraction with metaheuristic optimization algorithms, *Energy* **183** (2019) 912-925. https://doi.org/10.1016/j.energy.2019.06.152
[16] K. Priya, N. Rajasekar, Application of flower pollination algorithm for enhanced proton exchange membrane fuel cell modelling, *International Journal of Hydrogen Energy* **44** (2019) 18438-18439. https://doi.org/10.1016/j.ijhydene.2019.05.022
[17] S. Xu, X. Wang, Z. Wang, Parameter estimation of proton exchange membrane fuel cells using eagle strategy based on JAYA algorithm and Nelder-Mead simplex method, *Energy* **173** (2019) 457-467. https://doi.org/10.1016/j.energy.2019.02.106
[18] A. Fathy, M. A. Elaziz, A. G. Alharbi, A novel approach based on hybrid vortex search algorithm and differential evolution for identifying the optimal parameters of PEM fuel cell, *Renewable Energy* **146** (2020) 1833-1845. https://doi.org/10.1016/j.renene.2019.08.046
[19] X. Chen, N. Wang, Cuckoo search algorithm with explosion operator for modeling proton exchange membrane fuel cells, *International Journal of Hydrogen Energy* **44** (2019) 3075-3087. https://doi.org/10.1016/j.ijhydene.2018.11.140
[20] H. M. Hasanien, M. A. Shaheen, R. A. Turky, M. H. Qais, S. Alghuwainem, S. Kamel, M. Tostado-Véliz, F. Jurado, Precise modeling of PEM fuel cell using a novel Enhanced Transient Search Optimization algorithm, *Energy* **247** (2022) 123530. https://doi.org/10.1016/j.energy.2022.123530
[21] M. Abdel-Basset, R. Mohamed, A. El-Fergany, R. K. Chakrabortty, M. J. Ryan, Adaptive and efficient optimization model for optimal parameters of proton exchange membrane fuel cells: A comprehensive analysis, *Energy* **233** (2021) 121096. https://doi.org/10.1016/j.energy.2021.121096
[22] S. Mirjalili, Moth-flame optimization algorithm: A novel nature-inspired heuristic paradigm, *Knowledge-Based Systems* **89** (2015) 228-249. https://doi.org/10.1016/j.knosys.2015.07.006
[23] P. Singh, S. Bishnoi, Modified moth-Flame optimization for strategic integration of fuel cell in renewable active distribution network, *Electric Power Systems Research* **197** (2021) 107323. https://doi.org/10.1016/j.epsr.2021.107323
[24] M. Talaat, A. Alblawi, M. Tayseer, M. Elkholy, FPGA control system technology for integrating the PV/wave/FC hybrid system using ANN optimized by MFO techniques, *Sustainable Cities and Society* **80** (2022) 103825. https://doi.org/10.1016/j.scs.2022.103825
[25] X. Zhang, P. Wang, H. Yang, Q. Cui, Optimal dispatching of microgrid based on improved moth-flame optimization algorithm based on sine mapping and Gaussian mutation, *Systems Science & Control Engineering* **10** (2022) 115-125. https://doi.org/10.1080/21642583.2022.2042424
[26] A. A. Zhigljavsky, *Theory of global random search*, Springer Science & Business Media, 2012, 9401134367. https://doi.org/10.1007/978-94-011-3436-1
[27] M. Abdel-Basset, R. Mohamed, M. Elhoseny, R. K. Chakrabortty, M. J. Ryan, An efficient heap-based optimization algorithm for parameters identification of proton exchange membrane fuel cells model: Analysis and case studies, *International Journal of Hydrogen Energy* **46** (2021) 11908-11925. https://doi.org/10.1016/j.ijhydene.2021.01.076
[28] Q. Niu, H. Zhang, K. Li, An improved TLBO with elite strategy for parameters identification of PEM fuel cell and solar cell models, *International Journal of Hydrogen Energy* **39** (2014) 3837-3854. https://doi.org/10.1016/j.ijhydene.2013.12.110
[29] S. Yang, R. Chellali, X. Lu, L. Li, C. Bo, Modeling and optimization for proton exchange membrane fuel cell stack using aging and challenging P systems based optimization algorithm, *Energy* **109** (2016) 569-577. https://doi.org/10.1016/j.energy.2016.04.093
[30] D. Yousri, S. Mirjalili, J. T. Machado, S. B. Thanikanti, A. Fathy, Efficient fractional-order modified Harris hawks optimizer for proton exchange membrane fuel cell modeling, *Engineering Applications of Artificial Intelligence* **100** (2021) 104193. https://doi.org/10.1016/j.engappai.2021.104193
[31] H. Rezk, A. Olabi, S. Ferahtia, E. T. Sayed, Accurate parameter estimation methodology applied to model proton exchange membrane fuel cell, *Energy* **255** (2022) 124454. https://doi.org/10.1016/j.energy.2022.124454
[32] E. A. Gouda, M. F. Kotb, A. A. El-Fergany, Investigating dynamic performances of fuel cells using pathfinder algorithm, *Energy Conversion and Management* **237** (2021) 114099. https://doi.org/10.1016/j.enconman.2021.114099

[33] H. M. Sultan, A. S. Menesy, S. Kamel, A. Selim, F. Jurado, Parameter identification of proton exchange membrane fuel cells using an improved salp swarm algorithm, *Energy Conversion and Management* **224** (2020) 113341. https://doi.org/10.1016/j.enconman.2020.113341
[34] X. Zhu, N. Yousefi, Optimal parameter identification of PEMFC stacks using adaptive sparrow search algorithm, *International Journal of Hydrogen Energy* **46** (2021) 9541-9552. https://doi.org/10.1016/j.ijhydene.2020.12.107
[35] I. Alsaidan, M. A. Shaheen, H. M. Hasanien, M. Alaraj, A. S. Alnafisah, A PEMFC model optimization using the enhanced bald eagle algorithm, *Ain Shams Engineering Journal* **13** (2022) 101749. https://doi.org/10.1016/j.asej.2022.101749
[36] M. K. Singla, P. Nijhawan, A. S. Oberoi, Parameter estimation of proton exchange membrane fuel cell using a novel meta-heuristic algorithm, *Environmental Science and Pollution Research* **28** (2021) 34511-34526. https://doi.org/10.1007/s11356-021-13097-0
[37] A. A. El-Fergany, H. M. Hasanien, A. M. Agwa, Semi-empirical PEM fuel cells model using whale optimization algorithm, *Energy Conversion and Management* **201** (2019) 112197. https://doi.org/10.1016/j.enconman.2019.112197
[38] O. Hachana, Accurate PEM fuel cells parameters estimation using hybrid artificial bee colony differential evolution shuffled complex optimizer, *International Journal of Energy Research* **46** (2022) 6383-6405. https://doi.org/10.1002/er.7576
[39] O. Hachana, A. A. El-Fergany, Efficient PEM fuel cells parameters identification using hybrid artificial bee colony differential evolution optimizer, *Energy* **250** (2022) 123830. https://doi.org/10.1016/j.energy.2022.123830
[40] H. M. Sultan, A. S. Menesy, S. Kamel, M. Tostado-Véliz, F. Jurado, Parameter Identification of Proton Exchange Membrane Fuel Cell Stacks Using Bonobo Optimizer, *2020 IEEE International Conference on Environment and Electrical Engineering and 2020 IEEE Industrial and Commercial Power Systems Europe (EEEIC/I&CPS Europe)*, 2020, pp. 1-7. https://doi.org/10.1109/EEEIC/ICPSEurope49358.2020.9160597
[41] E. A. Gouda, M. F. Kotb, A. A. El-Fergany, Jellyfish search algorithm for extracting unknown parameters of PEM fuel cell models: Steady-state performance and analysis, *Energy* **221** (2021) 119836. https://doi.org/10.1016/j.energy.2021.119836
[42] A. S. Menesy, H. M. Sultan, A. Korashy, F. A. Banakhr, M. G. Ashmawy, S. Kamel, Effective parameter extraction of different polymer electrolyte membrane fuel cell stack models using a modified artificial ecosystem optimization algorithm, *IEEE Access* **8** (2020) 31892-31909. https://doi.org/10.1109/ACCESS.2020.2973351
[43] A. A. Z. Diab, M. A. Tolba, A. G. A. El-Magd, M. M. Zaky, A. M. El-Rifaie, Fuel cell parameters estimation via marine predators and political optimizers, *IEEE Access* **8** (2020) 166998-167018. https://doi.org/10.1109/ACCESS.2020.3021754
[44] X. Rao, Z. Shao, A. H. Ahangarnejad, E. Gholamalizadeh, B. Sobhani, Shark Smell Optimizer applied to identify the optimal parameters of the proton exchange membrane fuel cell model, *Energy Conversion and Management* **182** (2019) 1-8. https://doi.org/10.1016/j.enconman.2018.12.057
[45] A. A. Z. Diab, H. I. Abdul-Ghaffar, A. A. Ahmed, H. A. Ramadan, An effective model parameter estimation of PEMFCs using GWO algorithm and its variants, *IET Renewable Power Generation* **16** (2022) 1380-1400. https://doi.org/10.1049/rpg2.12359
[46] J. M. Corrêa, F. A. Farret, L. . Canha, M. G. Simoes, An electrochemical-based fuel-cell model suitable for electrical engineering automation approach, *IEEE Transactions on Industrial Electronics* **51** (2004) 1103-1112. https://doi.org/10.1109/TIE.2004.834972
[47] A. Askarzadeh, L. dos Santos Coelho, A backtracking search algorithm combined with Burger's chaotic map for parameter estimation of PEMFC electrochemical model, *International Journal of Hydrogen Energy* **39** (2014) 11165-11174. https://doi.org/10.1016/j.ijhydene.2014.05.052
[48] J. M. Correa, F. A. Farret, V. A. Popov, M. G. Simoes, Sensitivity analysis of the modeling parameters used in simulation of proton exchange membrane fuel cells, *IEEE Transactions on Energy Conversion* **20** (2005) 211-218. https://doi.org/10.1109/TEC.2004.842382
[49] R. F. Mann, J. C. Amphlett, M. A. Hooper, H. M. Jensen, B. A. Peppley, P. R. Roberge, Development and application of a generalised steady-state electrochemical model for a PEM fuel cell, *Journal of Power Sources* **86** (2000) 173-180. https://doi.org/10.1016/S0378-7753(99)00484-x

[50] H. Saleem, S. Karmalkar, An Analytical Method to Extract the Physical Parameters of a Solar Cell From Four Points on the Illuminated J-V Curve, *IEEE Electron Device Letters* **30** (2009) 349-352. https://doi.org/10.1109/LED.2009.2013882
[51] Z. B. Zabinsky, *Stochastic adaptive search for global optimization*, Springer Science & Business Media, 2013, 1441991824. https://doi.org/10.1007/978-1-4419-9182-9
[52] J. Feng, W. Z. Shen, Optimization of Wind Farm Layout: A Refinement Method by Random Search, *International Conference on aerodynamics of Offshore Wind Energy Systems and wakes (ICOWES 2013)*, 2013, pp. 624-633.
[53] S. Z. Ramadan, *A Hybrid Global Optimization Method Based on Genetic Algorithm and Shrinking Box*, Modern Applied Science **10** (2016) 67-82. https://doi.org/10.5539/mas.v10n2p67
[54] M. Anfal, H. Abdelhafid, Optimal Placement of PMUs in Algerian Network using a Hybrid Particle Swarm–Moth Flame Optimizer (PSO-MFO), *Electrotehnica, Electronica, Automatica* **65** (2017) 191-196. https://www.researchgate.net/publication/320144224_Optimal_placement_of_PMUS_in_algerian_network_using_a_hybrid_particle_swarm-moth_flame_optimizer_PSO-MFO
[55] H. Zhao, H. Zhao, S. Guo, Using GM (1, 1) Optimized by MFO with rolling mechanism to forecast the electricity consumption of Inner Mongolia, *Applied Sciences* **6** (2016) 20. https://doi.org/10.3390/app6010020
[56] L. Zhang, K. Mistry, S. C. Neoh, C. P. Lim, *Intelligent facial emotion recognition using moth-firefly optimization*, Knowledge-Based Systems **111** (2016) 248-267. https://doi.org/10.1016/j.knosys.2016.08.018
[57] X. Wang, Modeling of two-phase transport in the diffusion media of polymer electrolyte fuel cells, *Journal of Power Sources* **185** (2008) 261-271. https://doi.org/10.1016/j.jpowsour.2008.07.007
[58] A. Askarzadeh, Parameter estimation of fuel cell polarization curve using BMO algorithm, *International Journal of Hydrogen Energy* **38** (2013) 15405-15413. https://doi.org/10.1016/j.ijhydene.2013.09.047
[59] K. Priya, N. Rajasekar, Application of flower pollination algorithm for enhanced proton exchange membrane fuel cell modelling, *International Journal of Hydrogen Energy* **44** (2019) 18438-18449. https://doi.org/10.1016/j.ijhydene.2019.05.022
[60] B. Mohanty, R. Madurai Elavarasan, H. M. Hasanien, E. Devaraj, R. A. Turky, R. Pugazhendhi, Parameters Identification of Proton Exchange Membrane Fuel Cell Model Based on the Lightning Search Algorithm, *Energies* **15** (2022) 7893. https://doi.org/10.3390/en15217893
[61] S. A. Mujeer, X. Chandrasekhar, M. S. Kumari, S. R. Salkuti, An accurate method for parameter estimation of proton exchange membrane fuel cell using Dandelion optimizer, *International Journal of Emerging Electric Power Systems* (2023). https://doi.org/10.1515/ijeeps-2023-0025
[62] A. J. Riad, H. M. Hasanien, R. A. Turky, A. H. Yakout, Identifying the PEM Fuel Cell Parameters Using Artificial Rabbits Optimization Algorithm, *Sustainability* **15** (2023) 4625. https://doi.org/10.3390/su15054625a

J. Electrochem. Sci. Eng. **14(2)** (2024) 193-212; http://dx.doi.org/10.5599/jese.2136

Open Access : : ISSN 1847-9286
www.jESE-online.org

Original scientific paper

Anticorrosive characteristics of imidazole derivative on carbon steel in 1 M HCl

Asma Barrahi[1], Mohamed El Faydy[2], Loubna Adlani[3], Fouad Benhiba[1,4], Danil R. Bazanov[5], Natalia A. Lozinskaya[5], Mohamed Maatallah[6], Ismail Warad[7], Burak Dikici[8], Abdelkbir Bellaouchou[1], Abdelkader Zarrouk[1,✉]

[1]*Laboratory of Materials, Nanotechnology and Environment, Faculty of Sciences, Mohammed V University in Rabat, P.O. Box. 1014, Rabat, Morocco*
[2]*Laboratory of Organic Chemistry, Inorganic, Electrochemistry, and Environment, Faculty of Sciences, Ibn Tofaïl University, PO Box 133, 14000, Kenitra, Morocco*
[3]*Laboratory of Advanced Materials and Process Engineering, Faculty of Sciences, Ibn Tofail University, P.O. Box. 133, 14000 Kenitra, Morocco*
[4]*Higher Institute of Nursing Professions and Health Techniques of Agadir Annex Guelmim, Morocco*
[5]*Department of Chemistry, Lomonosov Moscow State University, 119991 Moscow, Russia*
[6]*Laboratory of Molecular Chemistry, Faculty of Sciences Semlalia, Cadi Ayyad University, PO Box 2390, Marrakech, Morocco*
[7]*Department of Chemistry, AN-Najah National University, P.O. Box 7, Nablus, Palestine*
[8]*Ataturk University, Department of Mechanical Engineering, 25240 Erzurum, Turkey*

Corresponding author: ✉azarrouk@gmail.com

Received: October 17, 2023; Accepted: February 21, 2024; Published: April 2, 2024

Abstract

The novelty of the work is to scrutinize for the first time the 4R,5S- 2,4,5-tris(4-ethoxy-phenyl)-4,5-dihydro-1H-imidazole (TEPI) as a corrosion inhibitor for carbon steel (C35E) in the acidic medium. The inhibitory properties of TEPI were assessed through various methods, including electrochemical, spectroscopic, and surface analysis, as well as quantum chemical calculations. The protective effect of C35E was seen to expand as the TEPI amount was extended but to diminish as temperature was augmented, fulfilling 98.3 % at 1 mM under 303 K. Certain thermodynamic and kinetic indices were estimated and explored. The TEPI complied with the Langmuir adsorption isotherm when it adsorbs on the C35E surface. TEPI behaviour was revealed by polarization trials to be of mixed type. The establishment of an adsorption-linked preventive TEPI layer on the C35E surface has been disclosed thanks to surface analysis. The outcomes of scanning electron microscopy coupled with energy dispersive X-ray spectroscopy clearly illustrate that TEPI can efficiently adsorb at the C35E interface, substantially reducing C35E steel corrosion. UV-visible analysis of the inhibited electrolyte clearly reveals the complexation of iron cations with TEPI molecules. The density functional theory (DFT), Monte Carlo(MC) and

molecular dynamic simulation (MDS) were adopted to check out the adsorption characteristics of the TEPI onto C35E surface. The laboratory outcomes have been proven by DFT and MDS.

Keywords
Corrosion inhibition; C35E steel; electrochemical methods; surface analysis; quantum chemistry calculations

Introduction

Corrosion is an electrochemical process that occurs between metallic materials and the environment, resulting in metal dissolution, process contamination, environmental damage, and economic losses [1,2]. Corrosion impacts a wide range of materials, from integrated circuits to reinforced concrete bridges. Metallic materials, and especially carbon steel, which are the primary building blocks for many structures, are highly susceptible to corrosion when they come into contact with moist environments, are submerged in fresh or salt water, or are in the presence of more or less corrosive solutions [3,4]. The assistance life of supported concrete structures has been extended by the development of numerous innovative materials and technologies. These methods, such as chloride extraction, cathodic protection, protective coatings and sealants, significant re-legalization, and corrosion inhibitor pinnacles, can prevent and reduce steel consumption in concrete.

One of the most efficacious, beneficial, dynamic, and financially rewarding strategies for preventing metal rust is the benefit of organic inhibitors [5,6]. Organic substances with heteroatoms of oxygen, nitrogen, and sulfur often enclose the ability to prevent rusting [7-12]. Organic compounds possess unshared electrons in bonds of π and heteroatoms that can be readily given to a metal vacant d orbital, rendering them effective inhibitors.

Imidazole and its derivatives are extensively used in the treatment of bacterial, viral, inflammatory, and cancerous conditions [13,14]. Furthermore, it has been proven that imidazole possesses outstanding corrosion inhibition capabilities for concrete structures. It may function as a corrosion inhibitor to stop environmental corrosion of carbon steel since it contains nitrogen atoms in the imidazole ring and conjugated π-electron system [15,16].

The primary novelty of our study lies in scrutinizing the performance of new imidazole derivatives, namely (4R,5S)-2,4,5-tris(4-ethoxyphenyl)-4,5-dihydro-1H-imidazole (TEPI), that was utilized as an organic inhibitor in acidic medium. To assess the performance of TEPI as an inhibitor and the corrosion rate of C35E, electrochemical methods were used. The C35E surface and its corrosive medium were scrutinized through the combination of scanning electron microscopy (SEM), energy dispersive X-ray spectroscopy (EDX), and UV-vis spectroscopy, respectively. Furthermore, theoretical calculations based on density functional theory (DFT), Monte Carlo (MC), and molecular dynamic (MD) simulation were used to back up the experimental findings.

Experimental

Materials

The material that operated as the working electrode in electrochemical measurements is carbon steel (C35E), and its weight and chemical composition are offered in Table 1. The surface area of C35E samples serving as electrodes was 1 cm^2. After polishing the electrode surface with various grades of Sic paper and prior to being desiccated at ambient temperature, the samples were scoured with distilled water.

By diluting hydrochloric acid of 37 % with distilled water, a corrosive medium of 1M HCl was produced. The concentration range of TEPI was 1 mM to 1000 nM, while its molecular structure is shown in Figure 1.

Table 1. *Chemical composition and element weights of carbon steel C35E*

Element	C	Fe	Ti	Co	S	Ni	Si	Mn	Cr	Cu
Content, wt.%	0.370	Balance	0.011	0.009	0.016	0.059	0.230	0.680	0.077	0.160

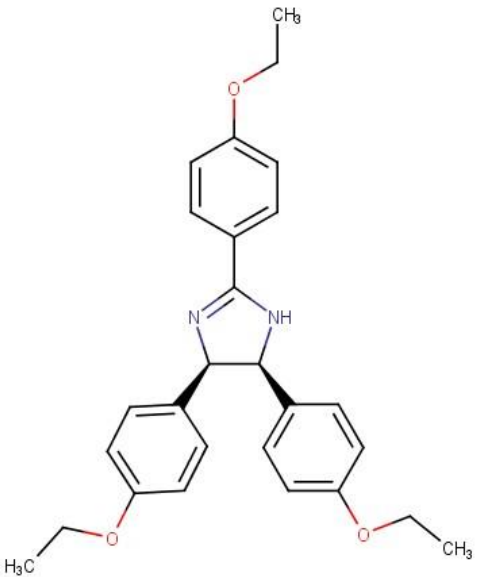

Figure 1. *Molecular structure of 4R,5S)-2,4,5-tris(4-ethoxyphenyl)-4,5-dihydro-1H-imidazole (TEPI)*

Electrochemical measurements

The 3-electrode cell was adopted for the electrochemical exams, with a saturated calomel serving as the reference electrode (SCE), a platinum wire as the auxiliary electrode, and C35E as the working electrode with an area of 1 cm^2. The C35E electrode was first immersed in the test medium for 1800 s to obtain a reliable, steady-state value of open circuit potential (E_{ocp}). After measuring the open circuit potentials, the electrochemical exams took place. The electrochemical impedance spectroscopy (EIS) was conducted at E_{ocp}, in the frequency range between 100 kHz and 10 mHz, and *ac* amplitude of 10 mV peak-to-peak, using 10 points per frequency decade. EIS diagrams were simulated using Z-view. Then, potentiodynamic polarization (PDP) was enrolled at the potential of -800 to -100 mV at a sweep speed of 0.5 mV s^{-1}. Inhibition performances (η / %) taken from EIS and PDP were determined using equations (1) and (2).

$$\eta_{pp} = \left(\frac{i_{corr°} - i_{corr1}}{i_{corr°}} \right) 100 \quad (1)$$

where $i_{corr°}$ and i_{corr1} denote the corrosion current densities before and after TEPI addition.

$$\eta_{EIS} = \left(\frac{R_{p1} - R_{p0}}{R_{p1}} \right) 100 = 100\,\theta \quad (2)$$

where R_{p1} and R_{p0} denote the polarization resistances prior and after TEPI addition, respectively, while θ is the surface coverage degree.

For the uninhibited solution, data from electrochemical measurements were taken from our previously published study [17]. This decision was made as the experiments were conducted under identical conditions and with the same equipment.

Ultraviolet-visible spectroscopy

To better comprehend how the TEPI interacts with the C35E surface in an aggressive medium, as well as the development of iron-TEPI complexes, the inhibited and uninhibited solutions of 1.0 M HCl were subjected to UV-visible spectroscopy employing a JASCO V-700 UV-Visible spectrophotometer before, and after 3 days of C35E submersion.

Combination of scanning electron microscopy and energy dispersive X-ray

The surface morphologies of C35E exposed to 1M HCl medium without and with 0.001M of TEPI for 24 hours at 303 K were investigated by SEM. It normally operates with an EDX unit and an acceleration voltage of 20 kV. SEM results obtained in the absence of the inhibitor were taken from the work already published by our research team [18].

Calculations involving quantum chemistry

Theoretical studies utilizing density functional theory were executed to better apprehend the association among the molecular characteristics of TEPI and their inhibition effectiveness [18,19]. The computation was carried out through the Gaussian 09 prog. package [20] and the DFT technique with the B3LYP functional and 6-31G (d, p) and 6-311G (d, p) basis sets [21-24]. The theoretical descriptors such as the energy of the highest occupied (E_{HOMO}), unoccupied molecular orbital (E_{LUMO}), energy gap (ΔE), electron transferred fractions (ΔN), chemical hardness (η), electronegativity (χ), dipole moment (μ), and polarizability (α) were determined by the application of equations cited in past studies [25,26].

Monte Carlo and molecular dynamic simulations

Materials Studio 8 software was used to evaluate the TEPI adsorption processes on the C35E surface. The Fe (110) surface simulation was carried out by putting the surface crystal in a cell measuring 2.73×2.70×3.71 nm^3 using a 6-couche slab model for each layer, making up an (11×11) unit cell. The liquid phase was made up of 500 H_2O, $5Cl^-$, and $5H_3O^+$. On top of the liquid layer, a 40- vacuum layer was created to prevent interaction between the surface and periodic repeating planes. The simulations were carried out at 303 K under NVT ensemble control using an Andersen thermostat. The simulation was performed by Forcite code in a COMPASS force field for 1000 ps with a time step of 0.1 fs. The diffusion of Cl^-, H_3O^+, and H_2O in inhibitor membranes was also simulated [27,28].

Results and discussion

The polarization curves

Figure 2 depicts the polarization graphs at 303 K prior and after multiple amounts of TEPI added in the 1 M HCl medium. Table 2 supplies details on the relevant extrapolated electrochemical indices, such as corrosion potential (E_{corr}), corrosion current (i_{corr}), and cathodic and anodic Tafel slopes (β_c and β_a). A preliminary analysis of Tafel branches revealed that adding TEPI to the acidic environment lessens both anodic and cathodic current densities, implying that the presence of TEPI limits both C35E dissolving and cathodic hydrogen evolution. Furthermore, it is evident that the inhibitory effect of TEPI on the reduction of hydrogen (H^+) is considerably greater than on the C35E dissolution reaction. It is also noted that the cathodic segments of the polarization current potential curves result in Tafel lines that are nearly parallel. This phenomenon reveals that the process of hydrogen evolution remains unchanged with the addition of TEPI. Most likely, the reduction of

hydrogen ions on the C35E surface takes place mostly through a charge transfer mechanism [29]. In this manner, the surface area available for H^+ ions became reduced while the actual reaction mechanism remains unaltered. Table 2 clarifies that TEPI amounts have a small effect on β_c but a big impact on β_a. Also, the β_a deviations display that TEPI affects the anodic process kinetics. The practically constant values of β_c for TEPI suggest that it was initially adsorbed onto the C35E surface and hindered by simply obstructing the C3E active sites without changing the cathodic mechanism. The E_{corr} value moved in the positive direction after the TEPI was added, and its shift is less than 27.66 mV, inferring that the TEPI performs as a mixed-type corrosion inhibitor [30]. However, as the amount of TEPI rises, the i_{corr} decreases, which could be owing to the TEPI adsorbing on the C35E surface. The inhibition efficiency rose with the TEPI amount, getting 97.7 % at 1 mM imidazole. TEPI offers high performance relative to the imidazoles mentioned in the literature, and this is due to the molecule's high electron densities provoked by the existence of π-electrons in the imidazole and ethoxy phenyl rings and lone pair electrons in nitrogen atoms.

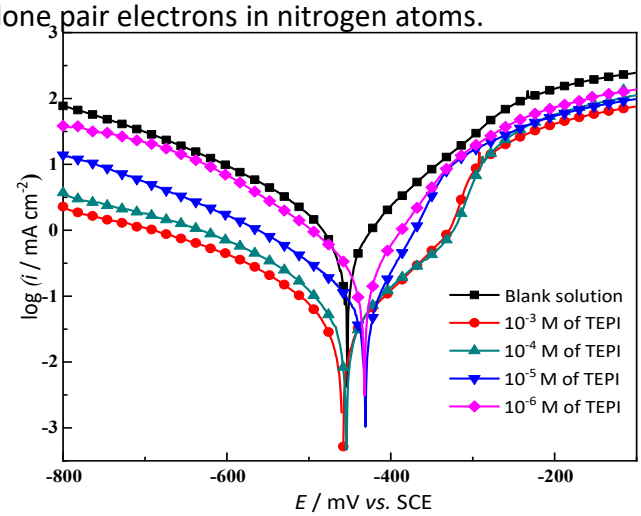

Figure 2. *PDP segments for C35E corrosion in 1 M HCl ahead of and after TEPI addition*

Table 2. *Extrapolated indices for C35E corrosion in 1 M HCl prior and after TEPI addition*

Medium	C / μM	$-E_{corr}$ / mV *vs.* SCE	i_{corr} / μA cm^{-2}	Tafel slopes, mV dec^{-1}		η_{pp} / %
				$-\beta_c$	β_a	
Blank	---	456.3	1104	112	155.4	---
TEPI	1000	457.77	24.61	98.0	83.2	97.7
	100	453.64	38.15	94.0	97.7	96.5
	10	428.64	60.15	98.7	48.3	94.6
	1	431.45	140.53	77.7	50.9	87.3

Electrochemical impedance spectroscopy

The corrosion behavior of C35E in the acidic medium prior and after TEPI addition was investigated by electrochemical impedance spectroscopy (EIS), and its outcomes are displayed in Figure 3. All collected impedance spectra display simply one depressed half-circle bonded to charge transfer during the corrosion process [31], and their size improves with rising TEPI concentration. The impedance loops in Nyquist plots do not produce perfect half-circles, typically ascribed to the roughness of the metal interface and/or frequency dispersion [32]. Comparable capacitive loops might illustrate that, in the lack or presence of TEPI, the charge transfer mechanism controls the electrode reactions. The capacitive loop clearly grows when TEPI is present, showing a strong inhibiting impact of TEPI. A single-phase angle peak can be seen in the Bode graphs (Figure 4), implying a single time constant. The peak amplitude at intermediate frequency becomes more extensive as the concentration of TEPI increases, indicating the adsorption of more TEPI molecules

on the C35E steel surface. This leads to a reduced metal dissolution rate [33]. To derive the EIS information, the EIS spectra were simulated by applying the equivalent circuit portrayed in Figure 3, and the acquired information is tabulated in Table 4. In this circuit, R_s stands for the resistance of the electrolyte solution, CPE denotes the constant phase element characterizing the double-layer capacitance (C_{dl}), while R_p stands for the polarization resistance. To suit the EIS half-circles, CPE has been swapped for C_{dl} [34]:

$$Z_{CPE} = A^{-1} (i\omega)^{-n} \quad (3)$$

where A denotes the coefficient of CPE, n denotes the exponent of CPE (dependent on a degree of surface roughness), i denotes the imaginary unit and ω the angular frequency. As a result, C_{dl} is determined by employing the formula below [34]:

$$C_{dl} = (A\ R_p^{1-n})^{1/n} \quad (4)$$

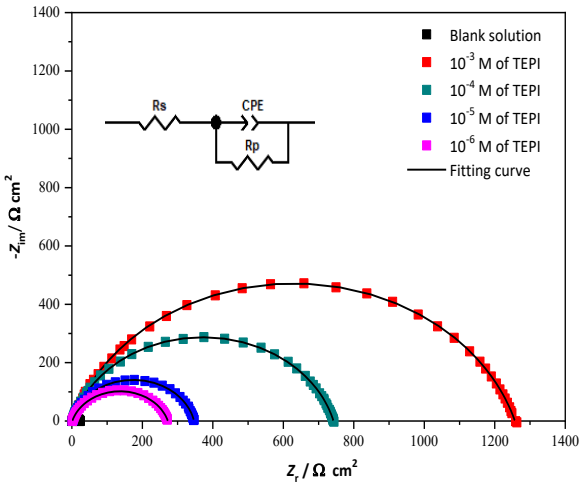

Figure 3. *Nyquist plots of C35E corrosion in 1 M HCl prior and after TEPI addition*

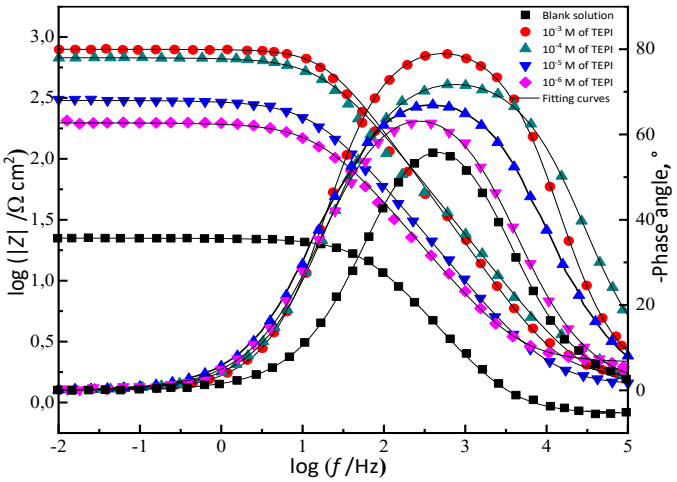

Figure 4. *Bode plots for C35E corrosion in 1 M HCl prior and after TEPI addition*

Table 3 displays that χ^2 (Chi-square is the fitting precision) was close to 0.001, offering that this model provided an outstanding match for the EIS spectra. The R_p values expand with increasing TEPI amounts, whereas the C_{dl} values reflect an opposite trend, which might result from greater coverage on the C35 surface by TEPI adsorption, leading to improved inhibition performance. The diminution in C_{dl} implies a decline of the local dielectric constant and/or growth in the thickness of the electrical double layer, implying that the TEPI molecules perform *via* adsorption on the C35E/solution interface [35]. Furthermore, the readings of n in the presence of TEPI were higher than in the absence of TEPI, signifying growth in the homogeneity of the C35E surface with adsorbed inhibitor [30]. It is clear that the inhibition effectiveness was inhibitor amount dependent, reaching 98.3 % at 0.001 M, proving that TEPI is a potent corrosion inhibitor for C35 in the acidic medium.

Table 3. *EIS factors for C35E corrosion in 1 M HCl prior and after TEPI addition*

	C / μM	R_s / Ω cm^2	R_p / Ω cm^2	C_{dl} / μF cm^{-2}	A / μΩ^{-1} s^n cm^{-2}	n	χ^2	η_{EIS} / %	θ
Blank	0	0.83	21.57	116.2	293.9	0.845	0.002	-	-
TEPI	1000	1.16	1256.0	10.5	22.9	0.880	0.006	98.3	0.983
	100	1.64	741.0	13.7	28.5	0.868	0.009	97.1	0.971
	10	1.82	344.0	33.7	60.2	0.860	0.008	93.7	0.937
	1	1.20	271.0	35.5	81.6	0.859	0.009	92.1	0.921

Temperature influence and activation factors

The temperature has a powerful impact on corrosion rate and inhibitor performance, particularly in acidic medium. Corrosion happens more quickly as the temperature increases. The performance of inhibition of TEPI was investigated at various temperatures varying from 303 to 333 K prior and after the addition of 0.001 M TEPI for examining the mechanism of inhibition and estimating activation factors of the corrosion process by exploiting PDP experimentations presented in Figure 5. The related electrochemical indices are gathered in Table 4.

Figure 5 and data in Table 4 demonstrate that the growth in i_{corr} becomes apparent when the temperature augments prior and after the addition of TEPI and that the improvement in the uninhibited solution is more noticeable when compared to the rise in the inhibited solution, meaning that the temperature rise slows the process of adsorption of TEPI molecules on the C35E surface. The effectiveness only dropped by 5.1 % when TEPI was present in the temperature range, demonstrating the potent inhibitory power of TEPI and its independence from temperature [35].

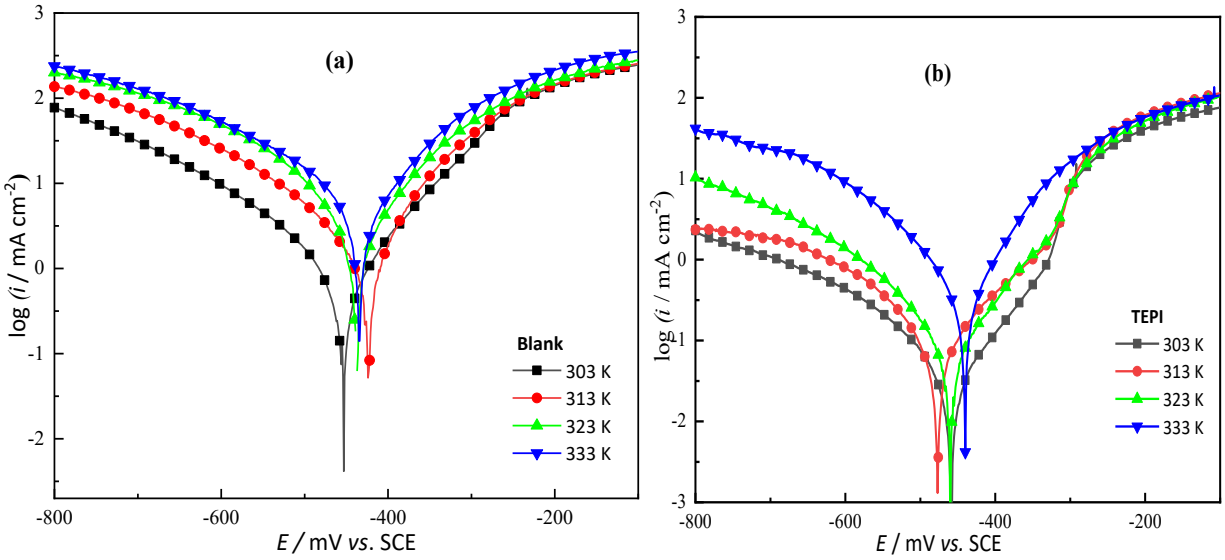

Figure 5. *PDP segments for C35E corrosion in 1 M HCl without (a) and with 1 mM of TEPI (b) under temperatures varying from 303 to 333 K*

Table 4. *PDP factors for C35E corrosion in 1 M HCl without and with 1 mM of TEPI under temperatures varying from 303 to 333 K*

Medium	*T* / K	-E_{corr} / mV *vs.* SCE	i_{corr} / µA cm^{-2}	Tafel slopes, mV dec^{-1}		η_{pp} / %
				-β_c	β_a	
Blank	303	456.3	1104	112	155.4	---
	313	423.5	1477.4	131.3	91.3	-
	323	436.3	2254.0	117.8	91.4	-
	333	433.3	3944.9	134.6	103.9	-
TEPI	303	457.8	24.6	98.0	83.2	97.8
	313	475.5	62.4	100.2	93.3	95.8
	323	441.8	129.6	94.9	90.9	94.2
	333	436.1	287.5	93.1	66.4	92.7

The information on temperature influence was exploited to determine the activation kinetic parameters through Arrhenius and the transition-state relationships, Equations (5) and (6):

$$i_{corr} = A e^{\left(\frac{-E_a}{RT}\right)} \quad (5)$$

$$i_{corr} = \frac{RT}{Nh} e^{\left(\frac{\Delta S_a}{R}\right)} e^{\left(\frac{-\Delta H_a}{RT}\right)} \quad (6)$$

where A denotes the Arrhenius pre-exponential factor, T is temperature, R is the universal gas constant, h denotes the Planck's constant, N denotes the Avogadro number, E_a symbolizes the energy of apparent activation, ΔH_a denotes the enthalpy, and ΔS_a denotes the entropy of apparent activation.

The magnitudes of E_a, ΔS_a, and ΔH_a listed in Table 5 were determined from the slope of Arrhenius plots (Figure 6a) and the intercept and slope of the transition state plots (Figure 6b), respectively.

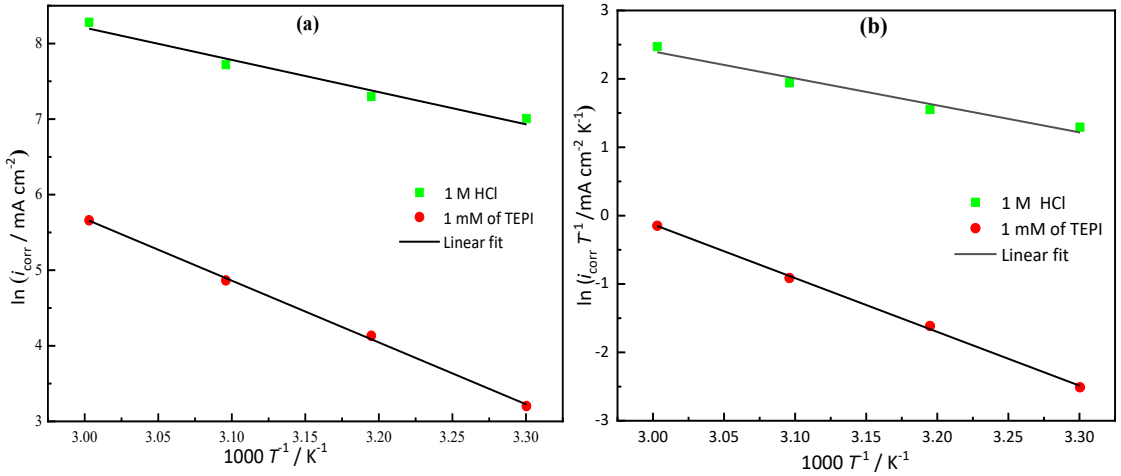

Figure 6. *Arrhenius (a) and transition-state (b) plots for C35E dissolution in 1 M HCl prior and after addition of 1 mM TEPI*

Inspection of Table 5 shows that the magnitude of E_a is augmented when TEPI is present, strongly pointing out that TEPI molecules are fixed to the C35E surface through physical adsorption (electrostatic interactions) [36]. The corresponding magnitude of ΔH_a for TEPI is higher than in its absence, suggesting that the dissolution of C35E becomes slower in the presence of TEPI. Furthermore, the magnitudes of ΔH_a are both positive and reflect the endothermic character of the C35E dissolution process [37,38]. Related magnitudes of ΔS_a for TEPI were negative in its absence or presence in the medium. Besides, the magnitude of ΔS_a for TEPI is higher than in its absence, exhibiting a rise in the disorder during the transformation of the reactants into activated complexes.

Table 5. *E_a, ΔH_a and ΔS_a values for C35E dissolution in 1 M HCl prior and after the addition of 1 mM TEPI*

	E_a / kJ mol^{-1}	ΔH_a / kJ mol^{-1}	ΔS_a / J mol^{-1} K^{-1}
Blank	35.4	32.7	-79.2
TEPI	67.9	65.3	-2.5

Adsorption isotherm

The thermodynamic details of the adsorption process assist in comprehending the inhibition mechanism for an inhibitor on the metal surface. Physical and chemical adsorption are two main kinds of interactions that may characterize molecular adsorption [39]. In this context, the surface coverage values (θ) (defined by Eq. (2)) for different TEPI concentrations can be calculated from the EIS data (Table 3) to present the best adsorption isotherm. Multiple attempts have been undertaken to fit the θ values to adsorption isotherms, including Langmuir, Temkin, and Frumkin, as illustrated in Figure 7. The correlation coefficient (R^2) values and the slopes of the straight lines depicted in Figure 7 remain relatively close to unity for Temkin and Frumkin. At the same time, for Langmuir,

they are equal to unity. Therefore, the Langmuir adsorption isotherm demonstrates the best potential adsorption model of the TEPI molecules onto the C35E surface in the acidic medium, which may be formulated in linear terms as follows [32]:

$$\frac{C}{\theta} = \frac{1}{K_{ads}} + C \quad (7)$$

where K_{ads} denotes the adsorption equilibrium constant.

Equation (8) links K_{ads} value to Gibbs free energy ΔG_{ads}^0 [32]:

$$\Delta G_{ads}^0 = -RT \ln (55.5\ K_{ads}) \quad (8)$$

where R denotes the constant of universal gas and 55.55 stands for H_2O concentration.

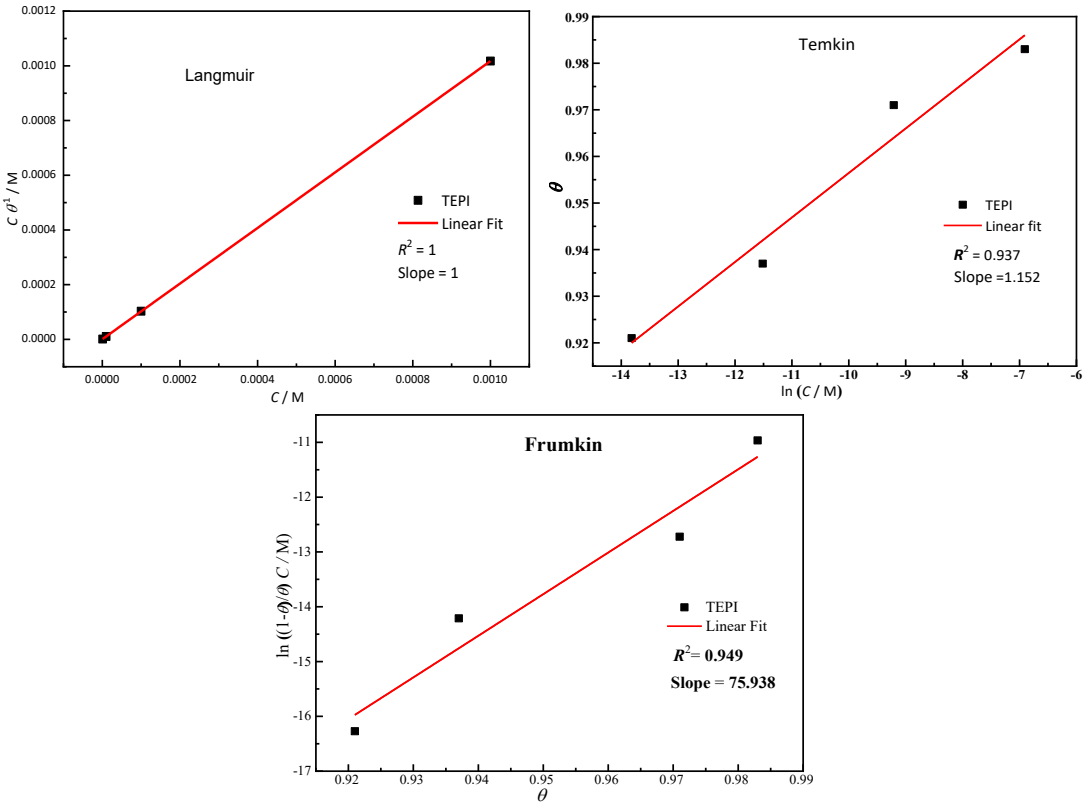

***Figure 7**. Various isotherm models for C35E in 1 M HCl with 1 mM TEPI at 303 K*

The values of ΔG_{ads}^0 and K_{ads} are listed in Table 6. The high magnitude of K_{ads} demonstrates that TEPI molecules adsorb powerfully on the C35E surface [39]. The ΔG_{ads}^0 value means the TEPI molecules are chemisorbed at the C35E surface [40]. The TEPI molecules contributing lone electron pairs and/or electrons and Fe empty orbitals work together to form chemical bonds with Fe unfilled orbitals.

***Table 6.** K_{ads} and ΔG_{ads}^0 for TEPI adsorption*

	K_{ads} / M^{-1}	ΔG_{ads}^0 / kJ mol^{-1}	Slope	R^2
TEPI	1.652×10^6	-46.2	1	1

UV-visible spectroscopy

The complexation process between Fe ions and the inhibiting molecules can be utilized to investigate the underlying mechanism of anticorrosion prevention of carbon steel since Fe is an essential element of C35E. The earlier study, however, revealed that a modification in wavelength with the increase or decrease in absorbance implies the development of a complex involving Fe and molecules present in the corrosive medium [41]. The UV-visible spectrum of TEPI in the acidic

medium prior to C35E submerging showed two absorption bands at 210 and 273 nm because of an n-π* and π-π* electronic transitions, resulting from the heteroatoms lone pair on the pyridine ring (Figure 8). After 3 days of C35E submerging, the bands appeared to have shifted blue (the first to 207 nm and the second to 255 nm), with a rise in absorbance. These modifications occurred probably due to the formation of complexes among Fe^{2+} ions and TEPI species in the acidic medium.

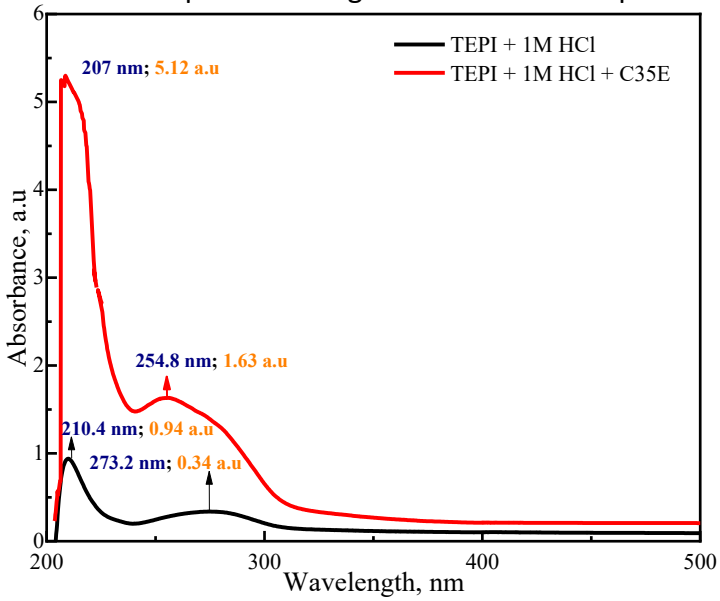

Figure 8. *UV-visible absorption spectra of 1 M HCl containing 0.001M of TEPI prior and after C35E dipping*

SEM/EDX analysis

Figure 9 shows the scanning electron micrographs of C35E samples prior and after 24 h of soaking in 1 M HCl, without and with 1 mM of TEPI at 303 K. Figure 9a1 displays the polished steel sample without flaws other than polishing scratches. In Figure 9b1, the specimen surface was poorly harmed, with profound holes indicating severe corrosion. When TEPI was added to the 1 M HCl medium, the C35E surface area exhibited a few small pinholes and low damage (Figure 9c1), demonstrating its strong ability to reject corrosive ions. This ability generally results from TEPI adsorption on the C35E surface by developing a protective and compact film.

The EDX spectra presented in Figures 9a2-c2 show characteristic peaks of prevailing elements such as Fe, C, Mn and Cr, constituting C35E samples (*cf*. Table 1). Also, the presence of oxides visible through the O peak is prominent for C35 samples left in 1.0 M HCl, without and with the presence of 1 mM TEPI inhibitor.

Table 7 summarizes all EDX results presented as wt.% and at.% of identified elements of C35E samples before and after 24 hours of immersion in 1.0 M HCl, without and with 1 mM TEPI. It appears that the at.% of chlorine ions in the absence of TEPI is 46.30 %, whereas it decreases to 0.38 % in its presence. The reduction of Cl^- ions in the presence of TEPI suggests that this inhibitor can be deposited on the C35E surface, protecting against attack by Cl^- ions. The percentage of atomic content of iron (Fe) for C35E immersed in the 1M HCl is 46 %. However, when C35E was dipped in the optimal concentration (1 mM) of TEPI, it increased to 83.29 %. This increase suggests that the presence of TEPI hinders the dissolution reaction of C35E in the acidic solution. Additionally, the percentage atomic content of oxygen (O) significantly decreased from 46.30 to 33.66 %. Conversely, the percentages for nitrogen (N) show a notable increase from 0 to 3.76 % in the presence of TEPI. These findings confirm the presence and formation of a protective film of TEPI on the C35E surface in 1 M HCl.

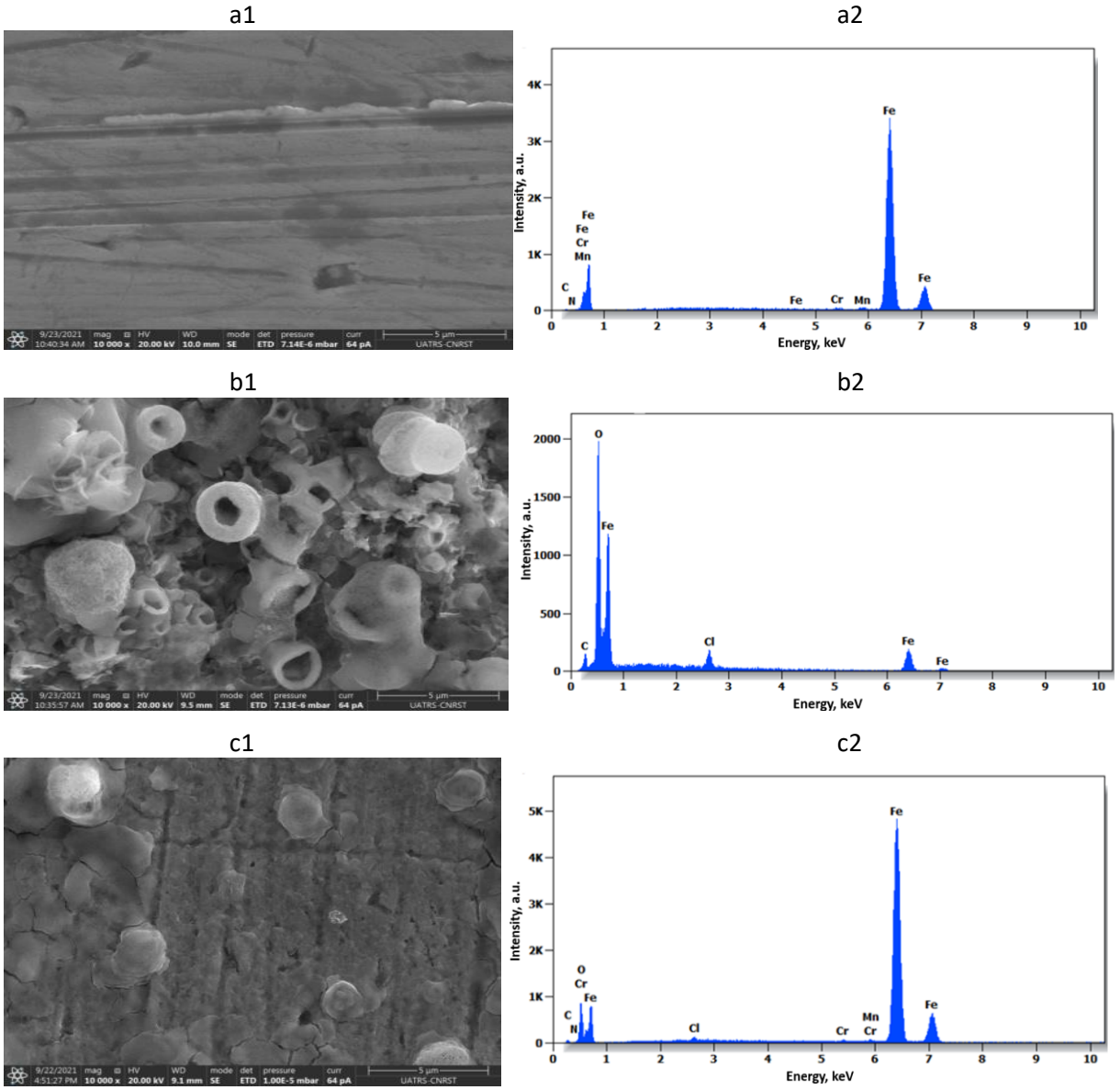

Figure 9. *SEM/EDX for C35E prior (a) and after 24 hours of soaking in 1 M HCl (b) and with 1 mM of TEPI (c) at 303 K (a1) and (b1) images are taken from [18].*

Table 7. *Percentages of atomic and weight contents of elements of C35E surface in the absence and presence of 0.001M TEPI obtained from EDX spectra*

Element	C35E (a2)		1 M HCl (b2)		TEPI (c2)	
	Content, wt.%	Content, at.%	Content, wt.%	Content, at.%	Content, wt.%	Content, at.%
C	1.43	6.17	1.40	4.05	2.66	8.24
N	0.81	3.01	-	-	1.42	3.76
O	-	-	21.24	46.30	14.49	33.66
Cl	-	-	3.70	3.64	0.37	0.38
Cr	0.33	0.33	-	-	0.30	0.22
Mn	0.77	0.73	-	-	0.66	0.45
Fe	96.66	89.76	73.66	46.00	80.09	53.29
Total	100.00	100.00	100.00	100.00	100.00	100.00

Properties of TEPI based on DFT calculations

Quantum computing based on the DFT method allows us to support experimental conclusions. To do this, we started by determining the exact geometry of the evaluated inhibitor for its neutral (TEPI) and protonated (TEPI-H) forms, optimizing the geometry of each form without any geometric

restrictions, and identifying the frontier molecular orbital density distributions and other quantum chemical descriptors for each form.

Figure 10 shows the most stable configuration of the inhibitory molecule in its TEPI and TEPI-H forms. The distribution of HOMO and LUMO molecular orbitals and the electron density mapped with the iso-surface of the electrostatic potential (ESP) are shown in Figure 11. A closer analysis of HOMO distribution shows that it has a total localization of electron density at surface level. This suggests a high electron-donating capacity due to many local sites favoring the adsorption of this molecule to the metal surface in question. However, the LUMO distribution takes place at the level of an ethoxyphenyl structure, and the dihydro-imidazole of the molecule studied shows that these two parts are ready to receive electrons. These HOMO and LUMO distribution properties may lead to parallel adsorption with the Fe(110) metal support. This observation is well illustrated by the calculation of the electron density mapped with the iso-surface of the electrostatic potential (ESP) (Figure 11). The potential areas, both positive and negative, are represented by the colors red and blue, respectively. Oxygen and the non-protonated nitrogen atoms are the sites most vulnerable to electrophilic attack, further promoting adsorption power on the metal surface.

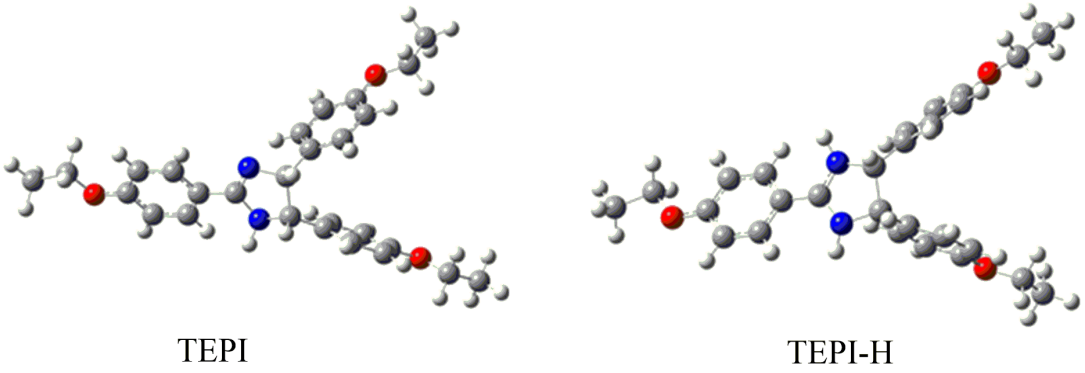

Figure 10. *Optimized geometry of TEPI and TEPI-H B3LYP/6-31G(d,p) in aqueous medium*

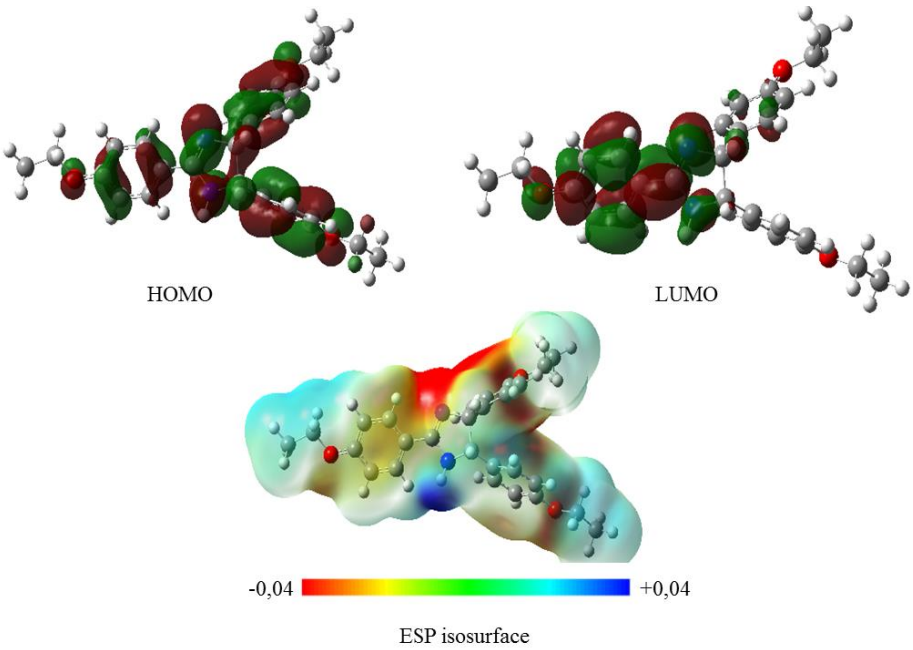

Figure 11*. HOMO and LUMO electron distributions and the electrostatic potential (ESP) of TEPI in aqueous medium*

The values of the calculated descriptors are presented in Table 8.

Table 8. *Calculated values of quantum chemical descriptors of TEPI in aqueous medium generated from the B3LYP/6-31G(d,p) level*

Compound	E_{HOMO} / eV	E_{LUMO} / eV	ΔE / eV	χ / eV	η / eV	ΔN	A / a.u.	μ / D
TEPI	-5.706	-0.810	4.897	3.258	2.448	0.319	413.496	3.173
TEPI-H	-6.152	-1.965	4.186	4.059	2.093	0.182	417.187	7.955

The HOMO (LUMO) energy value is associated with the electron-donating (accepting) ability of the corrosion inhibitor [42]. The high energy value of the HOMO indicates that it is easier for the TEPI to donate electrons to empty d orbitals in metals, which facilitates good adsorption and increases the value of corrosion inhibition efficiency.

In general, a low value of (ΔE) signifies that the molecule strongly interacts with the metal surface and acts as an effective corrosion inhibitor [43]. While it is difficult to discuss this parameter without comparing it with that of a similar compound, it is important to note that the energy gap of the TEPI in neutral and protonated forms is low (Table 8), especially in the protonated form, compared to numerous of mentioned corrosion inhibitors [43,44]. This observation confirms that the TEPI can easily adsorb on the metal surface, causing higher protection. The calculated global reactivity descriptors show that this molecule has a high nucleophilic power. This is consistent with the value of the calculated electron transfer index (0.319 and 0.182 for TEPI and TEPI-H, respectively), which, according to Koopmans, improves corrosion inhibition effectiveness [45]. The high values of the dipole moment and the polarizability of the proposed molecule (the dipole moment and the polarizability for the neutral form are 3.173 D and 413.496 a.u, respectively, and are 7.955 and 417.187 D for the protonated form) are also in agreement with this conclusion.

The calculated quantum descriptors show high structural chemical reactivity for both forms, with high inhibitory efficacy, which was experimentally proven.

Monte Carlo and molecular dynamic simulation results

To evaluate the properties of the proposed TEPI molecule as a corrosion inhibitor and to show its behavior with respect to the metallic surface, Monte Carlo (MC) and molecular dynamic (MD) simulations were performed. The objective of this simulation was to determine the lowest adsorption energy of our molecule when it is in contact with the iron surface by looking for its spontaneous configuration both in a vacuum and in an aqueous medium and finding its binding and interaction energy.

Recall that the binding and interaction energies are calculated from the energy of the total energy of the entire system (E_{Total}), the energy of the inhibitor ($E_{Inhibitor}$), and the energy of the Fe (110) surface ($E_{Surface}$) according to equations (9) AND (10).

$$E_{Interaction} = E_{Total} - E_{Inhibitor} - E_{Surface} \quad (9)$$

$$E_{Interaction} = E_{Binding} \quad (10)$$

Figure 12 shows the adsorption configuration of the TEPI inhibitor molecule on the metal surface, with the structural arrangement leading to the most stable adsorption energy. The energy results of this simulation, performed in aqueous medium, are summarized in Table 9.

The results of this study suggest that the proposed molecule can be a good corrosion inhibitor for steel since it has a high affinity towards the metallic surface. Its mode of adsorption is parallel and nearby, with significant adsorption energies in both phases. This adsorption energy becomes very high even in a corrosive medium (presence of H_2O, H_3O^+ and Cl^-), which indicates an easy and stronger interaction between the TEPI organic molecule and steel.

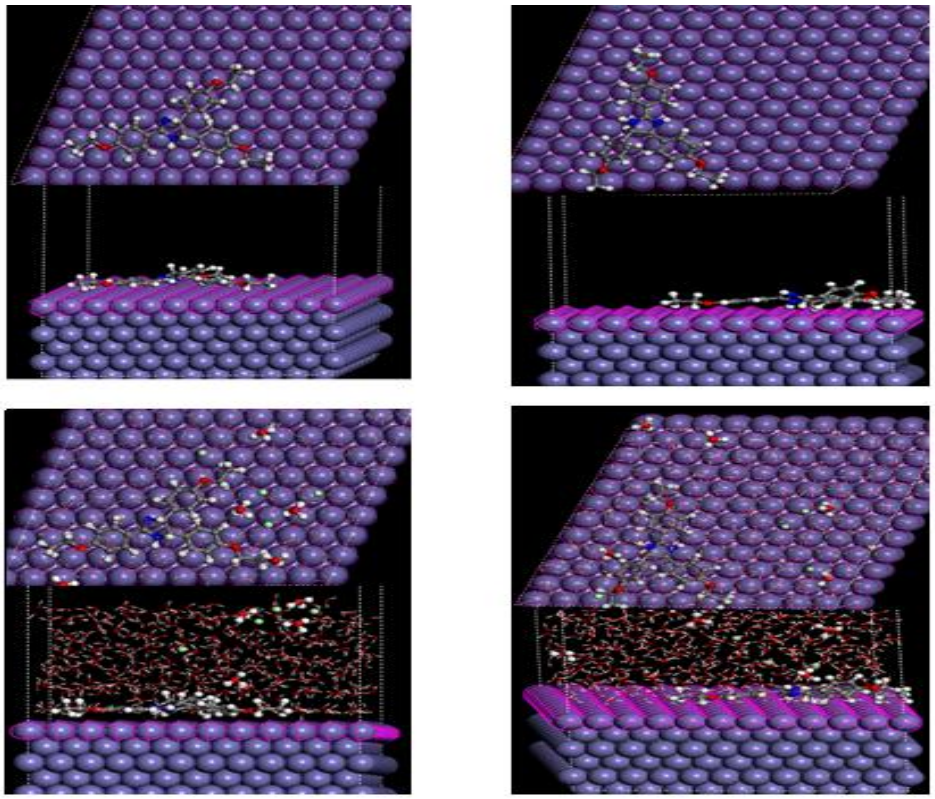

Figure 12. *Top and side views of the equilibrium adsorption geometries of TEPI and TEPI-H on the Fe (110) surface in aqueous medium*

Table 9. *The output energies calculated by MC simulation for adsorption of the studied inhibitor on Fe (110) surface in vacuum and aqueous medium*

Compounds	Energy, J mol^{-1}						
	Total	Adsorption	Rigid adsorption	Deformation	dE_{ad} / dN_i*		
					H_2O	H_3O	Cl
TEPI	-7305.074	-7497.324	-7692.210	194.886	-13.049	-148.616	-149.802
TEPI-H	-7342.728	-7534.977	-7728.602	193.624	-14.329	-147.804	-155.079

*dE_{ads} - change in adsorption energy, dN_i - change in the quantity of molecules adsorbed

Table 10. *MD simulation of TEPI and TEPI-H onto a Fe (110) surface at 303 K yielded interaction and binding energies*

Compound	$E_{Interaction}$ / kJ mol^{-1}	$E_{Binding}$ / kJ mol^{-1}
TEPI	1113.656	-1113.656
TEPI-H	1258.035	-1258.035

TEPI can adsorb efficiently on the metal surface in its neutral or protonated form thanks to the oxygen and nitrogen atoms of the imidazole ring and the phenyl rings. The presence of the oxygen atoms strengthens the polarity of the tails (ethoxyphenyl) of the molecule, which allows effective coverage of the surface and improves its inhibition properties.

To confirm these results and predict the binding energy, a molecular dynamic simulation was performed, and the equilibrium of the system was evaluated and confirmed by the stable average values of the energy fluctuations, taking into account the temperature factor (at experimental temperature 303 K). This simulation showed that the molecule can efficiently adsorb onto the surface while maintaining its orientation. The data in Table 10 also indicate that the binding energies

of the molecule with the Fe surface are very high and positive, suggesting a high stability of the adsorbed molecule [46,47].

The results of the MD and MC simulations show high adsorption of the two forms studied on Fe (110), which indicates that the inhibitor studied is highly effective against the corrosion phenomenon, as was already reported in the experimental section.

Corrosion inhibition mechanism

PDP findings confirmed the mixed nature of TEPI adsorption with the predominant cathodic type. Furthermore, the values of adsorption and thermodynamics parameters show that adsorption processes are both chemically and physically based. Therefore, the mechanism of corrosion inhibition could be explained by the adsorption process of the inhibitor onto the metal surface. It is reasonable to assume that TEPI molecules in the HCl medium may exist in the protonated form in equilibrium with the equivalent neutral molecular form according to:

$$TEPI + xH^+ \leftrightarrow (TEPIH)^{x+} \quad (11)$$

At first, a significant number of Cl^- ions from the HCl medium was adsorbed onto the positively charged C35E surface, creating a negative charge region. Subsequently, the protonated $(TEPIH)^+$ would be electrostatically adsorbed (physisorption) on this newly generated negatively charged surface, forming a protective film $(FeCl^-TEPIH^+)_{ads}$ and thus preventing the anodic corrosion reaction. Similarly, the cathodic reaction mechanism can be described as follows:

$$Fe + H^+ \rightarrow (FeH^+)_{ads} \quad (12)$$

$$(FeH^+)_{ads} + e^- \rightarrow (FeH)_{ads} + H^+ + e^- \rightarrow Fe + H_2\uparrow \quad (13)$$

The protonated $(TEPIH)^+$ ions were also adsorbed in the cathodic sites, where they compete with H^+ for electrons, reducing the production of H_2.

In addition to physisorption, chemisorption can occur by the displacement of pre-adsorbed water molecules from the C35E /aqueous medium interface. The O atoms (ethoxy) and/or N atoms of the imidazole ring might establish coordination bonds with the vacant d-orbital of iron atoms using their free electron pairs. Furthermore, the excess negative charge collected on the C35E surface can be transferred from the iron d-orbital to the empty π* orbital of TEPI molecules (retro-donation) (Figure 13), boosting TEPI adsorption on the C35E surface. Finally, the adsorbed inhibitor layer was formed on the C35E surface, acting as a barrier between C35E and 1 M HCl medium and preventing acid corrosion of C35E steel.

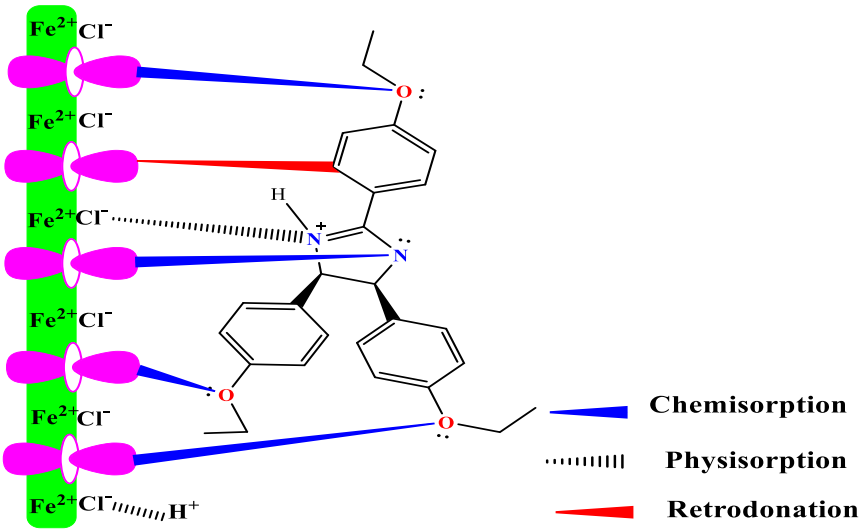

Figure 13. *Possible adsorption mechanism of TEPI on C35E steel surface in HCl medium*

Conclusion

The findings of this investigation reveal that TEPI is a good inhibitor of C35E steel corrosion in 1 M HCl at 303 K. It has been encountered that when the amount of TEPI rises, the effectiveness values for inhibition rise noticeably, achieving about 97 % in 1 mM HCl. According to the findings of PDP, TEPI is functioning as a mixed-type inhibitor. Adsorption of TEPI on the C35E steel surface in 1 M HCl rules the Langmuir adsorption isotherm model. Both SEM and UV-vis confirm that TEPI has an adsorption action on the surface of the C35E. In the same way, the calculated quantum descriptors show high structural chemical reactivity for both forms, with high inhibitory efficacy as experimentally proven. The results of the MD and MC simulations show strong adsorption of the two forms studied on Fe (110), providing better protection for the steel in question.

References

[1] D. H. Xia, C. Deng, D. Macdonald, S. Jamali, D. Mills, J.-L. Luo, M.G. Strebl, M. Amiri, W. Jin, S. Song, Electrochemical measurements used for assessment of corrosion and protection of metallic materials in the field: A critical review, *Journal of Materials Science & Technology* **112** (2021) 151-183. https://doi.org/10.1016/j.jmst.2021.11.004

[2] H. Wei, B. Heidarshenas, L. Zhou, G. Hussain, Q. Li, K. K. Ostrikov, Green inhibitors for steel corrosion in acidic environment: state of art, *Materials Today Sustainability* **10** (2020) 100044. https://doi.org/10.1016/j.mtsust.2020.100044

[3] R. Rodrigues, S. Gaboreau, J. Gance, I. Ignatiadis, S. Betelu, Reinforced concrete structures: A review of corrosion mechanisms and advances in electrical methods for corrosion monitoring, *Construction and Building Materials* **269** (2021) 121240. https://doi.org/10.1016/j.conbuildmat.2020.121240

[4] L. Xiong, P. Wang, Z. He, Q. Chen, J. Pu, R. Zhang, Corrosion behaviors of Q235 carbon steel under imidazoline derivatives as corrosion inhibitors: Experimental and computational investigations, *Arabian Journal of Chemistry* **14** (2021) 102952. https://doi.org/10.1016/j.arabjc.2020.102952

[5] P. Ren, J. Li, L. Wang, H. Guo, B. Lei, Z. Feng, G. Meng, Organo-Cerium as a Quick Repair Agent for Coating Damage on Carbon Steel, *Journal of Materials Engineering and Performance* **32** (2023) 9755-9764. https://doi.org/10.1007/s11665-023-07815-7

[6] S. Chen, Z. Huang, M. Yuan, G. Huang, H. Guo, G. Meng, Z. Feng, P. Zhang, Trigger and response mechanisms for controlled release of corrosion inhibitors from micro/nanocontainers interpreted using endogenous and exogenous stimuli: A review, *Journal of Materials Science & Technology* **125** (2022) 67-80. https://doi.org/10.1016/j.jmst.2022.02.037

[7] M. Benabdellah, R. Touzani, A. Aouniti, A. Dafali, S. El Kadiri, B. Hammouti, M. Benkaddour, Inhibitive action of some bipyrazolic compounds on the corrosion of steel in 1 M HCl: Part I: Electrochemical study, *Materials Chemistry and Physics* **105** (2007) 373-379. https://doi.org/10.1016/j.matchemphys.2007.05.001

[8] N. Chafai, S. Chafaa, K. Benbouguerra, D. Daoud, A. Hellal, M. Mehri, Synthesis, characterization and the inhibition activity of a new α-aminophosphonic derivative on the corrosion of XC48 carbon steel in 0.5 M H_2SO_4: experimental and theoretical studies, *Journal of the Taiwan Institute of Chemical Engineers* **70** (2017) 331-344. https://doi.org/10.1016/j.jtice.2016.10.026

[9] M. El Faydy, B. Lakhrissi, C. Jama, A. Zarrouk, L. O. Olasunkanmi, E. E. Ebenso, F. Bentiss, Electrochemical, surface and computational studies on the inhibition performance of some newly synthesized 8-hydroxyquinoline derivatives containing benzimidazole moiety against

the corrosion of carbon steel in phosphoric acid environment*, Journal of Materials Research and Technology* **9** (2020) 727-748. https://doi.org/10.1016/j.jmrt.2019.11.014

[10] M. Belayachi, H. Serrar, H. Zarrok, A. El Assyry, A. Zarrouk, H. Oudda, S. Boukhris, B. Hammouti, Eno E. Ebenso, A. Geunbour, New pyrimidothiazine Derivative as Corrosion Inhibitor for Carbon Steel in Acidic Media, *International Journal of Electrochemical Science* **10** (2015) 3010-3025. http://www.electrochemsci.org/papers/vol10/100403010.pdf

[11] H. Bendaha, A. Zarrouk, A. Aouniti, B. Hammouti, S. El Kadiri, R. Salghi, R. Touzani, Adsorption and corrosion inhibitive properties of some tripodal pyrazolic compounds on mild steelin hydrochloric acid systems, *Physical and Chemical News* **64** (2012) 95-103. https://www.researchgate.net/publication/263422004_Adsorption_and_corrosion_inhibitive_properties_of_some_tripodal_pyrazolic_compounds_on_mild_steel_in_hydrochloric_acid_systems

[12] H. Zarrok, R. Salghi, A. Zarrouk, B. Hammouti, H. Oudda, Lh. Bazzi, L. Bammou, S.S. Al-Deyab, Investigation of the Inhibition Effect of N-1-Naphthylethylenediamine Dihydrochloride Monomethanolate on the C38 Steel Corrosion in 0.5 M H_2SO_4, *Der Pharma Chemica* **4(1)** (2012) 407-416. https://www.derpharmachemica.com/pharma-chemica/investigation-of-the-inhibition-effect-of-n1naphthylethylenediamine-dihydrochloride-monomethanolate-on-the-c38-steel-cor.pdf

[13] B. Narasimhan, D. Sharma, P. Kumar, Biological importance of imidazole nucleus in the new millennium, *Medicinal Chemistry Research* **20** (2011) 1119-1140. https://doi.org/10.1007/s00044-010-9472-5

[14] L. Zhang, X. Peng, G.L. V Damu, R. Geng, C. Zhou, Comprehensive review in current developments of imidazole-based medicinal chemistry, *Medicinal Research Reviews* **34** (2014) 340-437. https://doi.org/10.1002/med.21290

[15] A. Khormali, S. Ahmadi, Synergistic effect between oleic imidazoline and 2-mercaptobenzimidazole for increasing the corrosion inhibition performance in carbon steel samples, *Iranian Journal of Chemistry and Chemical Engineering* **42** (2023) 321-336. https://doi.org/10.30492/ijcce.2022.546098.5091

[16] C. Zhang, J. Hu, Z. Yang, Z. Zheng, S. Geng, X. Zhong, Effects of the number of imidazoline ring and the length of alkyl group chain of imidazoline derivatives on corrosion inhibition of carbon steel in HCl solution: Molecular simulation and experimental validation, *Petroleum* **4** (2021) 447-457. https://doi.org/10.1016/j.petlm.2021.03.002

[17] G. Laadam, M. El Faydy, F. Benhiba, A. Titi, H. Amegroud, Arej S Al-Gorair, H. Hawsawi, R. Touzani, I. Warad, A. Bellaouchou, A. Guenbour, M. Abdallah, A. Zarrouk, Outstanding anticorrosion performance of two pyrazole derivatives on carbon steel in acidic medium: Experimental and quantum-chemical examinations, *Journal of Molecular Liquids* **375** (2023) 121268. https://doi.org/10.1016/j.molliq.2023.121268

[18] F. Benhiba, Z. Benzekri, Y. Kerroum, N. Timoudan, R. Hsissou, A. Guenbour, M. Belfaquir, S. Boukhris, A. Bellaouchou, H. Oudda, A. Zarrouk, Assessment of inhibitory behavior of ethyl 5-cyano-4-(furan-2-yl)-2-methyl-6-oxo-1,4,5,6-tetrahydropyridine-3-carboxylate as a corrosion inhibitor for carbon steel in molar HCl: Theoretical approaches and experimental investigation, *Journal of the Indian Chemical Society* **100** (2023) 100916. https://doi.org/10.1016/j.jics.2023.100916

[19] F. Benhiba, N.K. Sebbar, H. Bourazmi, M.E. Belghiti, R. Hsissou, T. Hökelek, A. Bellaouchou, A. Guenbour, I. Warad, H. Oudda, A. Zarrouk, E.M. Essassi, Corrosion inhibition performance of 4-(prop-2-ynyl)-[1,4]-benzothiazin-3-one against mild steel in 1M HCl solution: Experimental and theoretical studies, *International Journal of Hydrogen Energy* **46 (51)** (2021) 25800-25818. https://doi.org/10.1016/j.ijhydene.2021.05.091

[20] M. Yadav, S. Kumar, R.R. Sinha, I. Bahadur, E.E. Ebenso, New pyrimidine derivatives as efficient organic inhibitors on mild steel corrosion in acidic medium: Electrochemical, SEM, EDX, AFM and DFT studies, *Journal of Molecular Liquids* **211** (2015) 135-145. https://doi.org/10.1016/j.molliq.2015.06.063

[21] M. J. Frisch, G. W. Trucks, H. B. Schlegel, G. E. Scuseria, M. A. Robb, J. R. Cheeseman, G. Scalmani, V. Barone, B. Mennucci, G. Petersson, Gaussian 09, Revision D. 01, Gaussian, Inc., Wallingford CT. http://www.gaussian.com

[22] A.H. Al Hamzi, H. Zarrok, A. Zarrouk, R. Salghi, The Role of Acridin-9(10*H*)-one in the Inhibition of Carbon Steel Corrosion : Thermodynamic, Electrochemical and DFT Studies, *International Journal of Electrochemical Science* **9** (2013) 2586-2605. https://doi.org/10.1016/S1452-3981(23)14334-3

[23] H. Fakhry, M. El Faydy, F. Benhiba, T. Laabaissi, M. Bouassiria, M. Allali, B. Lakhrissi, H. Oudda, A. Guenbour, I. Warad, A. Zarrouk, A newly synthesized quinoline derivative as corrosion inhibitor for mild steel in molar acid medium: Characterization (SEM/EDS), experimental and theoretical approach, *Colloids and Surfaces A: Physicochemical and Engineering Aspects* **610** (2021) 125746. https://doi.org/10.1016/j.colsurfa.2020.125746

[24] V. Barone, M. Cossi, Quantum calculation of molecular energies and energy gradients in solution by a conductor solvent model, *The Journal of Physical Chemistry A,* **102** (1998) 1995-2001. https://doi.org/10.1021/jp9716997

[25] M.E. Belghiti, Y. Karzazi, S. Tighadouini, A. Dafali, C. Jama, I. Warad, B. Hammouti, S. Radi, New hydrazine derivatives as corrosion for mild steel in phosphoric acid medium. Part B: Theoretical investigation, *Journal of Materials and Environmental Science* **7** (2016) 956-967.

[26] Q. Nuha, A. Wazzan, Journal of Industrial and Engineering Chemistry DFT calculations of thiosemicarbazide, arylisothiocynates, and 1-aryl-2,5-dithiohydrazodicarbonamides as corrosion inhibitors of copper in an aqueous chloride solution, *Journal of Industrial and Engineering Chemistry* **26** (2014) 291-308. https://doi.org/10.1016/j.jiec.2014.11.043

[27] C. Verma, J. Haque, E. E. Ebenso, M. A. Quraishi, Results in Physics Melamine derivatives as effective corrosion inhibitors for mild steel in acidic solution: Chemical, electrochemical, surface and DFT studies, *Results in Physics* **9** (2018) 100-112. https://doi.org/10.1016/j.rinp.2018.02.018

[28] A. Mishra, C. Verma, H. Lgaz, Synthesis, characterization and corrosion inhibition studies of N-phenyl-benzamides on the acidic corrosion of mild steel: Experimental and computational studies, *Journal of Molecular Liquids* **251** (2017) 317-332. https://doi.org/10.1016/j.molliq.2017.12.011

[29] M. El Faydy, F. Benhiba, Y. Kerroum, A. Guenbour, F. Bentiss, I. Warad, B. Lakhrissi, A. Zarrouk, Synthesis and anticorrosion characteristics of new 8-quinolinol analogs with amide-substituted on C35E steel in acidic medium: Experimental and computational ways, *Journal of Molecular Liquids* **325** (2021) 115224. https://doi.org/10.1016/j.molliq.2020.115224

[30] A. El yaktini, A. Lachiri, M. El Faydy, F. Benhiba, H. Zarrok, M. El Azzouzi, M. Zertoubi, M. Azzi, B. Lakhrissi, A. Zarrouk, Practical and Theoretical Study on the Inhibitory Inflences of New Azomethine Derivatives Containing 8-hydroxyquinoline Moiety for the Corrosion of Carbon Steel in 1 M HCl, *Oriental Journal of Chemistry* **34(6)** (2018) 3016-3029. https://doi.org/10.13005/ojc/340643

[31] M. Rbaa, P. Dohare, A. Berisha, O. Dagdag, L. Lakhrissi, M. Galai, B. Lakhrissi, M.E. Touhami, I. Warad, A. Zarrouk, New Epoxy sugar based glucose derivatives as eco friendly corrosion inhibitors for the carbon steel in 1.0 M HCl: Experimental and theoretical investigations, *Journal of Alloys and Compounds* **833** (2020) 154949. https://doi.org/10.1016/j.jallcom.2020.154949

[32] M. El Faydy, M. Galai, M.E. Touhami, I.B. Obot, B. Lakhrissi, A. Zarrouk, Anticorrosion potential of some 5-amino-8-hydroxyquinolines derivatives on carbon steel in hydrochloric acid solution: Gravimetric, electrochemical, surface morphological, UV-visible, DFT and Monte Carlo simulations, *Journal of Molecular Liquids* **248** (2017) 1014-1027. https://doi.org/10.1016/j.molliq.2017.10.125

[33] F. Bentiss, F. Gassama, D. Barbry, L. Gengembre, H. Vezin, M. Lagrenée, M. Traisnel, Enhanced corrosion resistance of mild steel in molar hydrochloric acid solution by 1,4-bis(2-pyridyl)-5H-pyridazino[4,5-b]indole: Electrochemical, theoretical and XPS studies, *Applied Surface Science* **252** (2006) 2684-2691. https://doi.org/10.1016/j.apsusc.2005.03.231

[34] E. Alibakhshi, M. Ramezanzadeh, G. Bahlakeh, B. Ramezanzadeh, M. Mahdavian, M. Motamedi, *Glycyrrhiza glabra* leaves extract as a green corrosion inhibitor for mild steel in 1 M hydrochloric acid solution: Experimental, molecular dynamics, Monte Carlo and quantum mechanics study, *Journal of Molecular Liquids* **255** (2018) 185-198. https://doi.org/10.1016/j.molliq.2018.01.144

[35] N. Anusuya, J. Saranya, P. Sounthari, A. Zarrouk, S. Chitra, Corrosion inhibition and adsorption behaviour of some bis-pyrimidine derivatives on mild steel in acidic medium, *Journal of Molecular Liquids* **225** (2017) 406-417. https://doi.org/10.1016/j.molliq.2016.11.015

[36] P. Muthukrishnan, B. Jeyaprabha, P. Prakash, Adsorption and corrosion inhibiting behavior of Lannea coromandelica leaf extract on mild steel corrosion, *Arabian Journal of Chemistry* **10** (2017) S2343-S2354. https://doi.org/10.1016/j.arabjc.2013.08.011

[37] P. R. Ammal, M. Prajila, A. Joseph, Effect of substitution and temperature on the corrosion inhibition properties of benzimidazole bearing 1 , 3 , 4-oxadiazoles for mild steel in sulphuric acid : Physicochemical and theoretical studies, *Journal of Environmental Chemical Engineering* **6** (2018) 1072-1085. https://doi.org/10.1016/j.jece.2018.01.031

[38] H. Zarrok, A. Zarrouk, R. Salghi, Y. Ramli, B. Hammouti, S.S. Al-Deyab, E.M. Essassi, H. Oudda, Adsorption and inhibition effect of 3-methyl-1-propargylquinoxalin-2 (1H)-one on carbon steel corrosion in hydrochloric acid, *International Journal of Electrochemical Science* **7** (2012) 8958-80973. https://doi.org/10.1016/S1452-3981(23)18044-8

[39] I.B. Obot, N.O. Obi-Egbedi, Adsorption properties and inhibition of mild steel corrosion in sulphuric acid solution by ketoconazole: Experimental and theoretical investigation, *Corrosion Science* **52** (2010) 198-204. https://doi.org/10.1016/j.corsci.2009.09.002

[40] L. Bai, L. J. Feng, H. Y. Wang, Y. Bin Lu, X. W. Lei, F. L. Bai, Comparison of the synergistic effect of counterions on the inhibition of mild steel corrosion in acid solution: Electrochemical, gravimetric and thermodynamic studies, *RSC Advances* **5** (2015) 4716-4726. https://doi.org/10.1039/c4ra12286k

[41] A. Sedik, D. Lerari, A. Salci, S. Athmani, K. Bachari, İ. H. Gecibesler, R. Solmaz, Dardagan Fruit extract as eco-friendly corrosion inhibitor for mild steel in 1 M HCl: Electrochemical and surface morphological studies, *Journal of the Taiwan Institute of Chemical Engineers* **107** (2020) 189-200. https://doi.org/10.1016/j.jtice.2019.12.006

[42] I. Lukovits, I. Bakó, A. Shaban, E. Kálmán, Polynomial model of the inhibition mechanism of thiourea derivatives, *Electrochimica Acta* **43** (1998) 131-136. https://doi.org/10.1016/S0013-4686(97)00241-7

[43] D. Kumar, V. Jain, B. Rai, Imidazole derivatives as corrosion inhibitors for copper: A DFT and reactive force field study, *Corrosion Science* **171** (2020) 108724. https://doi.org/10.1016/j.corsci.2020.108724

[44] M. Li, Y. Ouyang, W. Yang, Y. Chen, K. Zhang, Z. Zuo, X. Yin, Y. Liu, Inhibition performances of imidazole derivatives with increasing fluorine atom contents in anions against carbon

steel corrosion in 1 M HCl, *Journal of Molecular Liquids* **322** (2021) 114535. https://doi.org/10.1016/j.molliq.2020.114535

[45] T. Koopmans, Ordering of wave functions and eigenenergies to the individual electrons of an atom, *Physic*a **1** (1933) 104-113. https://doi.org/10.1016/S0031-8914(34)90011-2

[46] M. Goyal, H. Vashisht, A. Kumar, S. Kumar, I. Bahadur, F. Benhiba, A. Zarrouk, Isopentyltriphenylphosphonium bromideionic liquid as a newly effective corrosion inhibitor on metal-electrolyte interface in acidic medium: Experimental, surface morphological (SEM-EDX & AFM) and computational analysis, *Journal of Molecular Liquids* **316** (2020) 113838. https://doi.org/10.1016/j.molliq.2020.113838

[47] A. Attou, M. Tourabi, A. Benikdes, O. Benali, H. B. Ouici, F. Benhiba, A. Zarrouk, C. Jama, F. Bentiss, Experimental studies and computational exploration on the 2-amino-5-(2-methoxyphenyl)-1,3,4-thiadiazole as novel corrosion inhibitor for mild steel in acidic environment*, Colloids and Surfaces A* **604** (2020) 125320. https://doi.org/10.1016/j.colsurfa.2020.125320

J. Electrochem. Sci. Eng. **14(2)** (2024) 213-229; http://dx.doi.org/10.5599/jese.2139

Open Access : : ISSN 1847-9286
www.jESE-online.org

Original scientific paper

Electrochemical behaviour of thermally treated aluminium 2024 alloy exposed to *B. mojavensis*

Nelson Vejar✉, Joseph Rozas and Roberto Solis

Centro de Investigación y Desarrollo en Ciencias Aeroespaciales, Fuerza Aérea de Chile. Av. José Miguel Carrera 11087, Santiago, Chile

Corresponding author: ✉*nelsonvejar.v@gmail.com;* Tel.: +56-2-2976 1329

Received: October 17, 2023; Accepted: February 7, 2024; Published: March 13, 2024

Abstract

The copper-rich zone plays a key role in understanding the deterioration process of 2024 aluminium alloy. The intermetallic on the surfaces makes this alloy susceptible to both local corrosion and microbial colonization. The adhesion of bacteria on the surface could deteriorate the metallic substrate in a phenomenon known as microbiologically influenced corrosion (MIC). The triggering mechanism of MIC in 2024-T3 is unclear. An electrochemical study was conducted to determine the influence of the second phase (Al_2Cu) on the corrosion of the 2024-T3 aluminium alloy exposed to bacteria. The 2024-T3 alloy was thermally treated to increase the amount of Al_2Cu by nearly 67 % on the surface. The bacterium under study was collected from the corrosion products of a Chilean Air Force aircraft. The isolated bacterium was identified by 16S RNA sequencing as Bacillus mojavensis (99.99 %). Results obtained by electrochemical impedance spectroscopy showed a decreased impedance of 2024-T3 and an increased impedance of heat-treated, both samples exposed to bacteria. The increased impedance could be associated with the antibacterial effect due to the high ion release of copper on the surface, which can inhibit biofilm formation and biocorrosion.

Keywords

Aluminium alloy; thermal treatment; second phases; biocorrosion; impedance

Introduction

The copper is incorporated in approximately 4-5 % by weight of an aluminium matrix and has allowed the development of 2024 aluminium alloy. The second phase (θ phase) is composed of Al_2CuMg and $Al_2CuMgFe$, improving the mechanical properties of this alloy. Due to this, 2024 aluminium alloy is widely used in the aerospace industry. Despite its good mechanical properties, the θ phases make this material susceptible to corrosion [1,2] and bacterial colonization [3].

The adherence of microorganisms on a metal surface could potentially trigger an increased corrosion rate. The unusual corrosion rate phenomenon of metallic materials is known as

microbiologically influenced corrosion (MIC) [4]. Two mechanisms for MIC of 2024 aluminium alloys have been documented: (a) the production of water-soluble organic acids by bacteria and fungi and (b) the formation of differential aeration cells [5]. In recent years, a relation between the enzymatic activity and the adhesion of bacteria on aluminium alloy 2024 and 6063 substrates was found [6]. Paez *et al.* [6] found that *Pseudomonas aeruginosa* increases the concentration of oxygen and hydroxyl ions on the surface due to catalase activity. This phenomenon can promote accelerated corrosion [7]. The accelerated deterioration of 6063 aluminium alloys was attributed to changes in the chemical composition of the surfaces. There is evidence that the chemical characteristics associated with the second phase on the metallic surface can affect bacterial colonization; however, this has not been addressed [8-11]. Rosales and Iannuzi [12] evaluated the thermal treatment 2024-T351 on the MIC phenomenon promoted by the fungus *Hormoconis resinae*. The electrochemical results showed a relation between the thermal treatment and the corrosion. Still, a direct relationship between the concentration and distribution of the second phase and the MIC phenomenon was not described.

A diversity of bacteria and fungi have been isolated from aircraft, and the most common corrosive organism found was the fungus *Hormoconis resinae* [13,14]. In recent years, changes in the chemical composition of fuels and surface treatment to inhibit corrosion have caused a community modification from fungi to bacteria [15]. Bacteria collected by our research group have shown dual behaviour. The corrosion was accelerated [16] and inhibited [17]. Recent research demonstrated increased cathodic current associated with bacterial activity (*Bacillus* species) [18].

This paper aims to determine the effect of the alloying element distribution in the 2024-T3 surface on susceptibility to MIC. Bacteria collected (*Bacillus mojavensis*) from a corrosion product was used. The increased amount of Al_2CuMg precipitates on the surface of the 2024 alloys was obtained using different thermal treatments.

Experimental

Metallic substrate pretreatment

The 2024-T3 sheet (50×50×0.2 mm) was provided by the National Aeronautical Company of Chile (Spanish abbreviation, ENAER). The chemical composition of this alloy was (in wt.%): 0.087 Si, 0.151 Fe, 4.940 Cu, 0.780 Mn, 1.480 Mg, 0.006 Cr, 0.009 Ni, 0.029 Zn, 0.039 Ti, 0.010 Sn, and Al balanced. The metallic surfaces were mechanically polished using #800, # 1000, and #1500 SiC paper. Then, the samples were washed using an ultrasonic ethanol bath for 5 min to remove the solid particles from the mechanical polishing. All samples were sterilized by UV light for 12 min [16] before the microbiological procedure.

Isolation and identification of bacterial strains

The bacterial strain was collected from the corrosion products on an aircraft surface exposed to the coastal environment (north of Chile). The biological sample was maintained in a sterilized flask (1.5 mL) and transported to the laboratory. The bacterium was inoculated (0.1:10) aseptically in a nutritive broth (Luria Bertani, LB). The composition of the culture broth in water (ultra-pure, Milli-Q quality, 18.2 MΩ cm^{-1}) consisted of 10 g L^{-1} tryptone, 5 g L^{-1} yeast extract and 10 g L^{-1} NaCl. The flask was placed in an incubator (Biobase) at 30 °C for 16 h and serial dilutions of the solution (10^{-1} to 10^{-6}) were prepared using sterile phosphate buffer (pH 7.0). Next, 100 µL of each dilution was spread on LB medium plates and incubated at 30 °C for 24 h [18]. The strain was stored at -18 °C to ensure the bacterial material purity. The microorganisms were identified by sequencing the 16 s rRNA gene. The sequences obtained were assembled, analysed, and edited manually using the ChromasPro software (Technelysium Pty Ltd.) for a final sequence extension of ~450 bp. The strain was taxonomically

classified using the Naïve Bayesian rRNA classifier function from the RDP-Ribosome Database Project [19]. A neighbouring junction tree based on 16S rRNA gene sequences available in databases was generated using the ‘‘NCBI Blast” to determine the phylogenetic distance between isolated bacteria. A 97-100 % match for the GenBank dataset genetically unknown material was considered an acceptable identification [20]. The morphology of the bacteria was characterized by an optical microscope (Bio2T-PLLedpplan, Bel Engineering).

Thermal treatments

The thermal treatments were carried out in a furnace (Barnstead Thermolyne 600,0), and the subsequent stages applied to 2024 aluminium alloy are described below.

a. ThT 01: First, the alloys were treated by 2 h at 510 ± 6 °C (liquid phase/LP). Then, the specimens were removed from the furnace and cooled in a desiccator to 21 °C.
b. ThT 02: The metallic samples were treated by 2 h at 510 ± 6 °C. Then, the samples were cooled inside the furnace to 20 °C, the temperature drop rate was 4 °C min^{-1}
c. ThT 03: The samples were treated by 2 h at 510 ± 6 °C. Then, the specimens were cooled inside the oven in two stages, 410 °C for 45 min and 310 °C for 45 min. Finally, the specimen samples were removed from the furnace and cooled in a desiccator to 21 °C.
d. ThT 04: First, the alloys were treated during 2 h at 510 ± 6 °C. Then, the samples were cooled inside the furnace in three stages: 410 °C for 45 min, 310 °C for 45 min, and finally, cooled to 20 °C, the temperature drop rate was 4 °C min^{-1}.
e. ThT 05: First, the samples were heated from 20 to 510 ± 6 °C; the temperature rise rate was 4 °C min^{-1}. Then, alloys were heated for 2 h at 510 ± 6 °C. Finally, the specimens were removed from the furnace and cooled in a desiccator to 21 °C.
f. ThT 06: First, the alloys were heated inside the furnace from 20 to 510 ± 6 °C, the temperature rise rate was 4 °C min^{-1}. Then, alloys were heated for 2 h at 510 ± 6 °C. Finally, the samples were cooled inside the furnace to 20 °C. The temperature drop rate was 4 °C min^{-1}.

Electrolyte-culture medium

The metallic substrates were exposed to two different systems: a sterile electrolyte-culture (EC) medium (pH 4.8) and an inoculated EC medium with collected bacteria. The EC medium contains (in g L^{-1}): 0.22 $(NH_4)_2SO_4$, 18.70 $NaSO_4$, 0.58 NaCl, 1.20 KH_2PO_4, 0.23 $MgSO_4 \times 7H_2O$, 0.25 $CaCl_2 \times 2H_2O$, 0.024 g yeast extract and 0.024 g tryptone [18].

Previously to the inoculation of microorganisms (10 vol.%), the bacteria were grown in LB broth at 27 °C overnight and pelleted. The inoculated EC medium has 10^7 CFU mL^{-1}, which was determined by monitoring the optic density (UV-Vis at 620 nm) and using the McFarland method. Every 4 days, 70 % of the medium was removed and replaced with fresh sterile EC, and the bacteria was inoculated to maintain the density near a steady state during the experiment. The pH values were monitored by a pH meter (Hanna- EDGE).

Electrochemical impedance spectroscopy

Electrochemical measurements were performed with a three-electrode cell configuration. A pure graphite rod (diameter, 6 mm) and a saturated calomel electrode (SCE) were used as a counter and reference electrode, respectively. A delimited area (12.5 cm^2) of the working electrode (2024-T3 sheet) placed at the bottom of the electrochemical cell was sealed with an O-ring. The electrolyte consisted of a sterilized and inoculated EC medium. The electrochemical measurements were carried out using a potentiostat (VSP, Bio-Logic, USA) after exposing the metallic sample to sterile

and inoculated EC for 3, 7, 14, and 21 days at 27 °C. The open circuit potential (OCP) was measured until its stabilization before each electrochemical measurement. The EIS data were performed at OCP, from 100 kHz to 10 mHz with 7 points per decade and using 10 mV peak-to-peak sinusoidal potential. The Kramers-Krönig relation was utilized to adjust the frequency range analysed, and impedance data were fitted using a home-developed software called SIMAD (LISE UPR 15 CNRS, France). The equivalent circuits were proposed by EIS data analysis using a DRTtools (Distribution of Relaxation Times tools) of MATLAB software [21]. All measurements were carried out in triplicate to ensure reproducibility.

Distribution and morphology characterization

The metallic samples dimensioned in 1×2 cm were mounted in Bakelite resin using a compression mounting system (Buehler SimpliMet 2), then were cloth polished (Struers LaboPol-5 / 0.03 mm alumina suspension) and washed in acetone and deionized water. The images were evaluated using software (Imagen-Pro Plus) to determine the area of the intermetallic zone.

The morphologies of the metallic substrates (2024-T3 and thermally treated) were evaluated with scanning electron microscopy (SEM), TESCAN S8000. An accelerating voltage of 15 kV was used for the local surface analyses.

Results and discussion

Collection, isolation, and identification of bacteria

The biological sample was collected from the inside of an aircraft wing, which had been exposed to motor oil (Figure 1a). The bacteria were isolated through several serial dilutions and plating rounds of LB solution (Figure 1c) and observed by a microscope that revealed a rod-like shape, the size was close to 1-1.3 µm (Figure 1d).

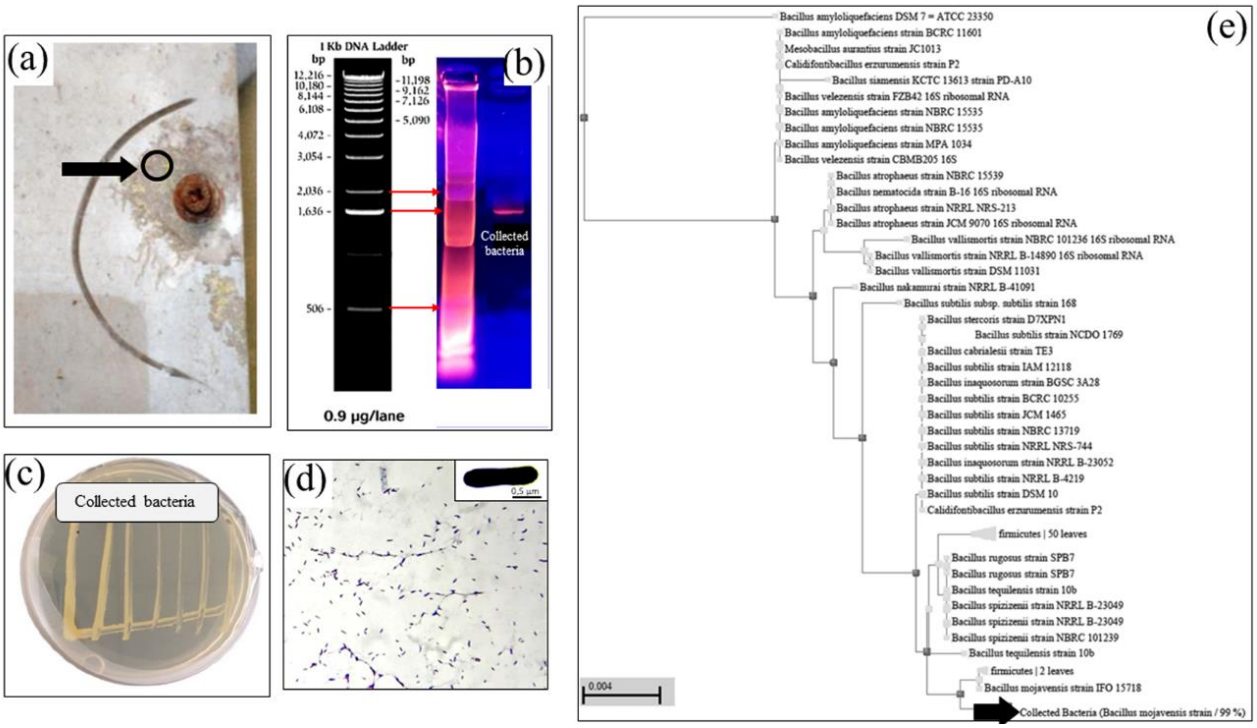

Figure 1. *Isolation and identification of bacteria: (a) collection site, (b) fluorescent images of electrophoresis, (c) growth bacteria on LB-dish, (d) optic image, and (e) phylogenetic tree of members of the genus Bacillus, based on 16S rRNA gene sequences*

To ensure a good identification, after performing the PCR (polymerase chain reaction), an agarose gel electrophoresis was performed (Figure 1b), which indicates the base pairs are in the range of 1400 to 1600 bp. Using the Basic Local Alignment Search Tool (BLAST) database, the 16S rDNA sequence analysis revealed a close relation of collected bacteria with the *Bacillus mojavensis* strain (99.99 %) [22]. Figure 1e shows the neighbour-joining tree based on 16S rRNA gene sequences, showing the phylogenetic relationships.

Thermal treatments

The thermal treatment of 2024-T3 samples included homogenization, quenching, cold work, and natural aging. The main alloying elements are copper and magnesium, contributing to strength through aging phenomena [23]. It is possible to obtain a coherent precipitate (intermetallic compound) with the matrix, small, spherical, and well distributed, which mechanically increases the resistance of the alloy in a homogeneous way.

To evaluate the influence of the intermetallic compound on the susceptibility to corrosion and microbial colonization, this phase was highly concentrated, that is, a thermal treatment that reverses the morphology of the precipitation of T3 treatment. No regulated and established thermal treatments are normally used for this, so in the present study, a series of different thermal treatments that largely concentrated the intermetallic phase of the alloy were carried out. Six unconventional treatments focused on the greatest quantities of the intermetallic phase, with *ThT 05* being the one with the greatest amounts of this phase.

At temperatures below the solvus, this alloy equilibrium state consists of two solid phases: solid solution α, plus an intermetallic compound phase θ (Al_2Cu). When such an alloy is converted to a completely solid solution by keeping it above the solvus temperature, and then the temperature decreases below the solvus, the solid solution becomes supersaturated, and the alloy seeks the two-phase equilibrium condition; the second phase tends to form by precipitation in the solid state [24]. According to the above, with the ThT 05 treatment, the diffusion and concentration of the intermetallic compound in different alloy sectors (such as grain boundaries) were promoted due to the times and cooling used, achieving efficient inversion of treatment of T3.

The thermal treatments performed on aluminium alloys were characterized by optical microscopy. The images obtained and a scheme of the methodology applied are presented in Figure 2.

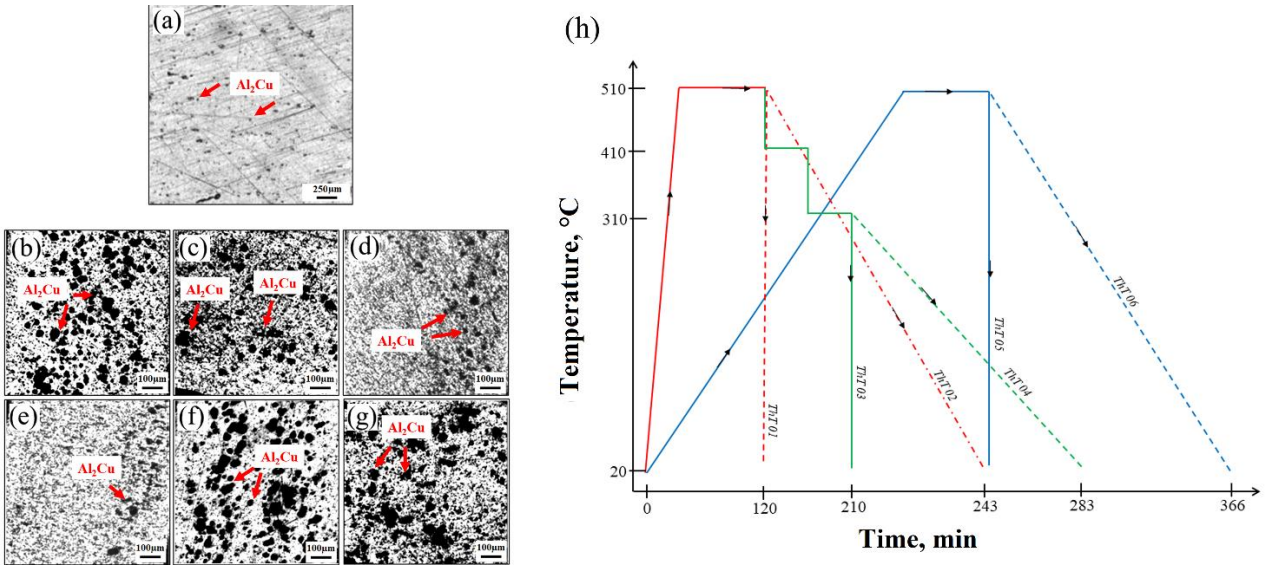

Figure 2. *Optic microscopy images of alloy 2024: (a) 2024-T3, and thermally treated (b) ThT 01, (c) ThT 02, (d) ThT 03, (e) ThT 04, (f) ThT 05, and (g) ThT 06. (h) Scheme of thermal treatment methodology*

Subsequently, the images were evaluated using software to determine the area of the intermetallic precipitates. The results were expressed as a percentage and presented in Table 1.

The percentage of the coverage area of precipitates (second phase) after the heat treatment of 2024 aluminium samples (Table 1) shows increased second phases in the ThT 05 sample compared to the other treatments, with a percentage of ~67.7 %. The heated samples under a temperature rise rate of 4 °C/min (Figure 2h) allowed a high intermetallic concentration with the size of the second phase of ~25 µm (Figure 2g, ThT 05) compared with 5 µm of 2024-T3 (not shown). These results allow us to evaluate the effect of intermetallic of ThT 05 with 2024-T3 exposed to bacteria.

Table 1. *Coverage area of Al_2Cu on the metallic surface of aluminium alloy 2024*

Thermal treatment	2024-T3	ThT 01	ThT 02	ThT 03	ThT 04	ThT 05	ThT 06
Coverage area, %	1.3 ± 0.10	47.2 ± 0.20	38.9 ± 0.15	33.7 ± 0.25	35.9 ± 0.17	67.7 ± 0.13	44.3 ± 0.15

Electrochemical impedance spectroscopy and graphical method analysis

Figures 3 and 4 show the 2024-T3 and ThT 05 EIS plots, respectively. The metallic samples were exposed to a sterile and inoculated medium with *B. mojavensis*.

To facilitate obtaining the EIS parameters through the graphical method, the data were corrected for the electrolyte resistance values, which are reflected in the Nyquist plots with graphs plotted from the origin and observing a constant slope from high to medium frequencies in impedance modulus *vs.* frequency graphs.

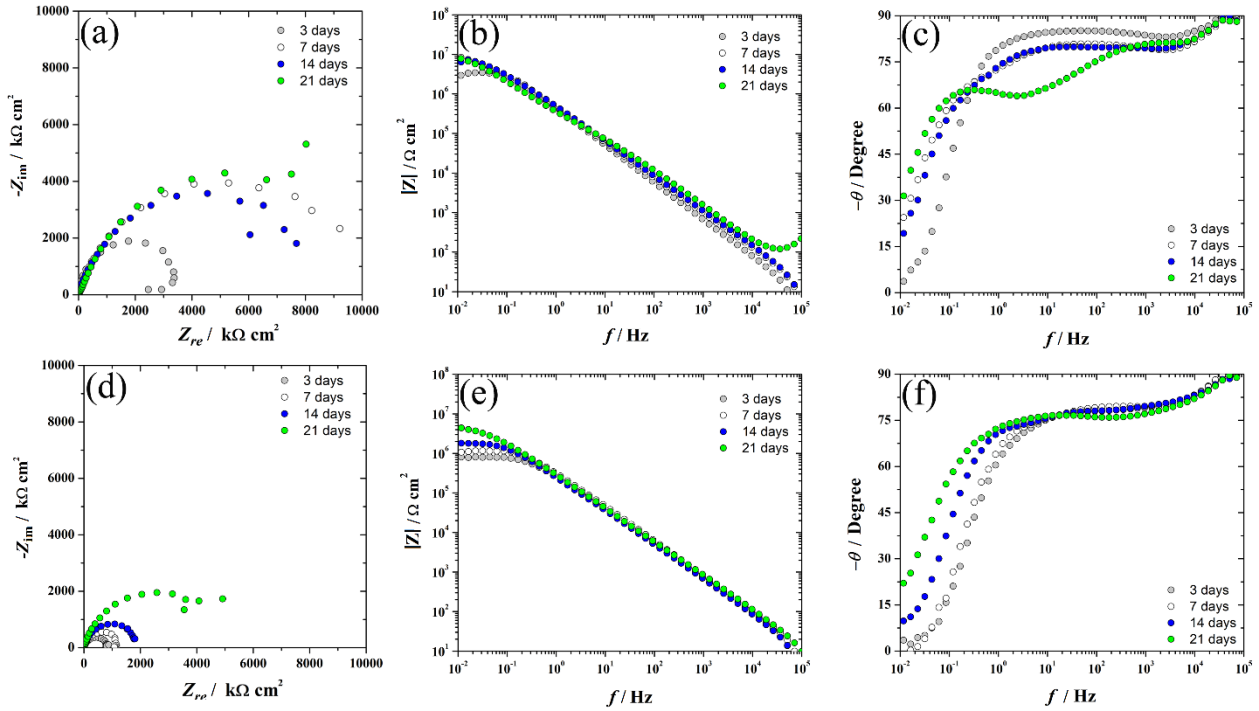

Figure 3. *EIS plots of 2024-T3 exposed to (a, b and c) sterile and (d, e and f) inoculated EC medium with Bacillus mojavensis*

The CPE (constant-phase element) parameters of Q and α were obtained using the graphical method, as shown in Figure 5, and corresponding data are presented in Table 2. The polarization resistance (R_p) and open circuit potential (OCP) were resumed in Figure 6.

The impedance of a CPE is given by Eq (1):

$$Z_{CPE}(\omega) = \frac{1}{(j\omega)^{\alpha} Q} \quad (1)$$

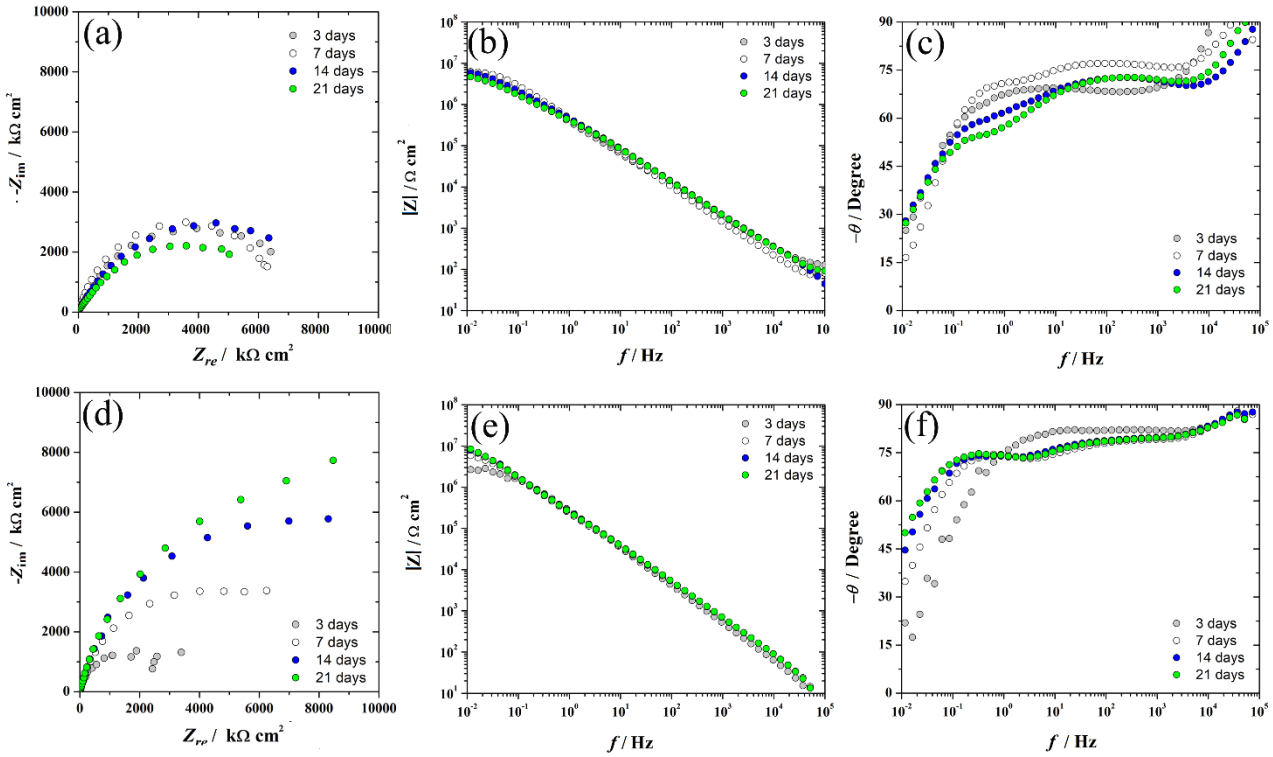

Figure 4. *EIS plots of ThT 05 exposed to (a, b and c) sterile and (d, e and f) inoculated EC medium with Bacillus mojavensis*

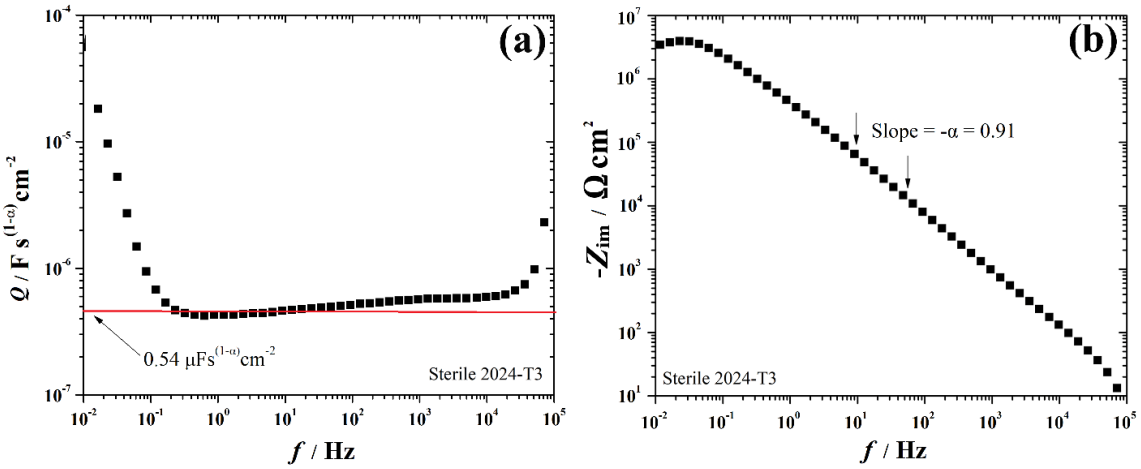

Figure 5*. Graphical analysis of the impedance calculated for EC described by a CPE: (a) variation of the parameter Q of the CPE and (b) variation of the imaginary impedance part as a function of the frequency*

The α parameter (Eq. 1) is dimensionless and varies between 0 and 1. When $\alpha = 1$, it corresponds to a pure capacitor system. Note that the values can also be determined by a graphical method using log Z_{lm} *vs*. log frequency plots, particularly from the negative slope in the frequency range where the CPE appears, as shown in Figure 5(b). In addition, Q is expressed in F s$^{(\alpha-1)}$ cm^{-2}, which can be calculated using the values determined graphically according to Eq. (2):

$$Q = \frac{-1}{Z_i \omega_\alpha} \sin\frac{\alpha\pi}{2} \quad (2)$$

Figure 5(a) shows the variation of Q parameter as a function of the frequency for the 2024-T3 sample after exposure to the solution at 21 °C, revealing that the effective Q values are determined from the plateau at the middle-frequency range [25]. The Q values were determined at the medium frequency range, corresponding to the oxide film element. The Q values represent the heterogeneity of the surfaces and are useful when compared with a control system.

On the other hand, the electrolyte resistance (R_e) values were obtained from Nyquist plots at high frequency, from $Z_{real,}$ when Z_{im} = 0. The R_e gives information about the electrolyte near the metallic surface, and chemical reactions on the surface strongly influence this parameter. The low-frequency graphical method and fitting data were applied to determine the impedance values of the oxide film.

Table 2. *EIS parameters of samples 2024-T3 and ThT 05 after 3, 7, 14 and 21 days of exposure to sterile and inoculated EC solution at 21 °C. Values estimated by graphical method*

Sample	Parameter	Exposure time, day			
		3	7	14	21
Sterile 2024-T3	R_e / Ω cm^2	820.3 ± 10.4	905.4 ± 15.4	1084.6± 8.5	723.3± 7.8
	R / kΩ cm^2	2901.2	8346.6	6406.9	7728.3
	Q / μF s$^{(α-1)}$ cm^{-2}	0.47	0.39	0.41	0.35
	$α$	0.91	0.88	0.89	0.73
Inoculated 2024-T3	R_e / Ω cm^2	1025 ± 17.1	999.3 ± 27.3	722.3 ± 11.1	913.8 ± 8.9
	R / kΩ cm^2	883.2	1040.4	1691.5	5188.9
	Q / μF s$^{(1-α)}$ cm^{-2}	0.61	0.57	0.63	0.55
	α	0.84	0.84	0.85	0.85
Sterile ThT 05	R_e / Ω cm^2	1275 ± 10.1	1400 ± 13.3	1206 ± 15.9	1178 ± 20.2
	R / kΩ cm^2	6419.5	6378.8	6313.4	5212.8
	Q / μF s$^{(1-α)}$ cm^{-2}	0.35	0.33	0.28	0.27
	α	0.76	0.85	0.80	0.80
Inoculated ThT 05	R_e / Ω cm^2	638.8 ± 13.5	805 ± 19.6	941.3 ± 21.2	852.3 ± 10.8
	R / kΩ cm^2	3674.3	6467.3	9089.4	9861.2
	Q / μF s$^{(1-α)}$ cm^{-2}	0.71	0.78	0.61	0.66
	α	0.91	0.84	0.84	0.84

From the EIS results, the specimens of 2024-T3 exposed to sterile EC medium (Figure 3a-c) showed an increased impedance related to exposure time, while the metallic samples exposed to inoculated EC with *B. mojavensis* (Figure 3d-f) showed a decreased impedance for all times compared with the samples exposed to sterile EC medium (Figure 3a-c). General impedance analysis showed an increased impedance with the exposure time for all samples exposed to sterile and inoculated media.

The decreased impedance of alloys exposed to inoculated EC could be attributed to the metabolic activity of bacteria. The effects of corrosion due to the *Bacillus genus* have been reported for 7075 [26] and 2024 alloys [18]. The accelerated corrosion was associated with changes in local pH due to the catalase enzyme, which affects the cathodic reaction. For our studies, the local pH was not determined because the EIS results did not suggest a pH change to an alkaline direction. Still, another process could be associated with organic acid production, which can dissolve the aluminium matrix [27].

The presence of bacteria on ThT 05 surfaces (Figure 4c-f) showed an increased impedance value at all exposure times compared with the samples exposed to a sterile EC medium (Figure 4a-c). Moreover, the impedance increased with the exposure time of all samples in sterile and inoculated medium.

The Q values obtained from EIS (Table 2) of metallic samples exposed to *B. mojavensis* showed an increased value due to the presence of microorganisms in comparison with samples exposed to sterile media. The alfa values of the CPE obtained are very similar, indicating that the system has a deviation of the ideality of a capacitor. Values of 0.61-0.91 were found, and decreased values were shown for ThT 05 exposed to bacteria, due to a diffusion phenomenon that may associated with organic materials from dead cells adsorbed on the metallic surfaces.

R_e values are generally stable for each system in time, and the change of R_e with the exposition time is similar. The values of 2024-T3 exposed to sterile media and bacteria are almost the same

due to the same corrosion product. This means the mechanism is very similar, suggesting that bacteria only influence kinetic reactions. A decreased R_e value of ThT 05 exposed to *B. mojavensis* was observed, probably due to the dead cell and lysis, which can release active compounds and molecules that could react with the metallic surface, changing the R_e.

OCP results (Figure 6a) showed a displacement to positive values for 2024-T3 and ThT 05 exposed to bacteria, in contrast to samples exposed to sterile EC. However, these changes could have a different cause because bacteria increase corrosion of 2024-T3 and inhibit corrosion of ThT 05.

The change towards positive values is associated with microorganisms on the metal surface. Results obtained by Starosvetsky *et al*. [28] showed that bacteria adhered to a steel surface shift the potential in a positive direction by approximately 100 mV. The results were attributed to the formation of corrosion products. Little and Lee [3] indicated that a shift in positive values of OCP could reflect bacterial growth and a change in the local environment induced by the metabolic activities of the bacteria, resulting in metal corrosion.

On the other hand, the decreased OCP values of ThT 05 could be attributed to the increased second phases on ThT 05 (copper-rich). These cathodic sites could shift their potential to the cathodic region.

Figure 6b shows the resistance values of the 2024-T3 and ThT 05 samples exposed to sterile and inoculated EC with B. mojavensis. The resistance values were obtained from the Bode plot (modulus) at 20 mHz. The values were compared with both, those obtained with the Nyquist plot when Z_{im} = 0 (low frequency) and the curve fitting method. A marked decrease in values can be observed for 2024--T3 exposed to bacteria compared to those exposed to a sterile medium. The decreased resistance may be due to the activity of bacteria, which accelerate the degradation of the metallic substrate. On the other hand, in the case of ThT 05, an increase in corrosion resistance values was observed, possibly due to the antibacterial properties of copper [29]. An accumulation of dead cells on the metallic surface was speculated, which could show a protective effect of bacteria over the corrosion process.

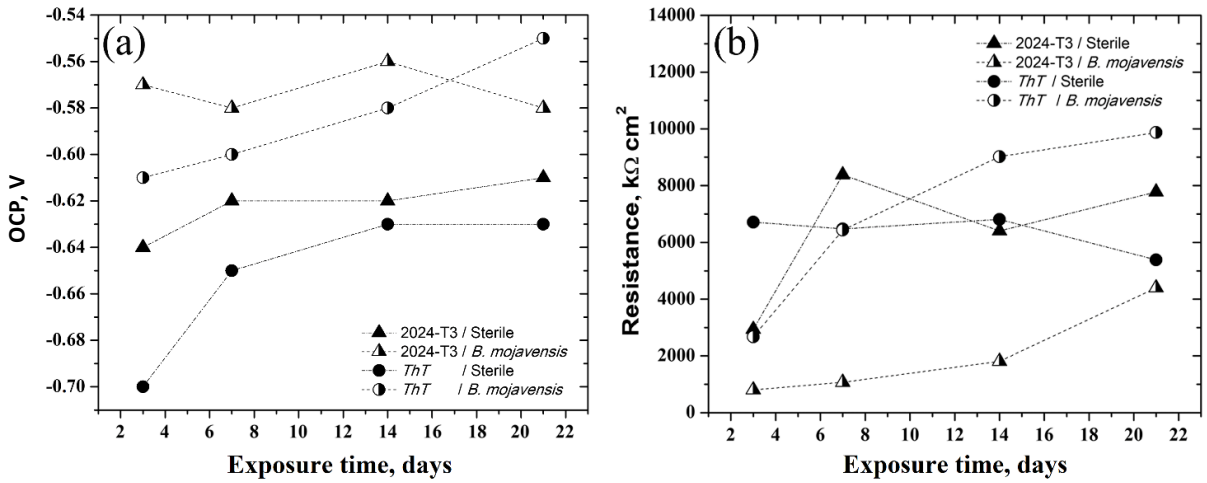

Figure 6. *Open circuit potential (a) and oxide film resistance (b) of 2024-T3 and ThT 05 exposed to sterile and inoculated EC media*

Equivalent circuit and fitting of experimental data

In order to obtain an equivalent circuit, the data were fitted with different software. Due to the change observed on the metallic substrate, a specific difficulty of EIS experiments is the stability during a measurement. Testing the integrity of measured data is an important analysis issue. The Kramers-Kronig relation was used to determine the integrity, this was carried out using an evaluation between the real and imaginary part of the electrical impedance defined by plotting the measured data Z' and Z'' against those calculated from the integrals [30].

A more detailed analysis may be obtained by an examination of residual errors shown in Figure 7, indicating that the measurement model provided a good fit to the data.

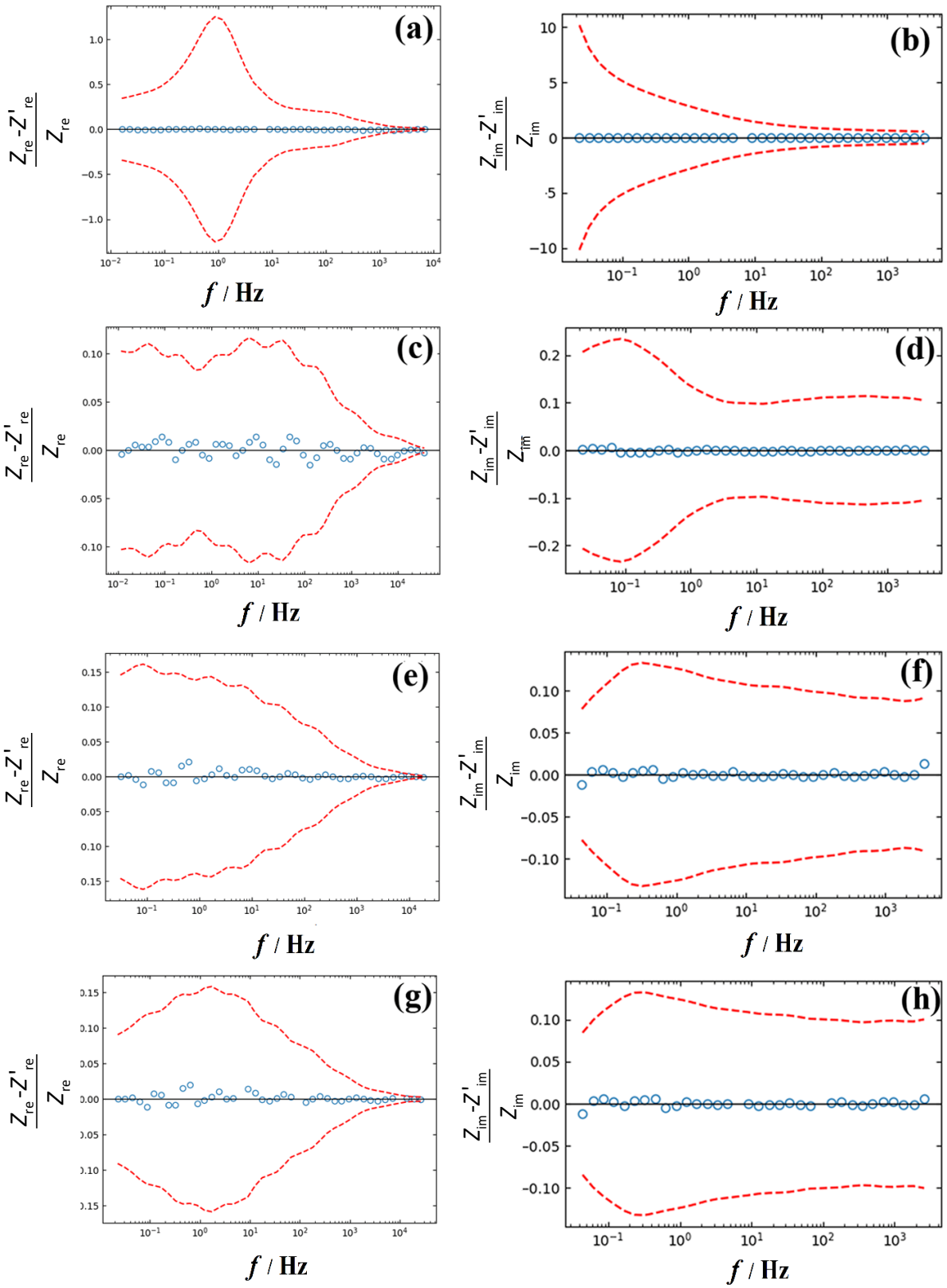

***Figure 7**. Normalized residual errors resulting from a measurement model fit (Z´) and of the measurement of metallic samples (Z) at 21 days of exposition to the sterile electrolyte of (a,b) 2024-T3 and (c,d) ThT 05, and exposed to inoculated media (e,f) 2024-T3 and (d) ThT 05. (a, c, e and g) real part and (b, d, f and h) imaginary part*

Figure 7 shows the residual errors (circles) of real and imaginary parts of the Nyquist plot. Red dashed lines represent 95.4 % confidence intervals for the model. The residual errors fall within the 95.4 % confidence interval for the model, and thus, the data may be considered consistent with the Kramers-Kronig relations. This method allows us to have data within the reliable frequency range, which will later be used for a second approach using Zview software and DRTtool.

The main goal of the DRT is to identify the characteristic distribution of typical EIS timescales. The experimental data measured at given frequencies are "fitted" against a model (Z_{DRT}) obtained from the following expression.

$$Z_{DRT} = R_{\infty} + \int_{-\infty}^{\infty} \frac{\gamma(\tau)}{1 + j\omega\tau} \mathrm{d}\tau \quad (3)$$

where ω is the angular frequency, R_{∞} is the ohmic resistance, j is the imaginary part, and $\gamma(\tau)$ is the desired DRT function. The "model" is commonly approximated using Voigt circuits. This approximation can be understood by writing $\gamma(\tau)$ as a sum of Dirac distributions $\delta(\tau)$ centered at times τ_1, τ_2 , … , τ_{1M}, *i.e.*

$$\gamma(\tau) = \sum_{m=1}^{M} x_m \delta(\tau - \tau_m) \quad (4)$$

where x_m are unknown parameters to be estimated by fitting. The results are shown in Figure 8 (a-b), where γ(τ) is the distribution function of relaxation times.

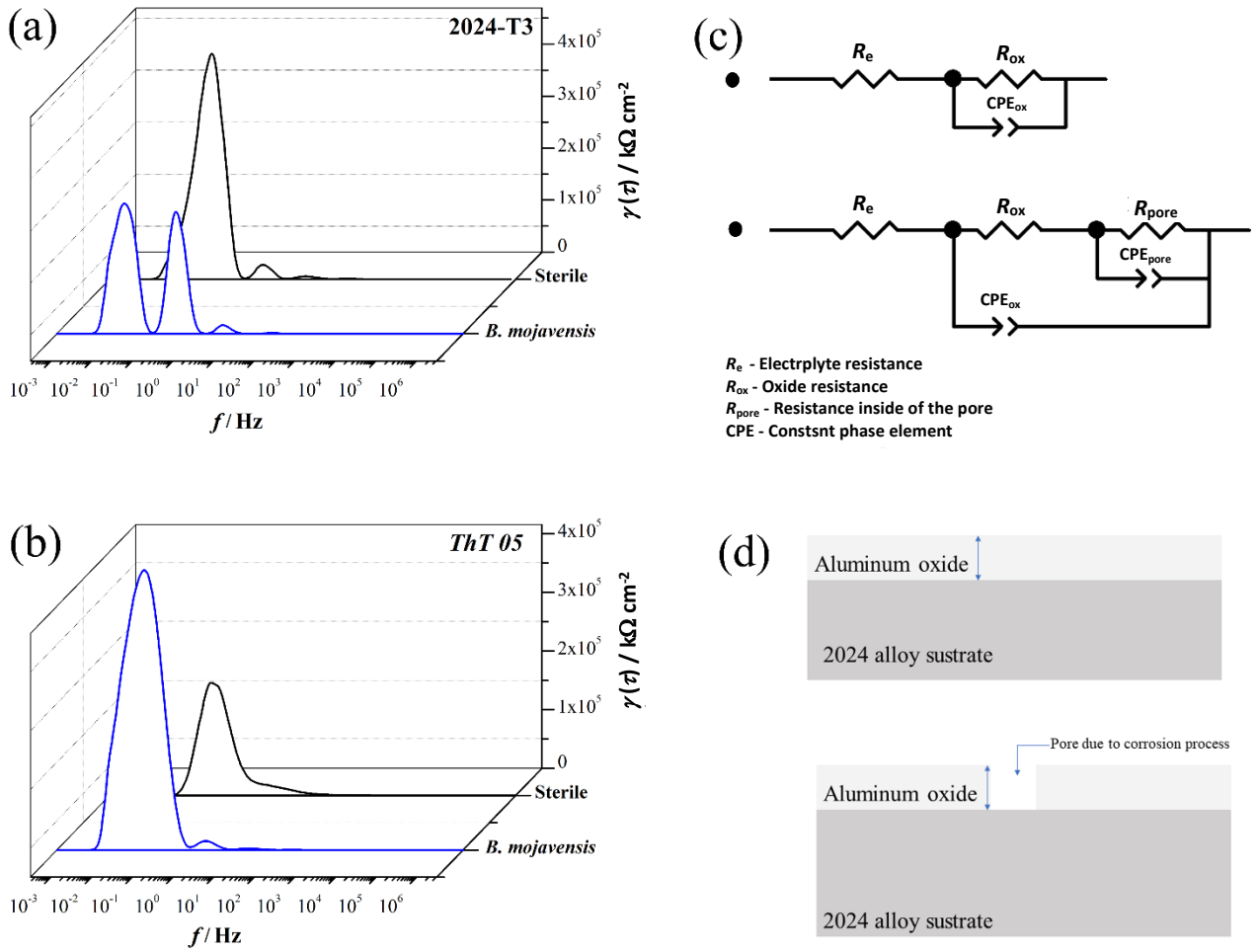

Figure 8. *DRT-function (γ(τ)) plots of (a) 2024-T3 and (b) ThT 05 exposed to inoculated media. (c) proposed equivalent circuits and (d) scheme of oxide film*

The analysis of the distribution of relaxation times, in general, showed single-time constants associated with the aluminium oxide and pores due to the corrosion process. For 2024-T3 exposed to bacteria, an extra time constant is obtained, which could be associated with biofilms adhered to metallic surfaces [29]. The proposed equivalent circuit considering time constants is shown in Figure 8c. A representative scheme of surface conditions is shown in Figure 8d.

To validate the equivalent circuit, these were considered to fit data using Zview. The fitted impedance data of 2024-T3 and ThT 05 exposed to sterile and inoculated media with *B. mojavensis* are presented in Figure 9, where measured data are shown by circles and fitted data by lines. The results showed a good correlation with the circuit selected. The results showed a CPE (constant phase element) behavior, which could be related to the heterogeneous surface.

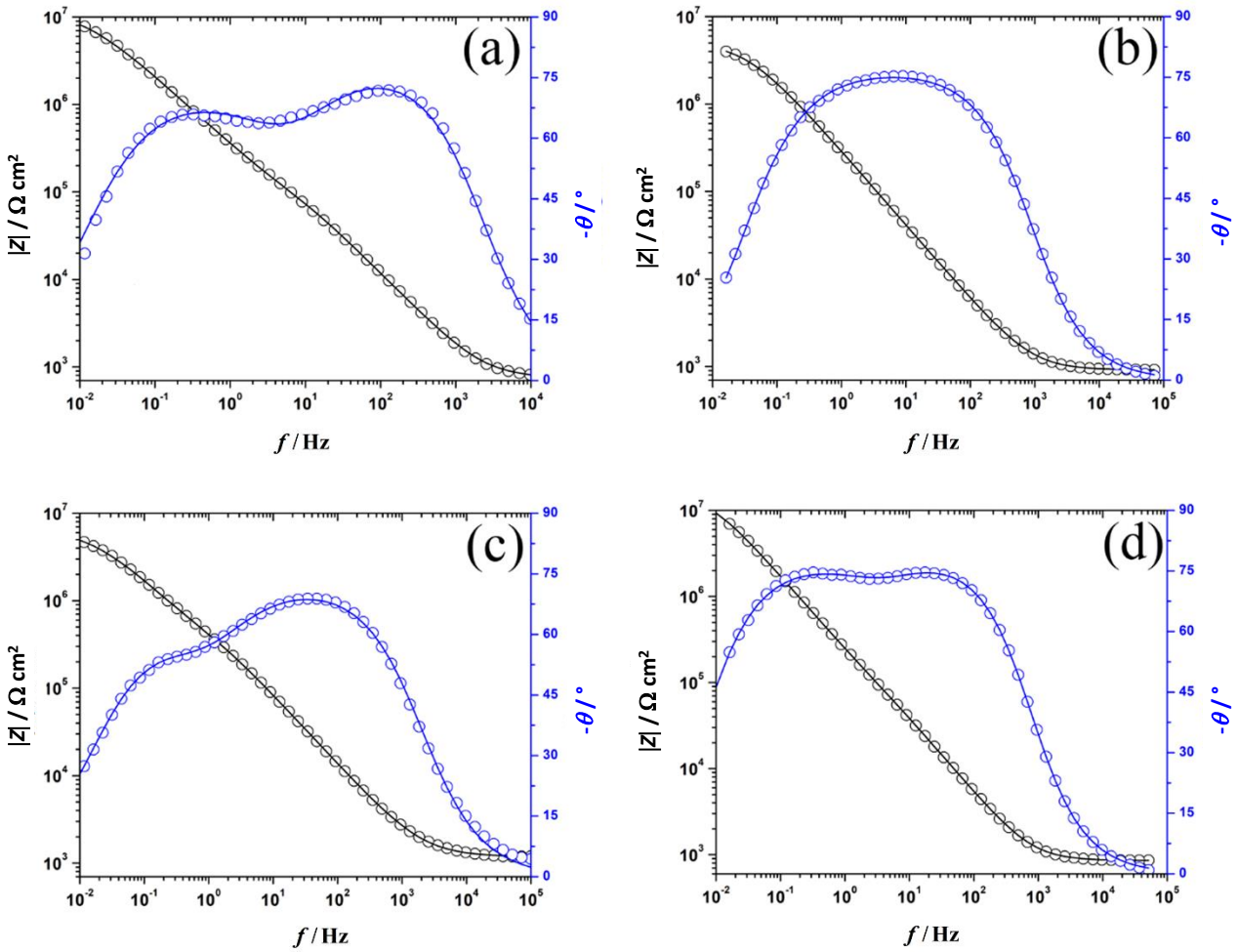

***Figure 9**. Fitted Bode impedance data of metallic samples at 21 days of exposition. Sterile electrolyte (a) 2024-T3 and (b) ThT 05, and inoculated media (c) 2024-T3 and (d) ThT 05. The circles represent the experimental data and lines the fitted data*

Resistance data analysis

Resistance values were obtained at low frequency using log modulus *Z vs*. log *f* but these values could also be obtained by Nyquist plots, as shown in Figure 10.

An alternative way to obtain the resistance values could be using SIMAD with a proposed circuit and the Kramers-Kronig correlation (k-kC). However, due to the discarded values of data due to k-kC, not all results of resistance were obtained. The values considering different methods are shown in Table 3

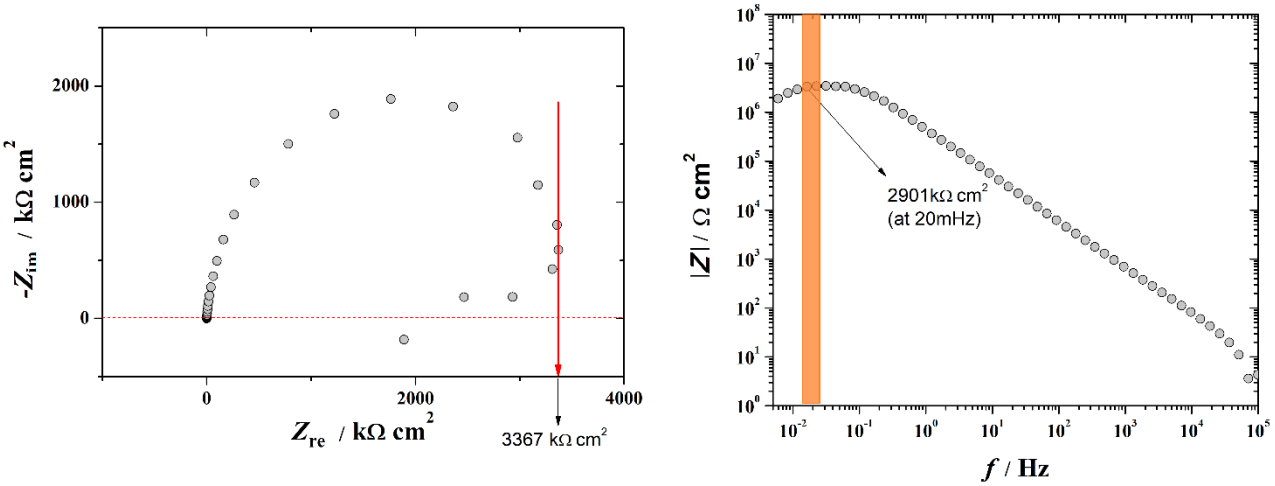

***Figure 10**. Determination of resistance values by graphical analysis from (a) Nyquist and (b) Bode plot of alloy exposure 3 days to sterile electrolyte*

***Table 3.** Comparison of resistance values obtained by different methods*

Samples	Time, day	Graphical method		Software method	
		Modulus graph	Nyquist graph	SIMAD	Kramers-Kronig
		R / kΩ cm² (at 20 mHz)	R / kΩ cm²* (HF at Z_{im}=0)	Resistance, kΩ cm²	
Sterile 2024	3	2901	3367	3800	Not applied
	7	8346	9238	9600	Not applied
	14	6406	7702	8400	Not applied
	21	7728	8002	13000	9600
Sterile ThT 05	3	6419	6425	8400	Not applied
	7	6378	6333	15000	10000
	14	6313	6310	9200	Not applied
	21	5212	5001	6800	Not applied
Inoculated 2024	3	883	93	800	Not applied
	7	1040	30	1300	Not applied
	14	1691	334	1900	Not applied
	21	5188	1701	4900	Not applied
Inoculated ThT 05	3	3674	1388	2800	Not applied
	7	6467	3375	8800	Not applied
	14	9089	5853	15000	1800
	21	9861	7754	18000	4800

*R_{HF}- Resistance obtained at high frequency

Table 3 shows that the resistance values vary from one method to another, the method where it is extrapolated to the Z_{real} axis contains a greater error because the graphs do not close completely, which requires an approximation of the graph that is not good for all the data. SIMAD only allows us to determine the electrolyte resistance because the circuit used has a good response only at high frequencies, while at high frequencies, the values obtained for resistance were inconsistent. Due to the above, the authors decided to carry out the analysis of data obtained by the graphic method. Despite this, the data have been evaluated and considered qualitatively due to the complexity of the system.

Scanning electron microscopy

The effect of the *B. mojavensis* bacterium on 2024-T3 samples was observed by SEM. The results are shown in Figure 10. The alloy exposed to sterile EC (Figure 11a) showed a typical surface with

corrosion products associated with the second phase. EDS analysis (Figure 11c) suggests an inter-metallic phase chemical composition could be Al_2CuMg or Al_2Cu, since these are the predominant precipitating phases that occur in 2XXX alloys [31]. SEM images of alloy exposed to inoculated EC with bacteria *B. mojavensis* show a highly degraded surface with lost material (Figure 11b). EDS examination of the alloy corrosion product (Figure 10d) showed a copper-rich site probably associated with an accumulation of copper by local corrosion, due to the presence of precipitating phases rich in Cu [32].

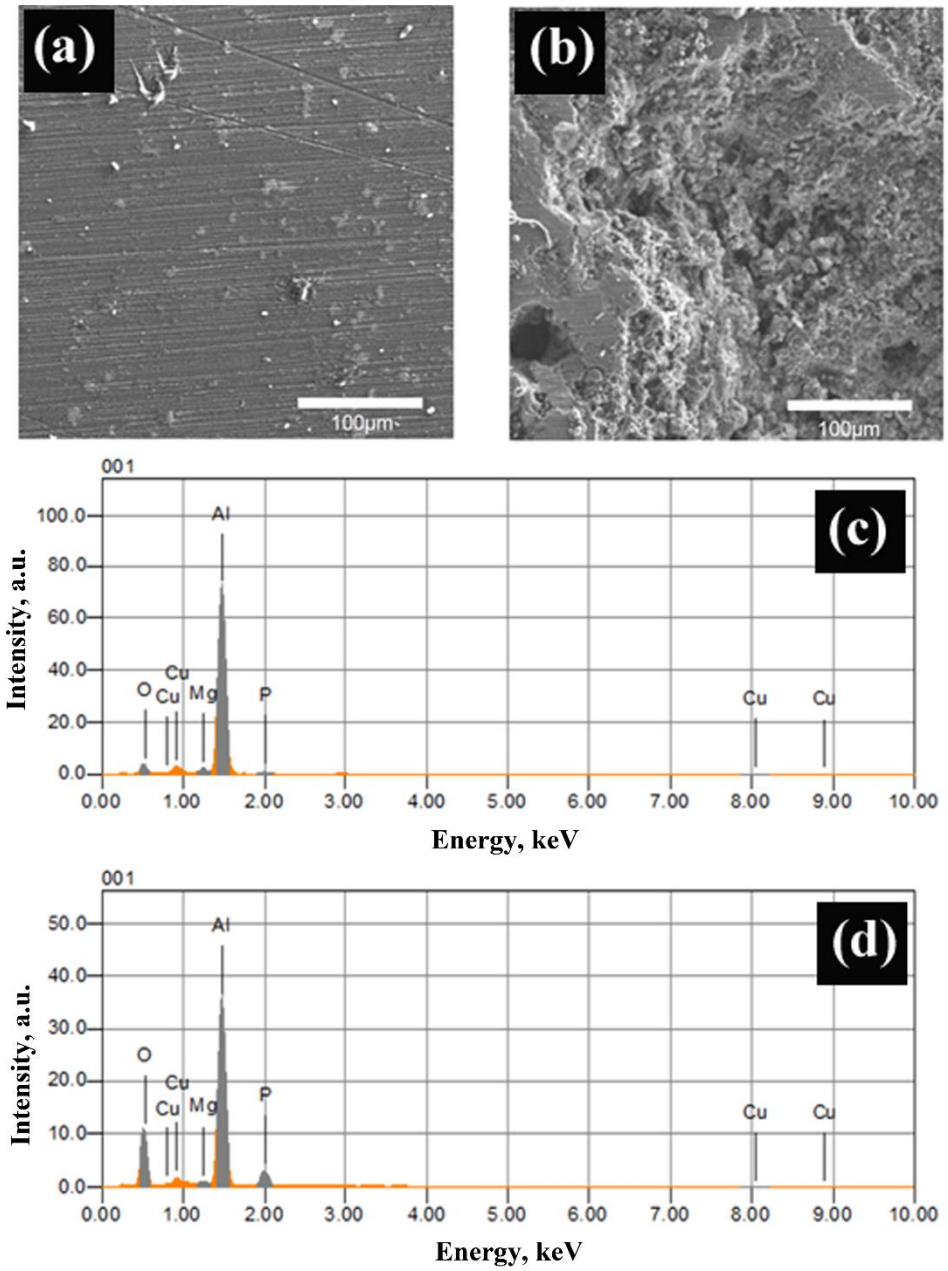

Figure 11. *SEM images of 2024-T3 exposed to (a) sterile and (b) inoculated electrolyte with B. mojavensis. Corresponding EDS (c) and (d)*

Conclusions

The present work evaluated the effect of the presence of second phases in the corrosion catalyzed by *B. mojavensis* bacteria. The electrochemical results showed the following important results:

1. Alloys with adequate heat treatment allowed to obtain surfaces with approximately ~67 % of the surface area corresponding to Al_2Cu type precipitates.

2. Alloys 2024-T3 showed accelerated corrosion when exposed to *B. mojavensis* bacteria.
3. Alloys designated ThT 05 showed a marked increase in impedance when exposed to *B. mojavensis* bacteria, suggesting a considerable slowing of corrosion.

The effect of the second phase in the corrosion and biocorrosion processes is crucial for understanding the phenomenon. The presence of Al_2Cu precipitates acts as cathode sites in aluminium alloys and is the cause of local and accelerated corrosion in these alloys in a chloride medium. The second phase could also affect the biocorrosion processes. However, using ~67 % on metal surfaces, the corrosive effect is masked by many precipitates, which does not allow adequate visualization of the bacteria in the corrosive process. Rather, a protective effect was observed, and the analysis was difficult using the techniques used. Detailed studies and methods such as XPS, are required to characterize the corrosion products.

***Acknowledgements**: This work was supported by Agencia Nacional de Investigación y Dearrollo (ANID grants 11170419).*

References

[1] F. Ezzohra, E. Garchani, H. Lgaz, H. Lee, S.M. Ibrahim, M. Chafiq, Y. Gun, M. Rachid, Effects of heat treatment on the corrosion behavior and mechanical properties of aluminium alloy 2024, *Journal of Materials Research and Technology* **25** (2023) 1355-1363. https://doi.org/10.1016/j.jmrt.2023.05.278

[2] G. S. Chen, K.-C. Wan, M. Gao, R. P. Wei, T. H. Flournoy, Transition from pitting to fatigue crack growth—modeling of corrosion fatigue crack nucleation in a 2024-T3 aluminium alloy, *Materials Science and Engineering A* **219** (1996) 126-132. https://doi.org/10.1016/S0921-5093(96)10414-7

[3] B .J. Little, J. S. Lee, *Microbiologically Influenced Corrosion*, John Wiley & Sons Inc., Hoboken, New Jersey, USA, 2007. https://doi.org/10.1002/047011245X

[4] J. Yang, Y. Zhang, W. Chang, Y. Lou, H. Qian, Microbiologically influenced corrosion of FeCoNiCrMn high-entropy alloys by *Pseudomonas aeruginosa* biofilm, *Frontiers in Microbiology* **13** (2022) 1009310. https://doi.org/10.3389/fmicb.2022.1009310

[5] S. Sivasankaran, Aluminium Alloys - Recent Trends in Processing, Characterization, Mechanical Behavior and Applications, InTech Open, London, United Kingdom, 2017. https://doi.org/10.5772/68032

[6] J. Espinoza-Vergara, P. Molina, M. Walter, M. Gulppi, N. Vejar, F. Melo, M. Urzua, H. Muñoz, J. H. Zagal, X. Zhou, M. I. Azocar, M. A. Paez, Effect of pH on the Electrochemical Behavior of Hydrogen Peroxide in the Presence of *Pseudomonas aeruginosa*, *Frontiers in Bioengineering and Biotechnology* **9** (2021) 749057. https://doi.org/10.3389/fbioe.2021.749057

[7] S. Baeza, N. Vejar, M. Gulppi, M. Azocar, F. Melo, A. Monsalve, J. Pérez-Donoso, C.C. Vásquez, J. Pavez, J.H. Zagal, X. Zhou, G.E. Thompson, M. A. Páez, New evidence on the role of catalase in *Escherichia coli*–mediated biocorrosion, *Corrosion Science* **67** (2013) 32-41. https://doi.org/10.1016/j.corsci.2012.09.047

[8] L. Kuchariková, T. Liptáková, E. Tillová, D. Kajánek, E. Schmidová, Role of chemical composition in corrosion of aluminium alloys, *Metals (Basel)* **8** (2018) 581. https://doi.org/10.3390/met8080581

[9] L. M. Escobar, J. R. Rivera, E. Arbelaez, L. F. Torres, A. Villafañe, D. Díaz-Báez, I. Mora, G. I. Lafaurie, M. Tanaka, Comparison of Cell Viability and Chemical Composition of Six Latest Generation Orthodontic Wires, *International Journal of Biomaterials* **2021** (2021) 8885290. https://doi.org/10.1155/2021/8885290

[10] I. B. Beech, J. Sunner, Biocorrosion: Towards understanding interactions between biofilms and metals, *Current Opinion in Biotechnology* **15** (2004) 181-186. https://doi.org/10.1016/j.copbio.2004.05.001
[11] F. Mansfeld, The interaction of bacteria and metal surfaces, *Electrochimica Acta* **52** (2007) 7670-7680. https://doi.org/10.1016/j.electacta.2007.05.006
[12] B. M. Rosales, M. Iannuzzi, Aluminium AA2024 T351 aeronautical alloy. Part 1. Microbial influenced corrosion analysis, *Materials Science and Engineering A* **472** (2008) 15-25. https://doi.org/10.1016/j.msea.2007.06.079
[13] D. Hu, W. Lin, J. Zeng, P. Wu, M. Zhang, L. Guo, C. Ye, K. Wan, X. Yu, Profiling the microbial contamination in aviation fuel from an airport, *Biofouling* **35** (2019) 856-869. https://doi.org/10.1080/08927014.2019.1671977
[14] C. J. McNamara, T. D. Perry, R. Leard, K. Bearce, J. Dante, R. Mitchell, Corrosion of aluminium alloy 2024 by microorganisms isolated from aircraft fuel tanks, *Biofouling* **21** (2005) 257-265. https://doi.org/10.1080/08927010500389921
[15] R. Smith, *Biodeterioration and biodegradation*, Springer Dordrecht, Germany, 1991. ISBN 978-1-85166-626-3
[16] N. D. Vejar, J. Sacre, B. Collao, J. Perez-Donoso, M. A. Páez, F. Pineda, B. Worker, M. Sancy, Enhanced corrosion of 7075 alloy by the presence of *Bacillus megaterium*, *International Journal of Electrochemical Science* **11** (2016) 9723-9733. https://doi.org/10.20964/2016.11.33
[17] M. Sancy, A. Abarzúa, M.I. Azócar, J.M. Blamey, F. Boehmwald, G. Gómez, N. Vejar, M. Páez, Biofilm formation on aluminium alloy 2024: A laboratory study, *Journal of Electroanalytical Chemistry* **737** (2015) 212-217. https://doi.org/10.1016/j.jelechem.2014.08.015
[18] N. Vejar, S. Gutiérrez, N. Tareelap, C. Alvarado, R. Solís, C. Guerra, F. Pineda, M. Sancy, M. Páez, Influence of *Bacillus safensis* and *Bacillus pumilus* on the electrochemical behavior of 2024-T3 aluminium alloy, *Bioelectrochemistry* **143** (2022) 107950. https://doi.org/10.1016/j.bioelechem.2021.107950
[19] Q. Wang, G.M. Garrity, J.M. Tiedje, J.R. Cole, Naïve Bayesian classifier for rapid assignment of rRNA sequences into the new bacterial taxonomy, *Applied and Environmental Microbiology* **73** (2007) 5261-5267. https://doi.org/10.1128/AEM.00062-07
[20] C. Pillay, J. Lin, Metal corrosion by aerobic bacteria isolated from stimulated corrosion systems: Effects of additional nitrate sources, *International Biodeterioration & Biodegradation* **83** (2013) 158-165. https://doi.org/10.1016/j.ibiod.2013.05.013
[21] J. H. Kwon, P. Choi, S. Jo, H. Oh, K.Y. Cho, Y. K. Lee, S. Kim, K. S. Eom, Identification of electrode degradation by carbon corrosion in polymer electrolyte membrane fuel cells using the distribution of relaxation time analysis, *Electrochimica Acta* **414** (2022) 140219. https://doi.org/10.1016/j.electacta.2022.140219
[22] M. Kiran Kumar, C. Tyagi, A. Sahu, N. Desai, J. Manjhi, K. C. Mohan, Y. P. Reddy, S. K. Tiwari, L. K. Tomar, V. K. Sharma, Identification and Characterization of Staphylococcus aureus 16S rRNA gene isolated from different Food Specimens from South Indian Region, *Journal of Drug Delivery and Therapeutics* **10** (2020) 24-32. https://doi.org/10.22270/jddt.v10i5.4340
[23] A. Monsalve, L. Parra, D. Baeza, R. Solís, H. Palza, Mechanical properties and morphological characteristics of ARALL reinforced with TRGO doped epoxy resin, *Revista Matēria* **23** (2018) e-12228. https://doi.org/10.1590/s1517-707620180004.0562
[24] *ASM Handbook, Volume 4*, *Heat treating*, ASM International, Materials Park, Ohio, USA, 1991. ISBN 978 087 1703 798
[25] V. Nelson, J. Rojas, C. Alvarado G., R. Solís, F. Pineda, M. Sancy, L. Muñoz, M. Páez, Alumoxane film for corrosion protection of 2024 aluminium alloy, *Journal of Materials Research and Technology* **26** (2023) 4942-4956. https://doi.org/10.1016/j.jmrt.2023.08.192

[26] N. D. Vejar, J. Sacre, B. Collao, J. Perez-Donoso, M. A. Páez, F. Pineda, B. Worker, M. Sancy, Enhanced Corrosion of 7075 Alloy by the Presence of *Bacillus megaterium*, *International Journal of Electrochemical Science* **11** (2016) 9723-9733. https://doi.org/10.20964/2016.11.33
[27] R. Jia, D. Yang, D. Xu, T. Gu, Anaerobic Corrosion of 304 Stainless Steel Caused by the *Pseudomonas aeruginosa* Biofilm, *Frontiers in Microbiology* **8** (2017) 2335. https://doi.org/10.3389/fmicb.2017.02335
[28] D. Starosvetsky, J. Starosvetsky, R. Armon, Y. Ein-Eli, A peculiar cathodic process during iron and steel corrosion in sulfate reducing bacteria (SRB) media, *Corrosion Science* **52** (2010) 1536-1540. https://doi.org/10.1016/j.corsci.2010.01.013
[29] S. Sagadevan, S. Vennila, A.R. Marlinda, Y. Al-Douri, M. Rafie Johan, J. Anita Lett, Synthesis and evaluation of the structural, optical, and antibacterial properties of copper oxide nanoparticles, *Applied Physics A* **125** (2019) 489. https://doi.org/10.1007/s00339-019-2785-4
[30] C. You, M.A. Zabara, M.E. Orazem, B. Ulgut, Application of the Kramers-Kronig Relations to Multi-Sine Electrochemical Impedance Measurements, *Journal of The Electrochemical Society* **167** (2020) 020515. https://doi.org/10.1149/1945-7111/ab6824
[31] M.-L. de Bonfils-Lahovary, L. Laffont, C. Blanc, Characterization of intergranular corrosion defects in a 2024 T351 aluminium alloy, C*orrosion Science* **119** (2017) 60-67. https://doi.org/10.1016/j.corsci.2017.02.020
[32] E. Ghanbari, A. Saatchi, X. Lei, D.D. Macdonald, Studies on pitting corrosion of Al-Cu-Li alloys Part II: Breakdown potential and pit initiation, *Materials* **12** (2019) 1786. https://doi.org/10.3390/ma12111786

J. Electrochem. Sci. Eng. **14(2)** (2024) 231-245; http://dx.doi.org/10.5599/jese.2181

Open Access : : ISSN 1847-9286
www.jESE-online.org

Original scientific paper

Corrosion inhibition performance of copper using N-benzylhydrazinecarbothioamide in a 3.5 % NaCl solution

Arafat Toghan[1,2,✉], Hanan Alhussain[1], Azza Attia[3], O. K. Alduaij[1], Ahmed Fawzy[4], A. M. Eldesoky[5] and Ahmed A. Farag[6,✉]

[1]*Chemistry Department, College of Science, Imam Mohammad Ibn Saud Islamic University (IMSIU), Riyadh 11623, Saudi Arabia*
[2]*Chemistry Department, Faculty of Science, South Valley University, Qena 83523, Egypt*
[3]*Chemistry Department, Faculty of Science and Arts, Najran University, Najran, Saudi Arabia*
[4]*Chemistry Department, Faculty of Science, Assiut University, Assiut 71516, Egypt*
[5]*Department of Chemistry, University College in Al-Qunfudhah 21912, Umm Al-Qura University, Saudi Arabia*
[6]*Egyptian Petroleum Research Institute (EPRI), Nasr City, 11727 Cairo, Egypt*

Corresponding authors: ✉ arafat.toghan@yahoo.com, aatahmed@imamu.edu.sa; ✉ ahmedafm@yahoo.com

Received: November 14, 2023; Accepted: February 7, 2024; Published: February 19, 2024

Abstract

In this report, N-benzylhydrazinecarbothioamide (BHCTA) was investigated as an organic inhibitor for the corrosion of copper substrate in 3.5 wt.% sodium chloride electrolyte at 298 K. The inhibition efficiency of BHCTA was examined using electrochemical, chemical and theoretical tools. The gained outcomes indicated a supreme inhibition efficiency of BHCTA which exceeded 95 % upon addition of 1.00 mM of BHCTA. Such supreme efficiency was discussed on the basis of decisive adsorption of BHCTA molecules on the copper substrate that hinders concurrently the anodic oxidation and cathodic reduction reactions progressions. The adsorption of BHCTA on the copper surface was discovered to obey Langmuir isotherm. The resulting value of $\Delta G_{ads}^{0} = -35.7$ *kJ mol*$^{-1}$ *indicates that BHCTA molecules adsorb on the copper surface through a spontaneous mix of physisorption and chemisorption processes. A scanning electron microscope was used to examine the effect of BHCTA adsorption on the morphology of the copper surface. Theoretical calculations showed that BHCTA has good adsorption properties on Cu substrate. There is a good consistency between the applied experimental and theoretical tools, confirming the validity of the gained outcomes.*

Keywords

Copper corrosion; aqueous NaCl; organic inhibitor; adsorption

Introduction

Corrosion of metals is undoubtedly the most significant problem with significant financial consequences associated with utilizing metals in the workplaces. Similar to numerous metals, copper and its alloys are widely utilized in the chemical and electronic sectors because of their exceptional electrical conductivity, ductility, and corrosion resistance [1]. Copper-surface can readily develop an oxide layer in mild environmental conditions which has a slight protective effect, but copper can still sustain significant damage in environments where chloride ions are present. The rate of corrosion is usually reduced when a protective oxide layer forms on the metal surface. Unfortunately, some dissolved chemicals, especially nitrates, sulfates, and chlorides, weaken this barrier by producing soluble products. In water or other humid environments, copper will eventually undergo chemical degradation. As a result of these chemical attacks, the metal dissolves due to oxidation brought by dissolved oxygen. Localized and perhaps more dangerous pitting corrosion resulted from this. Applying corrosion inhibitors, or substances that can stop the corrosion process, strengthens metal resistance to corrosive chemicals. It is worth noting that one of the most important things that distinguishes heterocyclic organic inhibitors from others is that they contain some electron-donating atoms such as nitrogen, sulfur, and oxygen, which help them to adsorb spontaneously onto the surface of the metal and form a protective layer against corrosion.

Finding a potent copper inhibitor in a chloride solution has enormous practical significance. It is commonly agreed that the anodic dissolving of Cu in chloride surroundings is affected by the chloride content. At chloride content lesser than 1 M, the Cu dissolving happens *via* creation of CuCl, that is not sufficiently protecting and is changed to solvable $CuCl_2^-$ *via* reaction with extra chloride [2,3]. The dissolving mechanism of Cu in chloride solutions can be described by equations (1) and (2):

$Cu + Cl^- \leftrightarrow CuCl + e^-$ (1)

$CuCl + Cl^- \leftrightarrow CuCl_2^- + e^-$ (2)

Higher complexes of copper, like $CuCl_3^{2-}$ and, $CuCl_4^{3-}$, as well as those with less chlorides, like CuCl and $CuCl_2^-$, are produced at concentrations greater than 1 M [3]. Using organic inhibitors is one of the most crucial strategies for shielding copper from corrosion [4]. Chen *et al.* investigated the organic inhibitor 2,4,6-trimercapto-1,3,5-triazine for copper corrosion in 0.5 M NaCl solution. It was demonstrated that the examined compound is a mixed corrosion inhibitor, with its highest corrosion inhibition efficacy reaching 95.6 % [5]. Liao *et al.* [6] investigated the combined effects of sodium diethyldithiocarbamate as a corrosion inhibitor for copper corrosion in 3 % NaCl solution that achieved 99 % protective efficacy. It is also important to remember that the main characteristic that sets benzyl hydrazine carbothioamide compounds apart from other materials, is their environmental safety. This allows for a variety of uses, particularly in the pharmaceutical and medical industries, where they can be used as effective corrosion inhibitors as well as for anti-inflammatory, analgesic, anti-bacterial, and anti-cancer purposes. In particular, benzyl hydrazine carbothioamide and related compounds are efficient inhibitors of corrosion. The polar groups of these compounds and their capacity to form combinations with the metal surface-an additional benefit-likely contribute to their improved adsorption on metallic surfaces under abrasive conditions. Furthermore, the abundance of π-electrons and pairs of unshared electrons in the nitrogen and sulfur atoms interact with the d-orbitals of any metal to create a shielding coating.

In view of all said above, the present work aims to explore the corrosion inhibition performance of copper by N-benzylhydrazinecarbothioamide (BHCTA) in a 3.5 wt.% NaCl solution at 298 K, using a number of chemical and electrochemical methods. Figure 1 displays the chemical structure of N-benzylhydrazinecarbothioamide (BHCTA). By joining various experimental outcomes and quantum

chemical calculations, possible adsorption and inhibition mechanisms of BHCTA on the copper substrate can be revealed. To date, scientists remain interested in enhancing the heterocycles capacity to further inhibit metallic corrosion. Adding additional components or functions to their structure is one of the motivations of this work.

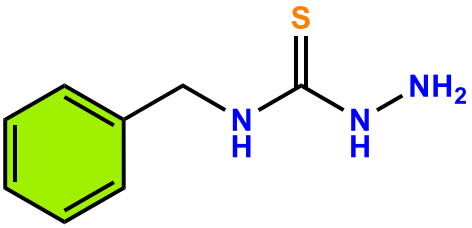

Figure 1. *Chemical structure of BHCTA inhibitor*

Experimental

Chemicals and reagents

All the chemical reagents employed in the experimentation were of analytical quality and not purified additionally. N-benzylhydrazinecarbothioamide with purity 97 % was obtained from Sigma Aldrich Co. USA., and sodium chloride extra pure AR, 99.9 %, ethanol from resident trader El-Nasr Co.

Working electrode (WE) and solution preparation

The working electrode (WE) was built of copper bar with 0.5 cm^2 exposed superficial area. The WE substrate was polished regularly with diverse grades of emery papers to a smooth substrate, and then decreased using ethanol/acetone mixture and blushed with water. For the preparation of the corrosive medium, 35.20 g of NaCl was dissolved in distilled water to obtain a concentration of 3.5 wt.%. Different concentrations (0.05 to 1.00 mM) of the inhibitor molecule (BHCTA) were prepared by dissolving the appropriate amounts of powder in distilled water. 1.00 mM of BHCTA

Weight-loss measurements

Using varying grades of emery papers, rectangular copper coupons of 5.0×3.0×0.3 cm were gradually polished, then degreased with ethanol/acetone mixture, blushing with water, and dried to be ready for tested. The coupons were weighed accurately and immersed in 3.5 wt.% NaCl electrolyte for 12 h, in the absence and presence of different dosages of BHCTA inhibitor at 298 K. The coupons were then removed, meticulously cleaned, rinsed with water, dried, and precisely weighed once again. In this test, three analogous coupons were performed, and the average corrosion rate was calculated. Equations (3)-(5) illustrate how corrosion rate (*CR*), surface coverage (θ), and corrosion inhibition efficiency (η_{WL} / %) were calculated:

$$CR = \frac{\Delta W}{St} \quad (3)$$

$$\theta = \frac{CR - CR_{Inh}}{CR} \quad (4)$$

$$\eta_{WL} = \left(\frac{CR - CR_{Inh}}{CR} \right) 100 \quad (5)$$

where *S* is copper substrate area, cm^2; *t* is exposure time, h; *CR* and CR_{Inh} are corrosion rates, mg cm^{-2} h^{-1} in the absence and presence of BHCTA inhibitor, respectively.

Electrochemical measurements

Three-electrode setup was used in this study, where the Pt-electrode served as auxiliary electrode, Cu-electrode as WE, and the saturated calomel electrode (SCE) served as reference

electrode. Using the Potentiostat/galvanostat Voltalab 80 and Voltamaster 4 software, the open circuit potential (OCP), electrochemical impedance spectroscopy (EIS), and potentiodynamic polarization (PDP) curves were measured at 298 K. The study examined the corrosion behavior of WE in testing solutions without and with BHCTA inhibitor. EIS measurements were performed at OCP over the frequency range of 100 kHz-30 mHz, with a single amplitude perturbation of 10 mV. The impedance data was examined using ZsimpWIN software in accordance with the relevant equivalent circuit. At a sweep rate of 0.2 mV s^{-1}, the polarization curve was scanned within ±250 mV with respect to E_{corr}. Every electrochemical test was performed at 298 K. Each test included three parallel trials to guarantee the repeatability of data.

Quantum chemical calculations

Using Gaussian 09 software [7], the reaction between the BHCTA molecule and the Cu substrate was theoretically calculated. A 6-311G (d, p) basis set was used in DFT-B3LYP methods for the geometric optimization of the BHCTA molecule. Using Monte Carlo simulation, the strength of the interactions between the investigated chemical and the copper surface was ascertained. The Materials Studio program was used to run these simulations. The Cu (111) surface was used in these simulations, and the details that were used were the crystallographic force area, 303 K temperature, NVT group, and a time step of 1 fs.

Surface morphology examination

In order to evaluate the substrate morphology, copper was submerged in a 3.5 wt.% NaCl solution for a full day, both with and without a 1 mM BHCTA inhibitor. After rinsing the copper substrate with bi-distilled water, it was dehydrated at ambient temperature. The Cu substrate morphological investigations were assessed by JOEL MODEL 6390.

Results and discussion

Open circuit potential (OCP) assessment

Figure 2 shows the OCP fluctuation of Cu electrode in 3.5 wt.% of NaCl electrolyte as a function of time, in the absence and presence of different dosages of BHCTA inhibitor at 298 K.

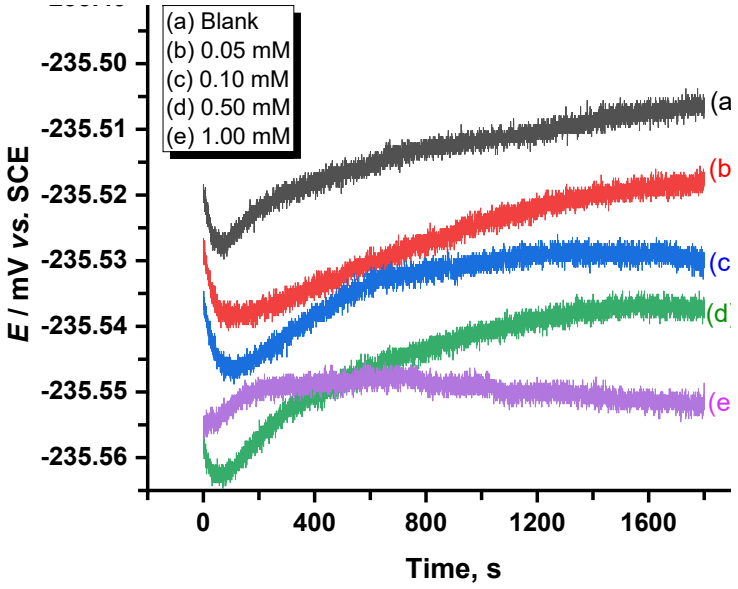

Figure 2. *OCP curves for corrosion of Cu in 3.5 wt.% NaCl solution in the absence and presence of different concentrations of BHCTA inhibitor at 298 K*

The constant potential, which corresponds to E_{corr} of Cu electrode, was easily reached in NaCl solution [8]. Physical electrostatic attraction takes place between the positive charge of the protonated BHCTA molecules and the negative charge of the Cu electrode in inhibited NaCl electrolyte. It was reported [9] that an organic inhibitor can be classified as either anodic or cathodic type inhibitor if its OCP movement differs by at least 85 mV from the measurement made for the blank uninhibited electrolyte. Figure 2 shows that in the presence of the examined inhibitor, the shift in E_{corr} is rather small and so, the BHCTA may be considered as inhibitor of a mixed-type.

Potentiodynamic polarization (PDP) assessment

For assessment of the appropriateness of the BHCTA inhibitor for Cu electrode in 3.5 wt.% NaCl electrolyte, the potentiodynamic polarization (PDP) measurements at 298 K were investigated. Figure 3 displays the PDP for corrosion of Cu tested in 3.5 wt.% NaCl electrolyte in the absence and presence of four different dosages of BHCTA inhibitor. The parameters from the PDP tests such as anodic Tafel slope (β_a), cathodic Tafel slope (β_c), corrosion current density (i_{corr}), and corrosion potential (E_{corr}) were obtained using Voltmaster software attached to Potentiostat/Galvanostat Voltalab 80. It is obvious that by addition of BHCTA inhibitor to the blank electrolyte (3.5 wt.% NaCl), the anodic dissolving of Cu electrode and the cathodic progression decreased. The values of i_{corr} were decreased from 5.1717 µA cm^{-2} for the blank electrolyte to 0.2896 µA cm^{-2} for the inhibited electrolyte with 1 mM of BHCTA. Because it reduces both anodic and cathodic processes, the BHCTA inhibitor can be regarded as a mixed-type inhibitor [10]. The anode dissolution speed slows down as a result of BHCTA molecules being adsorbed on the Cu substrate, limiting the anode reaction active sites. This is owing to the adsorption of BHCTA inhibitor molecules on the active positions of Cu substrate by growing surface handling, and creating a barrier film that delays dissolving of Cu electrode. To assess the efficacy of BHCTA inhibitor to overturn dissolving of the Cu electrode in 3.5 wt.% NaCl electrolyte, the inhibition effectiveness (η_{PDP}, %) was considered using equation (6) [11]:

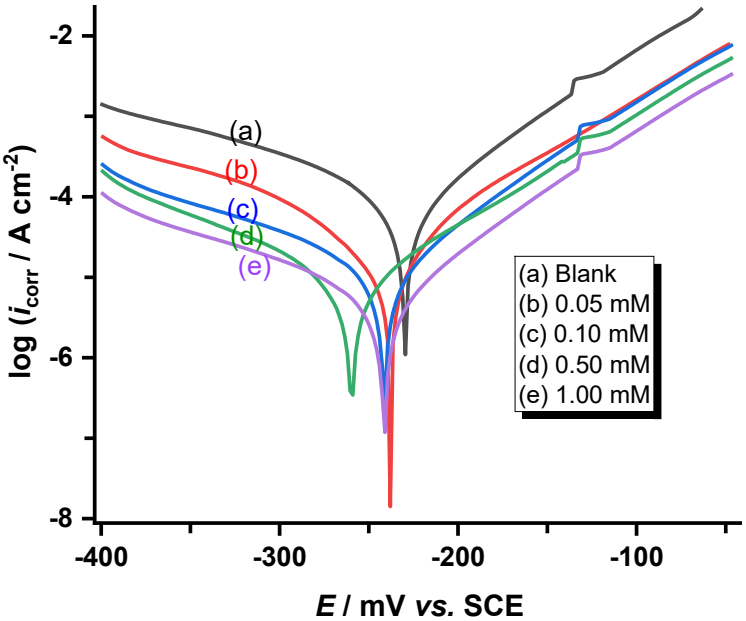

Figure 3. *PDP curves for the corrosion of Cu in 3.5 wt.% NaCl solution in the absence and presence of different concentrations of BHCTA inhibitor at 298 K*

$$\eta_{PDP} = \left(\frac{i_{corr}^{\ 0} - i_{corr}}{i_{corr}^{\ 0}} \right) 100 \qquad (6)$$

where i_{corr}^0 and i_{corr} denote the values of corrosion current density (μA cm^{-2}) of the Cu electrode in 3.5 wt.% NaCl electrolyte without and with of BHCTA inhibitor, respectively.

The assessed values of PDP parameters are summarized in Table 1. With varying BHCTA inhibitor doses, the Tafel slopes display key features [12]. The η_{PDP} increases dramatically and the i_{corr} reduces rapidly when the concentration of BHCTA corrosion inhibitors rises. It discloses that the i_{corr} decreased by addition of BHCTA inhibitor, and E_{corr} moves slightly to more negative values. Clearly, the η_{PDP} is improved by using BHCTA as organic inhibitor. The maximum inhibition efficiency (94.4 %) was reached at 1.00 mM of BHCTA inhibitor.

Table 1. *PDP parameters for Cu corrosion in 3.5 wt.% NaCl solution in the absence and presence of different concentrations of BHCTA inhibitor at 298 K*

C_{BHCTA} / mM	$-E_{corr}$ / mV	i_{corr} / μA cm^{-2}	β_a / mV dec^{-1}	$-\beta_c$ / mV dec^{-1}	η_{PDP} / %
0.00 (blank)	229.5	5.17	84	171	-
0.05	237.8	1.61	78	165	68.9
0.10	240.7	0.95	73	153	81.7
0.50	240.9	0.48	76	139	90.8
1.00	258.8	0.29	77	127	94.4

Electrochemical impedance spectroscopy assessment

The behavior of organic inhibitors in inhibiting corrosion process and protective mechanism of inhibitors on metals are usually studied using Electrochemical impedance spectroscopy (EIS) . Figure 4 shows the Nyquist and Bode plots of Cu electrode in 3.5 wt.% NaCl electrolyte without and with various dosages of BHCTA inhibitor at 298 K. Figure 4(a) displays the Nyquist plots of copper in 3.5 % NaCl solutions with and without BHCTA molecules. Depressed semicircular forms are evidently produced. Nyquist curves show that diameter of the semicircle rises when the BHCTA inhibitor is present. This indicates that the inclusion of BHCTA enhances the inhibition process without altering other components of the corrosion mechanism.

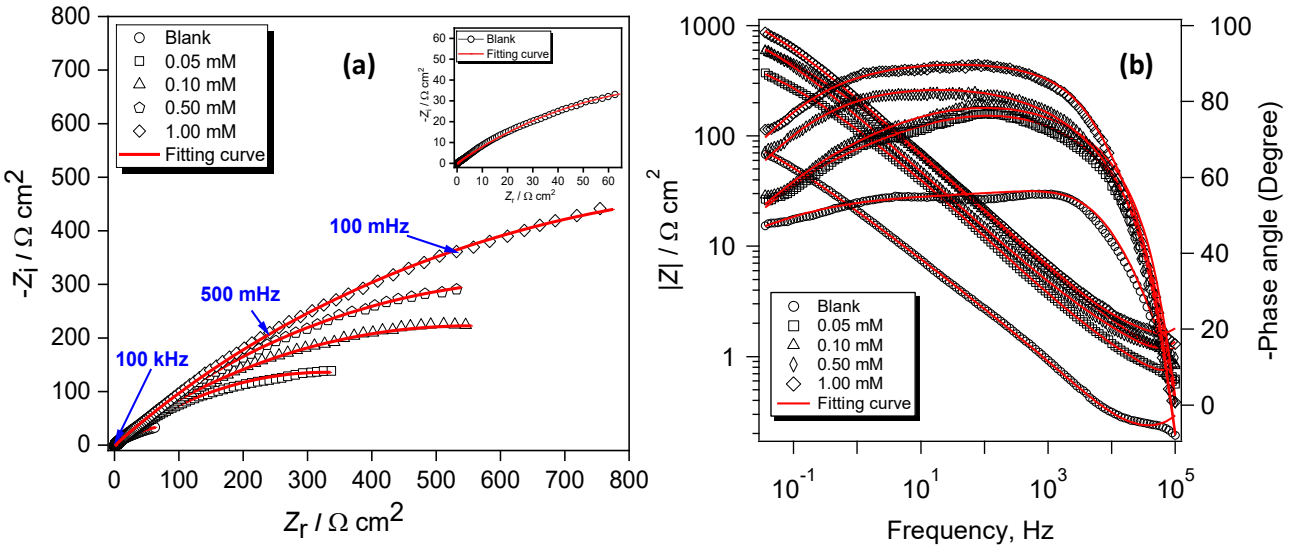

Figure 4. *EIS spectra represented as (a) Nyquist plots and (b) Bode plots for Cu corrosion in 3.5 wt.% NaCl solution in the absence and presence of different concentrations of BHCTA inhibitor at 298 K*

The produced Nyquist plots of copper corrosion in 3.5 % NaCl solutions did not provide ideal semicircles, what is typical behavior of solid electrodes and is frequently ascribed to the roughness caused by the heterogeneity of the electrode surface, and inhibitor adsorption. High-frequency

semicircles are frequently thought of as being produced by the charge transfer resistance (R_{ct}) and double-layer capacitance (C_{dl}). As the concentration of BHCTA rises, more molecules of the compound are adsorbed on the Cu surface, forming a more compact protective coating, which causes the diameter of the capacitance arc to be increased [13]. It can be seen in Figure 4(a), that the maximum diameter of capacitance arc is reached when the BHCTA concentration becomes 1.00 mM. At large concentrations, the sulfur, amino groups, and benzene rings present in BHCTA molecules can form molecular collections in the form of hydrogen bonds. This could be the cause of extremely high corrosion inhibition value of BHCTA molecules.

Bode modulus plots for Cu electrode in 3.5 wt.% NaCl solution in the absence and presence of BHCTA inhibitor are presented in Figure 4(b). Bode plots show that the impedance moduli increase markedly with BHCTA concentrations compared with that of the blank electrode. Since BHCTA effectively blocked the copper surface from corroding, the rise in impedance modulus and phase angle can be explained. The impedance data was fitted and analyzed using the equivalent circuits $R_s(Q)R_{ct}$. In this case, R_{ct} is the charge transfer resistance and R_s is the solution resistance. The double-layer capacitor with some pores is represented by the CPE (Q, n), which n values are close to unity. The double-layer capacitors within certain pores are usually represented by CPEs within n values $1 > n > 0$ [14]. Examining the data shown in Figure 4b, increasing measured impedance moduli with increasing inhibitor concentrations may lead to increased CPE impedance and decreased Q values. The R_{ct} can be used to compute the inhibition efficiency (η_{EIS} / %) of BHCTA for the Cu electrode in the manner shown by equation (7) [15]:

$$\eta_{EIS} = \left(\frac{R_{ct} - R_{ct}^{0}}{R_{ct}} \right) 100 \quad (7)$$

where R_{ct}^0 and R_{ct} denote the charge transfer resistances of the Cu electrode in 3.5 wt.% NaCl electrolyte without and with BHCTA inhibitor, respectively. For the copper electrode in the corrosive solution without inhibitor, the R_{ct}^0 value was determined to be 203 Ω cm^2. It was discovered that the R_{ct} values climbed to 652, 1066, 2503 and 3126 Ω cm^2 at concentrations of 0.05, 0.10, 0,50 and 1.00 mM. As a result, the inhibition efficiency increased by 69, 81.1, 91.9 and 93.6 %, respectively. The R_{ct} values rises as the concentration of BHCTA rises because more BHCTA molecules are adsorbed on the Cu electrodes. The findings show that BHCTA molecules have an easy time adhering to the copper surface and achieving an equilibrium of adsorption that prevents copper corrosion.

Weight loss assessment

The corrosion rates and anti-corrosion efficiencies for copper samples inhibited with various concentrations of BHCTA after immersion in 3.5 wt.% NaCl solution for 12 h at 298 K using weight loss test are listed in Table 2 and plotted in Figure 5. As can be seen from Figure 5, the addition of BHCTA inhibits the corrosion of copper at various concentrations. Data in Table 2 show that the corrosion rate decreases with the increase of BHCTA concentration up to 1.00 mM.

Table 2. *WL parameters calculated for corrosion of Cu in 3.5 wt.% NaCl solution in the absence and presence of different concentrations of BHCTA inhibitor at 298 K*

C_{BHCTA} / mM	CR / mg cm^{-2} h^{-1}	θ	η_{WL} / %
0.00 (blank)	0.0131	–	–
0.05	0.00435	0.668	66.8
0.10	0.00257	0.804	80.4
0.50	0.00117	0.911	91.1
1.00	0.00062	0.953	95.3

The weight loss data show that BHCTA has the best inhibiting effect at 1.00 mM at which the maximum inhibition efficiency reached 95.3 %. This demonstrates how the BHCTA molecules prevent copper corrosion. As recorded in Table 2, higher inhibition of BHCTA molecules is related to the active centers of lone pairs of heteroatoms as well as π-electrons of benzene ring that increase the adsorption progression at the Cu substrate [16].

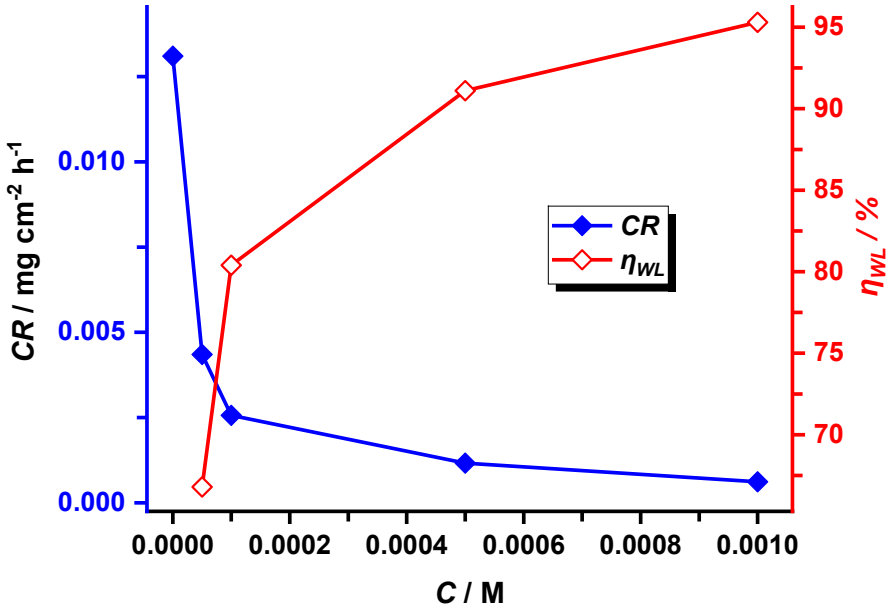

Figure 5. *Variation of CR and η_{WL} of Cu in 3.5 wt.% NaCl solution in the absence and presence of different concentrations of BHCTA inhibitor at 298 K*

Adsorption isotherms

The interaction of organic particles on a metal substrate is a regular dislocation interaction, in which H_2O particles adsorbed at the metal substrate are exchanged by inhibitor molecules. The isotherm parameters of adsorption process make a significant base for elucidation the interaction between the organic particles and the metal substrate. The inhibitor dosage is correlated to the expanse of inhibitor molecules adsorbed on the metal substrate, and displacement adsorption progression is stated by equation (8):

$$\text{Inhibitor}_{(sol)} + x\text{H}_2\text{O}_{(ads)} \leftrightarrow \text{Inhibitor}_{(ads)} + x\text{H}_2\text{O}_{(sol)} \quad (8)$$

where x denotes the quantity of H_2O molecules that is replaced by an organic molecule during a displacement process. On the basis of weight loss data, the adsorption behavior of BHCTA molecules on the Cu substrate in 3.5 wt.% NaCl solution in the presence of different concentrations of BHCTA at 298 K was modeled with various isotherms, *i.e.* Langmuir, Temkin, Freundlich and Frumkin isotherms as illustrated in Figure 6(a-d). Among these four types of isotherms, the Langmuir isotherm was found as the best fitting model (R^2 = 0.9998). The Langmuir isotherm design can be represented by equation (9) [17]:

$$\frac{C_{inh}}{\theta} = \frac{1}{K_{ads}} + C_{inh} \quad (9)$$

where θ and K_{ads} denote the surface coverage calculated from the weight loss results, and the equilibrium constant of adsorption, respectively.

Figure 6 (a) of Langmuir isotherm which signifies a linear relation between C_{inh}/θ and C_{inh} suggests that BHCTA molecules adsorbed on Cu substrate adapt to Langmuir model. The calculated value of $K_{ads} = 33.33\times10^3$ L mol^{-1}, demonstrates high adsorption capacity of BHCTA molecules on the Cu

substrate. The slope of Langmuir plot was found to be 1.0286, which implies that only one BHCTA molecule may roughly replace one water molecule.

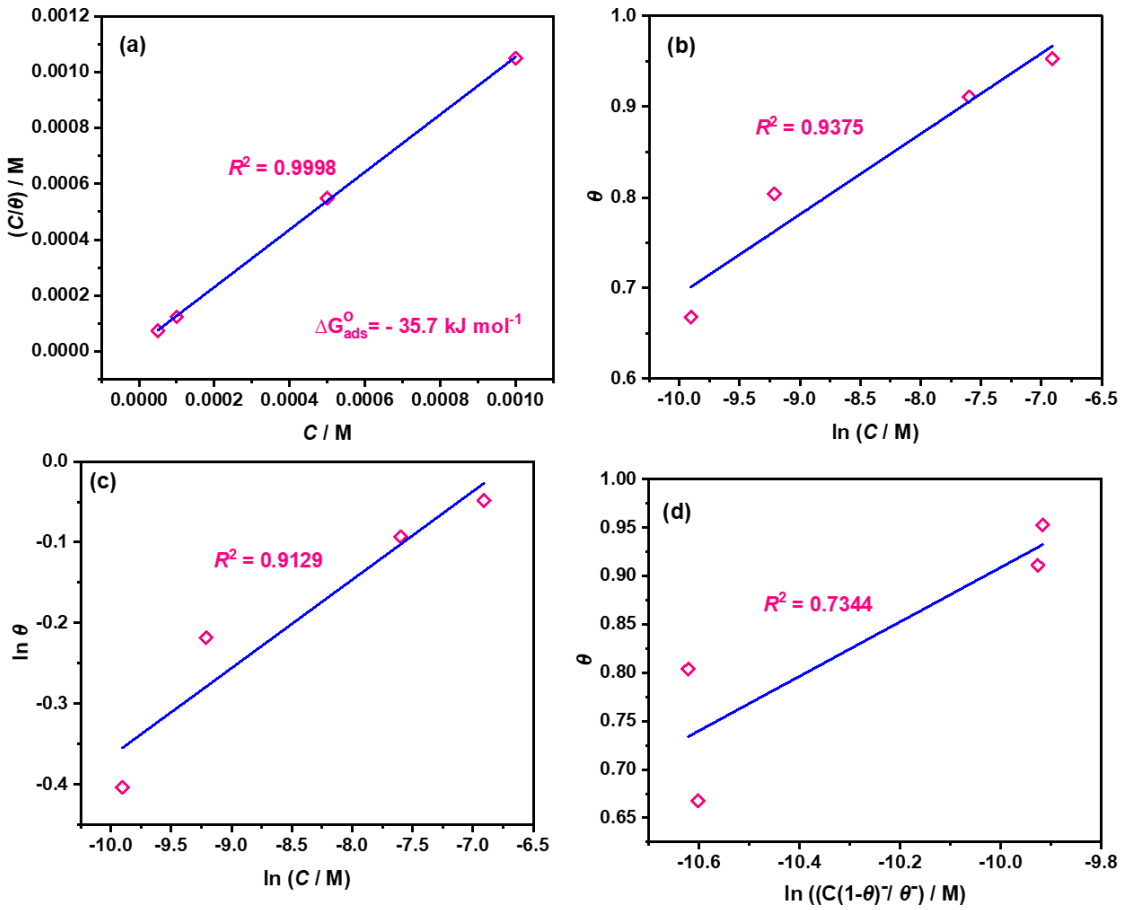

Figure 6. *Adsorption isotherm models of (a) Langmuir, (b) Temkin, (c) Freundlich, and (d) Frumkin, for the corrosion of Cu in 3.5 wt.% NaCl solution in the presence of different concentrations of BHCTA inhibitor at 298 K*

The Gibbs-free energy (ΔG_{ads}^0) can be calculated using the value of K_{ads} *via* equation (10) [18]:

$$K_{ads} = \frac{1}{55.5}\exp\left(\frac{-\Delta G_{ads}^{\ 0}}{RT}\right) \quad (10)$$

where R and T display the universal gas constant (8.314 J mol^{-1} K^{-1}) and thermodynamic temperature, K, respectively. The number 55.5 is related to the quantity of H_2O in the electrolyte, mol L^{-1}. An increased spontaneous adsorption reaction is generally indicated by larger K_{ads} and higher negative ΔG_{ads}^0 values. Physisorption is supported by values of ΔG_{ads}^0 about −20 kJ mol^{-1}, whereas chemisorption is implied by values around −40 kJ mol^{-1} or higher. The result of ΔG_{ads}^0, which is −35.7 kJ mol^{-1}, suggests that a combination of physisorption and chemisorption processes is involved in the adsorption of BHCTA molecules on the copper surface.

Quantum chemistry assessment

Quantum chemical calculations are the most efficient way of investigating the connection between corrosion inhibition efficiency and molecular structure of inhibitor molecules [19]. In this investigation, the inhibition effect of BHCTA molecules on the copper substrate was investigated through density functional theory (DFT) calculations. The optimized geometric construction of the BHCTA molecule, as well as the electron densities of the highest occupied molecular orbital (HOMO) and lowest unoccupied molecular orbital (LUMO), are displayed in Figure 7.

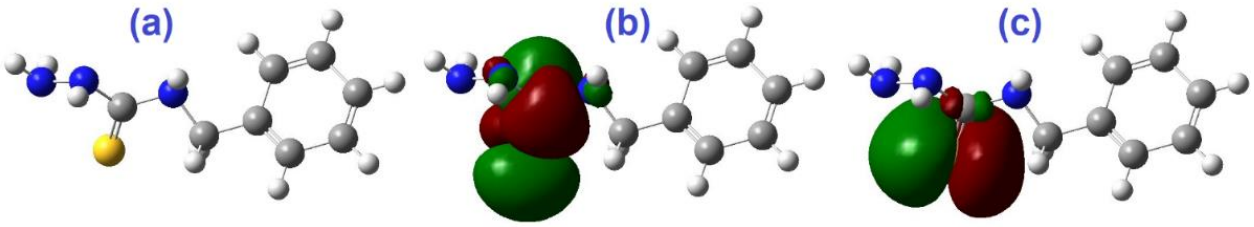

Figure 7. *Optimized structure (a) and frontier orbital distribution of BHCTA molecule (b) LUMO and (c) HOMO*

Generally, higher value of E_{HOMO} of inhibitor molecule denotes a stronger ability to supply metals with electrons [20]. In contrast, higher electron acceptability of inhibitor is indicated by a lower E_{LUMO} value. As a result, BHCTA corrosion inhibitor molecules have good adsorption on the copper surface through electron transfer from the unshared pair of electrons of S and N atoms to the vacant d-orbitals of copper, as well as π-electrons of the benzene ring. They perform well against corrosion in addition to the reverse retransfer of Cu atom valence electrons to BHCTA molecules. As per the Koopman formula, the ionization potential, $I = -E_{HOMO}$ and electron affinity, $A = -E_{LUMO}$, were considered as I = 8.261 eV and A = −4.536 eV. The electronegativity (χ), hardness (η) and fraction of electrons transferred (ΔN) can be considered based on equations (11) - (13) [21]:

$$\chi = \frac{I + A}{2} \tag{11}$$

$$\eta = \frac{I - A}{2} \tag{12}$$

$$\Delta N = \frac{\chi_{Cu} - \chi_{inh}}{2(\eta_{Cu} + \eta_{inh})} \tag{13}$$

The χ_{inh} and η_{inh} values were calculated to be 1.863 and 6.399 eV mol^{-1}, respectively while the values of χ_{inh} and η_{inh} for copper are 4.48 and 0 eV mol^{-1}, respectively. Furthermore, the dipole moment is considered as a crucial indicator for the reactivity of organic molecules as corrosion inhibitor. The higher dipole moment values in conjunction with lower energy gap ($\Delta E = E_{LUMO} - E_{HOMO}$) values will encourage the accumulation of the inhibitor on the metal surface, thereby enhancing the inhibition efficiency [22]. The calculated dipole moment for BHCTA molecules was found, μ = 3.131 D, indicating higher inhibition efficiency. According to Lukovits *et al*. [23], the inhibitor efficiency rose as its ability to supply electrons improved if the fraction of electrons transferred (ΔN) was less than 3.6. The computed ΔN of BHCTA inhibitor of 0.205 eV indicates that the BHCTA forms anti-corrosion adsorption layers on the copper surface through electron donor bonding.

Monte Carlo simulation assessment

Monte Carlo simulation was used to understand the inhibitory process and locate low adsorption energy (E_{ads}) sites on the metal surface [24]. This made it possible for researchers to determine the inhibitor preferential adsorption [25]. Preferred adsorption sites on metal surfaces are often described using these techniques. The simulation results and the configurations of the BHCTA molecule adsorption equilibrium on the Cu substrate are shown in Figure 8, where adsorption orientation of inhibitor on the Cu surface is almost flat. Based on Monte Carlo simulation, the adsorption energy (E_{ads}) of the BHCTA molecules was found to be -2025 kJ mol^{-1}. The strong chemical bond that BHCTA molecules create with Cu(111) surface demonstrates the high effectiveness of these molecules in preventing Cu corrosion. Additionally, they highlighted the effects of dipole

interactions and electronic transmission from the adsorbate to the substrate. Consequently, it is supposed that the adsorption of BHCTA on the Cu substrate insulates the invasion of Cl^- ions.

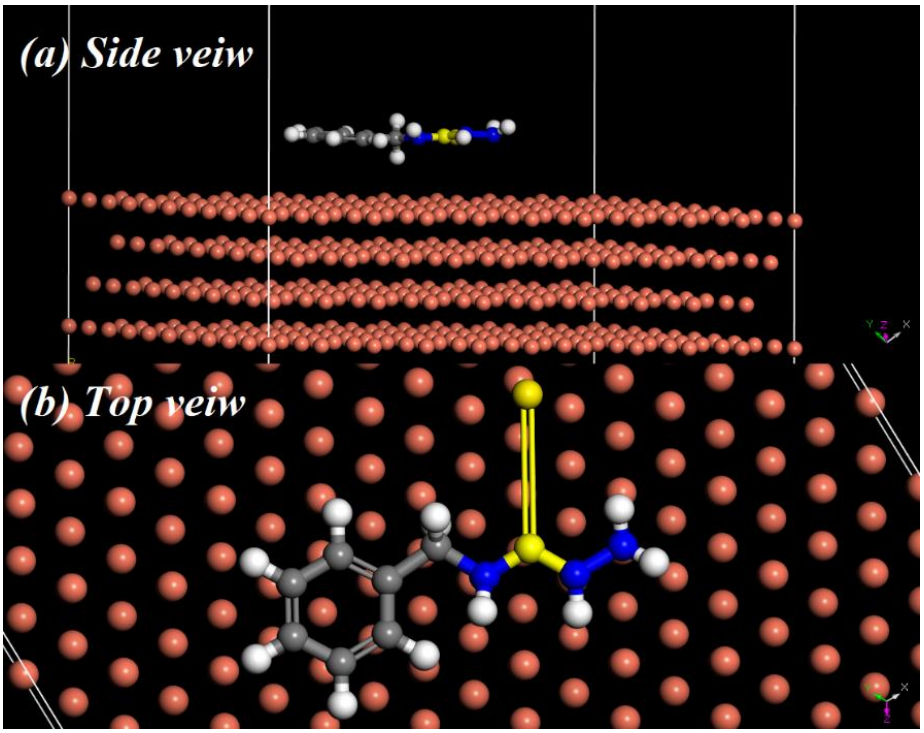

Figure 8. *Side (a) and top (b) views of adsorption position of BHCTA molecule on Cu surface*

Surface inspection

SEM images of the copper substrate after 12 h immersion in 3.5 wt.% NaCl solution without and with 1.00 mM of BHCTA inhibitor, are shown in Figure 9(a) and 9(b), respectively. Figure 9(a) depicts severe damage to the copper substrate as a result of the aggressiveness of corrosive 3.5 % NaCl electrolyte in the absence of an inhibitor. Figure 9(b), on the other hand, shows uniform and protected copper substrate after the addition of BHCTA inhibitor molecules to the corrosive electrolyte. This is due to the significant adsorption of BHCTA inhibitor molecules on the copper substrate, which protects its surface [26].

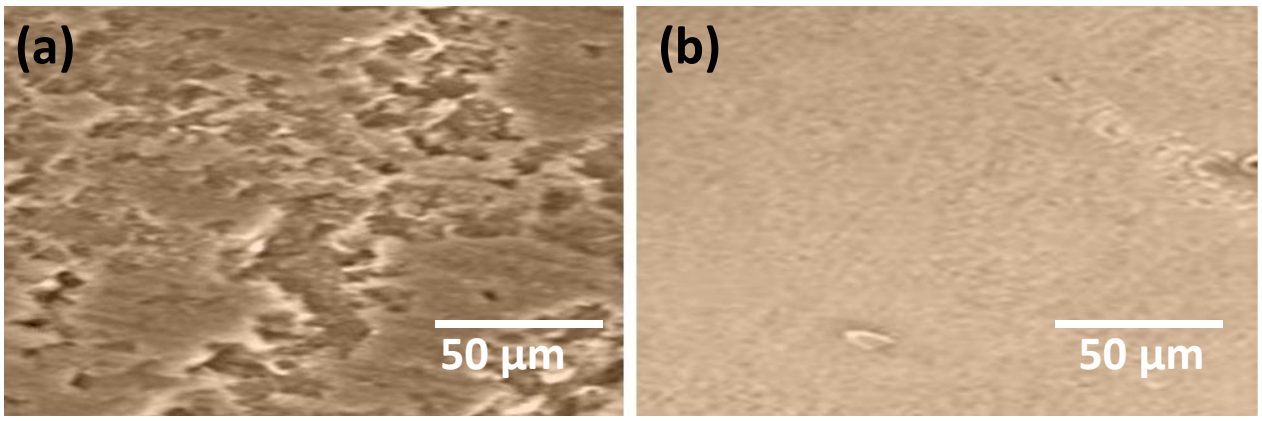

Figure 9. *SEM images of copper substrate after immersion in 3.5% NaCl solution for 12 h (a) without, and (b) with 1.00 mM of BHCTA inhibitor*

Corrosion inhibition mechanism

As illustrated in Figure 10, the postulated inhibition mechanism is based on the measured test and quantum chemistry study. The adsorption of Cl^- ion was substituted by the adsorption of BHCTA

molecules on Cu surface [27]. The physical adsorption (electrostatic) and the chemical adsorption created by chemical bonds combine, according to the adsorption results for the BHCTA on the Cu substrate. The presence of charged inhibitor molecules in the solution and the charged metal surface are necessary for physical adsorption. In order to create coordination-type bonds, the inhibitor molecule and the metal surface must share or transfer charges during the chemisorption process. Transition metals with unoccupied low-energy electron orbitals and inhibitor molecules with loosely bonded electrons or heteroatoms with lone pair electrons are necessary for this interaction. By substituting adsorbed Cl^- on the copper substrate with BHCTA molecules, covalent bonds can be formed between the metal surface and π-electrons of the benzene ring and the lone pair of heteroatoms. The Cu is shielded from corrosion by being isolated from the corrosive ions.

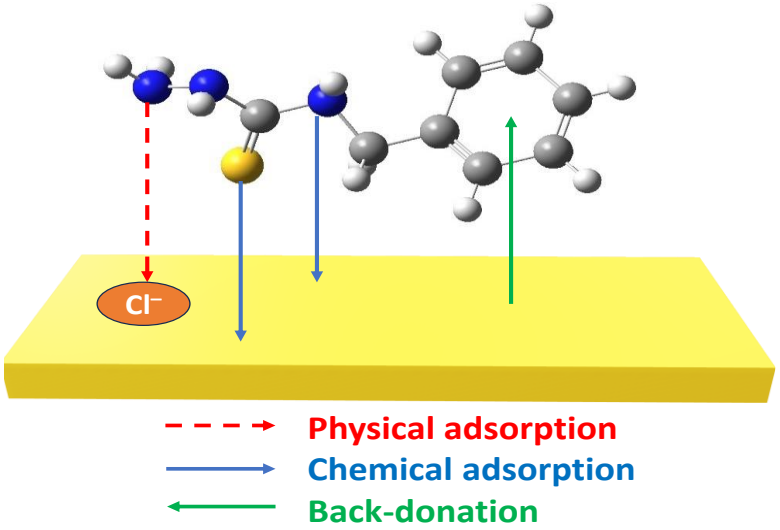

Figure 10. *Schematic diagram of the corrosion inhibition mechanism of BHCTA on copper surface*

Comparison of inhibition efficacy of different heterocyclic derivatives

It is still of interest to compare copper corrosion inhibition in the same media and conditions using BHCTA with the performance of other heterocyclic compounds and the results are summarized in Table 3. It is clear that BHCTA inhibitor has promising efficiency compared to a number of other heterocyclic derivative inhibitors [28-30].

Table 3. *Comparison of the inhibitory efficacy of different heterocyclic derivatives*

Inhibitor	C_{Inh} / mM	$C_{NaCl\ electrolyte}$ / %	Metal	*IE* / %	Ref.
2-Mercapto-4-amino-5-nitroso- 6-hydroxy pyrimidine (MAP)	1	3.5	Cu	90.7	[28]
1-[(2-Chloro-5-thiazolyl)-methyl]−4,5-di-hydro-N-nitro-1H-imidazol-2-amine (IMT)	2	3.5	Cu	97.2	[29]
(2E)−1-[(6-Chloro-pyridin-3-yl)-methyl]-N-nitro-imidazolidin-2-imine (IMP)				98.9	
4-amino-3-methyl-1,2,4-triazole-5-thione (MTSNH)	1	3.0	Copper-nickel (Cu-30Ni)	96.6	[30]
3-methyl-1,2,4-triazole-5-thione (MTS)				65.2	
N-benzylhydrazinecarbothioamide (BHCTA)	1	3.5	Cu	95.3	This work

Conclusions

1) The inhibitory performance of organic molecules BHCTA for copper corrosion was successfully explored in 3.5 wt.% NaCl solution at 298 K.

2) BHCTA molecules are effectively adsorbed on the Cu substrate and hinder concurrently the anodic oxidation and cathodic reduction progressions.
3) Corrosion inhibition efficacy reached more than 95 % upon addition of 1.00 mM of BHCTA.
4) Adsorption of BHCTA on the copper surface agrees with Langmuir isotherm and presents blend of chemisorption and physisorption characteristics.
5) Theoretical calculations show that BHCTA has good adsorption properties on the copper substrate.
6) SEM outcomes provide the foundation of defending layer of BHCTA over the copper substrate.
7) There is good consistency between experimental (PDP, WL, and EIS) and theoretical (DFT calculations and Monte Carlo simulation) tools, which strengthens the results obtained.

***Acknowledgements**: The authors extend their appreciation to the Deanship of Scientific Research, Imam Mohammad Ibn Saud Islamic University (IMSIU), Saudi Arabia, for funding this research work through Grant No. (221412010).*

References

[1] A. Fateh, M. Aliofkhazraei, A.R. Rezvanian, Review of corrosive environments for copper and its corrosion inhibitors, *Arabian Journal of Chemistry* **13** (2020) 481-544. https://doi.org/10.1016/j.arabjc.2017.05.021
[2] O.E. Barcia, O.R. Mattos, N. Pebere, B. Tribollet, Mass-Transport Study for the Electrodissolution of Copper in 1M Hydrochloric Acid Solution by Impedance, *Journal of The Electrochemical Society* **140** (1993) 2825-2832. https://doi.org/10.1149/1.2220917
[3] E.-S.M. Sherif, Corrosion Behavior of Copper in 0.50 M Hydrochloric Acid Pickling Solutions and its Inhibition by 3-Amino-1,2,4-triazole and 3-Amino-5-mercapto-1,2,4-triazole, *International Journal of Electrochemical Science* **7** (2012) 1884-1897. https://doi.org/10.1016/S1452-3981(23)13847-8
[4] A.M. Al-Sabagh, M.I. Abdou, M.A. Migahed, A.M. Fadl, A.A. Farag, M.M. Mohammedy, S. Abd-Elwanees, A. Deiab, Influence of ilmenite ore particles as pigment on the anticorrosion and mechanical performance properties of polyamine cured epoxy for internal coating of gas transmission pipelines, *Egyptian Journal of Petroleum* **27** (2018) 427-436. https://doi.org/10.1016/j.ejpe.2017.07.005
[5] W. Chen, S. Hong, H.Q. Luo, N.B. Li, Inhibition Effect of 2,4,6-Trimercapto-1,3,5-triazine Self-Assembled Monolayers on Copper Corrosion in NaCl Solution, *Journal of Materials Engineering and Performance* **23** (2014) 527-537. https://doi.org/10.1007/s11665-013-0788-4
[6] Q.Q. Liao, Z.W. Yue, D. Yang, Z.H. Wang, Z.H. Li, H.H. Ge, Y.J. Li, Inhibition of copper corrosion in sodium chloride solution by the self-assembled monolayer of sodium diethyldithiocarbamate, *Corrosion Science* **53** (2011) 1999-2005. https://doi.org/10.1016/j.corsci.2011.02.023
[7] N. S. Abdelshafi, A. A. Farag, F. E. Heakal, A. Badran, K. M. Abdel-Azim, M. E. Abdel-Raouf, M. A. Ibrahim, In-depth experimental assessment of two new aminocoumarin derivatives as corrosion inhibitors for carbon steel in HCl media combined with AFM, SEM/EDX, contact angle, and DFT/MDs simulations, *Journal of Molecular Structure* **1304** (2024) 137638. https://doi.org/10.1016/j.molstruc.2024.137638.
[8] H. Ma, S. Chen, L. Niu, S. Zhao, S. Li, D. Li, Inhibition of copper corrosion by several Schiff bases in aerated halide solutions, *Journal of Applied Electrochemistry* **32** (2002) 65-72. https://doi.org/10.1023/A:1014242112512
[9] A. Fawzy, M. Abdallah, M. Alfakeer, H. M. Ali, Corrosion Inhibition of Sabic Iron in Different Media Using Synthesized Sodium N-dodecyl Arginine Surfactant, *International Journal of Electrochemical Science* **14** (2019) 2063-2084. https://doi.org/10.20964/2019.02.08

[10] A. Fawzy, A. Toghan, O. K. Alduaij, N. Alqarni, A. M. Eldesoky, A. A. Farag, Electrochemical, spectroscopic, kinetic and surface analysis of the inhibitory performance of Alcian blue dye for copper corrosion in sulfuric acid solution, *International Journal of Electrochemical Science* **19** (2024) 100429. https://doi.org/10.1016/j.ijoes.2023.100429
[11] A.A. Farag, E.A. Badr, Non-ionic surfactant loaded on gel capsules to protect downhole tubes from produced water in acidizing oil wells, *Corrosion Reviews* **38** (2020) 151-164. https://doi.org/10.1515/corrrev-2019-0030
[12] B. Tan, S. Zhang, H. Liu, Y. Guo, Y. Qiang, W. Li, L. Guo, C. Xu, S. Chen, Corrosion inhibition of X65 steel in sulfuric acid by two food flavorants 2-isobutylthiazole and 1-(1,3-Thiazol-2-yl) ethanone as the green environmental corrosion inhibitors: Combination of experimental and theoretical researches, *Journal of Colloid and Interface Science* **538** (2019) 519-529. https://doi.org/https://doi.org/10.1016/j.jcis.2018.12.020
[13] A. Fawzy, O. K. Alduaij, A. Al Bahir, D. A. Alshammari, N. Alqarni, A. M. Eldesoky, A. A. Farag, A. Toghan, A comparative study of pyridine and pyrimidine derivatives based formamidine for copper corrosion inhibition in nitric acid: Experimental and computational exploration, *International Journal of Electrochemical Science* **19** (2024) 100403. https://doi.org/10.1016/j.ijoes.2023.100403
[14] E.M. Sherif, S.-M. Park, 2-Amino-5-ethyl-1,3,4-thiadiazole as a corrosion inhibitor for copper in 3.0% NaCl solutions, *Corrosion Science* **48** (2006) 4065-4079. https://doi.org/10.1016/j.corsci.2006.03.011
[15] A.A. Farag, Oil-in-water emulsion of a heterocyclic adduct as a novel inhibitor of API X52 steel corrosion in acidic solution, *Corrosion Reviews* **36** (2018) 575-588. https://doi.org/10.1515/corrrev-2018-0002
[16] H.A. Mohamed, A.A. Farag, B.M. Badran, Corrosion inhibition of mild steel using emulsified thiazole adduct in different binder systems, *Eurasian Chemico-Technological Journal* **10** (2008) 67-77.
[17] S.M. Shaban, E. a Badr, M.A. Shenashen, A.A. Farag, Fabrication and characterization of encapsulated Gemini cationic surfactant as anticorrosion material for carbon steel protection in down-hole pipelines, *Environmental Technology & Innovation* **23** (2021) 101603. https://doi.org/10.1016/j.eti.2021.101603
[18] N. Alqarni, Investigation of Expired Ticarcillin and Carbenicillin Drugs for Inhibition of Aluminum Corrosion in Hydrochloric Acid Solution, *International Journal of Electrochemical Science* **17** (2022) 2212113. https://doi.org/10.20964/2022.12.99
[19] E.A. Mohamed, H.E. Hashem, E.M. Azmy, N.A. Negm, A.A. Farag, Synthesis, structural analysis, and inhibition approach of novel eco-friendly chalcone derivatives on API X65 steel corrosion in acidic media assessment with DFT & MD studies, *Environmental Technology & Innovation* **24** (2021) 101966. https://doi.org/10.1016/j.eti.2021.101966
[20] A. Toghan, A. Fawzy, A. Al Bahir, N. Alqarni, M.M.S. Sanad, M. Khairy, A.I. Alakhras, A.A. Farag, Computational Foretelling and Experimental Implementation of the Performance of Polyacrylic Acid and Polyacrylamide Polymers as Eco-Friendly Corrosion Inhibitors for Copper in Nitric Acid, *Polymers (Basel)* **14** (2022) 4802. https://doi.org/10.3390/polym14224802
[21] A.A. Farag, A. Toghan, M.S. Mostafa, C. Lan, G. Ge, Environmental Remediation through Catalytic Inhibition of Steel Corrosion by Schiff's Bases: Electrochemical and Biological Aspects, *Catalysts* **12** (2022) 838. https://doi.org/10.3390/catal12080838
[22] H.S. Gadow, A. Fawzy, M. Khairy, M.M.S. Sanad, A. Toghan, Experimental and theoretical approaches to the inhibition of carbon steel corrosion by thiophene derivative in 1 M HCl, *International Journal of Electrochemical Science* **18** (2023) 100174. https://doi.org/10.1016/j.ijoes.2023.100174

[23] F.Z. I. Lukovits, E. Kálmán, Corrosion Inhibitors-Correlation between Electronic Structure and Efficiency, *Corrosion* **57** (2001) 3-8. https://doi.org/https://doi.org/10.5006/1.3290328
[24] A.A. Farag, A.S. Ismail, M.A. Migahed, Squid By-product Gelatin Polymer as an Eco-friendly Corrosion Inhibitor for Carbon Steel in 0.5 M H2SO4 Solution: Experimental, Theoretical, and Monte Carlo Simulation Studies, *Journal of Bio- and Tribo-Corrosion* **6** (2020). https://doi.org/10.1007/s40735-019-0310-0
[25] N. Alqarni, A. Fawzy, B. El-Gammal, A. Toghan, N.A. Hassan, Z. Algarni, Auspicious water treatment approach. Oxidative degradation of fluconazole and voriconazole antibiotics by CrO_3 in different acidic environments: Kinetics, mechanistic and thermodynamic modelling, *Journal of Saudi Chemical Society* **26** (2022) 101396. https://doi.org/10.1016/j.jscs.2021.101396
[26] A.A. Farag, M.A. Migahed, A.M. Al-Sabagh, Adsorption and inhibition behavior of a novel Schiff base on carbon steel corrosion in acid media, *Egyptian Journal of Petroleum* **24** (2015) 307-315. https://doi.org/10.1016/j.ejpe.2015.07.001
[27] A.G. Al-Gamal, A.A. Farag, E.M. Elnaggar, K.I. Kabel, Comparative impact of doping nano-conducting polymer with carbon and carbon oxide composites in alkyd binder as anti-corrosive coatings, *Composite Interfaces* **25** (2018) 959-980. https://doi.org/10.1080/09276440.2018.1450578
[28] K.F. Khaled, Studies of the corrosion inhibition of copper in sodium chloride solutions using chemical and electrochemical measurements, *Materials Chemistry and Physics* **125** (2011) 427-433. https://doi.org/10.1016/j.matchemphys.2010.10.037
[29] J. Shen, D. Yang, L. Ma, Z. Gao, A. Yan, Q. Liao, Exploration of neonicotinoids as novel corrosion inhibitors for copper in a NaCl solution: Experimental and theoretical studies, *Colloids and Surfaces A: Physicochemical and Engineering Aspects* **636** (2022) 128058. https://doi.org/10.1016/j.colsurfa.2021.128058
[30] K. Tassaoui, A. Al-Shami, M. Damej, A. Molhi, O. Mounkachi, M. Benmessaoud, Contribution to the corrosion inhibitors of copper-nickel (Cu-30Ni) in 3 % NaCl solution by two new molecules of triazole: Electrochemical and theoretical studies, *Journal of Molecular Structure* **1291** (2023) 135836. https://doi.org/10.1016/j.molstruc.2023.135836

J. Electrochem. Sci. Eng. **14(2)** (2024) 247-263; http://dx.doi.org/10.5599/jese.2228

Open Access : : ISSN 1847-9286
www.jESE-online.org

Original scientific paper

The effect of coating drying conditions on bronze corrosion protection

Helena Otmačić Ćurković, Angela Kapitanović✉, Martina Filipović and Petra Gorišek

University of Zagreb Faculty of Chemical Engineering and Technology, Research Laboratory for Corrosion Engineering and Surface Protection, Savska 16, HR 10000 Zagreb, Croatia

Corresponding author: ✉akapitano@fkit.unizg.hr; *Tel.: +385-1-4597-126*

Received: December 22, 2023; Accepted: February 8, 2024; Published: February 12, 2024

Abstract

Waterborne coatings present a green alternative to solvent-borne coatings as only a small amount of organic solvent is released into the environment during drying. However, for waterborne coatings, the drying process is much more challenging due to the slow evaporation of water. In this work, the influence of drying temperature on the protective properties of a waterborne acrylic coating was studied. Its performance in corrosion protection of bronze substrates, representing the bronzes used for the sculptures placed outdoors, was examined. Corrosion properties were evaluated by linear polarization measurements and electrochemical impedance spectroscopy during three-week exposure to artificial acid rain solution. It was found that drying at ambient temperature resulted in modest corrosion protection, while drying at 55 °C ensured greater initial corrosion resistance, which gradually degraded during exposure to acid rain solution accompanied by the coating blistering. Drying of one-layer coating at 40 °C resulted in the formation of clearly visible corrosion products. If the coating was applied in three layers, the drying process was more efficient, leading to slightly higher polarization resistance values without visible corrosion at the bronze surface. Furthermore, the studied waterborne acrylic coating provided good corrosion protection of patinated bronze surfaces. Additionally, it was found that for efficient corrosion protection, it is preferable that the coating contains a corrosion inhibitor in order to avoid substrate corrosion during coating drying. When applied properly, studied coating does not alter the state of surfaces, both bare and patinated, which is important for its application in bronze cultural heritage protection.

Keywords

Waterborne coatings; drying temperature; electrochemical impedance spectroscopy; polarization measurements

Introduction

Bronze cultural heritage placed outdoors is gradually covered with a natural patina due to the corrosion process. The formation of patina will take longer in less aggressive environments, but it will

proceed faster in polluted ones [1]. Bronze corrosion can result in the formation of both stable and unstable corrosion products. These unstable products can, in the presence of moisture and oxygen, cause further degradation and endangerment of works of art [2,3]. In order to prevent gradual surface deterioration, protective organic coatings are widely used [4].

Over the past few decades, new legislatives have altered the perspective on the effects of solvent-borne organic coatings on the environment and human health. For that reason, the coating industry has developed environmentally friendly waterborne coatings resulting in improved air quality and reduced hazard impact on the surroundings. Waterborne adhesives, paints and coatings are becoming of more interest because a high concentration of volatile organic compound (VOC) is replaced by water [5-7]. In addition, they contain anticorrosive pigments without heavy metals, resulting in a non-toxic and non-flammable solution [8-10].

Waterborne coatings drying occurs in three stages: 1) the solvent (water) evaporation, 2) the polymer nanoparticles deformation, where a densely packed structure is created, and 3) the polymer chains interdiffusion leading to coalescence [11,12]. The film particles will deform and achieve closer contact, forming a rigid film structure when the film is above the minimum film formation temperature [13,14]. The strength of the polymer interface is determined by the degree of entanglements between the polymer chains [15]. In addition, the rate of evaporation depends on the difference in vapour pressure between the water in the coating and the air being circulated over the substrate. A large amount of water in the coating results in a prolonged drying duration in cold and humid environments [16]. Slow coating drying means that if the coating is applied directly on the metal surface, there will be prolonged contact between the metal and the water, which can lead to substrate corrosion.

Hwang *et al.* [17] investigated how the morphology and surface characteristics of the waterborne UV-curable coatings were affected by the water drying conditions. After testing drying temperatures of 22, 50 and 80 °C and various drying durations, the researchers concluded that too low drying temperature led to surface cracking, peeling and blistering of a cured coating. The improvement of hardness and adhesion strength was noted at higher drying temperatures and rates.

Three drying temperatures (5, 23 and 35 °C) were examined by Stojanović *et al*. in the study on curing temperature influence on corrosion protection properties of waterborne and solventborne epoxy coatings [16]. For the solventborne coating, all tested drying temperatures resulted in a coating with stable, protective properties, whereas that was not the case for waterborne coating. When dried at 35 °C, it demonstrated the best level of corrosion resistance, while certain limitations were noted at lower testing temperatures. They concluded that elevated curing temperatures were needed to obtain higher performance of waterborne coatings, either in corrosion protection or physical properties. Also, raising the layer thickness had a beneficial impact, but only to a certain value, because it may result in prolonged drying time and insufficient water evaporation [16]. To achieve the optimum final qualities of a coating, in terms of application and surface morphology, adequate drying at the right temperature was found to be very important [16,17].

The aim of this work is to examine how drying temperature and a number of applied layers affect waterborne acrylic coatings' ability to protect bronze cultural heritage from corrosion. For cultural heritage protection, it is important that the coating does not alter the surface appearance, thus, for this study, two clear waterborne coatings were selected. One of these coatings is a commercial product (C2) and another is under development (C1). The main difference in these coatings is that C1 contains a corrosion inhibitor and less water. Our goal was not to study a particular coating or corrosion inhibitor but to examine the conditions under which waterborne acrylic coatings could be applied for protection of bronze cultural heritage. Drying waterborne coatings is quite challenging, as

too low temperature can lead to slow drying and substrate corrosion, while too high temperatures result in coating cracking. In addition, water in the coating can have different effects on bronzes of different compositions as well as on the patina that is usually present on bronze sculptures. Studies were conducted on different bronze substrates, typically found on objects of cultural heritage, to determine if the coating performance significantly depends on substrate properties. Besides bare bronzes, studies were also conducted on bronze surfaces covered by a layer of patina. Coating protection efficiency was examined using linear polarization measurements (LP) and electrochemical impedance spectroscopy (EIS) during the immersion in artificial acid rain.

Experimental

Sample preparation

In this study, three different kinds of bronzes were used: RG7, CuSn12 with 1.33 cm^2 of exposed surface and CuSn6 with 1.5 cm^2. All bronzes were obtained from Strojopromet Ltd., Croatia and their composition is presented in Table 1. In order to prepare working electrodes for electrochemical measurements, bronze discs, together with soldered copper wire, were embedded into an epoxy resin. Afterwards, the surface was polished with SiC papers (80, 800, 1200 and 2500), degreased in an ultrasonic ethanol bath and rinsed with deionized water. Part of the bronze samples was used for artificial patination, either chemically or electrochemically, as described in our previous work [18].

Table 1. *The composition of tested bronzes*

Sample	Content, wt.%			
	Cu	Sn	Zn	Pb
RG7	83.25	4.6	4.58	5.85
CuSn12	87.94	11.02	0.07	0.54
CuSn6	94.0	6.0	-	-

The investigation was conducted with two acrylic waterborne coatings named C1 and C2. Coating C1 is non-commercial and was obtained from the research department of one paint company, whereas C2 is a commercial product obtained from the same paint company. The main difference between these coatings is that C1 contains corrosion inhibitor and a slightly lower amount of water compared to C2. Both coatings were applied manually on bronze surfaces by brushing at room temperature.

RG7 bronze substrate served for the study of the influence of drying temperature and the number of layers of C1 coating on the corrosion protection properties. Three different drying temperatures (24, 55 and 40 °C) were tested. Examined experimental conditions are shown in Figure 1a. A comparative study between two waterborne coatings was performed on different bronze substrates: RG7, CuSn12 and CuSn6. For these studies, three layers of coatings were applied and dried at 40 °C, as presented in Figure 1b. Finally, various chemically or electrochemically patinated bronzes were also protected by waterborne coating C1 applied in three layers and dried at 40 °C (according to Figure 1b). Prior to further characterization, all samples were placed in a desiccator for 10 days.

The determination of dry film thickness on studied samples was conducted by PosiTector 600 (DeFelsko) and is presented in Table 2.

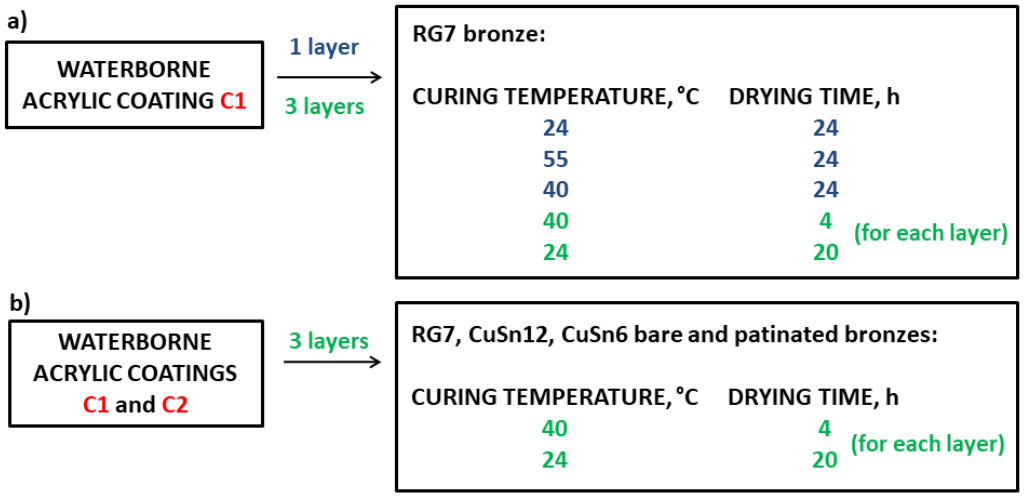

Figure 1. *Experimental conditions for application of the coatings for study of: (a) drying temperature influence, (b) substrate composition influence*

Table 2. *Thickness of coated samples for electrochemical measurements*

	Sample	Thickness, µm
RG7 bronze covered with C1 for investigation of drying temperature and the number of layers	1 layer, 24 °C	35 ± 8
	1 layer, 55 °C	30 ± 11
	1 layer, 40 °C	62 ± 14
	3 layers, 40 °C	27 ± 5
Various bronzes protected with C1 or C2 coatings	C1/CuSn12	15 ± 2
	C1/CuSn6	18 ± 8
	C1/RG7	27 ± 5
	C2/RG7	33 ± 6
	C2/CuSn6	49 ± 2
Sulphate patina protected with C1 coating	C1/CuSn12	11 ± 3
	C1/CuSn6	14 ± 5
	C1/RG7	13 ± 6
Electrochemical patina protected with C1 coating	C1/CuSn12	18 ± 5
	C1/CuSn6	16 ± 8

Coating characterization

The characterization of the protective properties of coatings was conducted by electrochemical measurements: linear polarization (LP) and electrochemical impedance spectroscopy (EIS). Measurements were carried out in simulated acid rain (0.2 g l^{-1} $NaNO_3$ (*p.a.*), from T.T.T., Croatia, 0.2 g l^{-1} $NaHCO_3$ (*p.a.*) and 0.2 g l^{-1} Na_2SO_4 (*p.a.*) from Kemika, Croatia in redistilled water) with pH 5 (adjusted with 0.5 M H_2SO_4, at room temperature). All corrosion tests were carried out with a potentiostat Bio-Logic SP-300, France. A three-electrode cell arrangement was used. A coated bronze served as a working electrode, a saturated calomel electrode (SCE) as a reference and a graphite rod as a counter electrode. Electrochemical measurements were conducted after 45 minutes of open circuit potential (E_{OCP}) stabilization. LP was conducted in a narrow potential range (± 25 mV *vs*. E_{OCP}). EIS was performed at E_{OCP} with an amplitude of 10 mV. The frequency range for EIS was 100 kHz to 10 mHz with 6 points per decade. The impedance analysis was conducted in ZSimpWin 3.60 software with data weighting factor 1.

In addition, gravimetric measurements were conducted in order to determine the percentage of mass increase during the coating soaking in acid rain solution. For this testing, both coatings (C1 and C2) were applied on aluminium foil and dried at 40 °C for 24 h. Each coating sample was weighed before and after drying using a Radwag AS 60/220.X2 Plus, analytical balance (Poland). After drying, samples were left to swell in the acid rain solution, from which they were periodically removed (after

8 and 126 h). The samples were weighed and immediately re-immersed in the solution. Excess water from the coating surface was removed with a gentle wiping by a towel.

Results and discussion

Effect of drying temperature and number of layers on the coating protective properties

The waterborne acrylic coating C1 was applied on RG7 bronze electrodes and dried at different temperatures. The coating was dried either at ambient temperature (24 °C) or at elevated temperatures (55 and 40 °C). In addition, samples with three-layer coating were prepared and dried at 40°C. These samples were prepared so that coating was applied in three thin layers whose total thickness was similar to that of one-layer coating. The intention was to determine if better protection is obtained by coating application in several thin layers or one thicker layer. The protective properties of these coatings were examined by linear polarization measurements during the three-week immersion of bronze samples in artificial acid rain solution. From such obtained polarization curves, polarization resistance values were determined and shown in Figure 2. In general, obtained polarization resistance (R_p) values are almost two orders of magnitude lower than those observed for bronze covered by Paraloid B44, the most common acrylic solvent-based coating for the protection of bronze cultural heritage, examined under similar conditions [19].

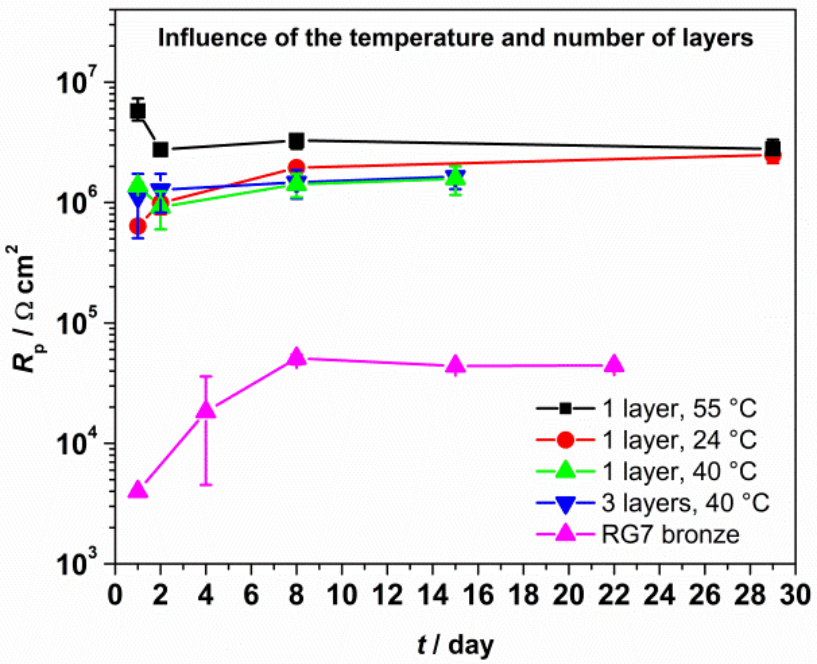

Figure 2. *Dependence of polarization resistance on immersion time in acid rain solution for differently dried coatings*

However, it is common to see that solvent-based coatings have superior performance to waterborne coatings. Initial measurements showed that higher drying temperature resulted in initially higher coating R_p values. On the other hand, initially, there was no significant difference between one- and three-layer coatings dried at the same temperature. However, with the prolonged immersion time an increase in R_p value was observed for coating dried at 24 °C and less pronounced for three-layer coating at 40 °C. For coatings dried at 55 °C and for one-layer coatings at 40 °C, R_p decreased on the second day of immersion, followed by a more or less exhibited increase in R_p with a further immersion period. In order to better understand the observed variations in R_p values, a more detailed analysis was carried out by means of electrochemical impedance spectroscopy.

EIS spectra obtained for bronze with coating cured at 24 °C are presented in Figure 3. The phase angle plot exhibited two maxima, already on the first day of immersion in acid rain solution. This is a clear indication of the presence of water in the coating and at the metal surface, as for the well-protective coatings with no water reaching the metal surface, only one wide phase angle maxima close to -90° would be observed [20-23]. It can be assumed that the coating was not fully dried, *i.e.,* the water remained in the coating and penetrated towards the metal surface. For the second day of immersion, an increase in impedance modulus values in the low-frequency region was observed. Finally, for the last day of immersion, an increase in the value of impedance modulus is visible at both high- and low-frequency regions. In addition, the width of the phase angle curve maximum at high frequencies increased compared to the second day. So, it appears that the protective properties of the coating have improved over time. In their study of different waterborne coatings dried at room temperature, Jianguo *et al.* [24] came to the conclusion that insoluble corrosion products accumulation in the pores of the coating leads to the closure of the pores and improved coating barrier properties. In our study, the presence of corrosion products below the clear coating was not visible to the naked eye (Figure 4a) but can be deduced from the shape of the EIS spectra. However, small bubbles were observed that formed during coating drying, which could lead to easier coating failure. A similar problem was observed by Hwang *et al*. [17] for coating dried at low temperatures.

EIS spectra were analysed by fitting the equivalent electrical circuit shown in Figure 5a to experimental data. The circuit includes three *R*-*Q* couples. Although only two phase angle maxima are clearly observed in the spectra shown in Figure 3, it was not possible to obtain a good fit of the spectra without using the model with three time constants. The electrolyte resistance in all measurements was around 500 Ω cm^2. The first *R*-*Q* couple is noted at the highest frequencies region and is related to the presence of corrosion products (R_F-faradaic resistance of electrochemical reaction involving corrosion products; Q_F-capacitance of corrosion products). *R*-*Q* pair related to the phase angle maxima in the medium to high-frequency region describes the properties of the coating (R_{po} – resistance of the pores in the coating and Q_f-constant phase element representing the coating capacitance), while the medium to low-frequency region is related to the corrosion process on the metal surface (R_{ct}-charge transfer resistance and Q_{dl}-constant phase element representing a double-layer capacitance). The coefficients n_F, n_f and n_{dl} describe nonideal capacitive behaviour. A similar model was used by Collazo *et al*. [25] for the description of EIS spectra of a waterborne resin applied on a galvanized steel substrate. However, in their work, the time constant related to the presence of corrosion products was observed in the medium frequency region.

The obtained impedance parameters are presented in Table 3. The general principle applied in this work for validation of fitting quality was that chi-square value for all fitted spectra must be below 10^{-3}, and that there are no more than one-half of parameters with relative standard error above 10 %. In this case, it can be observed that both Q_F and R_F values were increasing in time. This can be explained by the increase in the amount of corrosion products on the bronze surface. It should be stressed that for the first day, R_F-Q_F values are not fully reliable as only a few points at the high-frequency region correspond to this couple. Regarding the second *R*-*Q* couple, an increase in Q_f from the first to the second day of immersion is due to the penetration of water from the acid rain solution, as the water has a higher dielectric constant compared to organic coating. Such behaviour is often observed for organic coatings in contact with water [20,26,27]. However, on the 29th day of immersion, a decrease in coating capacitance is visible. Additionally, an increase in R_{po} and R_{ct} values is observed, as well as a decrease in Q_{dl} values. Usually, the opposite behaviour is expected as the result of water penetration into the coating and an increase of metal surface area

in contact with water. The improvement of corrosion resistance in time, observed in this work, could be caused by the formation of corrosion products that were closing the pores of the coating and covering the metal surface in the bottom of the pores. Low n_{dl} values obtained for the first day of immersion suggest the influence of diffusion, of species participating in corrosion reaction through the pores of the coating, on the overall corrosion rate.

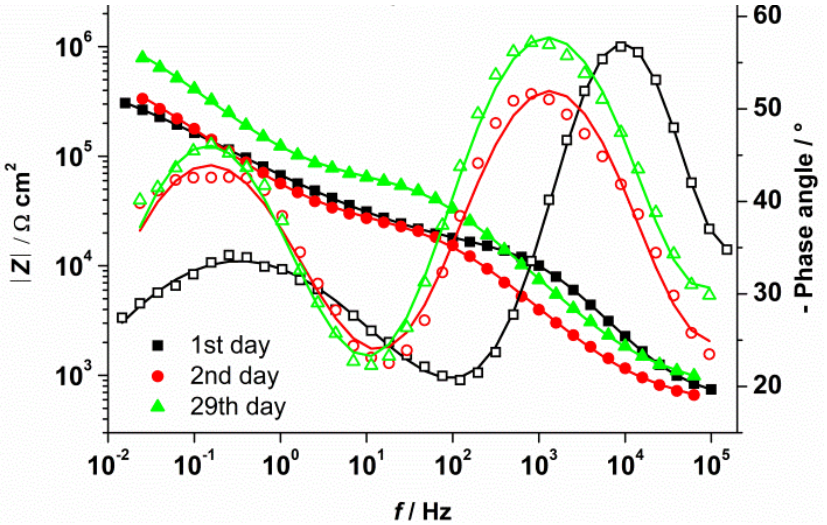

Figure 3. *EIS spectra for one layer of coating dried at 24°C (solid symbols-impedance; open symbols-phase angle). Experimental data are depicted in symbols and fitted data in lines*

Figure 4*. Surface image of RG7 bronze coated with one layer of waterborne acrylic coating C1 dried at: (a) 24 °C, (b) 55 °C and (c) 40 °C for 24 hours. Images were taken upon the immersion in acid rain solution*

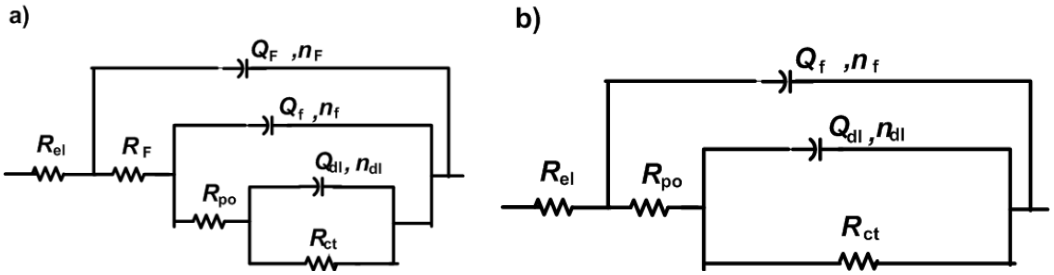

Figure 5. *Electrical equivalent circuits with (a) three time constants and (b) two time constants for analysis of EIS data (R_{el} - electrolyte resistance; R_F - faradaic resistance of electrochemical reaction involving corrosion products; Q_F - capacitance of corrosion products; R_{po}-resistance of pores in the coating; Q_f - constant phase element representing the coating capacitance; R_{ct} - charge transfer resistance; Q_{dl} - constant phase element describing the double layer capacitance; n_F, n_f and n_{dl} - coefficients describing the nonideal capacitive behaviour)*

Table 3. *EIS parameters for one layer of coating dried at 24°C*

	R_F / kΩ cm²	Q_F / μS sⁿ cm⁻²	n_F	R_{po} / kΩ cm²	Q_f/ μS sⁿ cm⁻²	n_f	R_{ct} / kΩ cm²	Q_{dl} / μS sⁿ cm⁻²	n_{dl}
1st day	0.56	0.001	0.99	10.06	0.04	0.87	600	9.30	0.47
2nd day	0.72	0.03	0.73	26.04	0.35	0.74	849	7.20	0.65
29th day	1.12	0.01	0.79	65.78	0.14	0.77	1770	3.22	0.70

The EIS spectra for the coated bronze, dried at elevated temperature (55 °C), are presented in Figure 6. On the first day of exposure, the phase angle plot exhibited a wide maximum at high and medium frequency range, which is typical of a well-protecting organic coating [20,21,28,29]. During the exposure to acid rain solution, the additional peak becomes visible in the lower frequencies region, indicating the occurrence of the corrosion of metal substrate caused by the penetration of water into the coating. These changes are accompanied by a decrease in impedance modulus values. For the analysis of EIS spectra for the first and the second day of exposure, an electrical equivalent circuit with two *R*-*Q* couples was required, where the first couple describes properties of the coating, while the second one describes the corrosion reaction on the metal surface (Figure 5b) [20-22,30,31]. The obtained EIS parameters are shown in Table 4. The decrease in coating protective properties can be observed from the decrease in R_{po} values. In addition, the decrease in R_{ct} and the increase in Q_{dl} values indicate the corrosion process on the metal substrate. Finally, an additional *R*-*Q* couple was required on the 29th day to describe the high-frequency region in EIS spectrum. As in the case of the previous sample, this was ascribed to the appearance of corrosion products. Interestingly, Q_f value didn't change in time despite the decrease in R_{po} values. This can be related to the appearance of surface blistering, which can be clearly observed on studied samples (Figure 4b). As blistering and swelling of the coating caused an increase in coating thickness, its capacitance wasn't changed much despite the entrance of the water. Considering this, it was possible that the selected drying temperature was too high, causing the cracking of the coating, which enabled the penetration of electrolyte and the formation of blisters.

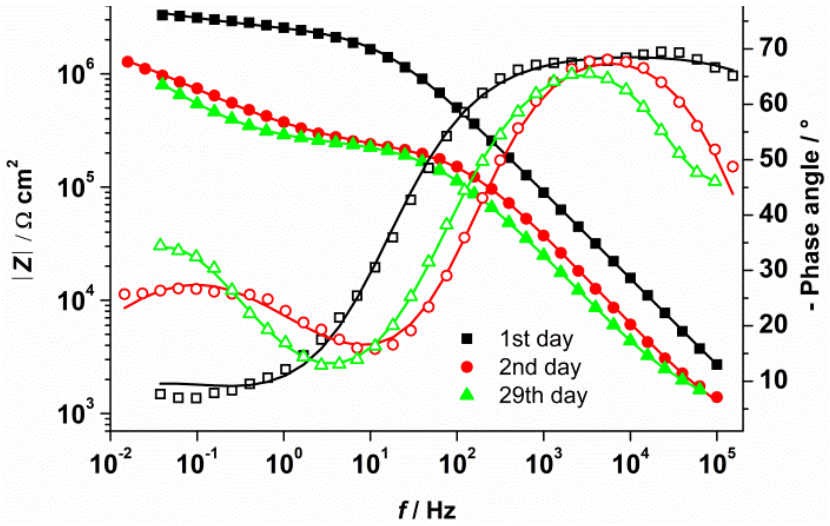

Figure 6. *EIS spectra for one layer of coating dried at 55°C (solid symbols-impedance; open symbols-phase angle). Experimental data are depicted in symbols and fitted data in lines*

Table 4. *EIS parameters for one layer of coating dried at 55°C*

	R_F / kΩ cm^{-2}	Q_F / μS s^n cm^{-2}	n_F	R_{po} / kΩ cm^{-2}	Q_f/ μS s^n cm^{-2}	n_f	R_{ct} / kΩ cm^{-2}	Q_{dl} / μS s^n cm^{-2}	n_{dl}
1st day	-	-	-	2485	0.01	0.77	2634	1.26	0.52
2nd day	-	-	-	217.7	0.02	0.81	2408	1.92	0.52
29th day	3.21	0.05	0.70	248.2	0.01	0.89	2200	3.40	0.68

The results above show that the ambient temperature was too low for coating drying and led to modest protective properties while drying at 55 °C. This resulted in excellent initial properties, but they deteriorated during exposure to an acid rain solution. For this reason, additional studies were performed with the coating dried at 40 °C. The EIS spectra of such samples are shown in Figure 7. In the Bode diagram, it can be seen that the impedance modulus values are lower than for the sample

dried at 55 °C. They decreased significantly from the first to the second day and then increased again by the end of the exposure. For the first and second days of exposure, two-phase angle maxima are clearly visible at high and low frequencies, which required an equivalent electrical circuit with two-time constants for analysis (Figure 5b). As for the previous samples, the presence of two time constants is a clear indication of the occurrence of the corrosion process on the metal surface. The data obtained from the EIS fitting are presented in Table 5. The decrease in R_{ct} and the increase in Q_{dl} values in time also indicate the corrosion process at the bottom of the coating, *i.e.,* on the bronze surface, caused by water penetration. The increase in Q_f is also ascribed to water ingress into the coating. For the analysis of EIS spectrum collected on 29th day of exposure, an additional time constant was needed, pointing to the accumulation of corrosion products. The formation of corrosion products led to an increase in R_{ct} value. Unlike for the sample dried at 24 °C, in this case, the presence of corrosion products was clearly observed on the metal surface, but there were no traces of coating blistering, as seen at 55 °C (Figure 4c).

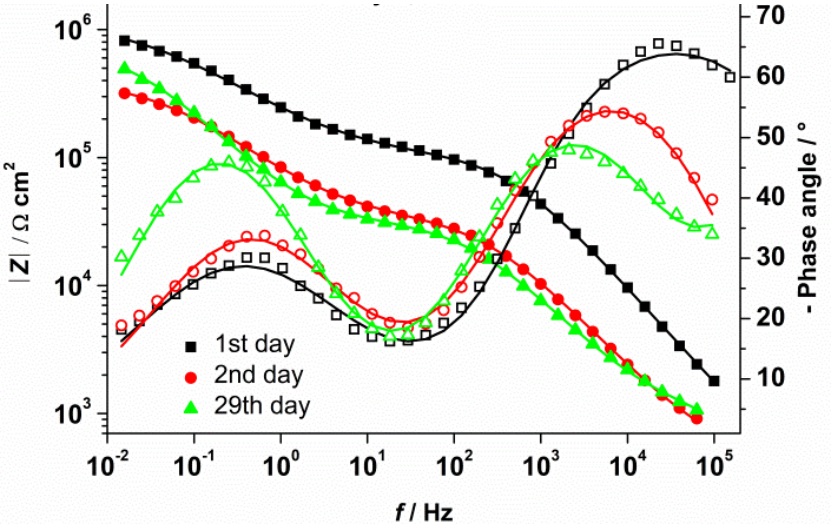

Figure 7. *EIS spectra for one layer of coating dried at 40°C (solid symbols-impedance; open symbols-phase angle). Experimental data are depicted in symbols and fitted data in lines*

Table 5. *EIS parameters for one layer of coating dried at 40°C*

	R_F / kΩ cm^{-2}	Q_F / μS s^n cm^{-2}	n_F	R_{po} / kΩ cm^{-2}	Q_f/ μS s^n cm^{-2}	n_f	R_{ct} / kΩ cm^{-2}	Q_{dl}/ μS s^n cm^{-2}	n_{dl}
1st day	-	-	-	107	0.02	0.76	1090	2.00	0.55
2nd day	-	-	-	34.75	0.14	0.73	384	5.01	0.61
29th day	1.45	0.04	0.71	30.89	0.18	0.73	728	5.75	0.72

Additionally, the influence of coating application in three layers (of total thickness not higher than one layer coating) was examined. Each additional layer was applied after 24 hours and cured at 40 °C for 4 hours. The obtained EIS spectra are presented in Figure 8. The Bode plot showed an increase in impedance modulus values, which was more pronounced at the beginning of the exposure. In the phase angle plots, again for the first two days, two maxima were observed that required the electrical equivalent circuit presented in Figure 5b for fitting. A circuit with three time constants (Figure 5a) was needed for the 29th day of exposure. The data obtained by fitting are shown in Table 6. Similarly to previous samples, an increase in Q_f value is observed on the second day of immersion, which is attributed to the water ingress into the coating. However, R_{po} and R_{ct} values increased at the same time, followed by a decrease in Q_{dl}. This could be attributed to the formation of corrosion products, but they were not observed on the metal surface (Figure 9) nor could be deduced from the impedance spectra.

Similar results were also obtained in our previous study on this coating [32]. The increase in R_{po} can be attributed to the swelling of the polymer particles due to water uptake into the coating and closure of the pores as the result of this process, as was concluded from the study of Lendvay-Gyorik *et al.* [33], as well in the study of Ecco *et al.* [34]. Similarly, Le Pen *et al*. [35] observed an increase in pore resistance of waterborne coating during the first days of immersion, which was attributed to the coalescence process. Such conclusions are also in agreement with an increase in R_{ct} values and lower Q_{dl} values for the second day of immersion. However, on the last day of immersion, an additional phase angle maximum in the high-frequency region is observed, corresponding to the presence of corrosion products. As the water was present in the coating and at the metal/coating interface, it is not surprising that, with time, some corrosion products accumulated on the surface and in the pores of the coating. However, they could not be seen by the bare eye (Figure 9) as for one layer coating.

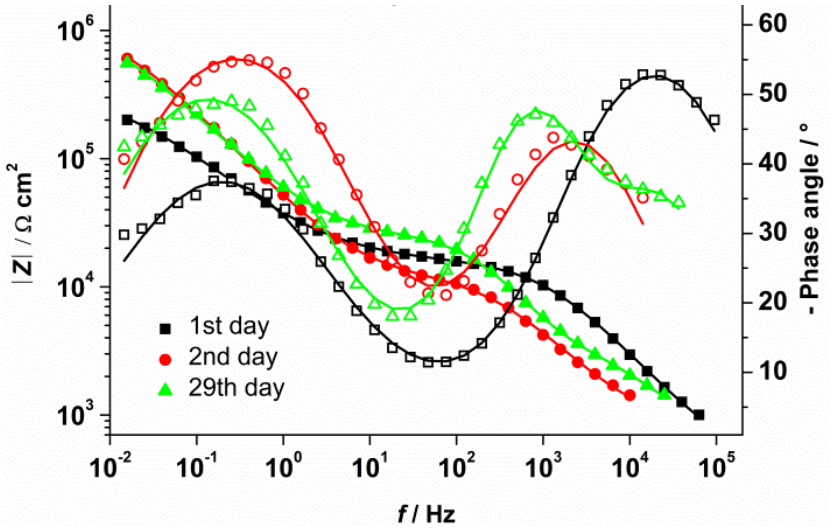

Figure 8. *EIS spectra for three layers of coating dried at 40°C (solid symbols-impedance; open symbols-phase angle). Experimental data are depicted in symbols and fitted data in lines*

Table 6. *EIS parameters for three layers of coating dried at 40°C*

	R_F / kΩ cm^2	Q_F / μS s^n cm^{-2}	n_F	R_{po} / kΩ cm^2	Q_f/ μS s^n cm^{-2}	n_f	R_{ct} / kΩ cm^2	Q_{dl} / μS s^n cm^{-2}	n_{dl}
1st day	-	-	-	15.8	0.08	0.75	351.8	12.1	0.61
2nd day	-	-	-	11.9	0.32	0.75	1200	5.43	0.72
29th day	3.39	0.05	0.83	21.1	0.07	0.88	1350	6.20	0.68

Figure 9*. Surface image of three layers of waterborne acrylic coating C1 coated on a RG7 bronze where each layer was dried at 40 °C for 4 hours*

From these results, it can be concluded that better protective properties are obtained if the coating is applied in three thinner layers than in one thicker layer, which can probably be ascribed to more efficient drying in the first case. In addition, the observed improvement of protective properties of the

three-layer coating during the sample immersion in acid rain solution was probably due to the coating swelling, while in the case of one-layer coating, the formation of corrosion products was a dominant phenomenon, visible by the naked eye, which can be related to coating cracking during the drying process.

Supplementary studies were conducted on bronze samples protected by coating C2, which is also an acrylic waterborne coating but with slightly higher water content and without a corrosion inhibitor that could reduce the corrosion rate of the metal substrate. Figure 10 presents the EIS spectrum for RG7 bronze protected with C2, applied in three layers and dried at 40 °C.

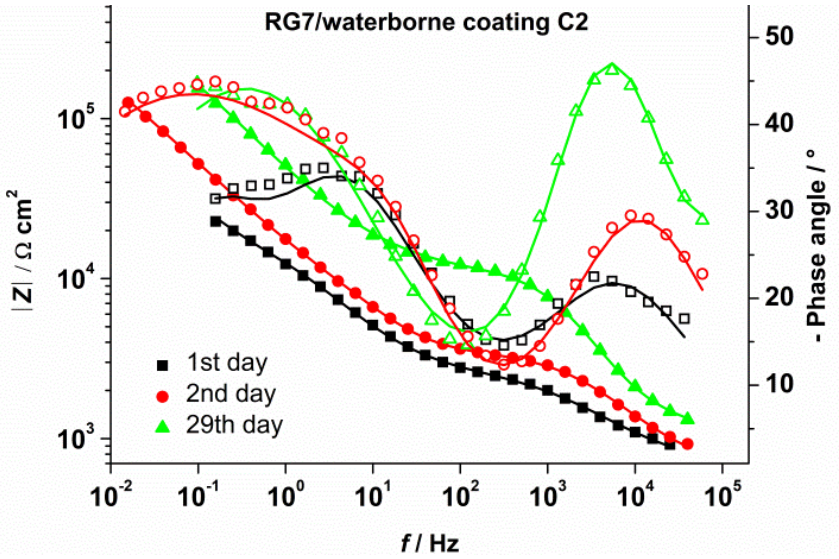

Figure 10. *EIS spectra for three layers of coating C2 dried at 40°C (solid symbols-impedance; open symbols-phase angle). Experimental data are depicted in symbols and fitted data in lines*

It can be observed that impedance modulus values increased in time, in a whole frequency range, which means that the corrosion resistance increases with the immersion time. Still, C2 coating showed lower protective properties compared to C1 coating. It is also interesting to note that the impedance modulus values, both at high and low frequencies, increased with the immersion time, indicating improved coating barrier properties. For these spectra, it was necessary to use an electrical equivalent circuit with three *R*-*Q* pairs in order to achieve satisfactory fitting quality. It is similar to the one presented in Figure 5a, but the R_F-Q_F couple is related to the medium-frequency region, as in these spectra, two phase angle maxima are observed in the medium and low-frequency regions. The EIS parameters obtained by fitting are listed in Table 7.

Table 7. *EIS parameters for three layers of coating C2 dried at 40°C*

	R_{po} / kΩ cm²	Q_f / μS sⁿ cm⁻²	n_f	R_F / kΩ cm²	Q_F/ μS sⁿ cm⁻²	n_F	R_{ct} / kΩ cm²	Q_{dl} / μS sⁿ cm⁻²	n_{dl}
1st day	2.04	1.18	0.66	19.7	15.9	0.69	33.0	51.3	0.83
2nd day	2.93	0.32	0.72	6.55	4.60	0.87	803	22.8	0.54
29th day	1.45	0.004	0.87	9.65	0.03	0.90	695	7.35	0.61

In general, for C2 coating, a greater decrease in capacitance values at all frequencies is observed, probably as a result of the swelling of the coating and closure of the pores, which also contributed to the R_{ct} increase. This time, R_{ct} values are significantly lower than for the previously tested C1 coating. This increase in resistance, once again, could be ascribed to the formation of corrosion products. Their presence here is not noticeable as one layer of C1 dried at 40 °C, but this time coating

turned bluish, indicating the presence of copper ions. The assumption is that the copper ions probably slowly came out through the coating during immersion in acid rain solution.

Further study includes gravimetric measurements, which were carried out with the aim to analyse water absorption by coating. Gravimetric measurements of both tested coatings showed the same trend, presented in Table 8. After 8 h of immersion in acid rain solution, an increase in mass could be observed, which is explained by the fact that the coating took up a certain amount of water. This phenomenon is found in the case of physically drying resins and paints. There are still many pores in the dry film through which water can penetrate, resulting in coating swelling [33]. However, after 5 days of immersion, mass loss was noticed. Although dry coating cannot be dissolved anymore, it is possible that water could still dissolve certain components and polymer particles of low-degree polymerization [33]. Roggero *et al*. [36] associated this mass loss with the release of plasticizer from the formulation. They noted possible leaching or release of soluble coating components due to water penetration into the coating. When comparing the two studied coatings, greater water absorption and consequent mass loss were obtained for C2 coating, which already contained a larger amount of water in its composition compared to C1.

Table 8. *Results of gravimetric analysis for coatings dried at 40 °C samples and immersed in acid rain solution*

Sample	Mass before immersion, g	Mass change after 8 h of immersion, %	Mass change after 126 h of immersion, %
C1	0.312	+ 30	+ 9
C2	0.361	+ 41	+ 29

Comparison between two waterborne coatings on different bronze substrates

Previous results have shown that incomplete coating drying can lead to substrate corrosion. Therefore, substrate corrosion resistance could be important for overall coating performance. For this reason, corrosion protection by C1 and C2 was examined on different bronze substrates. Linear polarization measurements were conducted to evaluate polarization resistance values during three weeks of immersion in artificial acid rain solution (Figure 11).

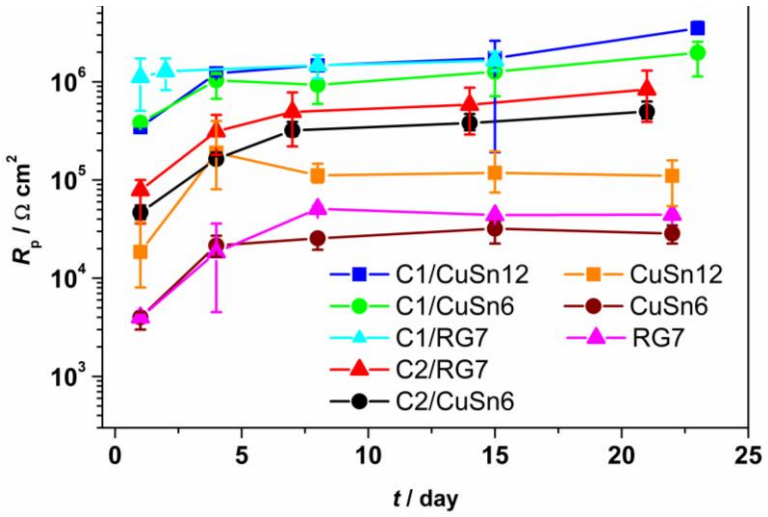

Figure 11. *Dependence of polarization resistance on time for two waterborne coatings on different bronze substrates*

It can be seen that the R_p values were higher for all bronzes protected with C1 than when protected with C2, although both provided corrosion protection to bronze surfaces. Another thing to emphasize is the trend of constant growth of resistance for all coated samples. This trend can be related to the coating swelling (expected in the first days of immersion) [35,18], although some

increase due to the plugging of the pores by corrosion products cannot be neglected. In principle, the higher the corrosion resistance of the bronze substrate alone, the higher the corrosion resistance of the coated sample. For all examined bronzes, significant corrosion protection can be achieved by both studied waterborne coatings, especially by C1 coating.

Waterborne coatings on patinated bronze substrates

As mentioned in the Introduction section, bronze exposed to a corrosive environment gradually covers with corrosion products called patina. Its composition depends on the concentration and type of present aggressive ions. Patina is also often formed artificially in order to achieve the aesthetically pleasant appearance of bronze sculptures. In this work, two types of bronze patina are used, chemically formed dark brown patina as a common type of artificial patina on bronze [37] and electrochemically formed green-bluish patina representing aged patina, consisting of copper sulphates or carbonates [3,38,39]. In this work, the protection of patinated substrates by waterborne coating C1 was investigated. Since the lower drying temperature resulted in the formation of small bubbles in the coating and a modest level of corrosion protection for bare bronze, while at higher temperature exposure to the corrosive medium resulted in coating blistering, the drying temperature for the protective coating of already reactive artificial patina substrates was 40 °C. The coating application was performed in three layers due to more efficient drying.

Studies were conducted using polarization resistance measurements during three weeks of exposure to an artificial acid rain solution (Figure 12). It can be observed that for all patinated bronzes, C1 coating provided a high level of corrosion protection. In the case of coated sulphide patina, the R_p values were the highest for CuSn12 bronze. Similarly to the case of bare bronze substrates, the trend of constant growth of resistance attributed to coating swelling was present [35,18]. Such a trend was also observed for electrochemical patina on two different bronze substrates protected with waterborne coating, only this time, the resistance was higher for CuSn6 bronze.

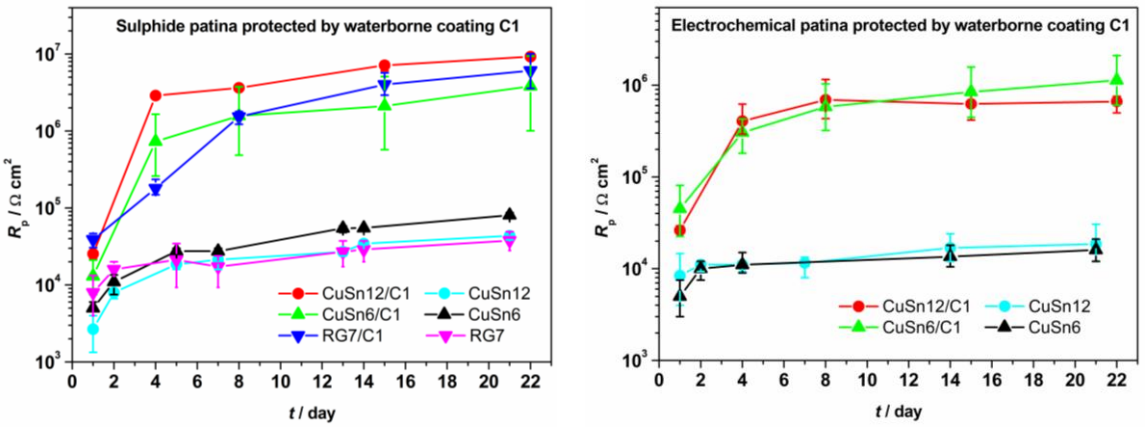

Figure 12. *Polarization resistance on time for waterborne coating C1 on differently patinated bronze substrates. (a) Sulphide and (b) electrochemical patina formed on various types of bronze*

Another important thing to emphasize is that the selected waterborne coating does not alter the visual appearance of the patinas, as shown in Figure 13. There was no change of colour of the patina upon the coating application, as well as during the exposure to acid rain [18]. This confirms the suitability of C1 coating for application on patinated bronze as it enhances the stability of the patina layer.

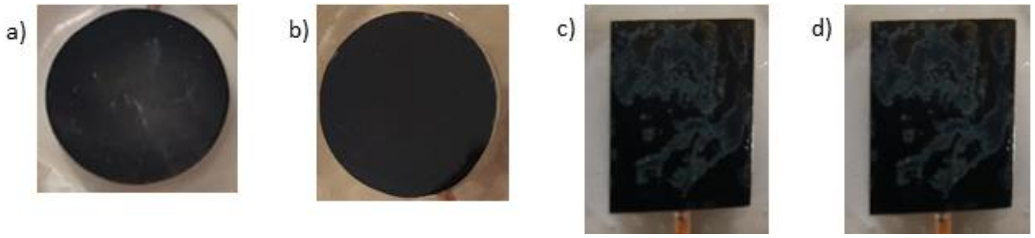

***Figure 13**. Visual appearance of bronze sample with (a) sulphide patina, (b) sulphide patina with C1, (c) electrochemical patina and (d) electrochemical patina with C1 before exposure*

Conclusions

The investigation of the influence of drying temperature on acrylic waterborne coating protective properties showed that the temperature had a significant impact on coating performance. It was found that drying at ambient temperature resulted in the formation of small bubbles in dry coating and modest corrosion protection. Although the sample polarization resistance values increased during the three-week immersion in artificial rain solution, from EIS spectra, it appeared that this was the consequence of the formation of corrosion products that were plugging the pores of the coating. Drying at 55 °C resulted in greater initial corrosion protection, but the degradation occurred during exposure to acid rain solution. Moreover, the coating blistering was observed. The one-layer coating dried at 40 °C showed inadequate protection stability as the formation of corrosion products was observed, however, when the coating was applied in three layers, there were no visible corrosion products. In addition, the resistance values increased for the whole exposure time, which was attributed to swelling of the polymer particles due to water uptake into the coating and closure of the pores.

The level of protection between two acrylic coatings that differ in the amount of water and the presence of corrosion inhibitor was compared. The coating with a lower amount of water and corrosion inhibitor exhibited better protective properties for different bronze substrates. In general, the higher the corrosion resistance of bare bronze, the better the performance of the coating.

This study also revealed that coating C1 is suitable for the protection of artificially patinated bronzes as the patina layer surface is not changed by coating application and remains stable in time.

***Acknowledgements**: This work was fully supported and funded by the Croatian Science Foundation under the project IP-2019-04-5030.*

***Conflicts of interest**: The authors declare to have no competing financial interest or personal relation that could influence the results of this work.*

References

[1] M. Wadsak, I. Constantinides, G. Vittiglio, A. Adriaens, K. Janssens, M. Schreiner, F.C. Adams, P. Brunella, M. Wuttmann, Multianalytical study of patina formed on archaeological metal objects from Bliesbruck-Reinheim, *Microchimica Acta* **133** (2000) 159–164. https://doi.org/10.1007/s006040070086

[2] D.A. Scott, *Copper and Bronze in Art: Corrosion, colorants, conservation*, Getty Publications, Los Angeles, California, 2002, p. 277.

[3] G. Di Carlo, C. Giuliani, C. Riccucci, M. Pascucci, E. Mesina, G. Fierro, M. Lavorgna, G.M. Ingo, Artificial patina formation onto copper-based alloys: chloride and sulphate induced corrosion processes, *Applied Surface Science* **421** (2017) 120-127. https://doi.org/10.1016/j.apsusc.2017.01.080

[4] E. Rocca, F. Mirambet, in *Corrosion of metallic heritage artefacts, investigation, conservation and prediction for long-term behavior*, P. Dillmann, G. Beranger, P. Piccardo, H. Matthiesen, Woodhead Publishing, City, USA, 2007, p. 308-334.
[5] J. Hu, K. Peng, J. Guo, D. Shan, G.B. Kim, Q. Li, E. Gerhard, L. Zhu, W. Tu, W. Lv, M.A. Hickner, J. Yang, Click crosslinking improved waterborne polymers for environment-friendly coatings and adhesives, *Applied Materials and Interfaces* **8** (2016) 17499–17510. https://doi.org/10.1021/acsami.6b02131
[6] R. Hischier, B. Nowack, F. Gottschalk, I. Hincapie, M. Steinfeldt, C. Som, Life cycle assessment of façade coating systems containing manufactured nanomaterials, *Journal of Nanoparticle Research* **17** (2015) 68. https://doi.org/10.1007/s11051-015-2881-0
[7] J.L. Hall, A. Pérez, E.L. Kynaston, C. Lindsay, J.L. Keddie, Effects of environmental conditions on the micro-mechanical properties of formulate waterborne coatings, *Progress in Organic Coatings* **163** (2022) 106657. https://doi.org/10.1016/j.porgcoat.2021.106657
[8] E. Almeida, D. Santos, J. Uruchurtu, Corrosion performance of waterborne coatings for structural steel, *Progress in Organic Coatings* **37** (1999) 131-140. https://doi.org/10.1016/S0300-9440(99)00064-8
[9] V. Duecoffre, W. Diener, C. Flosbach, W. Schubert, Emulsifiers with high chemical resistance: a key to high performance waterborne coatings, *Progress in Organic Coatings* **34** (1998) 200-205. https://doi.org/10.1016/S0300-9440(98)00032-0
[10] F. Galliano, D. Landolt, Evaluation of corrosion protection properties of additives for waterborne epoxy coatings on steel, *Progress in Organic Coatings* **44** (2002) 217-225. https://doi.org/10.1016/S0300-9440(02)00016-4
[11] T.D. Martins, M.T. Viciosa, M.B. Oliveira, A. Fernandes, J.F. Mano, C. Baleizão, J.P.S. Farinha, Reversible imine crosslinking in waterborne self-healing polymer coatings, *Progress in Organic Coatings* **180** (2023) 107552. https://doi.org/10.1016/j.porgcoat.2023.107552
[12] M.E. Belowich, J.F. Stoddart, Dynamic imine chemistry, *Chemical Society Reviews* **41** (2012) 2003-2004. https://doi.org/10.1039/c2cs15305j
[13] J.M.G. Martinho, J.P.S. Farinha, Analytical series: fluorescence decay methods for the characterization of latex film formation, *Journal of Coatings Technology and Research* **10** (2013) 42-49.
[14] S. Piçarra, C.A.M. Afonso, V.B. Kurteva, A. Fedorov, J.M.G. Martinho, J.P.S. Farinha, The influence of nanoparticle architecture on latex film formation and healing properties, *Journal of Colloid and Interface Science* **368** (2012) 21-33. https://doi.org/10.1016/j.jcis.2011.10.077
[15] A. Aradian, E. Raphaël, P.G. de Gennes, Strengthening of a polymer interface: interdiffusion and cross-linking, *Macromolecules* **33** (2000) 9444-9451. https://doi.org/10.1021/ma0010581
[16] I. Stojanović, I. Juraga, V. Alar, Influence of drying temperature on protective properties of waterborne and solventborne epoxy coating, *International Journal of Electrochemical Science* **9** (2014) 2507-2517. https://doi.org/10.1016/S1452-3981(23)07943-9
[17] H.-D. Hwang, J.-I. Moon, J.H. Choi, H.-J. Kim, S.D. Kim, J.C. Park, Effect of water drying conditions on the surface property and morphology of waterborne UV-curable coatings for engineered flooring, *Journal of Industrial and Engineering Chemistry* **158** (2009) 381-387. https://doi.org/10.1016/j.jiec.2008.11.002
[18] A. Kapitanović, H. Otmačić Ćurković, The influence of phosphonic acid pretreatment on the bronze corrosion protection by waterborne coating, *Journal of Solid State Electrochemistry* **27** (2023) 1861-1875. https://doi.org/10.1007/s10008-023-05490-1

[19] T. Kosec, A. Legat, I. Milošev, The comparison of organic protective layers on bronze and copper, *Progress in Organic Coatings* **69** (2010) 199-206. https://doi.org/10.1016/j.porgcoat.2010.04.010
[20] F. Mansfeld, Use of electrochemical impedance spectroscopy for the study of corrosion protection by polymer coatings, *Journal of Applied Electrochemistry* **25** (1995) 187-202. https://doi.org/10.1007/BF00262955
[21] E. Cano, D. Lafuente, D.M. Bastidas, Use of EIS for the evaluation of the protective properties of coatings for metallic cultural heritage: a review, *Journal of Solid State Electrochemistry* **14** (2010) 381-391. https://doi.org/10.1007/s10008-009-0902-6
[22] E. Cano, D.M. Bastidas, V. Argyropoulos, S. Fajardo, A. Siatou, J.M. Bastidas, C. Degrigny, Electrochemical characterization of organic coatings for protection of historic steel artefacts, *Journal of Solid State Electrochemistry* **14** (2010) 453-463. https://doi.org/10.1007/s10008-009-0907-1
[23] H. Wang, P. Zhang, G. Fei, Y. Ma, N. Rang, Y. Kang, Design and properties of environmental anticorrosion coating based on *m*-aminobenzenesulfonic acid/aniline/*p*-phenylenediamine terpolymer, *Progress in Organic Coatings* **137** (2019) 105274. https://doi.org/10.1016/j.porgcoat.2019.105274
[24] L. Jianguo, G. Gaoping, Y. Chuanwei, EIS study of corrosion behaviour of organic coating/Dacromet composite systems, *Electrochimica Acta* **50** (2005) 3320-3332. https://doi.org/10.1016/j.electacta.2004.12.010
[25] A. Collazo, B. Díaz, R. Figueroa, X.R. Nóvoa, C. Pérez, Corrosion resistance of a water-borne resin doped with graphene derivatives applied on galvanized steel, *Progress in Organic Coatings* **173** (2022) 107220. https://doi.org/10.1016/j.porgcoat.2022.107220
[26] A. Miszczyk, K. Darowicki, Water uptake in protective organic coatings and its reflection in measured coating impedance, *Progress in Organic Coatings* **124** (2018) 296-302. https://doi.org/10.1016/j.porgcoat.2018.03.002
[27] F. Bellucci, L. Nicodemo, Water transport in organic coatings, *Corrosion* **49** (1993) 235-247. https://doi.org/10.5006/1.3316044
[28] G. Grundmeier, W. Schmidt, M. Stratmann, Corrosion protection by organic coatings: electrochemical mechanism and novel methods of investigation, *Electrochimica Acta* **45** (2000) 2515-2533. https://doi.org/10.1016/S0013-4686(00)00348-0
[29] H. Qian, X. Fu, Y. Chi, R. Zhang, C. Zhan, H. Sun, X. Zhou, J. Sun, Study on electrodeposition and corrosion resistance of Cu-Sn alloy prepared in ChCl-EG deep eutectic solvent, *Journal of Solid State Electrochemistry* **26** (2002) 469-479. https://doi.org/10.1007/s10008-021-05086-7
[30] B. Dou, H. Xiao X. Lin, Y. Zhang, S. Zhao, S. Duan, X. Gao, Z. Fang, Investigation of the anti-corrosion properties of fluorinated graphene-modified waterborne epoxy coatings for carbon steel, *Coatings* **11** (2021) 254. https://doi.org/10.3390/coatings11020254
[31] J.B. Bajat, I. Milošev, Ž. Jovanović, V.B. Mišković-Stanković, Studies on adhesion characteristics and corrosion behaviour of vinyltriethoxysilane/epoxy coating protective system on aluminium, *Applied Surface Science* **256** (2010) 3508-3517. https://doi.org/10.1016/j.apsusc.2009.12.100
[32] A. Kapitanović, T. Kokot, H. Otmačić Ćurković, Bronze corrosion protection by bilayer systems: self-assembled monolayers of phosphonic acid/waterborne acrylic coating, *Progress in Organic Coatings* **186** (2024) 107984. https://doi.org/10.1016/j.porgcoat.2023.107984
[33] G. Lendvay-Györik, T. Pajkossy, B. Lengyel, Corrosion-protection properties of water-borne paint coatings as studied by electrochemical impedance spectroscopy and gravimetry.

Progress in Organic Coatings **56** (2006) 304-310. https://doi.org/10.1016/j.porgcoat.2006.05.012

[34] L.G. Ecco, J. Li, M. Fedel, F. Deflorian, J. Pan, EIS and in situ AFM study of barrier property and stability of waterborne and solventborne clear coats, *Progress in Organic Coatings* **77** (2014) 600-608. http://dx.doi.org/10.1016/j.porgcoat.2013.11.024

[35] C. Le Pen, C. Lacabanne, N. Pébère, Characterisation of water-based coatings by electrochemical impedance spectroscopy, *Progress in Organic Coatings* **46** (2003) 77-83. https://doi.org/10.1016/S0300-9440(02)00213-8

[36] A. Roggero, L. Villareal, N. Caussé, A. Santos, N. Pébère, Correlation between the physical structure of a commercially formulated epoxy paint and its electrochemical impedance response, *Progress in Organic Coatings* **146** (2020) 105729. https://doi.org//10.1016/j.porgcoat.2020.105729

[37] A. Kapitanović, H. Otmačić Ćurković, The effect of corrosion conditions on aging of artificial patina on three bronzes, *Coatings* **12** (2022) 936. https://doi.org/10.3390/coatings12070936

[38] K. Marušić, H. Otmačić-Ćurković, Š. Horvat-Kurbegović, H. Takenouti, E. Stupnišek-Lisac, Comparative studies of chemical and alectrochemical preparation of artificial bronze patinas and their protection by corrosion inhibitor, *Electrochimica Acta* **54** (2009) 7106-7113. https://doi.org/10.1016/j.electacta.2009.07.014

[39] G. Masi, J. Esvan, C. Josse, C. Chiavari, E. Bernardi, C. Martini, M.C. Bignozzi, N. Gartner, T. Kosec, L. Robbiola, Characterisation of typical patinas simulating bronze corrosion in outdoor conditions, *Material Chemistry and Physics* **200** (2017) 308-321. https://doi.org/10.1016/j.matchemphys.2017.07.091

J. Electrochem. Sci. Eng. **14(2)** (2024) 265-273; http://dx.doi.org/10.5599/jese.2291

Open Access : : ISSN 1847-9286
www.jESE-online.org

Original scientific paper

Additive concentration and nozzle moving speed influence on local copper deposition for electrochemical 3D-printing

Roman Babchuk, Dmytro Uschapovskiy, Victoria Vorobyova, Olga Linucheva, Mykhailo Kotyk and Georgii Vasyliev✉

National Technical University of Ukraine "Igor Sikorsky Kyiv Polytechnic Institute", 37, Prospect Beresteiskyi, Kyiv-56, 03056, Ukraine

Corresponding author: ✉g.vasyliev@kpi.ua; Tel.: +38-096-924-9888; Fax: +38-044-204-9773

Received: February 17, 2024; Accepted: March 21, 2024; Published: March 24, 2024

Abstract

The local deposition process from copper sulfate electrolyte was investigated depending on nozzle moving speed and additive concentration in the electrolyte. A 2×2 cm square model was created and sliced in Ultimaker Cura software, uploaded in a 3D printer, and printed from the copper electrolyte on the stainless-steel surface. Low additive concentration in the electrolyte was found to influence dendrite formation in the corner sections of a square model. Nozzle movement speed was found to influence the deposition area and the thickness of the metal. The lowest tested nozzle movement speed of 5 s / voxel increased the deposition area by nearly 40 % in horizontal direction compared to 2.5 s / voxel. Further increase of nozzle movement speed to 1.6 s / voxel does not change the deposition area. The thickness in the corners increases by 2.5 times compared to the straight section of the square when the nozzle movement speed increases from 5 to 1.6 s / voxel. The non-uniform thickness of the deposited metal is caused by a considerable reduction of nozzle movement speed when it moves through the corner. The results obtained in this work can be further used to develop electrochemical 3D printing technology.

Keywords

Additive manufacturing; copper electroplating; slicing; profilometry

Introduction

Additive manufacturing is a novel and fast-developing technique based on the bottom-up approach. Unlike traditional manufacturing, the part is produced by forming it from the material layer by layer when excessive material is mechanically or physically removed. Non-metallic additive manufacturing technologies are rapidly developing and, in some industries, have already replaced traditional ones, but metal parts additive manufacturing remains a challenge [1,2].

Most metal additive manufacturing technologies require high energy to melt the metal. Laser or electromagnetic sources are used [3,4]. Compared to them, the electrochemical additive manufacturing technique, when metal parts are formed by metal deposition from ions in the electrolyte solution is much cheaper because it does not require high energies and prior preparation of expandable materials.

Different techniques have been developed for electrochemical additive manufacturing (ECAM). They can be divided into two main groups: mask-based and maskless electrochemical manufacturing [5]. It is generally agreed that maskless manufacturing is a more promising technique because it does not require mask preparation and can be performed easily using only electrolyte and electrodes.

Several maskless ECAM techniques with different manufacturing speeds and accuracy are developing. Among them are fluidic force microscope (FluidFM) [6-10], meniscus-confined deposition [11-16], jet electrodeposition [17-19] and localized electrochemical deposition [20-24]. In the localized electrochemical deposition technique, the electric field distribution in the electrolyte determines the deposition area; the electrolyte composition and current mode determine the deposition rate. In our previous works, it was established that electrolyte composition can influence the slope of the polarization curve and influence the deposition area [24].

The aim of the present work is to study the influence of additive concentration in the electrolyte and the 3D-printer nozzle moving speed on the deposition area and thickness distribution of the deposited copper layer.

Experimental

The local electrochemical deposition process was investigated in square model printing. The appearance of the model in the UltiMaker Cura software is shown in Figure 1. The size of the object was 20×20 mm and the height was 2 mm. The object was sliced in g-code with the following parameters: nozzle moving speed F1200, coordinate movement direction (X60.178, Y60.179), layer height (Z0.001) that corresponds to 1 μm in the slicer. The g-code was loaded in a 3D printer.

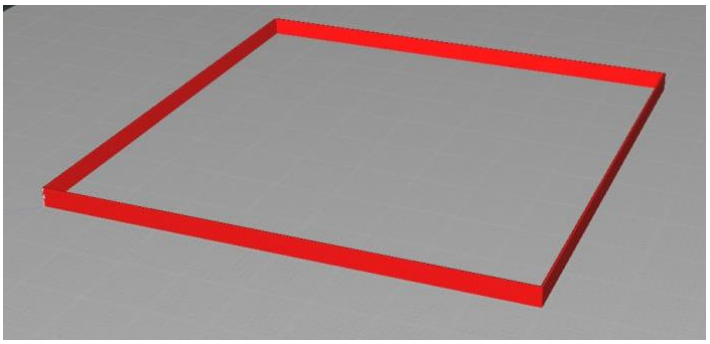

Figure 1. *The appearance of square model, used in 3D printing in the UltiMaker Cura software*

The laboratory setup is shown in Figure 2. The printing process is performed on the surface of the stainless-steel plate placed on the bottom of the plastic vessel. 1 L of electrolyte was poured into the vessel, and its level was 1.5-2 cm above the plate. The vessel was placed inside the 3D printer frame. The steel plate was attached to the negative pole of the direct current source, while the positive pole was attached to the anode placed inside the printer nozzle. The anode was made of lead. An insoluble lead anode was used because lead in a sulfate solution is chemically stable and is potentially cheaper than platinum. The main purpose of the insoluble anode application is to avoid the formation of monovalent copper ions in the solution, which can provoke the formation of coarse

crystalline sediments (disproportionation with the formation of metallic dispersed copper, which is transferred to the cathode and provokes the formation of dendrites). The printing process was started by turning on the current once the anode was placed in a certain position of vessel. The current source maintained a constant current value, varying the applied voltage.

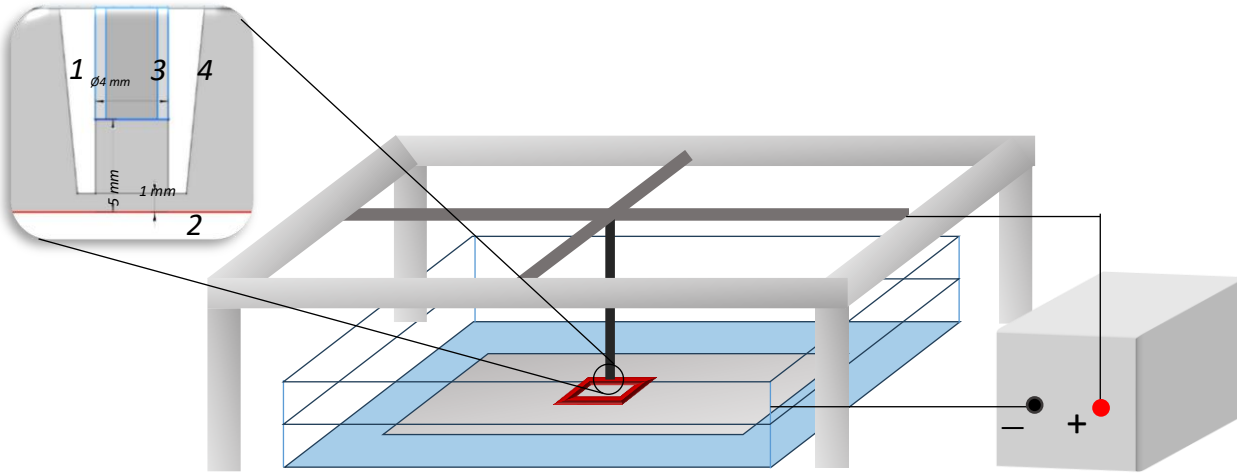

Figure 2. *The laboratory setup for local electrodeposition*

The copper plating electrolyte was used for metallic copper deposition. Two electrolyte compositions were used with different concentrations of the additive. Electrolyte compositions are given in Table 1, while deposition conditions are presented in Table 2. A total of 5 objects were printed in both electrolytes and at 3 different nozzle moving speeds.

Table 1. *Electrolytes composition*

Component	Content, g/L	
	Electrolyte 1	Electrolyte 2
$CuSO_4 \cdot 5H_2O$	200	200
H_2SO_4	75	75
KCl	0.3	0.3
Additive RUBIN T-200*	1 mL/L of Rubin T200-A 4 mL/L of Rubin T200-G 1 mL/L of Rubin T200-E	2 mL/L of Rubin T200-A 8 mL/L of Rubin T200-G 2 mL/L of Rubin T200-E

*Leveling and brightness additive, KIESOW OBERFLÄCHENCHEMIE GmbH & Co. KG

Table 2. *Deposition conditions used for local copper deposition investigation*

Exp. No	Electrolyte	Anode moving speed, s/voxel	Applied current density, A / cm^2	Deposition duration, h
1	1	2.5	4	6
2	1	1.6	4	6
3	2	5.0	4	6
4	2	2.5	4	6
5	2	1.6	4	6

The 3D-printed objects were characterized by 3D profilometry. Two cross-sections were measured and used for analysis: a cross-section of the edge and a cross-section of the corner (Figure 3).

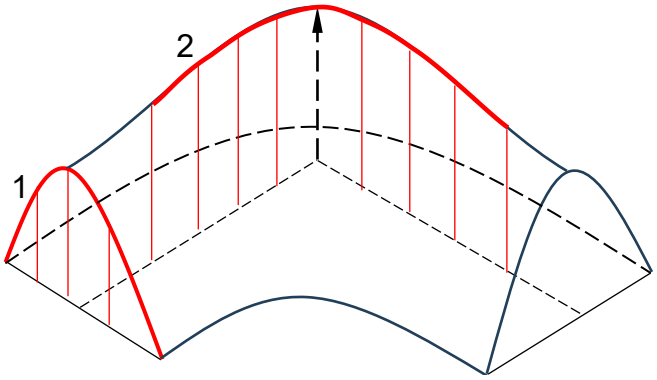

Figure 3. *The scheme showing cross-section regions in the printed square object used for analysis: 1 - cross-section of the edge; 2 - cross-section of the corner*

Results and discussion

The copper deposition process in the sulfate electrolyte is a simple electrochemical process that can be summarized with the equation:

$$Cu^{2+} + 2e^{-} = Cu \quad (1)$$

Every 2 electrons reduce one copper atom, which is deposited on the surface of the metal substrate. According to Faraday's law, the amount of electricity determines the mass of deposited metal. At the same time, the morphology of deposited metal depends on the kinetic parameters of the electrochemical process as well as the electric field distribution between the anode located in the nozzle and a cathode placed at the bottom of the vessel.

The photos of deposited objects are given in Figure 4. All the deposited objects are square-shaped. However, depending on the deposition conditions, the morphology of deposited metal is different.

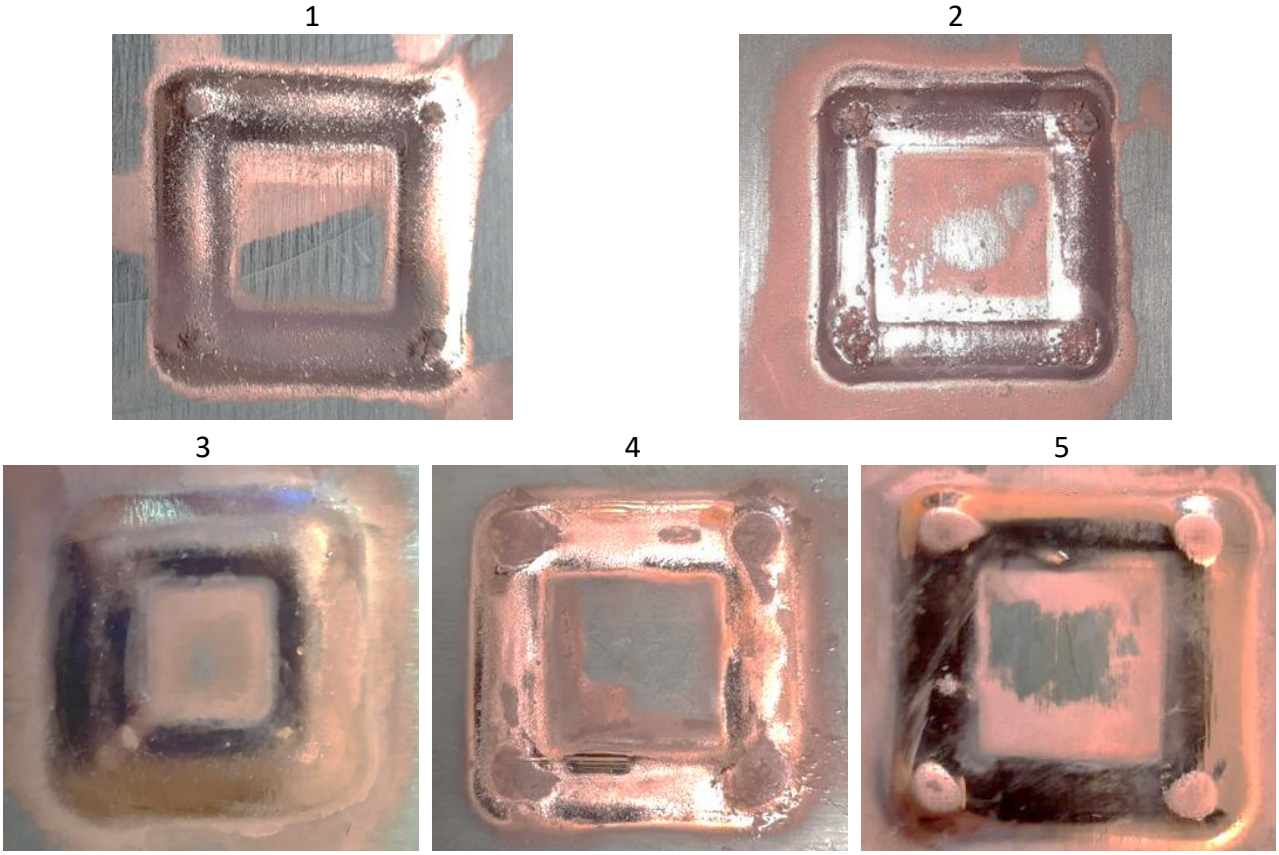

Figure 4. *Photographs of 3D-printed square objects: 1 to 5 - correspond to experiment numbers in Table 2*

In Electrolyte 1, with reduced additive content, the dendrites formation appears in the corners of the square (Figure 4.1, 4.2). Also, the reduction of nozzle moving speed leads to an increase in deposition area (Figure 4.3).

Depending on deposition conditions, size distribution in printed objects was measured using 3D profilometry. The profilograms are shown in Figure 5. The formation of dendrites is clearly visible in the corner section for the objects printed in Electrolyte 1 at both nozzle moving speeds. The cross-sections of printed objects are presented in Figures 6 and 7.

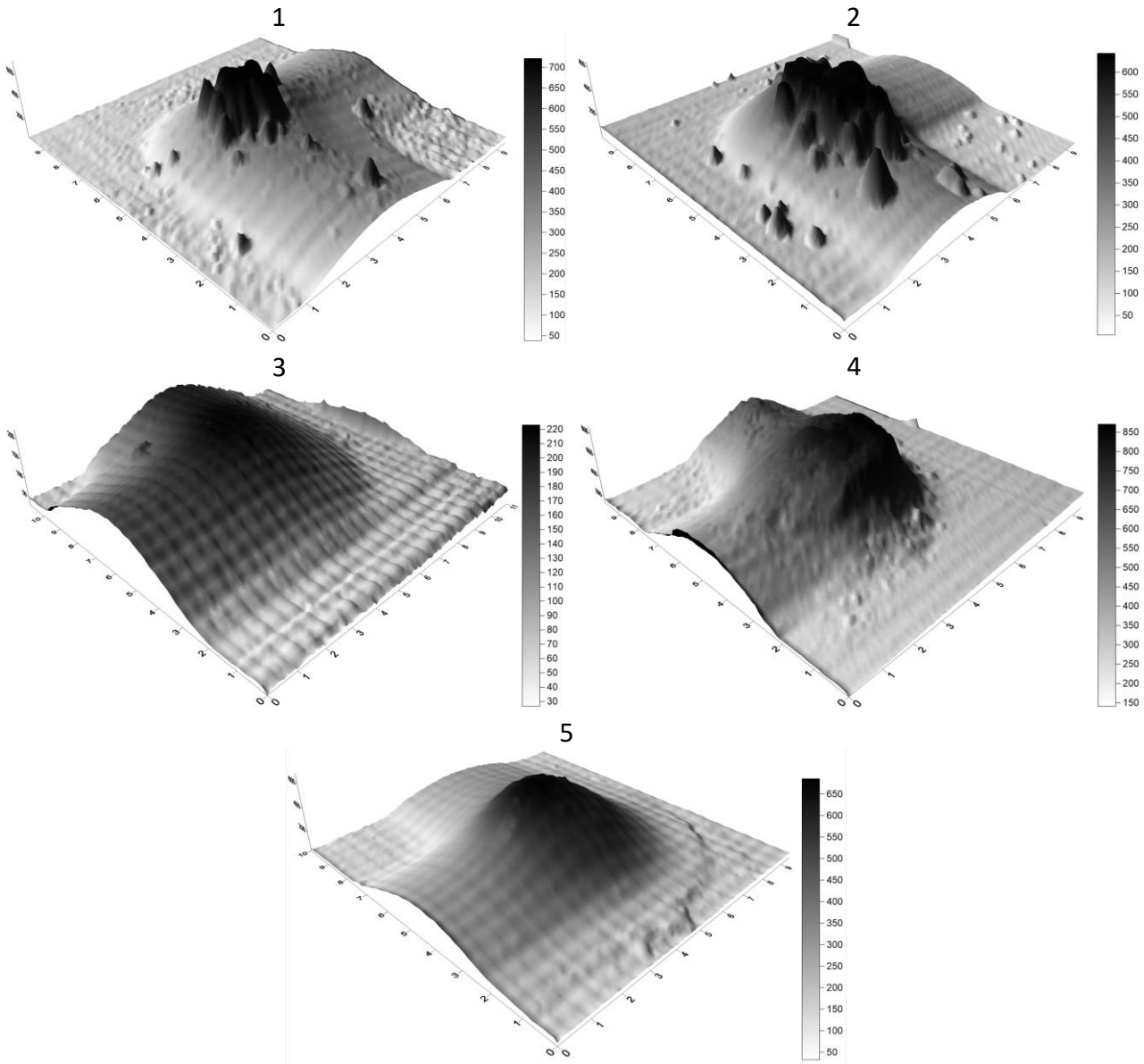

Figure 5. *Profilograms of 3D-printed square objects: 1 to 5 - correspond to experiment numbers in Table 2*

Figure 5 (1,2) shows active dendrite formation on the corner section of the square. The cross-section profile (Figure 7, curve 1, 2) shows that the height of dendrites is nearly the height of the deposited metal thickness. The reason for dendrite formation is the high current density in the corner section and a longer period of deposition because the anode stays longer above the corner compared to the straight section of the square edge. An increase in the thickness of the copper deposit, as well as the formation of dendrites at the corners, is associated with a decrease in the speed of movement and some delay of the nozzle when passing the corner of the trajectory. As a result, the amount of electricity that falls on this part of the trajectory increases, and because of

slowing down, the average current density will increase, which provokes dendrite formation. The dendrite formation problem is solved by increasing the additive concentration. The additive is known to increase the deposition polarization, thus reducing the deposition rate. In this work, the dendrite formation was hindered when additive concentration was corrected according to recommendation: 2 mL/L of Rubin T200-A, 8 mL/L of Rubin T200-G and 2 mL/L of Rubin T200-E.

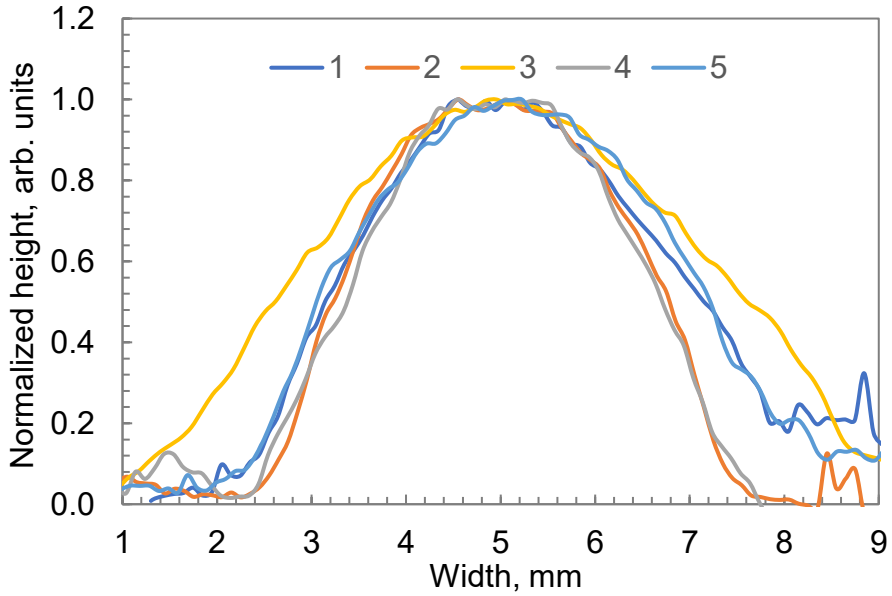

Figure 6. *Typical cross-section of the edge of the printed square object. Numbers 1 to 5 correspond to experiment numbers in Table 2*

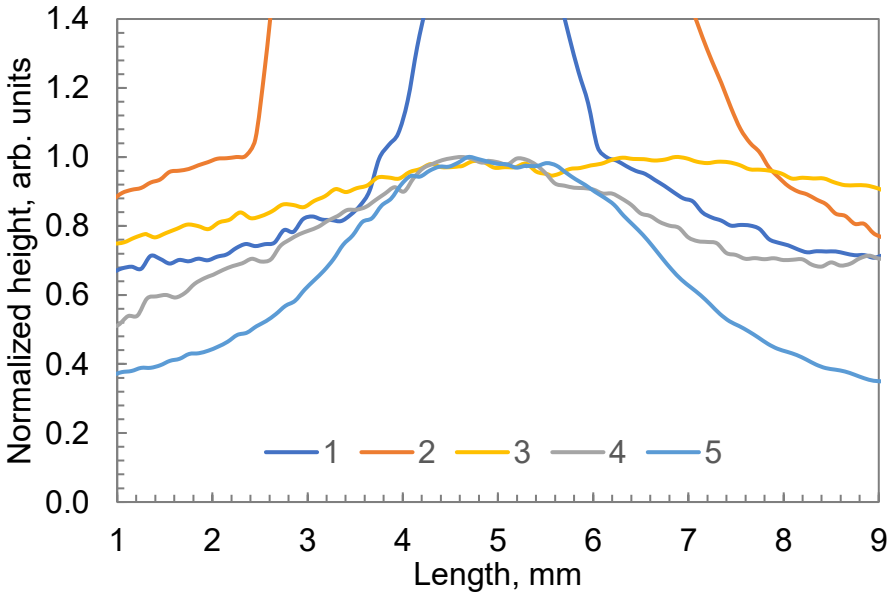

Figure 7. *Typical cross-section of the corner of the printed square object. Numbers 1 to 5 correspond to the experiment number in Table 2*

The movement speed of the nozzle influences the deposition process in both the corner and straight sections. Very low speed increased the deposited metal area. The cross-section of the edge shows a 40 % wider deposition area. The increase in nozzle movement speed from 2.5 to 1.6 s/voxel does not further reduce the deposited surface area.

In the corner section, the lowest tested speed of 5 s/voxel, the most uniform layer was deposited. The thickness of the deposited metal in the corner is only 15 % higher than on the edge. The next

tested speed of 2.5 s/voxel increased the thickness in the corner to 1.5 times, and when the nozzle speed reached 1.6 s/voxel, the corner thickness was nearly 2.5 times higher than the edge one.

The change in the deposited metal thickness in the corner section is caused by the reduction of nozzle movement speed (Figure 8). At the lowest tested speed of 5 s/voxel, the nozzle moves through the corner section with nearly the same speed as through the straight section. Thus, the amount of deposited metal remains the same. When the speed increases to 2.5-1.6 s/voxel, the nozzle passes the straight section faster than the corner section. So, the thickness of the deposited metal on the straight section becomes lower, and in the corner section – higher.

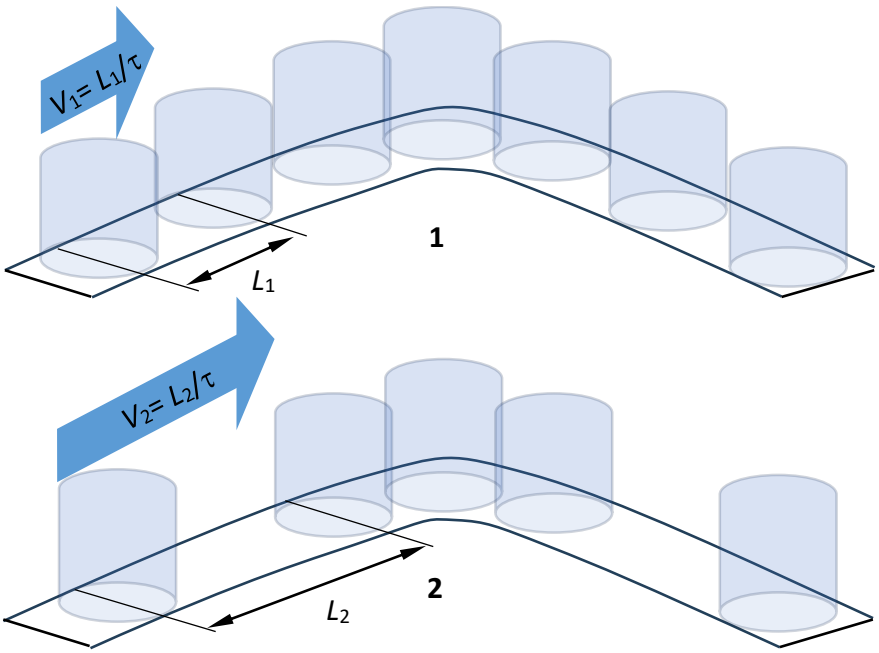

Figure 8. *Schematic explanation of nozzle moving speed influence on the thickness of deposited metal: 1 - low nozzle moving speed; 2 - high nozzle moving speed*

Further investigation should be aimed at current control over the corners in a manner that reduces the current value proportional to the speed reduction.

Conclusions

The local deposition process from copper sulfate electrolyte was investigated. The additive concentration in the electrolyte was found to influence dendrite formation. The dendrites are formed on the corner sections of a square model. The use of recommended additive concentration 2 mL/L of Rubin T200-A, 8 mL/L of Rubin T200-G and 2 mL/L of Rubin T200-E reduces the formation of dendrites.

Nozzle movement speed influences the deposition area of the metal and its thickness. The lowest tested nozzle movement speed of 5 s / voxel increased the deposition area by nearly 40 % compared to 2.5 s/voxel. Further increase of nozzle movement speed to 1.6 s/voxel does not change the deposition area.

The increase in nozzle movement speed influences the deposited metal thickness in the corner sections. The thickness in the corners increases by 2.5 times compared to the edges of the square when the nozzle movement speed increases from 5 to 1.6 s/voxel.

The results obtained in this work can be further used to develop electrochemical 3D printing technology. The further investigation direction should be aimed at current control over the corners in a manner that reduces the current value proportional to the speed reduction.

***Acknowledgements**: This work was supported by the Ministry of education and science of Ukraine (Reg. number 0122U001523, 2022).*

References

[1] I. Gibson, D. Rosen, B. Stucker, *Additive Manufacturing Technologies*, Springer, New York, USA, 2010, p. 472. https://doi.org/10.1007/978-1-4419-1120-9

[2] A. Serajuddin, Challenges, current status and emerging strategies in the development of rapidly dissolving FDM 3D-printed tablets: An overview and commentary, *ADMET and DMPK* **11** (2023) 33-55. https://doi.org/10.5599/admet.1622

[3] W. E. Frazier, Metal additive manufacturing: a review, *Journal of Materials Engineering and Performance* **23** (2014) 1917-1928. https://doi.org/10.1007/s11665-014-0958-z

[4] D. Herzog, V. Seyda, E. Wycisk, C. Emmelmann, Additive manufacturing of metals, *Acta Materialia* **117** (2016) 371-392. https://doi.org/10.1016/j.actamat.2016.07.019

[5] X. Li, P. Ming, S. Ao, W. Wang, Review of additive electrochemical micro-manufacturing technology, *International Journal of Machine Tools and Manufacture* **173** (2022) 103848. https://doi.org/10.1016/j.ijmachtools.2021.103848

[6] G. Ercolano, T. Zambelli, C. van Nisselroy, D. Momotenko, J. Vörös, T. Merle, W.W. Koelmans Multiscale additive manufacturing of metal microstructures, *Advanced Engineering Materials* **22** (2020) 1900961. https://doi.org/10.1002/adem.201900961

[7] L. Hirt, R.R. Grüter, T. Berthelot, R. Cornut, J. Vörös, T. Zambelli, Local surface modification via confined electrochemical deposition with FluidFM, *RSC Advances* **103** (2015) 84517-84522. https://doi.org/10.1039/c5ra07239e

[8] W. Ren, J. Xu, Z. Lian, P. Yu, H. Yu, Modeling and experimental study of the localized electrochemical micro additive manufacturing technology based on the fluidFM. *Materials* **13** (2020) 2783. https://doi.org/10.3390/ma13122783

[9] G. Ercolano, C. van Nisselroy, T. Merle, J. Vörös, D. Momotenko, W. W. Koelmans, T. Zambelli Additive manufacturing of sub-micron to sub-mm metal structures with hollow AFM cantilevers, *Micromachines* **11** (2020) 6. https://doi.org/10.3390/mi11010006

[10] W. Ren, J. Xu, Z. Lian, X. Sun, Z. Xu, H. Yu, Localized electrodeposition micro additive manufacturing of pure copper microstructures, *International Journal of Extreme Manufacturing* **4** (2021) 015101. https://doi.org/10.1088/2631-7990/ac3963

[11] A. Ambrosi, R. D. Webster, M. Pumera, Electrochemically driven multi-material 3D-printing. *Applied Materials Today* **18** (2020) 100530. https://doi.org/10.1016/j.apmt.2019.100530

[12] S. Burlison, M. Minary-Jolandan, Multiphysics simulation of microscale copper printing by confined electrodeposition using a nozzle array, *Journal of Applied Physics* **131** (2022) 055303. https://doi.org/10.1063/5.0072183

[13] Y. Guo, P. Liu, P. Jiang, Y. Hua, K. Shi, H. Zheng, Y. Yang, A flow-rate-controlled double-nozzles approach for electrochemical additive manufacturing. *Virtual and Physical Prototyping* **17** (2022) 52-68. https://doi.org/10.1080/17452759.2021.1989751

[14] X. Chen, X. Liu, P. Childs, N. Brandon, B. Wu, A low cost desktop electrochemical metal 3D printer, *Advanced Materials Technologies* **10** (2017) 1700148. https://doi.org/10.1002/admt.201700148

[15] F. Zhang, D. Li, W. Rong, L. Yang, Y. Zhang, Study of microscale meniscus confined electrodeposition based on COMSOL, *Micromachines* **12** (2021) 1591. https://doi.org/10.3390/mi12121591

[16] X. Chen, X. Liu, M. Ouyang, J. Chen, O. Taiwo, Y. Xia, P. Childs, N.P. Brandon, B. Wu, Multi-metal 4D printing with a desktop electrochemical 3D printer, *Scientific Reports* **9** (2019) 3973. https://doi.org/10.1038/s41598-019-40774-5

[17] S.J. Dover, A.E.W. Rennie, G.R. Bennett, Rapid Prototyping Using Electrodeposition of Copper, *Solid Freeform Fabric Symposium*, 1996, pp. 191-198. http://hdl.handle.net/2152/69936

[18] H. Fan, Y.P. Zhao, S.K. Wang, Technical study of Jet electrodeposition in manufacture of metal parts, *Key Engineering Materials* **667** (2016) 259-264. https://doi.org/10.4028/www.scientific.net/KEM.667.259

[19] C. Wang, L.D. Shen, M.B. Qiu, Z.J. Tian, W. Jiang, Characterizations of Ni-CeO_2 nanocomposite coating by interlaced jet electrodeposition, *Journal of Alloys and Compounds* **727** (2017) 269-277. https://doi.org/10.1016/j.jallcom.2017.08.105

[20] E. M. El-Giar, R. A. Said, G. E. Bridges, D. J. Thomson, Localized electrochemical deposition of copper microstructures, *Journal of The Electrochemical Society* **147** (2000) 586-591. https://doi.org/10.1149/1.1393237

[21] C. Y. Lee, C. S. Lin, B. R. Lin, Localized electrochemical deposition process improvement by using different anodes and deposition directions, *Journal of Micromechanics and Microengineering* **18** (2008) 105008. https://doi.org/10.1088/0960-1317/18/10/105008

[22] J. C. Lin, T. K. Chang, J. H. Yang, Y. S. Chen, C. L. Chuang, Localized electrochemical deposition of micrometer copper columns by pulse plating, *Electrochimica Acta* **55** (2010) 1888-1894. https://doi.org/10.1016/j.electacta.2009.11.002

[23] G. Vasyliev, V. Vorobyova, D. Uschapovskiy, O. Linyucheva, Local electrochemical deposition of copper from sulfate solution, *Journal of Electrochemical Science and Engineering* **12** (2022) 557-563. http://dx.doi.org/10.5599/jese.1352

[24] G. Vasyliev, V. Vorobyova, D. Uschapovskiy, O. Linyucheva, Influence of polarization curve slope on the accuracy of local copper electrodeposition from sulphate electrolyte, *Journal of Electrochemical Science and Engineering* **6** (2023) 971-980. https://doi.org/10.5599/jese.1899